THE UNIVERSITY OF HULL

Issues of Scale in Nuclear Graphite Components

being a Thesis submitted for the Degree of
Doctor of Philosophy, Department of Engineering
in the University of Hull

by

Matthew Holt, MEng

July 2008

Abstract

A conceptual model for the determination of the effect of specimen size on the strength of nuclear graphites was developed using abstraction techniques and finite element Analysis (FEA). The model was designed to be able to predict the response of nuclear graphites (primarily IM1-24 graphite) using fixed material properties under defined loading conditions and model constraints. Employing custom written C++ programs, randomly generated microstructural representations of IM1-24 graphite at a number of differing sizes were produced and subsequently had the stresses and strains through the model analysed using ANSYS FEA software.

In conjunction with the conceptual modelling, a comprehensive testing programme was designed and developed to gain a data set for the validation of the model outputs. Two types of graphite were selected for the testing programme. Logically, IM1-24 graphite and a control graphite R4340. A large number of varying sizes of specimen were tested to failure under compression, 3-point and 4-point flexural loading and all results recorded and analysed.

On completion of both programmes it was found that the modelling programme proved to be successful, in particular, the microstructural response of the virtual material when compared to the testing results. An issue of constant strain inherent in the models due to the loading conditions rendered the numerical results difficult to compare to the testing programme, but the data obtained for the testing programme has expanded the knowledge of the response of IM1-24 graphite at differing scales and loading conditions.

Acknowledgements

The author would like to thank British Energy Generation Ltd. for their funding and contribution throughout the course of the research, in particular Jim Reed and Alan Steer, who without their support this research would not have been possible.

The author also thanks Dr. Gareth Neighbour for all his guidance, assistance and invaluable knowledge, as well as his infinite patience.

Additionally, the author thanks all the family and friends who have provided time and resources to assist wherever they can over the several years it has taken to complete this thesis. There is unfortunately not enough room to list all of them here.

Table of Contents

List of Figures, Graphs and Tables

Chapter 1 - Introduction

The United Kingdom's nuclear reactors were built in accordance with stringent design codes for single components and consequently contain elements of redundancy within the reactor core. Currently, the majority of Advanced Gas-cooled Reactors (AGRs) are reaching the second half of their operating lives, which when designed excluded the possibility of cracked bricks within the core. The prediction of whether bricks will crack within the core is based on the measurement of small samples of material, even though the actual size of the core bricks is much greater.

Material properties are often described as being characteristic and are quoted as such irrespective of scale, *e.g.* properties such as the melting point or friction coefficient of a given material are constant regardless of the length, area or volume under investigation. However, this is not necessarily correct for all material properties. Figure 1.1 depicts a solid block of material at two different volumes, but with the same dimensional ratio. Assuming the smaller block was 1 unit x 1 unit x 1 unit and the larger block was 10 units by 10 units x 10 units, would these two specimens be expected to fail at the same stress? Would they both have the same material properties? And can they both be considered to behave in the same way under loading?

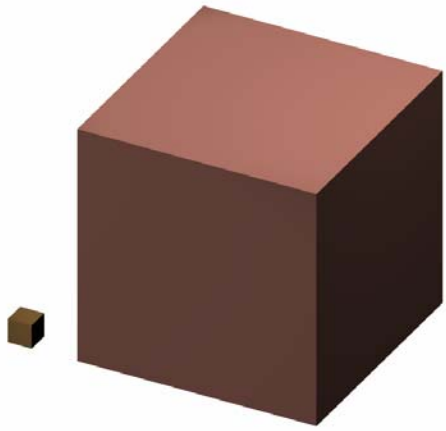

Figure 1.1 – Does volume change the perception of strength?

Many studies have been undertaken in which the properties of the material, most often strength, have been seen to vary with geometry, most often volume (e.g. Brocklehurst, 1977). Few studies have reached a fully satisfactory physical explanation with the potential to accurately predict the properties of large components. The difference in strength values with volumes is sometimes explained by Weibull theory (often referred to as the weakest link theory), which can be used to determine the probability that a specimen will have a certain strength. The theory works on the principle that the larger a specimen volume is, the more likely it is to contain critical flaws and defects that will ultimately lead to failure. However, it is unknown if Weibull methods work well for very small sample volumes and remains largely untested at large sample volumes.

It is useful to remind the reader of the relevance of the Griffith's equation (Griffith, 1921) for purely elastic materials to this work as it demonstrates a fundamental approach to the problem of fracture (whereas Weibull theory is empirical) such that strength is related to flaw size via the following equation:

$$\sigma = \sqrt{\frac{2E\gamma_S}{\pi a}} \qquad \text{Equation [1.1]}$$

The Griffith equation balances the surface energy, γ_s, Young's modulus, E, and crack length, a, with the stress level required to continue crack propagation. Given the complexity of the microstructure of polygranular graphite, the use of Equation 1.1 as a

basis to determine the mechanical properties, *e.g.* strength, of components with geometry or size is very limited. It is therefore useful to investigate further the relationship between the mechanical properties and geometry, *e.g.* strength and volume, of polygranular graphite.

As with most ceramic materials, nuclear graphites contain a distribution of flaw sizes. Often, an understanding of these distributions and their effect on strength is obtained by a statistical treatment. The most common treatment of specimen size effects with ceramic materials is to consider a statistical distribution as proposed by Weibull (1951). Essentially, the Weibull theory assumes a variation in flaw size and that propagation of a crack from the most critical flaw, under a given stress system, results in failure of the whole body. He first proposed a statistical model for brittle failure that described the survival probability $P_s(V_0)$ as the fraction of identical samples, each of volume V_0, which survive loading to a tensile stress, σ, such that

$$P_s(V_0) = \exp\left[-\left(\frac{\sigma}{\sigma_0}\right)^m\right] \qquad \text{Equation [1.2]}$$

where σ_0 is simply the tensile stress that allows 37% of samples to survive, and m is the Weibull modulus which is determined empirically using best fit curve methods. The lower the value of m, the greater the variability in strength. Having determined m, it is in theory possible to predict the dependence of strength upon specimen volume since the strength of a material is dependent upon the flaw size distribution within its volume. A large sample is more likely to fail at a lower stress than a smaller sample because there is a higher probability that it will contain a large flaw. The volume dependence on the strength of a material is described by Weibull theory as the probability that a batch of samples (n) will all survive a given stress (σ) is simply $[P_s(V_0)]^n$.

There is support for the logarithmic volume dependency with strength in other works. For example, Brocklehurst and Darby (1974) considered four types of tests on AGR moderator graphite: (a) uniform tensile tests; (b) bend tests on beams; (c) internal pressure tests on rings; and (d) tests on rings under diametral compression loading.

Their results suggested that the tensile/bend strength correlated very well with the logarithmic value of the volume. They found that the Weibull theory offered a qualitative explanation for their results for (a) the volume dependence of graphite; (b) the strength distribution at constant volume; and (c) the ratio of maximum stresses at failure in the different tests. However, they concluded that the Weibull theory is unable to account quantitatively and consistently for all strength data obtained in the different tests. Brocklehurst (1977) stated that the Weibull theory strictly only applies to brittle, linear-elastic materials, and since graphites show non-linearity in their stress-strain behaviour it is not surprising that the theory does not conform to experimental data.

A primary reason for investigating the issues of scale is to improve the basis on which data obtained from trepanned samples from within a graphite core are translated to the component as a whole. The current procedure for testing specimens of graphite is to trepan the samples from a reactor core and then to cut each sample into six slices (~19mm diameter, ~6mm thick). For each slice, the coefficient of thermal expansion (CTE) is measured, along with the dynamic modulus and the weight loss in order to create a profile through the brick. From a selected number of these slices, samples 6mm x 6mm x 19mm are cut and then tested in flexure (typically three-point flexural tests). The results from these flexural tests are then analysed and scaled accordingly to predict the response from the whole core.

It is an interesting feature of the Weibull theory that if the theory is used in isolation then a flexural sample of the same volume as a core brick may be expected to have a value of strength approximately equal to half that of a sample used in small scale testing. This remark demonstrates the need to investigate further and to determine the boundary where the Weibull theory ceases to be true for nuclear graphites and indeed other materials. It is important to realise that although the Weibull theory is largely unproven at the large scale it is NOT the aim to prove nor disprove the theory, nor is it the aim of this work to comment on the current methods used in scaling up properties to demonstrate or otherwise the integrity of fuel bricks. The aim is, however, to have a better physical understanding (which is absent in the weakest link model) on how engineering ceramic materials behave through using the technique of abstraction in systems modelling, particularly nuclear graphite. However, for any modelling technique developed and executed to have any “real world” relevance, there should be a

set of data available for comparison and validation. Performing mechanical tests on samples of graphite with differing dimensions and geometric shapes will enable the establishment of a basic theory relating scale to material properties. However, there are a number of factors which must be considered before proceeding with a testing programme. Design of experiments (DOE) can be used to correctly plan, execute and analyse an experiment and its results, giving an efficient way of reaching the desired goal without unnecessary experimentation. These factors include:

- Material property – which properties should be examined and which tests are most appropriate for determining them (*e.g.* tensile/compressive/bend strength, *etc.*)
- Geometry – what shape should the test specimens take (cuboid, cylindrical, existing specimen standard or custom design)
- Scale factor – the incremental change in scale between specimens
- Number of specimens – minimum number of specimens of each geometry and scale
- Test material – the grade of the material, as received manufactured
- Testing equipment – the selection of tests will determine what, and if any, specialist, equipment is required
- Analytical methods – the most suitable method of interpreting the results

Although AGR reactor cores were effectively produced by three different manufacturers (Neighbour, 2002) with the same specification and raw materials, there are variations in the material properties of the graphites due to differences in the manufacturing processes (*e.g.* graphitisation temperature). However, it can be expected that if the graphite produced by one of the manufacturers can be fully understood (*i.e.* a relationship is developed) then the same should apply to the others with just the absolute values of the material properties differing. Therefore, it is proposed to investigate the relationship between the mechanical properties and the geometry/size of graphite produced by one manufacturer. In addition, to enable the quick identification of any effects related to the graphite, a reference material should be selected with a homogeneous microstructure. The scale issues for the graphite can be compared to those of the reference material and normalised.

The combined approach of abstract modelling and validation through physical testing will enable a comprehensive study of the issues of scale relating to the behaviour of polygranular nuclear graphite. However, it is not anticipated that the study will provide a definitive answer to the question of *"How does size affect the material properties of graphite?"*. Nuclear graphite has been studied in great detail during the past 60 years and some aspects of its behaviour remain a mystery to the graphite community. This study intends to look at the issues associated with scale from a different angle, with the ultimate aim being to aid modelling the behaviour of a reactor core more accurately than is available at this point in time. Therefore, the objectives of the research are:

1. To develop a computer model for examining the link between scale and material properties using the technique of abstraction
2. To produce an experimental data set through performing a series of suitably defined tests that can be utilised by the modelling programme for validation purposes
3. To determine a relationship between scale and material properties (particularly strength) from analysing the data obtained from the modelling and validation stages of the research

This thesis is sectioned into four parts, Part A is a review of literature available on the graphite microstructure and its inherent properties, testing techniques employed to determine material properties, fracture mechanics and the development of microstructural feature characterisation, computer modelling techniques that enable the analysis of material structures and predict material properties, and the principles of abstraction. Following from this Part B sets out a conceptual model to explain the issues of scale, the development using the technique of abstraction and the predictions of the model obtained through finite element analysis. To validate the conceptual model, the development and execution of a comprehensive testing programme is detailed in Part C. Part D is an analysis of the effects of increasing scale on the measured material properties of graphite through comparing the modelling programme and testing programme results. Conclusions are also drawn in Part D as to how the approach can be utilised for a better understanding of the graphite microstructure and recommendations made for how the work can be furthered in future studies.

Part A: Literature Review

Chapter 2 – The Manufacture, Microstructure and Fracture of Graphite

This chapter provides a literature review of industrial graphite including its history, manufacture and applications. It also examines the microstructure of IM1-24 nuclear graphite, the typical mechanical properties of graphite, fracture of graphite and other ceramic materials, the issues relating to scale, and common testing techniques employed to determine various material properties. In addition to these subject areas, the review also covers numerical and computer modelling for graphite and other ceramics such as concrete, finite element analysis of brittle materials, and the concept of abstraction and its utilisation in structural analysis (further details on the aspects of the literature search are given in Appendix A).

2.1 The History and Manufacture of Graphite

Graphite is a form of carbon that occurs naturally throughout the world, particularly in Canada, India and Siberia. Natural graphite can commonly be found in metamorphic rocks and appears as a lustrous black carbon mineral, which is relatively soft and an excellent conductor of heat and electricity. Graphite sublimes at approximately 3500ºC and is extremely resistant to acid and thermal shock, as well as being chemically inert.

Natural graphite became used as a material for drawing during the middle ages, with the manufacture of pencils originating during the reign of Elizabeth I in 1564. One of its first uses as a dry lubricant was during the Napoleonic wars where the raw material was used to make gunpowder grains free flowing. During the second half of the 1800s, graphite was being used on a large scale for the production of crucibles for melting non-ferrous metals. As high temperature furnaces were developed at the end of the

nineteenth century, so was the ability to artificially manufacture graphite. Graphite developments continued with electrodes for electrochemical processes, graphite arc furnaces for melting steel, and electrographite brushes for electrical machines. Following on from these came the development of graphite-moderated nuclear reactors, graphite nozzles and nose cones for space vehicles, and carbon fibres that are in widespread usage today (Prince, 1977).

In the commercial field, natural graphite is categorised by three forms; amorphous, crystalline lump (or vein) and flake graphite. Amorphous graphite is formed by the crystallisation of carbon from surrounding organic sediments and occurs as distorted seams of minute particles within ungraphitised materials. Crystalline lump graphite occurs as a large vein and deposits are commonly found in fissures and other cavities in igneous or metamorphic rocks, with particles ranging in size from 2 mm to more than 2 m. Flake graphite is defined as thin flakes of graphite found dispersed on sediments such as marble, gneiss and schist, and is graded according to its graphitic carbon content (Boucher, 1994).

Graphite is manufactured using the process discovered by Edward Acheson in the 1890s, who had worked with Thomas Edison on the carbon-filament incandescent lamp. Whilst experimenting with silicon carbide, Acheson volatilised away the silicon in an electric arc furnace at approximately 4000ºC and discovered high quality graphite was left behind. Both the graphite and electricity industries have grown and been closely linked together since that time.

Manufacture begins with a high molecular weight hydrocarbon which is converted to coke through heating in the absence of air. The coke is then calcined at 1400ºC for approximately two hours in order to remove the impurities and volatile hydrocarbons and to stabilise the material by developing the crystal structure. The calcined coke is crushed and sieved to obtain a specific distribution of particle sizes (termed filler particles, and are typically 1 mm and smaller) to be employed in the manufacture of various grades of graphite. The coke particles are bound together using hot tar pitch (the binder) with a ratio of 3:1 at around 165 – 175ºC. A coal-tar pitch is preferred over others due to its thermoplasticity, high carbon content and low cost. The mixture is then

extruded through a die or moulded to form rough blocks before the next stage in the process.

At this stage the isotropy of the graphite can be determined, for this is influential in the behaviour of the graphite in-service. For example, once the filler and binder are mixed the particle orientation within the bulk material can be introduced. The coke used in the manufacture of PGA graphite is needle shaped and extruding at this stage aligns the filler particles in the direction of the extrusion. The Gilsocarbon coke used in the manufacture of IM1-24 is spherical and when moulded the particles tend to line up with their longest dimension perpendicular to the moulding force. Therefore, different mechanical properties can be obtained depending on the alignment of the filler particles.

Once the material has been shaped, the "green" article is baked at 1000ºC with the heating and cooling cycle taking between one and two months depending on the size of the batch. As the volatiles are released from the coke a pore network is created in their absence. The material is then impregnated with pitch to reduce the porosity and increase the density of the finished article. Graphitisation then takes place, during which the material is heated to about 3000ºC in a furnace packed with coke dust and sand through the application of an electric current. Crystal development takes place during this phase which lasts around 18 days in total (3 – 4 days to reach the required temperature, 1 day at that temperature, and approximately 14 days to cool). The properties of the material change noticeably particularly in regard to the ease of machining and improved thermal conductivity. Also during the graphitisation the purity of the material increases as many contaminants are volatised out and further purification can be achieved through injecting halogen gases during the graphitisation process (halogenation). Nuclear graphites must have low levels of impurities to avoid elements with high neutron absorption properties (Prince, 1979).

From the raw material coke arriving at the manufacturing plant to it leaving as graphite blocks ready for machining, the process takes approximately nine months. To construct the reactor, the blocks are machined into complex interlocking shapes (as discussed later) that enable the insertion of fuel and control rods and the circulation of carbon dioxide. All machining is performed in "clean" conditions to minimise contamination, for which the graphite is regularly checked, as well as the material condition and

dimensional accuracy. A diagram depicting the main stages of the manufacture process for graphite can be seen in Figure 2.1.1.

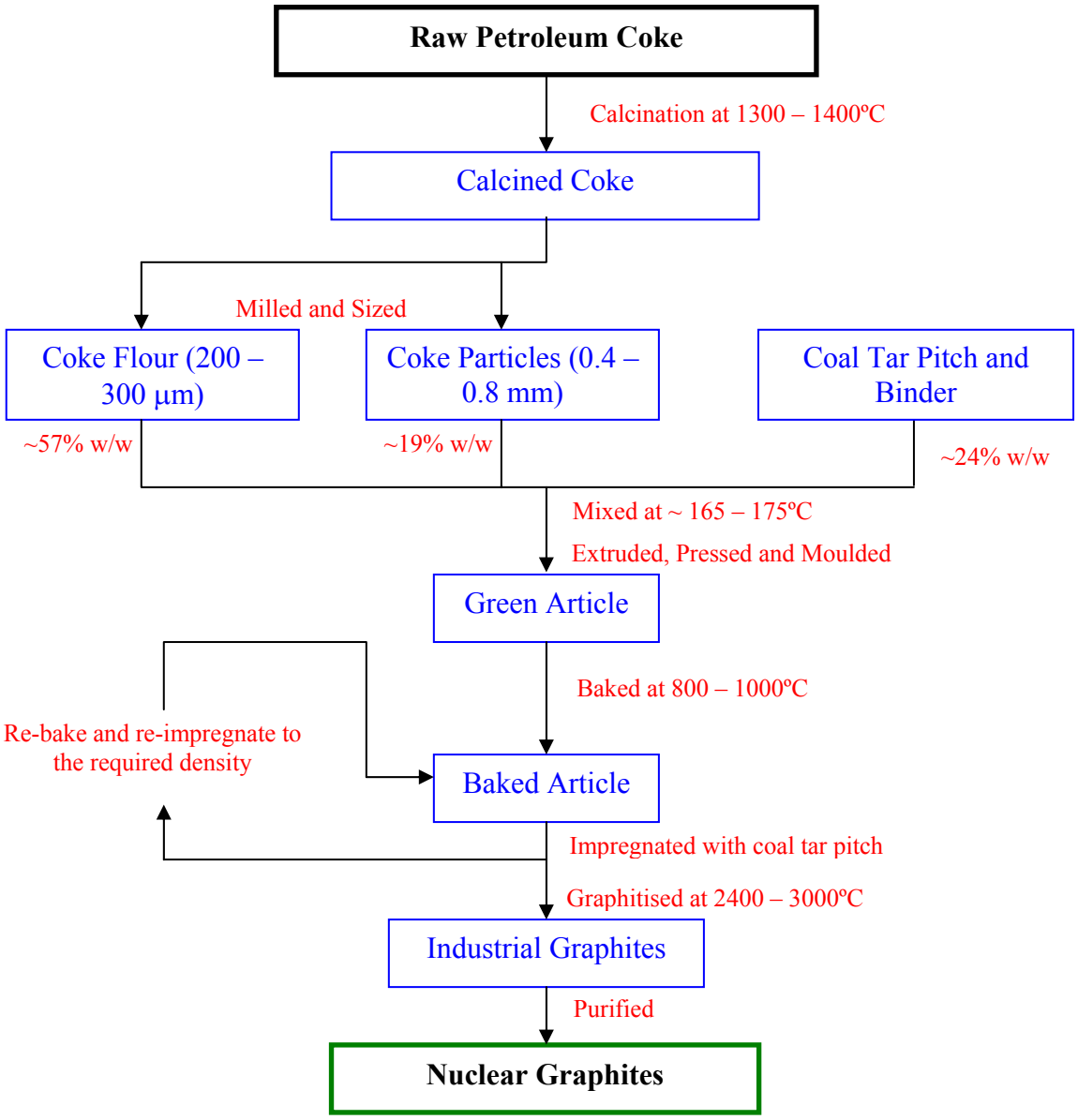

Figure 2.1.1 – Production process for the manufacture of nuclear graphites (Neighbour, 2003).

The use of graphite in the commercial nuclear industry dates back to 1952 and some of its typical applications are for that of the moderator, reflector, fuel sleeves and the control rod material. The properties inherent in the material make it ideal for use in a reactor core, and the fact that it can be manufactured relatively cheaply and is strong enough to act as a structural component only add to its desirability. Although all nuclear graphites provide the same function within a reactor core their properties vary dramatically from type to type. For instance, the two main graphites used in the UK

nuclear industry are IM1-24 (for AGR) and Pile Grade A (for Magnox), and both are used for the same applications, but have differing mechanical properties and microstructures. Fundamentally this comes from the manufacture of the graphites; the processes that the raw materials are subjected to during production determine the properties of the finished graphite.

The construction of an AGR core is based on a loosely-keyed, large brick/small brick design (see Figure 2.1.2) which is an improvement on the initial Magnox reactor core design.

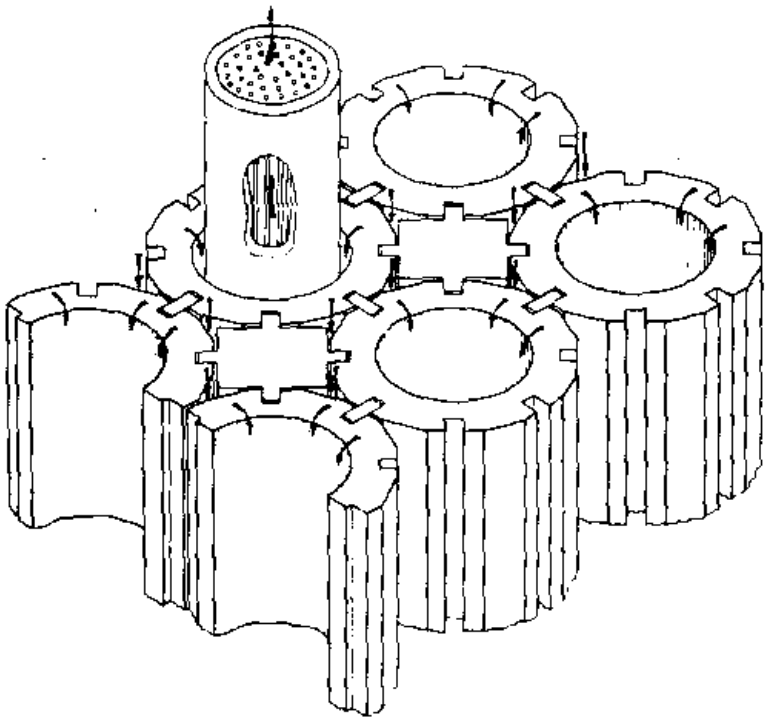

Figure 2.1.2 – Example of large brick/small brick AGR core design (Prince, 1979).

The fuel channel bricks (the circular bricks in Figure 2.1.2) stand approximately 1 metre high with the core constructed on a square lattice formed from spigotted columns of these large bricks. The interstitial spaces are taken up with smaller square bricks with each keyed into four adjacent large bricks. The large bricks may contain control-rod channels, flux-scanning equipment, graphite samples, or may even be solid depending on their location in the core. The interstitial square bricks may be held in position by either loose keys or integrally machined keys, the loose keys being used at locations

where fuel channel bricks come together. There is a vertical offset at the brick junctions between columns of small and large bricks for additional core stability, which can be seen in Figure 2.1.3. The construction of the AGR core in this manner allows the alignment of the fuel rods and control rod channels to be assured, whilst enabling the thermal expansion and contraction of the graphite to take place due to the clearances between keys and keyways. The looseness of the keys within the keyways is important to ensure that any external loads can be transmitted to successive brick columns and that no fractures are induced through the structure locking up (Carpenter and Norfolk, 1984). This feature is known as radial keying and is employed so that if the clearances are adequate, the graphite can shrink and expand without distorting the core lattice or the channel alignment. A similar system is used in the Magnox reactor cores. In addition, radial keying allows the channel spacing to stay uniform as the core periphery expands and contracts (see Figure 2.1.4). The system provides excellent insurance against unexpected dimensional changes and gives graphite a structural role.

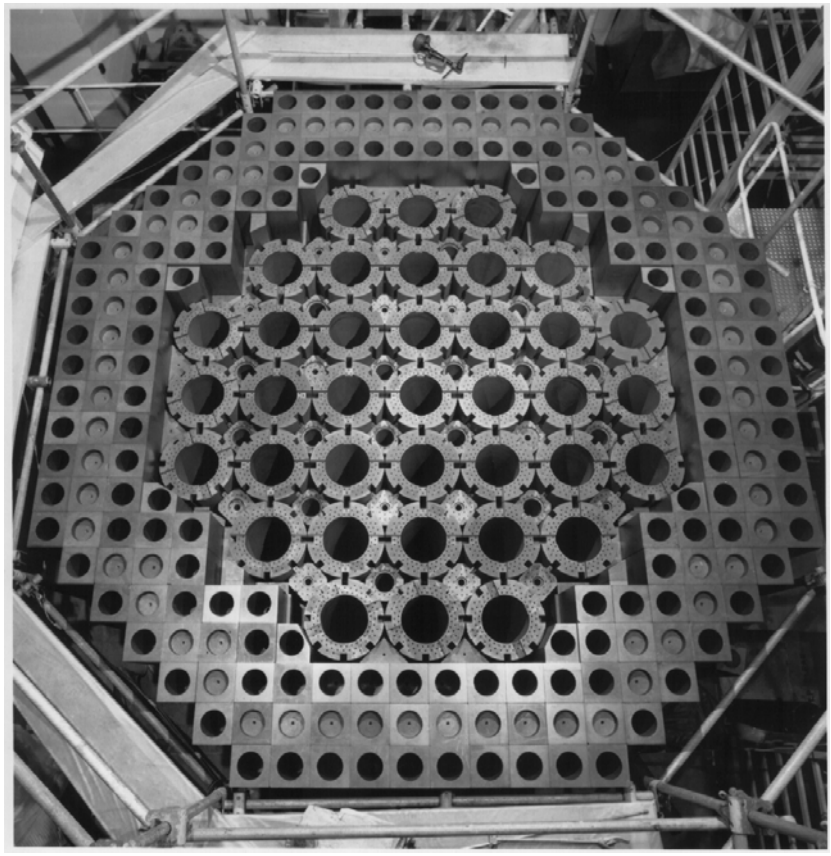

Figure 2.1.3 – Photograph of an AGR core prior to commissioning (courtesy of British Energy Generation Ltd.).

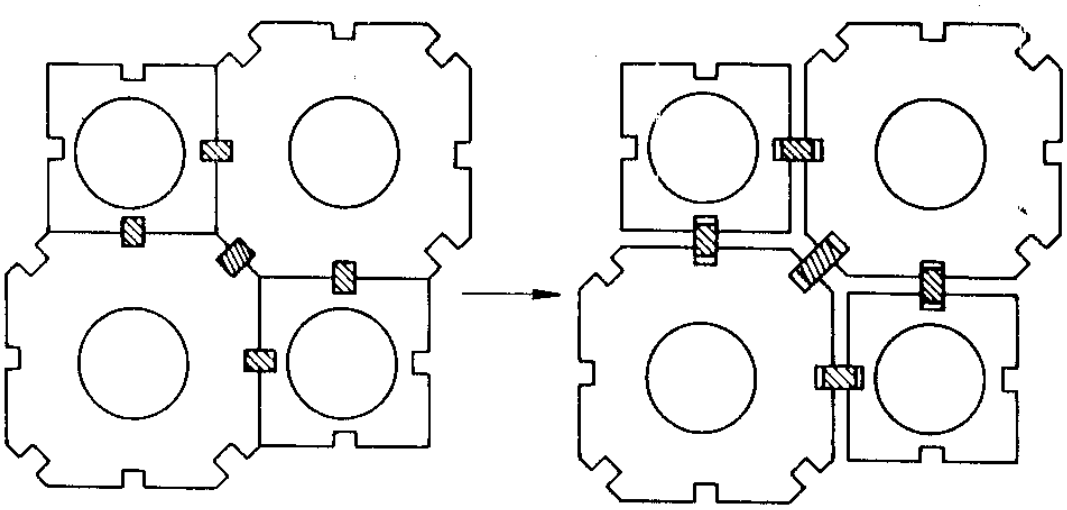

Figure 2.1.4 – Radial keying concept (Magnox reactor), the lattice can expand without distorting the structure (Carpenter and Norfolk, 1984).

An AGR core (Figure 2.1.3) consists of 332 fuelled columns, each containing eleven layers of radially keyed bricks. The channel alignment (and hence control rod insertion assurance) relies on both the loose keys and keys integral to the interstitial bricks, the latter bridging the fuelled bricks vertically to eliminate weak horizontal shear planes. The core periphery is connected via a restraint system to the reactor pressure vessel which is particularly important in resisting seismic disturbance. The core therefore expands as steel, requiring the keys to slide within the keyways.

To ensure optimum dimensional stability, graphite temperatures are kept below 550ºC throughout the reactor life, but shrinkage still occurs due to neutron irradiation (depicted in Figure 2.1.5a). Each component shrinks differently and distorts because the dose rates (fluence) are not uniform across the core, with the components nearest the fuel receiving the highest dose/fluence. In particular, shrinkage will reach a maximum before "turning around" to expand to the original volume, and beyond, due to the complex interaction of *c*-axis growth and *a*-axis contraction.

Throughout the reactor core's life different loads are applied to the keying system due to various influences such as brick distortion, gas pressure differences, vibration and differential thermal expansion. The stress pattern due to the internal stresses arising from the differential shrinkage is concentrated around the keyway root making this the most likely location for a crack to start. Due to differential shrinkage bricks also

become internally stressed (see Figure 2.1.5a) with tensile hoop stresses forming during shrinkage (before turnaround) and compressive hoop stresses forming during expansion (after turnaround). That is because, as long as the bore shrinks faster than the keyway root, the circumferential stress at the keyway root is compressive and so opposes the external load imposed through the key. However, later in the reactor's life the bore is the first to reach turnaround and stop shrinking, which reverses the internal stress pattern, *i.e.* it becomes tensile at the keyway root, augmenting the external load (Tucker and Wickham, 1990).

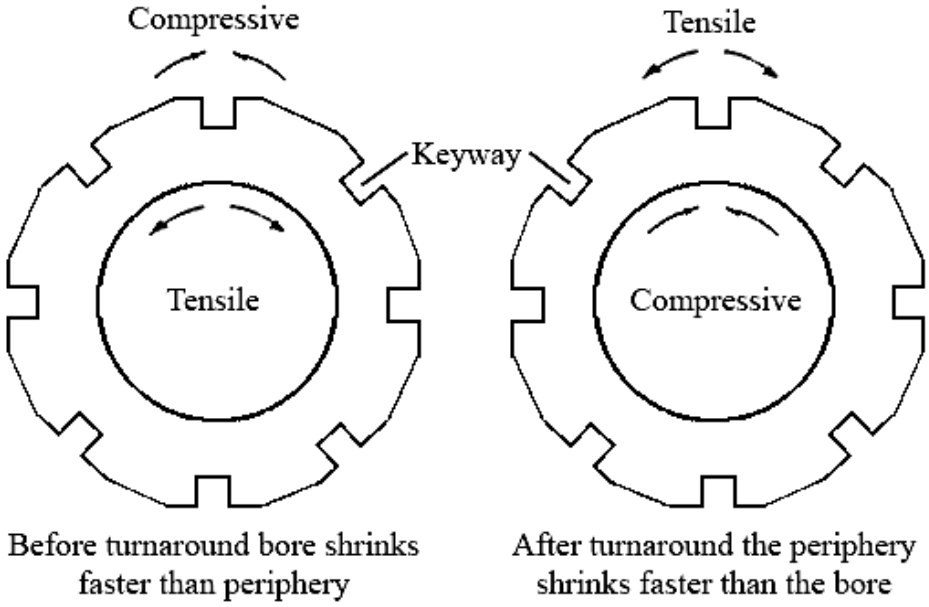

Figure 2.1.5a – Stresses on an AGR brick (Carpenter and Norfolk, 1984).

Figure 2.1.5b is a schematic to further demonstrate the dimensional change curve for AGR moderator graphite under irradiation. Initially the pores within the graphite close due growth along the *c*-axis of the crystallite; there then occurs transient pore generation caused by radiolytic oxidation that accommodates the *c*-axis growth and delays the turnaround; finally there is a steady state pore generation from the crystal growth. The two off-shoots from the curve indicate the theoretical case for unlimited pore closure and the case of unaccommodated crystal growth and undelayed pore generation.

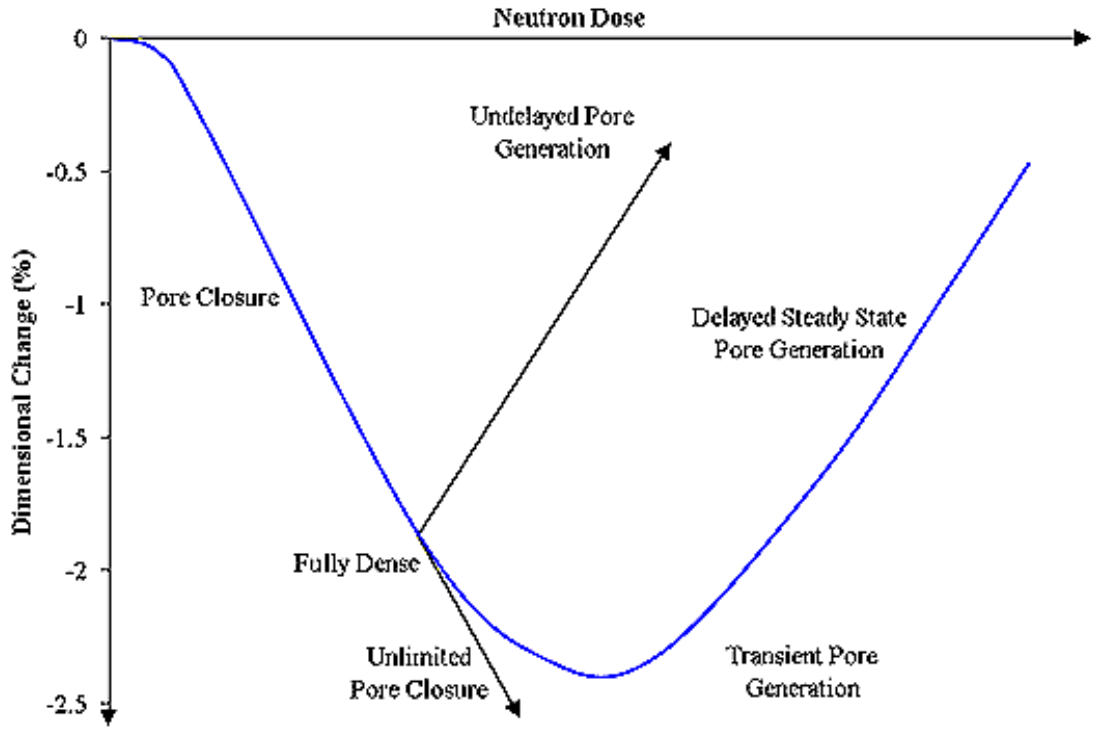

Figure 2.1.5b – Schematic of the dimensional change of AGR moderator graphite under irradiation (Neighbour, 2000).

2.2 Determination of the Mechanical Properties of Industrial Graphite

The following section is concerned with the mechanical properties of graphite at the macro scale, how some of these properties change and the most commonly used testing techniques to determine them. Although some atomic level detail is covered here, the microscopic structure of graphite and its failure mechanisms are covered in the next chapter.

As discussed previously, the core of a nuclear reactor (either Magnox or AGR) is manufactured from graphite and cannot be replaced. Graphite is the material of choice for nuclear reactors due to its ability to be employed as a moderator, slowing down neutrons from energies of up to 1.4 MeV to thermal energies of less than 1 eV in order to increase the efficiency of the reactor. It is particularly suited to the task because it has a low absorption rate, high elastic scattering because of its low atomic number, and a relatively low cost. It is also used as the primary structural material of the reactor

core. However, if the mechanical properties of the graphite deteriorate then the reactor's life may end prematurely.

Graphite is the form of carbon where the atoms are in their most stable lattice positions, even more stable than diamond and under heating it retains its integrity up to 3500ºC. It is used as a structural material even though it is weaker than structural metals at room temperature because it does not lose its strength as its temperature is raised – it actually gains strength between 1000ºC and 2500ºC. Also, its low coefficient of thermal expansion and high thermal conductivity give excellent resistance to thermal shock.

Graphite has a crystalline microstructure which consists of flat sheets of carbon atoms stacked on top on each other. Within a sheet, each atom is chemically bonded to its three nearest neighbours (SP2 hybridisation), creating an infinite lattice of hexagons (see Figure 2.2.1) making it a hexagonal close-packed (h.c.p.) structure. Two kinds of bonds link the atoms together, covalent and delocalised π bonds. Three strong covalent bonds link adjacent pairs and are reinforced by the π bond which is not associated with specific pairs of atoms, but is delocalised over the whole sheet. The hexagonal geometry is exactly right for both types of bond to have a maximum effect which therefore means the basal plane bonds are short and strong.

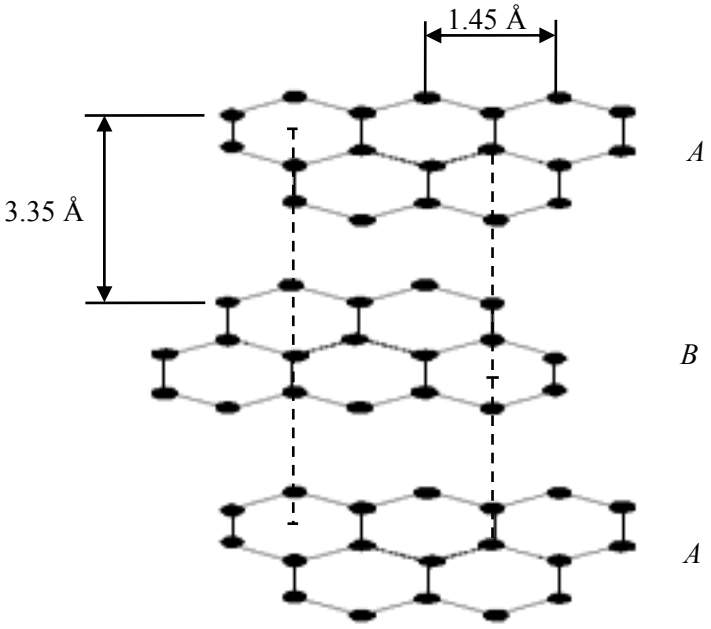

Figure 2.2.1 – Illustration of the crystal structure of graphite.

However, sheets adjacent to one another are much more loosely bonded with Van der Waals forces. For these adjacent sheets the minimum carbon-carbon separation is more than twice as far as that of the basal plane (3.35 Å compared to 1.45 Å) which allows the sheets to slide over each other. This weak bonding between sheets means that stacking faults can be easily accommodated. In perfect graphite successive sheets alternate between two out of three equivalent crystallographic positions, giving a stacking sequence of *…A B A B… etc.* With the absence of strong bonds to prevent the displacement, only a small amount of energy is needed to accommodate an extra sheet, giving an *…A B C A B…* structure (Amelinckx *et al.* (1965)). This provides two fracture mechanisms for the single crystal material, shear along the basal plane and cleavage.

The mechanical properties (and hence resistance to fracture) of polygranular graphite are influenced by the filler particle type and size, the binder type and the pore structure. The single crystals themselves are highly anisotropic (*i.e.* non-uniform physical properties along different dimensions), with a theoretical density of 2.265 g/cm^3. The level of anisotropy in the polycrystal is dictated by the degree of crystallite orientation within the filler particle or grain, and by the particle orientation caused by its geometric shape responding to the forming process (more so in the case of PGA graphite). For example, the most common filler grains used in the production of graphite are needle shaped (as is the case for PGA graphite). The needle-like filler grains can form a highly orientated structure and therefore a preferred deformation mechanism of slip along the layers, whereas the spherical shaped grains (as found in the Gilsocarbon graphites) would deform less easily in this direction.

In natural form, the crystallinity of graphite can vary greatly due to the inclusion of various other minerals found within the structure, and it exhibits a number of mechanical properties, but it is most commonly known for its high electrical and thermal conductivity. Synthetic graphites are man made materials that are created for many different applications from use within the steel industries to being utilised as a core component for the nuclear industry. Depending on the application and the type of graphite required, the mechanical properties of the synthetic form can, to a certain degree, be specified through the manufacturing process (as mentioned in Chapter 2.1 –

The History and Manufacture of Graphite), and as an example, the typical mechanical properties of IM1-24 graphite used in AGRs can be seen in Table 2.2.1.

Density	Coefficient of Thermal Expansion	Poisson's Ratio	Young's Modulus	Compressive Strength	Tensile Strength	Flexural Strength	Thermal Conductivity
1.804 - 1.819 g/cm^3	4.42 - 5.24 x 10^{-6} $(^oC)^{-1}$	0.2	9.5 - 12 GPa (Dynamic)	~ 80 MPa	18.8 - 22.7 MPa	24.4 - 28.9 MPa	119 - 166 $(Wm^{-1}C^{-1})$

Table 2.2.1 – Typical UK nuclear graphite mechanical properties (Nuclear Electric, 1996).

The mechanical properties of nuclear graphites can be determined in a number of ways, but the results obtained are strongly dependent of the selection of experiment, the particular grade of graphite, and the specimen geometry (particularly for the determination of the tensile, compressive and flexural strengths). No two specimens of graphite are likely to provide the exact same mechanical properties, even under identical test conditions due to the natural variability of the material. The random composition of the microstructure and the variability in the manufacturing process prevent perfect continuity of the properties of the material, and it is possible to have a 10% standard deviation from the mean in the results (Neighbour, 1993). This lack of reproducibility is one of the reasons why researchers have difficulties in predicting the behaviour of graphite in any form. This also limits the use of existing data to fully predict the response of nuclear graphite in a given situation and as such there exists no comprehensive resource for graphite mechanical properties to aid the design of graphite structures or components. A database was created by Hacker *et al.* (1998) for this purpose but the data contained within is not freely available to all researchers and the information contained is not in a consistent format for ease of reference.

Within the nuclear graphite industry and research environment the most commonly employed testing techniques to determine the strength and fracture properties are:

- Compression testing
- Tensile testing
- 3-point flexural testing
- 4-point flexural testing

The stress-strain behaviour of polygranular graphite is non-linear, and under uniaxial loading, the tensile strength for polycrystalline graphite is typically in the range of 10 – 30 MPa for the commercially available materials, whilst the compressive strength is generally a factor of three or four higher than the tensile strength. Compressive tests have indicated that the most common form of failure is through shear with the fracture plane being between 35º and 45º from the applied stress, though, some observations have been made of specimens splitting through the longitudinal axis whilst under compression, implying lateral strain failure. The flexural strength has been found to be in the range 24 – 39 MPa (depending on specimen size and geometry) with a bend to tensile strength ratio of approximately 1.30 (Brocklehurst, 1977). The elastic properties are difficult to determine to a high degree of accuracy due to the changes that occur with increasing temperature and strain. It has been shown that Young's modulus increases by approximately 40% at temperatures around 2000ºC, and that Poisson's ratio can increase with compressive strain, approaching 0.5 (Kelly, 1981). However, for virgin (unirradiated) nuclear graphites, these parameters are assumed to remain constant.

For reactor core graphite, a number of changes to the microstructure take place as the material is subjected to irradiation. The two primary mechanisms of material change that take place in a reactor core and age the graphite are radiolytic oxidation and neutron irradiation. Radiolytic oxidation occurs when the graphite is exposed to carbon dioxide in the presence of gamma radiation, and causes an increase in the porosity of the graphite as the material oxidises. The typical porosity of synthetic graphite is approximately 20%, but as this increases the mechanical properties of graphite decrease. With the increase in porosity there becomes a greater probability that failure will occur with the reduction of bulk materials ability to withstand applied stress and strain. Neutron irradiation occurs at the atomic scale when neutrons impact the crystal lattice and cause dislocations and defects in the lattice that alter the material properties. Both these mechanisms cause changes in the strength, elastic modulus and thermal conductivity, with neutron irradiation also causing changes in the coefficient of thermal expansion (CTE) (Grover and Metcalfe, 2002).

Work by Neighbour *et al*. (2000a) on GCMB graphite to study the change in compressive strength under irradiation interestingly showed that compressive strength of virgin graphite was determined as being approximately 20 MPa higher than the

expected value, but with a smaller standard deviation. The difference in result indicated a test specimen geometry factor that was not expanded upon further. Furthering this work, Neighbour *et al*. (2000b) determined the compressive strength, elastic modulus, coefficient of thermal expansion, specific heat capacity and the thermal and electrical conductivity of AGR moderator graphite at 60% weight loss (20% higher than the previous study) using the Knudsen equation as a treatment for each property. As with the majority of predictions of nuclear graphite properties due to the complexity of the material and lack of adequate microstructural model, the results are largely based on the data available from literature and industry sources. The main observations of the obtained data were that above 40% weight loss the strength and elastic modulus were likely to be overestimated due to lack of data available on which to base the predictions, and there is a sharp decrease in electrical conductivity. There were no significant changes in the other material properties measured.

In more detail, Hacker *et al*. (2000) looked at the effect of oxidation on the (CTE) of GCMB and PGA graphite. Though the testing results for this study were similar to those mentioned previously, an approach to modelling this effect incorporating percolation theory was introduced. This suggested that there is a continuous network of material that is able to transmit the thermal strains through the bulk in unoxidised graphite, and that as the material oxidises this network reduces but still retains enough continuous material to continue this transmission. The limit at which this will stop occurring is when the percolation does not span the whole bulk material, and is known as the percolation threshold. Hacker *et al*. applied the theory for electrical conductivity through the graphites (which utilises percolation and has been applied successfully in other research) and determined that the percolation threshold occurs at high levels of oxidation, in excess of 95% weight loss. This effectively implies that CTE is unaffected by oxidation, which is supported by the results obtained.

Neighbour and Hacker (2001) thermally oxidised a large number of AGR graphite specimens to gain differing weight losses up to approximately 80%. Their results showed a dramatic reduction in strength from 0% weight loss up to 40% (reducing from almost 100 MPa to approximately 5 MPa), with the reduction from 0% to 10% being approximately linear. Above 10% weight loss the change in compressive strength became markedly non-linear as the weight loss increased. It was noted that the failure

mode of the specimens began as fast fracture then turning to classical shear, before becoming more progressive failure and observing controlled crack growth in the highly oxidised specimens. The authors used the Knudsen relationship to describe the strength dependence on oxidation such that

$$\sigma = \sigma_0 \exp(-bx) \qquad \text{Equation [2.2.1]}$$

where σ is the oxidised specimen strength, σ_0 is zero oxidation strength, x is the fractional weight loss, and b is an exponent. It was found that Knudsen relationship over-predicted the strength of the material for weight losses under 10%, when b was calculated for the full range of data (given as 6.9). On considering only the weight loss data up to 40%, it was found the value calculated for b (6.4) provided a better indication of the strength of AGR graphite with respect to oxidation and generally did not over-predict the strength for weight losses less than 10%.

For the Japanese nuclear industry, studies on the effect of oxidation and irradiation on the mechanical properties of the selection of graphites for the High Temperature Test Reactor (HTTR) have been carried out by Imai *et al*. (1983), Matsuo (1986) and Matsuo *et al*. (1988). A range of graphite grades such as 7477, 7477PT, IG-11, IG110, SM1-24 and H327 have been oxidised in the studies listed, primarily to analyse the changes in bulk density, Young's modulus and Poisson's ratio. As with previously discussed work, under oxidation it was found that the properties deteriorate with increasing oxidation, but in addition it was observed that there was no change in Young's modulus or electrical conductivity when comparing irradiated and unirradiated results. A further study by Matsuo and Saito (1985) investigated the effect of irradiation and weight loss on the compressive and bending strength of Pechiney graphite under increasing fluence. Testing of the flexural specimens was carried out under 4-point loading and it was found that the flexural strength increased with increasing fluence, as did the compressive strength. However, they were not able to explain why this was the case, as they had expected the weight loss of the specimen to reduce the compressive and flexural strength. Young's modulus was observed to initially increase with increasing fluence which peaked and then began to fall off as the fluence became greater than 0.5 x 10^{20} n/cm^2 EDND. The same effect was seen in both the parallel and perpendicular

directions, with the elastic modulus being higher in the perpendicular direction. They were also able to develop a relationship between the flexural strength and the Young's modulus:

$$\sigma = kE^n \qquad \text{Equation [2.2.2]}$$

where k is a proportionality constant and n is a constant based on the direction (parallel or perpendicular) the specimen is cut, and whether flexural or compressive strength is being calculated.

In a different approach to determining the mechanical properties of graphite, Tucker *et al*. (1986) employed six different graphite failure models to study the effects of varying test and material parameters on the resultant properties without the requirement of extensive physical testing. These models are covered in more detail in Chapter 3.1 – Fracture and Statistical Models of Failure. Weibull modulus and the Rose/Tucker model (based on Buch, 1976) were used to analyse the statistical distribution of strength through flexural specimens, determining that the mean strength and the deviation about the mean is greater for 3-point loading than it is for 4-pt-loading, due to the stressed volume in 3-point loading being smaller than that of 4-point, and hence a reduced probability of a critical flaw being present. A fracture mechanics (Griffith, 1921) model was used to examine the effect of increasing porosity, resulting in a reduced flexural strength with increasing fractional porosity. The other models were also used to examine this phenomenon, but were unable to match experimental results as closely as the fracture mechanics model. The effect of altering the span for 3-point and 4-point flexural testing showed agreement with Brocklehurst's (1977) study in that there is decreasing strength with increasing stressed volume (the volume increase through adjusting the length of the span and thereby increasing the stressed volume), though the fracture mechanics model failed to show any dependence on volume. Additionally for 3-point and 4-point loading, the effect of notching the specimens was calculated, indicating that as the specimen width is increased (and hence the notch depth) the load to failure decreases, and the models were producing failure load values lower than that of the unnotched flexural tests, as would be expected. Further parameters were also computed (*e.g.* notch sensitivity, biaxial stress, neutron irradiation and radiolytic

oxidation) to give a broad range of data in order to analyse the suitability of the models. They concluded that the critical stress, critical strain and critical strain energy density models were unsuitable for describing graphite failure. The Weibull model was more successful but did not provide results as comparable to existing test data as the fracture mechanics and Rose/Tucker models. But ultimately, no single model could adequately describe the behaviour of graphite under various loading conditions.

Allard *et al.* (1991) attempted to characterise fracture behaviour in carbon materials by testing single edge notched beams (SENB) produced from several carbon-based materials. By utilising this style of test specimen the propagation of a crack can be followed from its starting point at the tip of the notch, and the fracture energy measured. For this particular study, the specimens were subjected to cyclic loading and unloading with incremental steps in the displacement of the test specimens until a maximum displacement value is reached. This method allowed for the plotting of crack growth resistance curves (or *R*-curve), and that of the stress intensity factor against the crack size (known as a *K*-curve) and is calculated by:

$$K = \left(\frac{3PS}{2BW^2} \right) \times Y\sqrt{a} \qquad \text{Equation [2.2.3]}$$

where P is the load, S is the span, B is the width, W is the depth, Y is a geometrical factor, and a is the crack size. Through analysing the results of the experiments by relating them to the microstructure, it was concluded that a non-brittle fracture behaviour was occurring and an increase in elastic modulus was observed with increasing span to depth ratio. The results were strongly influenced by the grain position and orientation (see Chapter 3.1 – Fracture and Statistical Models of Failure for further discussion).

Slagle (1967) used brittle ring tests on SGBF nuclear graphite to determine the compressive and tensile strengths, and also investigated the fracture path by notching one of the brittle ring specimens. He noted that cracking tended to occur at the ends of elongated pores positioned in sites containing small pores or material with a greater degree of non-uniformity than the bulk.

There are many investigations into graphite properties that concern elastic plastic fracture mechanics that do contain pertinent information, one of which is work performed by Sakai *et al.* (1983). Though they accepted that much of the research into graphite is based on linear elastic fracture mechanics (discussed in more detail in Chapter 2.3 – Fracture Mechanics and Fractograpy), they believe that graphite is not a purely linear elastic material, and that erroneous fracture mechanics parameters can be produced if the experimental setup is not considered correctly. For polycrystalline graphites, the constituents of the microstructure can cause nonlinearity in the mechanical properties, and at the time of writing they commented on the fact that specimen geometry was not considered in the determination of the critical stress intensity and the strain energy release rate.

The complexity involved in establishing elastic plastic fracture parameters has lead to researchers using an extension of the concepts of LEFM, most commonly being the crack-growth resistance curve (or R-curve and J_r-curve), crack opening displacement, and the J-integral. Sakai *et al.* (1983) proposed an empirical method for evaluating the nonlinear fracture parameters of G_C, R, the J-integral and Φ_P (the plastic energy dissipation rate). Using a chevron-notched specimen in tensile loading coupled with a loading-unloading testing technique, crack growth could be controlled and the kinetic energy of a moving crack could be ignored when considering the energy within the system. From the study they determined that the nonlinear fracture parameters were functions of the plastic energy dissipation rate, which is reasonable considering that this particular parameter is not considered in LEFM studies as no plastic deformation is assumed. Importantly, the critical stress intensity factor was found to be approximately four times larger than that determined by LEFM and is solely attributed to the plastic deformation of graphite. Consequently, approximately 38% of the total fracture energy is consumed by this plastic deformation and this obviously results in a resistance to crack growth not considered previously.

Kennedy (1993) took the approach of brittle-ring tests to determine the mean strength and variance for a variety of different isotropic graphites. The brittle ring test enabled Kennedy to use a smaller number of samples to gain data to calculate the variance of the material due to the way the tests are performed. The ring specimens were placed in compression until fracture, then the fractured ring rotated 45 degrees and placed in

compression again (effectively tested as a brittle c-ring specimen) where the initial fracture surface is in a position with almost zero stress. This reduced the number of specimens initially cut from the bulk material, and provides two sets of data on the stress volume during the tests as the c-ring specimen stress volume is larger than that of the initial ring. Comparing the obtained data with that of 4-point flexural tests of material cut from the same billet, it was found that the brittle ring tests showed good agreement provided that the stressed volume was taken into account, and a reduced number of specimens machined from the bulk material can be used to determine the coefficient of variance.

Sakai and Bradt (1993) conducted a review of the application of fracture mechanics to brittle materials and detailed the available test specimen geometries and techniques available to study *R*-curve behaviour. On considering specimen size requirements they suggested that the only constraint on thickness is that of the microstructural representation, *i.e.* ensuring that grain or crystal size is much smaller than the macroscopic dimensions. For the notches of the specimens the geometry is unimportant in that any can be used. However, there are two types predominantly used in fracture toughness determination, microcracks and indentation-induced microcracks. The former is simply a notch cut into the specimen, whereas the latter are surface cracks created by Vickers and Knoop indentation. Both have their advantages, indentation can enable the determination of fracture toughness from very small specimen sizes, whilst notches do not have any associated residual stresses surrounding the crack (which may introduce further complexity in the stress intensity calculation). The only constraints apparent for the notched specimen is that the notch tip be approximately equal to half the width of the notch slit and the relative notch depth be less than 0.6 (with the most common value being 0.5). It is recommended that the simplest geometries be selected for the testing as complex machining is difficult with hard, brittle materials.

The most appropriate specimen in terms of machining and consistency of results is the single-edge notched beam (SENB) shown in Figure 2.2.2, and can be tested under both 3-point and 4-point flexural loading. ASTM E399 (1981) contains information on a proposed standard 3-point flexural specimen and the associated shape factor values for calculation of the fracture toughness. Additionally, the compact tension specimen (CT) is also recommended for testing (Figure 2.2.3). This differs to the SENB in that the

specimen is tested in tension rather than 3- or 4-point flexural and has the distinct advantages that relatively long crack lengths are able to be produced and stable crack extension occurs, but has the disadvantage that the specimen is more difficult to machine to shape.

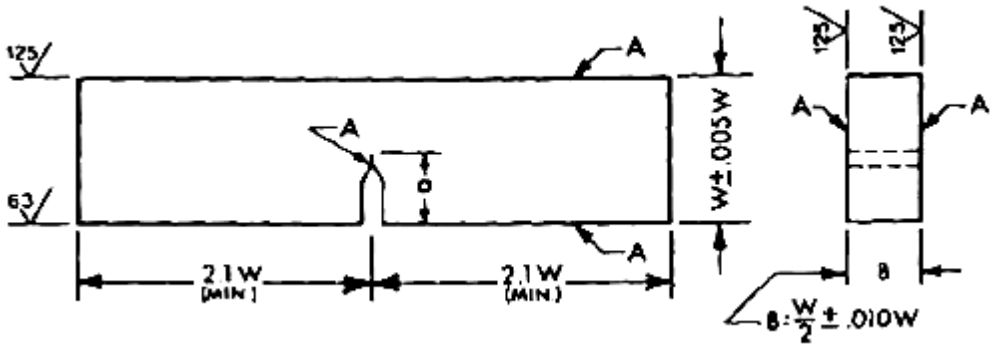

Figure 2.2.2 – Single-edged notched beam (SENB) specimen dimensions, ASTM E399 (1981).

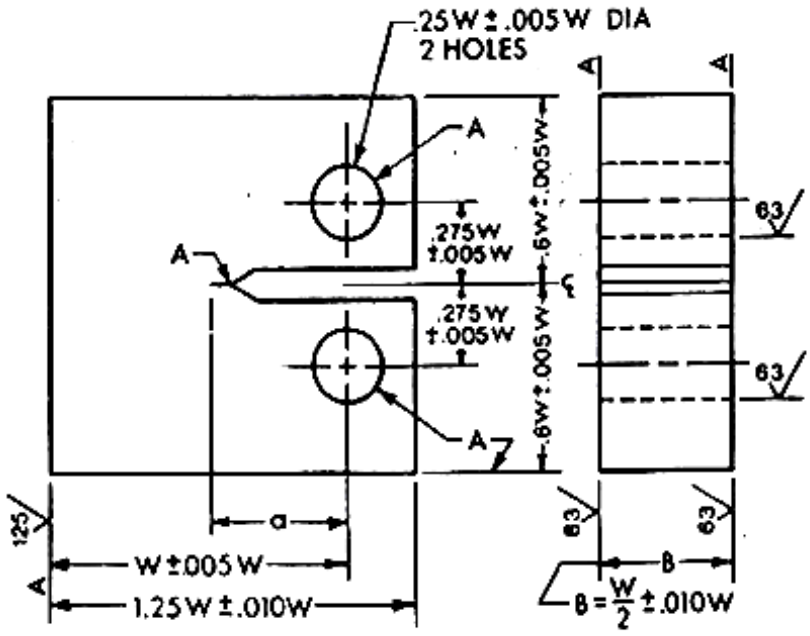

Figure 2.2.3 – Compact tension (CT) specimen dimensions, ASTM E399 (1981).

Extending the work of Sakai *et al.* (1983) into the field of nuclear graphites, Ouange *et al.* (2002) sought to explain the microstructural features present during controlled crack growth with a view to better understanding the failure of reactor core components. Employing both IM1-24 and PGA graphites, they reproduced the *R*-curves proposed by Sakai *et al.* (1983) for nuclear graphites and calculated the respective nonlinear fracture

toughness parameters. Evidence was found during analysis of the data that crack bridging (possibly contributing 20% of the work of fracture) and shear cracking of large particles are present during the loading-unloading cycle, and that points of friction are present that would account for a degree of energy dissipation. Additionally, crack branching at the tip and the tortuous path the crack takes would also contribute to the energy dissipation during crack growth. Detection of these mechanisms further highlight the complex microstructure graphite has and the problems inherent with successfully predicting failure, and that as analysis techniques become more sophisticated a full solution is not being found, only more factors that must be taken into consideration.

These are by no means the only test methods available for determining material parameters of brittle materials. Neighbour and McEnaney (1995) used acoustic emission techniques to detect the internal failure of irradiated Gilsocarbon sleeve graphite by monitoring the sound of internal fracture under loading, finding that the technique was unsuitable for determining the internal stress.

2.3 Fracture Mechanics and Fractography

The field of fracture mechanics arose due to engineers and scientists discovering that the majority of failures in structures and materials were caused by cracks developing both on the surface and within the microstructure. A method was needed to analyse the relationship between stress and failure and to investigate the various causes of cracking. One of the first breakthroughs came about whilst A. A. Griffith was researching the effect of surface scratches on the strength of solid materials for the Royal Aircraft Establishment in 1920. He developed a theory that quantatively related the flaw size to the fracture stress and enables the estimation of the theoretical strength of brittle materials.

The Griffith theory (Griffith, 1921) balances the strain energy that is available from the stress system against the energy required to create two new surfaces of the crack, and

states that the discrepancy between theoretical and measured strength is due to the presence of defects and flaws. The fracture stress, $\sigma_{Griffiths}$, is generally given as:

$$\sigma_{Griffiths} = \sqrt{\frac{2E\gamma}{\pi a}} \qquad \text{Equation [2.3.1]}$$

where E is the Young's modulus, γ is the energy required to create two new fracture surfaces, and a is the crack length. Given the complexity of the microstructure of polygranular graphite the use of Equation 2.3.1 as a basis to determine the mechanical properties of components ranging in geometry and size is very limited. For crack propagation to occur, two conditions must be fulfilled:

- it is energetically desirable,
- there is a molecular mechanism present for the transformation of energy.

For it to be energetically desirable, it is required that at every stage in the propagation of the crack that the energy stored in the material is reducing. Figure 2.3.1 depicts a crack propagating through a material. As the crack extends, the material highlighted by the shaded areas in the diagram is relaxed and strain energy is released. The released energy then becomes available to propagate the crack further.

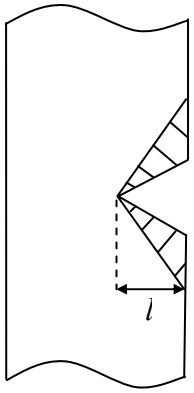

Figure 2.3.1 – Crack propagation through a solid material.

If it is assumed that the area of the shaded triangles is approximately l^2, then the release of the strain energy would be expected to be proportional to the crack length, for example, a crack length of 1 mm would be expected to release four times less strain energy than a crack of 2 mm in length.

The fracture surface energy (γ) is defined as the energy required to form the new crack surfaces and increases only as a first power of the crack length, *i.e.* a crack 2 mm long has twice the surface energy as a crack 1 mm long but releases four times the strain energy. This implies that a shallow crack is consuming more energy as surface energy than is being released as strain energy and therefore the conditions are energetically unfavourable for crack growth. These conditions are reversed as the crack length increases, and beyond the Griffith critical crack length (l_g) the crack is releasing more energy than it is consuming and it may continue to propagate in a catastrophic fashion.

In 1958 Irwin determined that the energy balance suggested by Griffith was between the stored strain energy and the surface energy plus the work done during plastic deformation and developed the concept of the strain energy release rate, G, which is the total energy released during crack propagation per unit increase in crack size. As the Griffith theory was applicable only to brittle materials, Irwin recognised that for more ductile materials the energy required to create new crack surfaces was negligible compared to the work done during plastic deformation.

For any given material, at the theoretical maximum stress the critical crack length is extremely small, whereas at zero stress it is infinitely long. The fracture surface energy and critical crack length are calculated by:

$$\gamma = 2Gl \qquad \text{Equation [2.3.2]}$$

$$l_g = \frac{2GE}{\pi S^2} \qquad \text{Equation [2.3.3]}$$

where G is the elastic strain energy release rate and S is the nominal tensile strength. As the fracture surface energy comprises the thermodynamic surface energy and the energy dissipated by the movement of dislocations at the crack tip, it can also be calculated in terms of the strength and crack length:

$$\gamma = \frac{\pi c S^2}{2E} \qquad \text{Equation [2.3.4]}$$

where c is the depth of the crack. However, this technique for the calculation of fracture surface energy can only really be used for homogeneous materials as it does not factor in the variability of strength observed in materials with non-uniform microstructures, and only considers 2-dimensions. When the strain energy release rate reaches a critical value, G_c, a crack will propagate and Irwin showed that this energy approach is equivalent to a stress intensity approach, K, and that the material property governing fracture may also be stated in terms of the critical stress intensity, K_I (in mode I fracture). This also leads to the definition of a new material property called fracture toughness, K_{IC}.

$$K_I = \sigma\sqrt{\pi a} \qquad \text{Equation [2.3.5]}$$

$$K_C = \sqrt{EG_C} \quad \text{for plane stress} \qquad \text{Equation [2.3.6]}$$

$$K_C = \sqrt{\frac{EG_C}{1-\upsilon^2}} \quad \text{for plane strain} \qquad \text{Equation [2.3.7]}$$

where υ is Poisson's ratio. The two versions of the calculation of fracture toughness are necessary as the value of fracture toughness is different under plane stress and plane strain conditions. Under the special case of plane strain deformation K_C becomes K_{IC}. The I denotes the first mode of loading most commonly used – crack opening, which is simply when a tensile stress is applied normal to the plane of the crack. The two other types of loading used to propagate a crack are:

- Sliding - when a shear stress is applied parallel to the plane and perpendicular to the crack front;
- Tearing – when a shear stress is applied parallel to the plane and parallel to the crack front.

Linear Elastic Fracture Mechanics (LEFM) was born from the demonstration of G and K being equivalent and is employed on the assumption that the material under investigation is both isotropic and linearly elastic. LEFM is only applicable when the plastic deformation is small compared to the size of the crack. Elastic Plastic Fracture Mechanics (EPFM) was developed alongside LEFM, most notably driven by Rice during the 1960s. He developed a new fracture toughness measure that described the

case of materials where the deformation at the crack tip no longer followed the approximation defined by LEFM by assuming that there is a non-linear elastic deformation ahead of the crack tip, and is known as the J integral. The J_{IC} elastic-plastic failure criterion is related to K_{IC} through the equation below:

$$K_{IC} = \sqrt{\frac{EJ_{IC}}{1-\upsilon^2}} \qquad \text{Equation [2.3.8]}$$

Davidge and Tappin (1968) studied the effective surface energy of four different brittle materials: alumina, polymethylmethacrylate (PMMA), glass and graphite (PGA). The emphasis was on two types of surface energy, γ_I which is the surface energy required for the initiation of fracture and γ_F which is the work of fracture (the value averaged over the whole fracture process). By producing flexural test samples with notches cut to one tenth of the thickness of the beam, experimental data was obtained in order to calculate the surface energy and work of fracture using two methods, those being an analytical method (Griffith) and the compliance analysis method (Tattersall *et al.*, 1966). Whilst the strain energy release rate is determined analytically by mathematically calculating the stress distribution around the notch tip, the compliance analysis derives the strain energy release rate from load/deflection data obtained experimentally. Both the methods should produce the same value. Additionally, the work of fracture was calculated and is given as:

$$\gamma_F = \frac{U}{2b(d-c)} \qquad \text{Equation [2.3.9]}$$

where U is the total work done (calculated as the area under the load/deflection curve), b is the specimen length, d is the specimen height and c is the notch depth.

The results obtained for γ_I using the two different methods gave good agreement with both producing similar and consistent values over the range of materials. It was found that the work of fracture decreased with increasing notch depth which was attributed to the change in energy dissipation processes as depth increases. Unlike other materials, it was also shown that crack initiation in graphite requires less energy than crack

propagation caused by the random nature of the microstructure and the crack having to negotiate obstacles in its path.

One of the most comprehensive studies of the fracture of graphite was performed by Brocklehurst (1977) and is still widely referred to and expanded upon today. At the time, one of the most difficult aspects of designing for any structure incorporating graphite was the lack of data available on the behaviour of graphite under loading. The study concentrated on collating as much data as possible obtained by other researchers to further the understanding of the intricacies of graphite properties and behaviour, and employing a fracture mechanics approach to analyse the response of the material under a variety of test conditions.

Through examining the effect of stress on different graphites at a microscopic level, Brocklehurst suggested that the stress distribution within the microstructure is controlled by the pore size and locations, thereby defining a fracture path within the material. These internal stresses are relieved when a crack starts to propagate due to the elastic strain reaching a critical value in a particular area such as at a grain boundary, implying that the strain applied to the surface of the material is absorbed by the elastic and plastic deformation occurring in the microstructure and through the formation of microcracks within the grains. Microcracks will continue to propagate until they are arrested by either a pore, or their path causes them to be out of orientation with the stress pattern and thus arrest (*i.e.* there is not enough energy present to continue their growth in a specific direction). As the number of these non-propagating cracks increases, they begin to join together when they are suitably aligned and continue to do so until there is enough strain energy present to initiate fracture at the grain boundary. Consequently, these cracks in the macrostructure will propagate through the material via the same mechanism until the failure of the component occurs. It was observed that the critical crack density was reached in regions of the material where there was a high concentration of stress near large areas of porosity. This fracture process aided in defining the cause of some of the effects observed in the experimental data such as a high work of fracture rate (when compared to that of the crystal basal plane) and the low resultant notch sensitivity. It was found that the coarser the grain of the material, the lower the notch sensitivity due to the fact that the size of the microstructural features determine the stress distribution, but are weaker than the finer grained graphites, though

very fine grained graphite tended to be more brittle. The fracture mechanism also points towards a weak-link behaviour, in that there is a critical flaw present within the material that will cause failure. By applying fracture mechanics and trying to develop a relationship based on inherent flaw size and work of fracture, it was noted that although this approach was partially successful the conditions of the tests themselves (such as the stress gradient used) could influence the effective inherent flaw size and therefore no unifying theory could be produced. This was also seen when examining the size effect on the strength of graphites. He experimentally determined that the grain size had less of an effect in flexural tests than in tensile but, conversely, fracture mechanics indicated that an effective defect size would be smaller. Ultimately, Brocklehurst surmised that graphite is a complex material for which it is difficult to generate a theory that could fully describe the behaviour and predict the material properties for use in structural design. In particular, he noted that the strength of graphite is not a constant property of the material, but appears to depend on the test employed to determine it, and varies with geometry, stress distribution and the applied strain.

Microcracks within a microstructure can have a great influence on the physical material properties, particularly on the elastic properties such as Young's, shear, and bulk modulus as well as Poisson's ratio. Case (1984) examined the theories available that related microcrack radius and their density to the changes in elastic modulii and suggested a method for determining the parameters in terms of the macroscopic variables of Young's modulus and Poisson's ratio. This is greatly advantageous as the density of microcracks and their mean size is difficult to determine experimentally. The presence of microcracks within a structure can drastically degrade the material properties, for example, in the case of Young's modulus it can reduce by 10 – 20 %. Geophysics research has suggested that there is a correlation between microcracking and the effect on material properties. Observations on granite have shown that if the rock comes under pressure and the microcracks close, then the mechanical and thermal properties significantly change. In terms of its use for estimating the effect of microcracks on the elastic modulii of graphite, the original theories are not of much use as they do not consider microcrack linking or secondary crack growth, though they do consider a random orientation of microcracks. As such, even by rewriting these theories in terms of easily calculated elastic properties they would not provide much useful information.

Up to this point the majority of papers discussed have concerned LEFM which is the most relevant branch of fracture mechanics to this thesis, but if considering elastic plastic fracture mechanics, as did Sakai *et al.* (1983) and Ouange *et al.* (2002) reviewed in Chapter 2.2 – Determination of the Mechanical Properties of Graphite, part of the problem with accurately predicting failure of a ceramic material using an overriding theory is that all ceramics have a different makeup and contain very different materials, whether it be two types of carbon as with graphite or just one like alumina. The particles that comprise ceramic materials are very different in shape and size and contribute greatly to the bulk material properties, but note that the effect of their geometry is not always considered.

Bazant has performed much research in this field and formulated several theories in order to consider these features. In a 1996 paper on size effect measurement, Bazant discussed the issues associated with selecting a standardized fracture test for examining the size effect and determining the fracture characteristics were examined. He stated that size effect impacts the problem of choice of standardized fracture test in two ways:

1. the fracture parameters must be independent of specimen size (and geometry) when geometrically similar specimens of different sizes are tested. This is the basic requirement of objectivity of a fracture model.
2. measurement of the size effect on nominal strength of concrete specimens can be exploited for determining the fracture parameters. The size effect is the most important feature of the fracture mechanics of quasibrittle materials, distinguishing it from other fracture theories.

He reviewed several test methods and their parameters, such as work of fracture, size effect and the Jenq-Shah methods (1985), noting that each method is non-linear and can be defined by two parameters, contrasting with LEFM which has only one parameter. There was particular reference to his own size effect method that consists of four different types of method for use depending on the situation being examined, with the main advantage they have for determining the fracture characteristics is that they only require the maximum loads of the specimens tested. Although stating that the size effect method can be used with ease compared to some of the other methods, the

concluding remarks indicate that the knowledge of size effect on the failure load of fracture specimens (coupled with the effect of shape) is very useful for measuring fracture properties, but the effect of size on values of fracture parameters must be avoided.

Interestingly, Bazant (1996a) comments on a Weibull statistical size effect which states that due to the redistribution of stresses caused by stable fracture growth prior to maximum load, when the Weibull probability integral is applied, the dominant contribution comes from the fracture process zone (whose size is nearly independent of the structure size). As the contribution from the rest of the structure is diminishing it means that the fracture cannot occur outside the process zone. And because this zone is approximately the same size regardless of specimen size, the Weibull-type size effect must disappear for large size specimens. A generalised version of the Weibull-type theory (in which material failure probability depends upon the average strain of a characteristic volume of the material, rather than the local stress) has shown to yield a realistic size-effect and also to approach the original size-effect law as its deterministic limit. Weibull theory and the statistical analysis of failure is discussed in more detail in the next section of the literature review.

In a further paper, Bazant *et al.* (1996b) investigated the nominal strength of notched graphite-epoxy fibre composite laminates, with the purpose of verifying the proposition that in quasibrittle materials the size effect is the transition between plasticity and linear elastic fracture mechanics, and generally occurs whenever the load-deflection curve does not have a yield plateau after maximum load is reached (brittle fracture occurs). Through testing a variety of notched laminate composites of the same thickness but of different sizes (though geometrically similar) under uniaxial tensile loading, Bazant found that the largest specimen size stress-strain curves were almost linear prior to failure (brittle behaviour), whereas the smaller specimens displayed non-linear behaviour before the peak stress (higher ductility). This behaviour represented a transition from ductile to brittle response as the specimen sizes increased.

The effect of structure size on the nominal strength of geometrically similar quasibrittle structures generally follows the approximate size effect law:

$$\sigma_N = Bf_u(1+\beta)^{-1/2}$$ Equation [2.3.10]

where β is the relative structure size (D/D_0); the nominal strength defined by:

$$\sigma_N = \frac{C_N p}{bD}$$ Equation [2.3.11]

(in which P is the maximum load; D is the characteristic dimension size (*e.g.* length); b is the width in the third dimension; C_N is the chosen coefficient to make σ_N coincide with the maximum stress; D_0 is the constant dependant on the fracture process zone and specimen geometry); B is the constant characterising the solution according to the plastic limit analysis based on strength concept; and f_u is the reference strength of the material (to make β dimensionless). This size effect law has been verified by numerous sources, especially for concrete, rocks and toughened ceramics. It also represents the limiting case for a non-local generalisation of the statistical Weibull-type theory for size effects.

Bazant and Novak (2000) put forward a theory for predicting the fracture initiation in quasibrittle materials, taking into account the size effect. They observed in a multitude of investigations that stochastic finite element models were not able to predict, at a given load, when failure in a material would occur, stating that this was due to fracture occurring from a microscopic flaw not taken into account in the finite element model. In addition they noted that although prediction of failure by FEA is feasible, it is not successful when applied to complex models and requires further analysis such as Monte Carlo simulation. Their aim was to develop an alternative method for the prediction of failure that could be used to analyse large size and more complex structures.

Using Bazant's previous work (2000) on the probability of failure as a basis, the model was further developed to investigate how this applies to modulus of rupture tests (flexural strength tests) as data from these experiments was widely available, and that failure tends to occur in the specimens before a large crack forms. Nonlocal stress was employed, but only in 2 dimensions and is independent of the width of the beam as test results analysed showed no dependence on width. The nonlocal averaging of the stress gives the equation an advantage over other methods of failure prediction (*i.e.* FEA) because it incorporates a microstructural mechanism of failure into the equation that

represents not only the stress and strain at a given point but also a strain field that stands for the representative volume of the material.

Focusing on the modulus of rupture of concrete beams, the model was developed to determine the size effect on flexural strength. Accepting that the random nature of the microstructure has an effect on the strength, and consequently the calculation of the size effect, the model was formed in two parts: a simple deterministic energy based size effect formula, and a computational model for the modulus of rupture.

During the design stage for the High Temperature Test Reactor (HTTR) located in Mito, Japan, the selection of the correct graphite for the structural components was vital in order for it to function correctly and have a suitable service life. Ishiyama *et al.* (1991) conducted an investigation into IG-11, IG-110 and IPX through examining the effects of stress, irradiation, oxidation, specimen volume and cumulative damage on the fatigue behaviour and fracture toughness. The difference between the two types of graphite is simply that IG-110 is purified IG-11. Though they concentrated mainly on the fatigue strength of the graphites, they determined that the minimum specimen thickness for (nearly) constant fracture toughness was dependent on the graphite under examination, in line with that suggested by Brocklehurst (1977) that each graphite type behaves differently dependent on its microstructure. Using a LEFM based crack opening displacement test they applied the ASTM (E318 and E399) calculation for the fracture toughness, and showed that for IG-110 and PGX graphites, the fracture toughness values were very close to those listed within literature. However, the method was not applicable to IG-11, where an EPFM approach yielded better results. With regards the effect of specimen size on strength, the fatigue failure experiments were performed on oxidised IG-110 but returned the result that specimen volume did not have a large effect on fatigue strength.

Eto *et al.* (1997) studied the response of IG-11 and PGX (fine grained isotropic and medium grained semi-isotropic, respectively) graphites in a biaxial stress state, for the purpose of researching the fracture criterion and assessing the design criteria of the HTTR. The experiments were performed both at the Japan Atomic Energy Research Institute (JAERI) and Oak Ridge National Laboratory (ORNL). Using tubular test specimens of a relatively large size, the tests were performed on a servohydraulic test

rig that generated a circumferential stress or torque by applying an internal pressure (water) or a torque force. The wall thickness of the PGX graphite was 5 mm in order to negate the effects of grain size on the results. Through statistical analysis of the data obtained, and only considering the first and fourth quadrants of the biaxial strength plots, they determined that the fracture criterion used to evaluate the graphites used during the design of the HTTR (*i.e.* maximum strain energy) was most appropriate for the PGX graphite and that the criterion was also conservative (1% fracture probability with 95% confidence limit). Interestingly, as the experiments were performed at two different locations, the test specimens that were produced were of differing sizes, and on collating the data from JAERI and ORNL it was discovered that no appreciable difference in the biaxial strength of IG-11 could be found.

In addition to the areas of fracture mechanics, a useful analysis is fractography which is the study of fracture surfaces to gain further insight into the behaviour of materials. As a tool for failure analysis it has been employed for centuries in metallurgical field and todays practices were developed in the 16th Century as part of quality control for metalworking. Fractography enables the determination of the failure of a material and the mechanisms involved through microscopic examination of the fracture surface and knowledge of the patterns left behind during failure. It can be used to locate the fracture origin, the direction of crack propagation, the mode of failure, any defects present within the material structure, and the stresses present to cause failure (Parrington, 2002).

All material failures occur in one of two forms, either brittle or ductile fracture, and both types have distinct characteristics that define them. Ductile fracture occurs in materials that undergo plastic deformation before failure, whereas brittle fracture occurs with little or no plastic deformation before failure. Ductile fracture tends to occur along planes where shear stress is at a maximum, for example in torsion a material will fail along the plane perpendicular to the axis of twist. In brittle materials fracture will take place along a crystallographic plane (cleavage plane) where the tensile stress is at a maximum and can break the atomic bonds between the planes, and is particular to body-centred cubic and hexagonal close-packed materials. For specimens placed under a compressive load, the mechanisms of failure are more complex with failure following a path that is at 45º to the direction of the applied force (Kalpakjian, 1995).

Brittle materials are very weak under a tensile stress compared to a compressive stress due to the presence of defects in the material such as scratches, flaws and cracks, and under tensile loading cracks will propagate rapidly resulting in catastrophic failure (also termed fast fracture). For graphite, the most commonly observed tensile fracture is intergranular fracture, where the crack propagates along the grain boundaries rather than through the grains (transcrystalline fracture). Fatigue fracture may also be considered to be a form of brittle fracture, caused by the development of cracks within the microstructure in the presence of flaws or defects and is usually due to repeated loading and unloading. Figures 2.3.2 and 2.3.3 show examples of intergranular and fatigue fracture in metals where similar features of fracture can be seen in all materials.

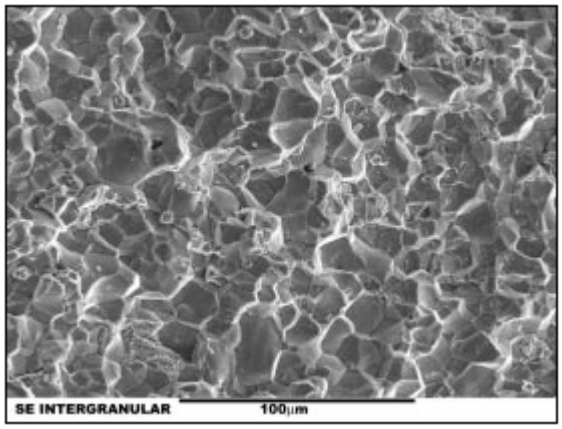

Figure 2.3.2 – Intergranular fracture of cast steel (Parrington, 2002).

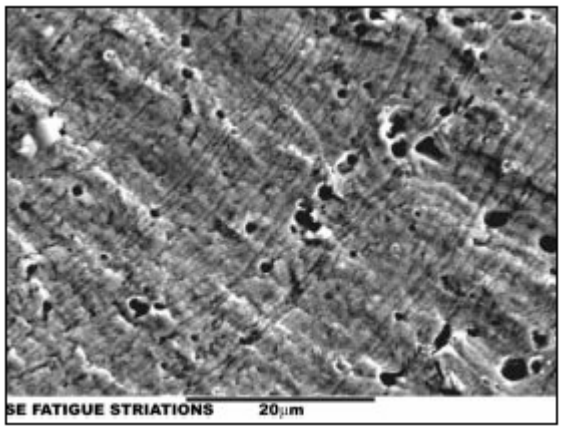

Figure 2.3.3 – Fatigue fracture in steel highlighting the striations caused during failure (Parrington, 2002).

After intergranular failure the grains and grain boundaries present in the material microstructure are well defined due to the crack propagating around them. The appearance of a brittle fracture surface is usually glass-like in nature, *i.e.* the fracture

surface appears bright due to changes in the direction of the cleavage planes as the crack propagates around the grains. The same detail can be seen in graphite failure as shown in Figure 2.3.4. The striations present after fatigue failure are caused by the movement of the crack front as the material undergoes cyclic loading-unloading. With metals, as the striations are uniformly spaced, the crack growth rate can be calculated but only if the cyclic stress frequency is known.

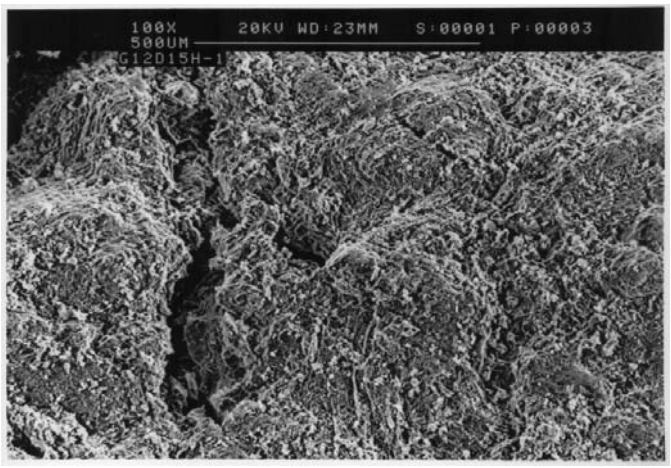

Figure 2.3.4 – Fracture surface of IM1-24 graphite after failure under compressive loading.

It can be seen from the micrograph of the graphite fracture surface the general features of brittle fracture that were described previously. The intergranular fracture surface is also known as ‘rock candy’ due to form of the grains, materials with a coarse grain structure resemble rock formations when viewed at high magnification.

2.4 Summary

This chapter has reviewed the history and manufacture of industrial graphite as well as the atomic structure, its application in nuclear reactors and the stresses it is primarily subjected to during its service life. It has also examined the fracture of graphite with emphasis on the testing techniques employed to determine material properties through the application of fracture mechanics. The information obtained from this section will aid in the development of a conceptual model of the structure of graphite, and also in devising a suitable mechanical testing programme against which model data can be validated.

Chapter 3 – Modelling Fracture and Failure in Graphite

The previous chapter discussed the history, manufacture and structure of graphite and the various techniques that have been employed to analyse the composition of the material, as well as the concept of fracture mechanics used to determine the behaviour of a material at a microstructural level. The following chapter discusses how these techniques have been employed to model brittle materials and the introduction of finite element analysis as a tool for microstructural analysis. It also covers the use of statistical analysis to determine the response of a material based on experimental data.

3.1 Fracture and Statistical Models of Failure

With all brittle materials there have been many investigations into the possibility of predicting failure of a component or structure, and as each material has its own unique characteristics and complexities there are often many different ways of approaching the problem. One unifying feature of all failure models is that they have their foundations in the observation of how the material responds to stress and strain, usually in laboratory conditions, and as such are based on the actual measurement of material properties. From this, the results are statistically analysed and empirical relationships are developed in order provide a method for predicting the conditions under which fracture will occur. This section aims to review the most successful fracture models and statistical techniques in order to understand in what respects they are successful and where they fall down.

Possibly the most widely used statistical analysis of fracture is the Weibull theory, developed by W. Weibull in 1939 and further expanded upon in 1951 and applies to linear elastic brittle materials. The theory is used to determine the probability of

survival of a component and is based on a weakest link model, that is, a structure is only as strong as its weakest link. This implies that as a component size increases it contains a higher probability of a critical flaw and therefore has a higher probability of failure. It also suggests that as the size of a component increases the strength will decrease. Weibull theory for uniaxial stress is generally given as:

$$P_S(V_0) = \int_V \left(\frac{\sigma - \sigma_u}{\sigma_0} \right)^m dV \qquad \text{Equation [3.1.1]}$$

where $P_S(V_0)$ is the survival probability (*i.e.* the fraction of identical samples, each of volume V_0, which survive stress σ); σ_u is the stress below which the failure probability is zero; σ_0 is the characteristic strength of the distribution (a constant); m is the Weibull modulus (or the measure of scatter of failure strengths for the given material) (Ashby *et al.* 1998).

Weibull's work enabled a method for the prediction of material failure that could be applied to any size of component providing they were geometrically similar. Since the development of the theory this has been proved untrue as it has been found that at small volumes the theory breaks down due to the grain size of the material becoming the defining characteristic feature of failure, and at large volumes it remains untested because of the impracticalities of the size of test specimens required. Indeed, Brocklehurst (1977) stated that tensile, flexural and internal pressure experiments he performed with Darby on near-isotropic graphites failed to give consistent values for the Weibull modulus with a m value of 18 being given in tensile, and a m value resulting in 6 for flexure. Weibull theory also tended to overestimate the effect of volume on material strength and produced predictions of strength that were lower than those experimentally obtained. However, tests to examine the changes in failure strength with respect to specimen size did show a pattern for graphites in that as the specimen size increased, so did the failure stress up to a given volume. Once this volume had been exceeded the failure strength started to decline. Figure 3.1.2 shows the results produced by Brocklehurst's tensile and flexural tests on specimens of differing volume.

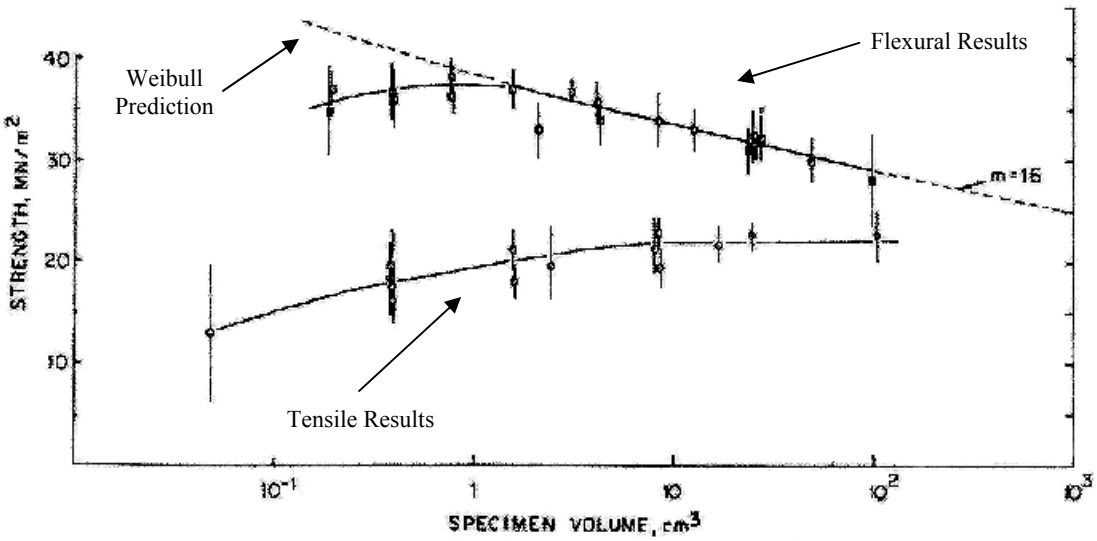

Figure 3.1.2 – Specimen volume versus strength graph with Weibull modulus produced by Brocklehurst, 1977.

Both the sets of data for the tensile and flexural tests show that initially there is an increase in strength with increasing volume. In the case of the tensile results, this effect reaches a plateau and above 8 cm^3 there is no further increase in maximum value. For the flexural test results, a Weibull prediction was made from data obtained from specimens of a constant volume (25 cm^3) calculated using Equation 3.1.3 (which is a derivation of the Weibull theory for flexural tests) and a modulus of 16. The results do show a good correlation with the Weibull prediction for specimen sizes greater than 1 cm^3, but below this the prediction does not correspond to the results obtained. This, as stated previously, is attributed to the effect of grain size having a pronounced impact on the failure mechanisms of graphite at small scales.

$$\frac{\sigma_1}{\sigma_2} = \left(\frac{V_2}{V_1}\right)^{1/m} \qquad \text{Equation [3.1.3]}$$

where V_1 and V_2 are different volumes of the same test specimen and σ_1 and σ_2 are the corresponding maximum stresses.

Lewis and Oyler (1976) tested the validity of Weibull theory's ability to predict failure strength through scaling the results determined at smaller sizes by performing 3-point

flexural tests on three differently manufactured types of alumina (slip-cast, dry-pressed and extruded). By substituting the equation for stress at failure in a flexural test specimen into the equation for risk of fracture (Equations 3.1.4 and 3.1.5), they were able to derive an expression for determining the Weibull parameters characteristic of the material (m, σ_u, σ_0) (Equation 3.1.6).

$$\sigma(x) = \sigma_{\max}\left(1 - \frac{2x}{L}\right) \text{ for } 0 \leq x \leq L/2 \qquad \text{Equation [3.1.4]}$$

$$B = \int_V n_1(\sigma)dV + \int_S n_2(\sigma)dS \qquad \text{Equation [3.1.5]}$$

$$\sigma_m(L) = \sigma_u + AL^{-2/m} \qquad \text{Equation [3.1.6]}$$

where σ_{max} is the nominal maximum stress of the flexural test, σ_m is the mean strength, σ_u is the stress below which the material will not fail, A is a parameter that is a function of the test specimen geometry, B is the probability of failure, n_1 and n_2 are functions relating the probability of failure to the stress, V is the volume of the sample, S is the surface area of the sample, L is the span, and x is the location of the stress.

Setting a thickness to width to span ratio of 1:3:12 for the slip-cast and dry-pressed alumina specimens and using purchased cylindrical rods of extruded alumina, 110 specimens in total were tested to failure at spans ranging from 1 cm to 13 cm. They found that the scaling curve predicted by Weibull did not fit with the experimental data. For the dry-pressed alumina it was a close approximation, but it over-predicted the flexural strength of the slip-cast and extruded alumina. They also discovered what they term 'anomalously low strengths' for the smallest two load spans (1 cm and 2 cm) though these were thought to be caused by microstructural variations in the test specimens. In the case of the three different types of alumina, Weibull theory is unable to accurately predict the failure strength of similar materials with differences in their microstructure. Additionally, Lewis and Oyler suggest that the number of test specimens they used of the slip-cast alumina, 30 specimens (which had the lowest porosity and the smallest grain size), were not enough as σ_u was actually higher than the obtained results. It could be argued that it is the calculation of σ_u is incorrect as it does not appear to factor in grain size or porosity, only the test specimen geometry. From the

results of the dry-pressed alumina, they saw a pattern of results that suggest that the Weibull modulus is not a material property, but may be a function of specimen size, but do not expand upon this further.

Fok *et al.* (2001) took the approach that Weibull theory cannot model brittle materials successfully with just two parameters, three must be used to provide more reliable results. Lewis and Oyler considered the three parameter approach in their study, but as Fok *et al.* point out, many Weibull analyses only model with two parameters through equating the third parameter σ_u to zero. By performing computer analyses using a Monte Carlo simulation to generate estimated failure stresses based on arbitrary values of m and σ, it was found on examining the returned two parameter and three parameter distribution results that they were fairly similar with little variation shown between the two sets of data (plotted as probability of failure versus stress graphs). Unfortunately, as far as could be determined, no actual test data was used to study the practical effect of using the three parameter version of Weibull theory and all results returned were of an arbitrary nature. It appears that initial supposition of Weibull's unsuitability for brittle materials is correct but no suggestion of why this is the case was put forward.

The use of three parameters for Weibull analysis was also examined by Warren (2001) through mathematical analysis of tensile, 3-point and 4-point flexural tests. He determined that if no threshold stress (σ_u) is considered then all three methods for the different test techniques will give the same Weibull modulus. However, when the threshold stress was considered due to the inclusion of a maximum crack size the Weibull modulus was shown to vary for the three tests, with the effects being most noticeable for stresses that approached the threshold value. The treatment also anticipated the largest increase in Weibull modulus for 3-point flexural and the smallest for tensile tests, which could be caused by the non-uniformity of stress distribution in the former but uniform in the latter. The difference between this examination of the probability of failure and the others is that a simple power law to represent flaw distribution was employed in the calculations to take into account the effect of microstructural features.

In another study of Weibull strength scaling based on results obtained during 3- and 4-point flexure, Quinn (2003) used Equation 3.1.3 as a basis for equating results obtained

under the two loading conditions for equal effective (or stressed) volumes. That is, for the same cross-sectional area samples:

$$\frac{\sigma_3}{\sigma_4} = \left(\frac{L_4}{L_3}\right)^{1/m} \left(\frac{m+2}{2}\right)^{1/m} \qquad \text{Equation [3.1.7]}$$

where the subscripts *3* and *4* denote 3- and 4-point flexural, respectively. If the spans are the same and, for example, the Weibull modulus is 15, then the strength for 3-point flexural will be approximately 15% greater than that for 4-point flexural. The same equation is produced if the same stressed volumes are considered, suggesting that the depth of the specimen has an effect on the results examined. The result of this treatment was to provide a method of scaling the results from one international test method to another without the need for considering flaw size and distribution, and in this the author succeeded. However, by neglecting the flaws within a particular material the mechanism of failure is being ignored and although two test specimens from different research groups can be compared at a similar scale without the need for experimentation of the same geometry specimens on the same test apparatus, the results do not give any further insight into how the material will behave at sizes not practical to test in a laboratory environment. Also, as it is not known for sure that the Weibull modulus is a constant for a given material, erroneous comparisons may be performed.

To further investigate the possibility that the Weibull modulus is not a constant for a given material, Fett *et al.* (2003) considered the effect of high and low stress gradients on ceramics under 4-point flexural and contact loading. They discovered that for higher stress gradients a lower Weibull modulus was produced than for the lower stress gradients. In addition to this it was determined that the flaw size distribution was responsible for the large scatter in strength for ceramics, though this conclusion appears to come from other sources of literature. What becomes apparent from this paper and the others reviewed that have investigated the aspects of Weibull theory is that no two papers come to the same conclusion and that Weibull theory cannot be said to be wholly applicable to materials that do not contain a uniform microstructure, or even brittle materials that do.

As an interesting aside, an investigation by Tarum (1999) for Delphi Automotive Systems looked at the possibility of employing the Weibull theory for analysis of components that have mixed modes of failure (for example a tyre which might fail due to a puncture caused by wear). He was able, with moderate success, to mix Weibull theory with what is termed a 'bathtub' model which can analyse a population with one or more distributions. It is more of a statistical analysis of the reliability of components than a prediction of failure, but showed that when treated correctly and with simple parameters (such as time taken to failure), Weibull theory can be employed and produce good results. It should be noted that Weibull theory has been successfully employed to study the failure of various materials, from pre-stressed wires and strands (Castillo *et al.*, 2006) to Yuen Long marble (Wong *et al.* 2006), and Weibull parameters have been calculated from bi-modal strength distributions (Absi and Glandus, 2002), all using computer based numerical techniques.

Recognising the difficulties of applying basic Weibull theory to all materials without incorporating new parameters, Neville and Kennedy (1991) developed an extreme-value function to be applied to failure caused by sharp defects. Based on determining the volume prone to failure, the function is defined as:

$$F(S) = \left(S/B\right)^D \Big/ 1 + \left(S/B\right)^D \qquad \text{Equation [3.1.8]}$$

where S is the failure prone volume, B is a scale parameter that describes the spread of the distribution, and D is a parameter describing the skew of the distribution. Applying the function to test data for concrete cylinders, glass rods and low-alloy steel, they found that their function fit the data better than Weibull theory by comparing the coefficients of correlation. On average the coefficient of correlation was 3% higher than Weibull, but although is not a great deal different, the extreme-value function takes into account that the volume prone to failure (effectively the volume under stress) does not remain constant throughout loading, and as such was able to generate accurate estimates of the probability of failure. What is not discussed is whether the extreme-value function is able to predict failure in components of varying size, or if it too underestimates the strength at small sizes and overestimates the strength at large sizes.

Taking an alternative approach, Todinov (2001) incorporated the distribution and different types of defect into a statistical model. Through characterising the type of defect (inclusions, particles and microcracks) by assigning it a specific maximum tensile stress and grouping them together with the assumption that the defects do not interact with one another, equations were developed that related to a number of scenarios that could instigate fracture of the material. Monte Carlo simulations were used to validate the equations within a specified volume and with random distributions of the defects. When the type and number of defects within the volume are known, the model produces exact values for the probability of failure at any specified point. Compared to the existing theory for statistical probability of failure (based on the Griffith fracture criterion), the proposed model showed good agreement when the number of defects present was high but disagreed when the number of defects present was low. As there was no comparison to real world data it is difficult to comment on how the method corresponds to actual material failure, but seems a promising method of predicting the cause of failure.

An interesting case study of use is that of the failure of concrete and rocks. Although the compositions and microstructures are substantially different to graphite, the mechanisms of failure are similar (as they are with the majority of brittle materials), and the techniques employed for analysis can be considered when assessing the information available on failure.

Holt *et al.* (2005) designed their investigation into the mechanical failure of rock with a testing programme in mind to validate the results they obtained from a computer based model. Particle Flow Code (PFC), which has been in development for over twenty years, uses 2-dimensional disks or 3-dimensional spheres (dependent on the required investigation) as a foundation for analysing the interaction of particles under stress. The distribution of sizes can be set randomly and the particles are all subject to Newton's equation of motion and conditions of moment equilibrium, and have a force-displacement relationship to simulate contact. This method of model construction automatically builds in porosity. Additionally, the particles can be 'bonded' together by defining conditions for contact and have a defined tensile and shear strength. The boundaries of the system are defined by walls, and the analysis takes place through moving the walls to apply a stress and displacement to the particles within. The

displacement is transferred to the particles through calculation of the contact forces which determine a new location and velocity of each particle and move them accordingly. As this is set as a time-step operation, only small increments in the movement and stress of each particle are calculated at each interval before the next displacement is applied, and repeated until the required overall displacement is reached. To validate the model, several tests were carried to determine the wave velocity, strength and stiffness, and a core scratch test (which examines bond strength between particles) on synthetic rock structures constructed from spherical glass beads bonded together with epoxy resin. Comparison of the model results and experimental data showed excellent agreement and validated the approach taken for modelling, with the exception that the core scratch experiments which provided a force required for separation four times that of the model. However, it can be argued that this demonstration of PFC is performed against an idealised microstructure. The glass beads used for the synthetic rock structures were perfectly spherical and do not fully represent the actual structure, as the epoxy resin used to glue the particles does not fully represent the natural process of grain bonding. Techniques such as this are becoming more common as computing power increases and the complex equations required to perform such analyses are made easier to solve. It can only be assumed that there are impracticalities associated with the physical testing of real rock samples.

LEFM has been applied in the study of concrete where it was found that it is only applicable in specific cases such as when only the microstructure is being considered, or very large samples are under investigation. For standard sized test specimens, linear elastic fracture mechanics theory has been shown to give inconsistent results and does not predict realistic failure loads. To address this issue, Reinhardt *et al.* (1986) completed a comprehensive testing programme of concrete specimens under three types of tensile loading; static, repeated and cyclic loading. By performing over one hundred tests on normal and lightweight concrete a large amount of data was collected in order to statistically analyse the fracture behaviour and attempt to develop a theory that is more applicable than LEFM for crack propagation due to the internal stress. By considering that the uncracked material behaves in a linear elastic fashion and that nonlinear behaviour occurs once cracks start to form, the data from the stress-displacement diagrams obtained during the testing programme was used as a starting point and two functions to fit the results developed and evaluated. The first function

was a power law proposed by Reinhardt, the second function a product of algebraic and exponential terms. The second function (Equation 3.1.9) proved to fit the data more closely than the power law, and provided a more accurate value for the fracture energy when compared with the experimental results.

$$\frac{\sigma}{f_t} = \left[1 + \left(c_1 \frac{\delta}{\delta_0}\right)^3\right] \exp\left(-c_2 \frac{\delta}{\delta_0}\right) - \frac{\delta}{\delta_0}(1 + c_1^{\,3}) \exp(-c_2) \qquad \text{Equation [3.1.9]}$$

where f_t is the tensile failure strength, δ is the displacement, δ_0 is the stress free crack opening displacement, c_1 and c_2 are material constants. This function was used as a failure criterion for concrete and was implemented in computer codes such as finite element analysis for modelling the material. This appears to be a feature of many of the papers reviewed, in that the description and prediction of failure in brittle materials is the first step in providing a complete model of the given material.

Phillips (1998) approached the problem of multiscale modelling from a different perspective through reviewing the various techniques employed by different researchers, and described the term 'multiscale' as:

"...what multiscale modelling schemes have in common is an organised attempt at information management....the ambition of such models is to find a way to keep only those degrees of freedom and to consider those processes that are vital to the description of the problem at hand, and nothing more."

At the time of publication he examined the modelling efforts that have studied the mechanics of materials in which space and time scales appear, or studies of the scale effect on mechanical response. On the basis that computing power is increasing all the time and that complex analyses are becoming easier to perform as a result, Phillips examined a selection of problems that were under investigation and reported very briefly on them. No actual techniques for modelling were included in the paper, and the majority of cases examined related to the effects of instabilities and defects have on microstructure. Although fairly comprehensive, the review does not cover the relation of microstructural details to the overall effect on material properties, it merely points to

the research currently being carried out. It concludes that the increase in computational power (in the form of the constant evolution of the PC) is enabling this particular area of interest to grow and studies previously too complex to provide useful data, are now yielding positive results.

Taking advantage of the increase in computational power, Osetsky and Bacon (2003) studied the more complex mechanisms of failure at the atomic level, in particular the effect of radiation damage in metals and how it affects the mechanical properties. Recognising that most failure models are based on microstructural behaviour, they sought to produce a model based on the behaviour of particles at the atomic level, the results from which could be used in microstructural models. Specifically, a model was produced that could examine how a dislocation within a crystal interacts with its environment (for example, what occurs when it comes into contact with an obstacle such as a void). The approach involved applying both a static relaxation technique which applied shear deformation to the dislocation when it came into contact with an obstacle, and molecular dynamics simulations that could plot the path of the dislocation. It enabled the examination of how a dislocation moves through a crystal under irradiation and gave a greater insight into the mechanisms involved, particularly the forces acting on the dislocations and those required to move it past obstacles. This information could then be fed back into continuum-scale model inspecting the strengthening of metals under irradiation, and could enable them to predict behaviour more accurately.

At the microscopic scale, Spychalski *et al.* (2002) employed computing techniques to model crack paths through assemblies of grains. Recognising that one of the defining characteristics of failure are the grains of the material, and using the criteria of the surface energy required for the grain boundary and grain interior to fail, software was developed that could take a digitised image of a polycrystalline material microstructure and convert it for analysis. From this image, the starting point and direction for crack propagation is defined and an algorithm calculates all the potential cracking paths along this route. Using another computer program called DIJKSTRA, the crack path requiring the least energy is calculated, and the results fed back into the custom software, and from this the fracture surface can be determined including geometrical and physical descriptions of the crack path. Putting the software into practice, the structures of both

ceramic materials and well-annealed metals were examined. The predictions of the crack paths through the microstructures examined produced information about how cracks propagate through polycrystalline materials, and they were able to quantitatively describe the relationship between the fracture parameters (specifically: fracture surface roughness, fracture surface energy along grain boundaries, and fracture energy) and the propagation of a crack. Three main conclusions were suggested for consideration in the design of granular materials with a higher resistance to cracking; the characteristics of a fracture surface becomes insensitive when the fracture energy along the grain boundaries is less than 60% of the fracture energy across the grain interior; the bridging effect of elongated grains causes significant deflection of the crack path (for grain boundary fracture energies less than 50% of the grain interior fracture energy); and, the models indicated a parabolic relationship between the fracture resistance and the percentage of special grain boundaries (defined as those grain boundaries that exhibit significantly higher values of fracture surface energy).

As it has been shown, there are different methods and techniques available for investigating the probability of failure in brittle materials, and particular reference has previously been made to Weibull theory. Brocklehurst (1977) showed that this cannot be successfully applied to nuclear graphites, and therefore, various other statistical analyses and fracture models have been developed within the global nuclear industry.

For predicting the properties of large sections of graphite from small scale specimens, Kennedy and Montgomery (1989) examined grades 2020 and IG-11 isotropic graphites in a statistical manner. Taking data obtained during flexural, tensile and brittle ring experiments, the aim was to analyse the results for quality assurance purposes and determine that the variability in the strengths of the two graphites would have little or no effect on large scale structures. Specimens were cut from large billets at differing locations to provide a random sampling of the microstructure, tested to failure, and the variance determined. The results showed that IG-11 had a less homogeneous structure in terms of variance, but was a stronger material and had less variability in strength than 2020 graphite. The location within the billet and the orientation from which they were cut showed to have a significant effect on the variability of the material properties, as would be expected from an isotropic material. Though the specimens tested were all of the same dimensions, Kennedy and Montgomery used the stressed volume of the

graphites for each of the tests as a measure of scale and performed a Weibull analysis to predict the strength of the large scale billet from the results obtained from the small scale samples, and further indicated the unsuitability of this method for predicting strength. Unfortunately, no further suggestion of a strength-scale relationship was put forward.

Arai *et al.* (1991) also statistically analysed the failure of graphite under uniaxial tension, flexure and compression, using IG-110 graphite in their experiments. Utilising a computer based program to interpret the data obtained from seven experiments, they found that for IG-110 graphite, there was an approximate 7% variability in strength in tension, 6% variability in flexure, and 5% in compression. In a different approach to Kennedy and Montgomery, Arai *et al.* did use Weibull theory to examine the results, but also employed a technique from the HTTR design guide to determine the specified minimum ultimate tensile and compressive strengths (SMUTS and SMUCS respectively), which is an approach grounded in engineering reliability. By developing normal distributions based on the test data, it enabled the calculation of SMUTS and SMUCS and proved to be close to the experimentally derived values for tension and compression, though still conservative by predicting ultimate strengths approximately 7 MPa and 18 MPa lower, respectively.

A general statistical theory for the prediction of failure in brittle materials was adapted to examine nuclear graphite by She and Landes (1993). The theory is based on the weakest link model, considering that one microcrack will ultimately cause the failure of the whole component, and assumes that there is a distribution of microcracks through the material with the critical strain energy release rate as the fracture criterion used for a single microcrack. The fracture strength resulting from the microcracks is characterised by a statistical distribution function that in turn calculates the failure probability. This distribution function is given as:

$$P_f = 1 - \exp\left\{ - N_0 \int_V \left[\left(\frac{1}{4\pi} \right) \iint_\Omega \Psi(\theta, \varphi, G_{cr}) d\Omega \right] dV \right\} \quad \text{Equation [3.1.10]}$$

where P_f is the probability of failure, N_0 is the density of the microcracks, V is the volume under loading, Ω is a solid angle in the spherical coordinate system, θ and φ are coordinates in the spherical coordinate system, G_{cr} is the critical strain energy release rate and represents the local failure criterion K_{cr} for the microcracks, Ψ is the distribution function of microcracks, and

$$\left(\frac{1}{4\pi}\right)\Psi(\theta,\varphi,Gcr)d\Omega \qquad \text{Equation [3.1.11]}$$

is the probability of occurrence of one microcrack. By assuming that the flaws present in the microstructure of graphite are penny shaped microcracks and are randomly distributed, and *f(a)* is the probability distribution function for the size of the microcracks, Equation 3.1.10 reduces to:

$$P_f = 1-\exp\left\{-N_0\int_V\left[\left(\frac{1}{4\pi}\right)\iiint_\Omega\left(\int_{acr} f(a)da\right)d\Omega\right]dV\right\} \qquad \text{Equation [3.1.12]}$$

The inputs needed to apply the model to graphite are then the distribution of the microcrack sizes, the density of the microcracks and the critical strain energy release rate. These parameters can be obtained as values from literature or by analysis of experimental data. With the model parameters determined from fracture data taken from 3- and 4-point flexural tests, it was shown that the model provided a prediction of failure that had good agreement with the test results, but was slightly conservative (it predicted a failure a lower stresses than was experimentally observed). The authors state that although the agreement is good, there is need for further validation by obtaining results for a variety of test geometries and conditions to be used as input parameters. However, using accurate microstructural data pertaining to the distribution of the defects within graphite would be a better approach, and they further suggest that detailed investigation into the sites of fracture initiation and how the microcracks develop and propagate would provide data and be a very good test of the validity of the model.

Possibly one of the most comprehensive fracture models for graphite is that proposed by Burchell (1995). An extensive review of the existing statistical methods and fracture models available enabled Burchell to define the most appropriate fracture parameters that need to be considered and the most effective method of employing them. Centred around a microstructural approach, the model was developed to consider the most relevant features of graphite that initiate fracture and cause failure. The porosity, filler particles and binder phase all influence crack propagation in one form or another, and data obtained by Burchell *et al.* (1987) during a microstructural study of the fracture of graphite enabled the development of the model based upon the processes of failure. By considering the microstructure to be constructed of cubic particles (of a size equal to the mean filler particle size) to allow for easier tessellation and analysis, and porosity being randomly distributed through the model (as are the pore sizes, based on a log normal distribution), it is assumed that a crack initiates in a pore and then propagates through the weakest planes in the particle (based on an LEFM approach). Each particle has an assigned critical stress intensity factor that, if exceeded, implies the particle has failed. The pore length is recalculated to add the length of the particle as it is now acting as a crack within the structure. Applying a probability that the crack will fracture particles ahead of it and a probability that the bulk material contains a defect that will lead to eventual failure allows the calculation of the failure probability. The parameters required for this model are the particle critical stress intensity factor, average filler particle size, bulk density, average pore size and associated distribution, average pore area, number of pores per cubic meter, and the specimen width and volume. All the parameters can be determined through image analysis of the microstructure of the graphite under observation with the exception of the critical stress intensity factor which can be obtained from literature. The input parameters are entered into a custom written code called SIFTING (Stress Induced FracTure IN Graphite), which uses an iterative method of calculating the propagation of the crack, and determines the failure probabilities as a function of stress.

The model was tested by analysing three different graphites of varying microstructure (H-451, IG-110 and AXF-5Q) to examine the results from coarse to fine grain material. Obtaining experimental data for each of the graphite types enabled the comparison to real world values, with the model being benchmarked against data for H-451, and validated against IG-110 and AXF-5Q. It was found that the model returned results that

were accurate predictions of the tensile strength of the graphites, and that for the H-451 graphite, the probability of failure predicted was extremely close to that determined experimentally. Small deviations were noted between the probabilities of failure at very low and very high stresses, in that the model underestimated the failure probability at low stress and overestimated the probability at high stress, but the differences were negligible. The results for the other two types of graphite were not quite as accurate as those for H-451, there was a good agreement between the sets of data. This could suggest that further microstructural analysis of the materials is required to gain more accurate input data, or that as the materials become more fine grained, the models fracture mechanics definition requires some refining. It is difficult to state why the model was extremely accurate for the coarser grained material and less so for the finer grained as there is not enough detailed information on how the microstructural features were analysed, but the fundamental fracture mechanics approach appears valid for the variation in graphite microstructure. One drawback to this fracture model is that while it examines the probability of failure based on stress, it does not quantitatively describe the effects of differing specimen geometries as it is based only on width and volume.

This section has considered some of the statistical models of the fracture of brittle materials, how the models are conceived and the techniques they are based upon (whether these are statistical distributions, fracture mechanics or microstructural features). As has been mentioned previously, the constant increase in computing power is allowing the development of more complex models of failure, and one area in particular that is becoming increasingly popular for structural modelling is that of finite element analysis (FEA).

3.2 Systems Ideas and Abstraction Techniques

When beginning any investigation into a problem it is very unlikely that the researcher would attempt to include all the relevant information during the planning stages. What is needed is an overview of the problem itself and the necessary contributing factors to the solution, then the process of finding an answer can begin in earnest. Conventionally, this simplification only takes place at the beginning of any research

project, but it does not necessarily have to stop there. The principle of simplifying a problem into easy to manage segments can be followed throughout the course of the research without detrimentally affecting the outcome. This section aims to give an overview of the technique of abstraction and highlight areas where the process has been successful. The Oxford English dictionary definition of abstract is:

"...existing in theory rather than practice; not concrete; not representational..."

In philosophical terms it is a thought process that distances ideas from the object under consideration. The concept of abstraction when applied to complex problems is the simplification of that problem by only focusing on the important features and discarding those that only complicate the issue further, essentially producing a theory that is not strictly representational of the problem as a whole, but does provide a solution. It is a concept that is currently widely recognised in the field of computer science as it allows firm details to be left undefined and ideas to be considered without the constraints of their implementation. A very basic example of the abstract thought process is many things can be *red*, and many things *sit on surfaces*, so the properties of *redness* and *sitting-on* are abstractions of those objects (Wikipedia, 2006).

Applying the technique of abstraction to engineering, Mistree and Allen (1993) reported that during the initial design phase of any product the components are split into entities that enable a holistic view of the problem where the entities can be arranged in any order and then rearranged at will until a solution is reached. From this the actual design and production stages can take place. They proposed that the functional requirements of the secondary design and production phases can be modelled by Living Systems Theory (LST) to improve the processes, where LST is a framework put forward to create a unifying theory for the hierarchical structure of life. It was developed to integrate the research findings of biological and environmental scientists and covers the lives of cells, organs, organisms, groups, organisations, communities, societies and supranational systems. It has also been used to model non-living systems as, in some cases, machines are used to carry out the functions of living systems, with the machine being substituted for a biological entity. What results is a high level of abstraction when examining a problem. By creating symbols to represent the critical functions of a system, the specific details can be ignored in the short term (or altogether) and the designer is able

to manipulate the functions to a desired outcome before moving on to a detailed analysis.

Putting abstraction into practice, Hacker (2001) produced a model to predict the co-efficient of thermal expansion (CTE) in nuclear graphites through the development of a microstructural model that describes the change in CTE under neutron irradiation and radiolytic oxidation. Due to the complex nature of graphite behaviour, the most effective way of studying these phenomena and producing a valid model was to employ the technique of abstraction which reduces the problem to its most simple and important components. The modelling process was broken down into a number of modules, starting simply and increasing in complexity upon the successful completion of each. These were:

Module 1: Semi-infinite single crystal
Module 2: Spherical single crystals
Module 3: Regular array
Module 4: Random array
Module 5: Bi-modal distributions
Module 6: Neutron irradiation and radiolytic oxidation effects

For the first module - by proposing that a single spherical grain can be described as a partially ordered array of single crystals containing porosity (Mrozowski and calcinations cracks), this can be abstracted to a single crystal 'onion skin' model (Figure 3.2.1).

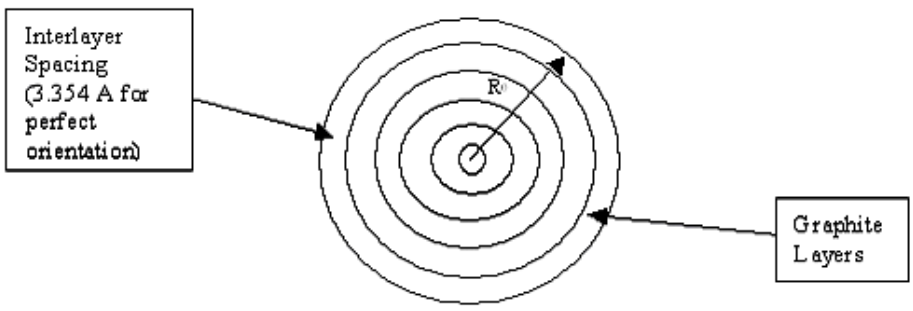

Figure 3.2.1 – Graphite single crystal 'onion skin' model (Hacker, 2001).

This ‘onion skin’ model is a 2-dimensional representation of a randomly orientated array of single crystals (termed spherical single crystals, or SSCs) and form Module 2. Employing Rodriguez *et al*. (1996) ‘particles in a box technique’ as a basis, Hacker was able to build arrays of SSCs for analysis which can then expand when conditions simulating irradiation and oxidation are applied to it.

Module 3 was the first module to consider more than one crystal, but kept them arranged in a simple array. The computer generated this in 2-dimensions, fixing the centre points of the SSCs in predefined locations. The number of layers in each SSC is determined randomly, and the distance between them (the lattice spacing) is dependent on the maximum number of layers. When temperature is applied to the model, the expansion of an individual SSC is calculated and the neighbouring SSCs displaced accordingly.

Module 4 was used to model the response of densely, randomly packed SSCs, and split into two parts, the dynamic solution and the static solution, in order to assess the optimum method for packing the spheres. The dynamic method comprised of randomly generating a number of SSCs within a defined area (in this case a square) and then ‘moving’ them based on their interactions with one another, to another location where they would not overlap. The dilation is computed in a similar fashion as each SSC expands with the applied temperature.

Although the results obtained from this technique were consistent with data from experimentation, Hacker found small gaps were created between SSCs during the modelling process. To overcome this problem he created the static solution based on the ‘particles in a box’ method of packing (also called a ‘drop and roll’ algorithm, Torquato *et al*, 2000). Using the technique described earlier by Rodriguez *et al.*, an array of SSCs is built, but as temperature is applied to the model the entire array simultaneously expands (the expansion of the SSCs is applied directly to the bulk material). This has the advantage over computing the displacements sequentially in that close contact between the particles is maintained. The results from this module gave dilations of the same order as those determined experimentally for AGR graphite.

Modules 5 and 6 were primarily concerned with refining the model and predicting the response of graphite under irradiation and oxidation. Through analysing micrographs of AGR graphite, a crude approximation of the 'filler' particle distribution was made (approximately 20% of the area comprises of filler particles with a mean diameter of approximately 500 μm). Applying the data to the model to simulate the microscopic structure of graphite, Hacker found that the resultant output was comparable with experimental data, even though this was still a simple model. Similarly, by incorporating data regarding the response of HOPG under irradiation (Kelly & Brocklehurst, 1971) and the linear relationship for the dimensional change, with fluence (Neighbour, 2000), the model was able to produce results comparable to those obtained experimentally, and predict the CTE beyond results available (suggesting that CTE falls sharply at high fluences).

For studying the effects of oxidation, it was simply a matter of randomly removing individual layers of the SSCs. Having determined that up to 20% weight loss oxidation occurs mainly in the binder phase, modelling the reaction of graphite from 0 – 80% weight loss was possible, finding that CTE rapidly decreased to zero above 60% weight loss, which unfortunately was not supported by the experimental findings (there was no significant reduction in CTE in excess of 60% weight loss). However, these discrepancies (and any others occurring in any of the modules) could be explained due to the finite size of the array, as a whole section of graphite is not under consideration, and the fact that all the modelling is 2-dimensional and not 3-dimensional. Although the prediction of oxidation and irradiation from the models does not conform precisely with the experimental data, Hacker has still produced a very good model with the ability to simulate changes in CTE with varying temperature in AGR graphite, all based on the abstraction technique, verifying that not all models need to be complex in order to obtain reasonably accurate results.

Taking a philosophical approach to the relationships between material structures and their properties, Östberg (2003) reflected on the current state of materials science as a whole to highlight some of the inconsistencies and problems associated with using models to predict material properties and failure. The reflections can be taken as an abstract view of the whole subject area, with the point being made that the majority of models to describe mechanical behaviour of materials are developed by scientists who

are experts in their field, but not necessarily experts in all aspects of the model they are creating. This leads to some aspects of the material in question being neglected and the model not being truly representative, and therefore not applicable to the material under all circumstances. The issue of scale is a good example of this as the mathematics behind a model for the small scale is not always the same for that at the large scale and, as such, either models exist for a variety of scales, or they are linked by arbitrarily derived parameters.

The main issue Östberg was concerned with was that of materials scientists relying too heavily on mathematics as a description to a problem, thereby distancing themselves from the physical form of the material they are studying, highlighting that Plato preferred geometrical descriptions rather than arithmetical in order to avoid complex mathematical equations (which, in essence, is the technique of abstraction), and that it also avoided the discrepancy between mathematical and physical modelling. It is worth noting that scientists currently use a derived value to explain the difference between a theoretically produced value and a physically determined one, without necessarily knowing the cause for the difference. What the paper infers is that while mathematics is useful for the description of material behaviour (and in some cases is perfectly correct) it is not always the best choice for modelling and that a physically based model could be employed to better effect.

3.3 Finite Element Analysis & Computer Based Modelling Techniques

Much of the literature searched for regarding any form of microstructural modelling was concerned with using mathematical and computer based finite element analysis (FEA) to examine failure and the mechanisms that contribute to it. FEA is (usually) a computer based mathematical program that analyses the resultant behaviour of a material based on conditions set within a system. Its origins lie in the finite element method (FEM) developed by Richard Courant in 1943, where the core philosophy is that a complex structural problem can be solved by reducing it into a series of smaller problems that can be solved individually using numerical techniques and then applied back to the whole. FEA divides complex geometries into, ideally, triangular uniform

sections that are easier to solve (called elements), with each element being connected to the other elements by corner points (or nodes) which allow a solution for the system to be obtained. Through equilibrium equations derived for each element, taking into account the physical properties of the material and the environment the model is located in, a series of simultaneous equations are produced, which are then solved for the unknown values using linear algebra or non-linear numerical techniques (depending on the particular analysis). As FEM can be a complex mathematical process, its applications only became more widely used with the advent of the PC, and the ability to manage the numerous calculations became easier. As computing power has increased, more complex analyses of components and structures can take place, and more accurate solutions for problems can be obtained.

Two of the most important aspects of FEA are the correct development of the structure being analysed and the conditions being applied to the model. For the majority of FEA software, the construction of the model is in dimensionless units and it is the users responsibility to ensure the model has the correct geometry in order to produce valid results. In conjunction with this, when setting the conditions for the model to be solved, it is important to fully recognise where forces are acting on the system being considered and apply them correctly. Setting the correct boundary conditions is key to gaining a reliable result. The following section details some of the FEA techniques employed to study brittle materials, and in addition, some other computer based techniques that have been used to model material structures.

As mentioned, the correct generation of the structure to be analysed is of great importance, not only to ensure correct geometry, but also to allow a regular finite element mesh to be produced and the FE analysis to be completed successfully and with confidence in the output data. The majority of models created in finite element analysis programs are solid representations of a material structure with the requisite material properties applied, and most software allow the user to build the model with a CAD (Computer Aided Design) interface. If this is not the case then it may be required to build the model in another fashion and import it for analysis (with many commercially available FEA programs, they are able to read in files from other commercially available CAD programs).

Finite element modelling of solid concrete structures was performed by Kotsovos and Pavlović (1985) using non linear techniques. Studies have shown that the behaviour of concrete under tensile stress is non linear during microcracking therefore, when microcracking ceases the behaviour should be linear. This observation became the basis of the model, whereby the non linear behaviour of concrete could be described by linear material properties. Initially thinking through the concrete response to increasing tensile stress in a logical fashion, Kotsovos and Pavlović developed constitutive laws for concrete and steel (for the steel-concrete structure being analysed) to describe the deformation of the two materials and implemented them in the FE program FINEL, utilising 8-noded isoparametric elements for concrete and 3-noded bar elements for steel with a relatively coarse mesh. For this particular study, the authors are not attempting to fully describe the properties of steel-concrete beams under loading as their own research indicated that FE based predictions are only 20% accurate at best. Instead, they took the approach that finite element analysis should be used as a design tool for researching the approximate behaviour of systems and as such did not attempt to validate the model against experimentally obtained data. Insight into the potential failure mechanisms of steel-concrete beams under loading was gained by performing a series of analyses on simple supported beams. Using an uncracked beam initially gave a reference to compare subsequent models to, such features as preformed cracks and tensile, compressive and shear reinforcement were investigated. It was found that microstructural systems could be successfully evaluated and provide useful information back to engineers regarding the design of concrete structures, even if exact failure criteria could not be determined.

In the case of this thesis, it was known that random material microstructures would have to be generated for analysis, and one of the methods researched was that of Rodriguez, *et al*. (1986), who described a process of building a model that simulates the arrangement of particles at late stage sintering, and therefore simulating the microstructure of a sintered material. A computer program, written in Pascal, was developed that randomly selected a particle (defined by a radius distribution function) and "dropped" it under gravity conditions from a randomly chosen point into a unit cell of fixed size. This particle rolls on to any previously "dropped" particles and continues to move until it reaches a stable position. The stable position is determined in the program by an algorithm that establishes if it has made contact at three different points.

This is repeated to build up an array of particles, randomly placed and sized within the boundaries of the unit cell. For analytical purposes the top and bottom rows of particles were not analysed, instead a parallelpiped was cut from the unit cell. The results showed that the simulations compared well with data derived from literature. On analysis of the structure, an average co-ordination number of 6 was determined (*i.e.* there were 6 contact points for each particle), the density of the random packings was calculated to be approximately equal to that of loose random packing in real world materials. However, although the simulation provided a suitable method of studying the evolution of the microstructure during sintering, it requires repeated modifications of the original packing and repeated analyses. As far as it is possible to determine from the work, no allowance is made for the weight of added particles causing existing particles to be moved into new positions, as would be expected during the real world process, making it appear that some particles are positioned in free space. Some improvement to the model could be made to compensate for this and allow tighter packing within a unit cell. Additionally, refining the work to allow for analysis of the particles at the fringes of the unit cell (*e.g.* top and bottom edges) would produce a more robust model. No FE analysis was to be performed as part of this work, it was purely the development of an algorithm to model a sintered microstructure.

Modelling the strength of concrete under compression using finite element analysis on the microstructure, Schneider *et al.* (1999) generated porous structures to simulate the microstructure of aerated autoclaved concrete (AAC) based on the observations made of porous structures in the material. These observations were converted into finite element meshes for analysis, with both 2-dimensional and 3-dimensional models being considered (the 2-dimensional models represented porous bodies with parallel cylindrical holes). Based on experimental data, they calculated the failure probability using an extended Weibull model. On comparison of the experimental and modelling results they found that the 2-dimensional models tended to underestimate the strength of the porous structures more than the 3-dimensional model, and that the probability of failure in brittle matrix materials shows a strong dependence on the distance between pores.

Generally, FEA is used to model a complete structure or structural component that would be impractical to test in real life, but Zhou and Zhai (2000) employed the

cohesive finite element method (CFEM) to study micro-mechanical failure in aluminium oxide. CFEM differs from regular FEM in that the elements used in the model are kinematically independent of each other. Rather than sharing common boundaries and being perfectly bonded, the elements are cohesive surfaces and transmit friction forces across them. As they are not rigidly connected, each surface can act as a potential crack surface or an internal failure site, which makes CFEM suitable for examining the characteristics of fracture. There is no need to incorporate fracture initiation into the model as the fracture will evolve naturally in response to the conditions it is placed under. Through modelling a centre-cracked Al_2O_3 specimen under tensile loading, Zhou and Zhai (2000) examined the effect of mesh density on solution convergence through low and high stiffness of the cohesive surfaces. They found that as the mesh was refined the crack length decreased and no convergence of the results was obtained at a low stiffness of the cohesive surfaces. When modelled at a higher stiffness they found that as the mesh was refined, the crack length remained essentially the same, indicating a convergence of the solution.

Though microstructural features are not always employed in FEA to study failure, alternatives can be used to represent the material structure in question. Clegg and Hayhurst (2000) used the Rankine plasticity model for brittle cracking and implemented it in the AUTODYN hydrocode to model the impact of steel spheres on alumina (95% pure Sintox-FA). AUTODYN is a finite element modelling software that uses a mesh-free smooth particle hydrodynamics solution technique. They simulated a 6.35 mm diameter sphere impacting a 25 mm thick alumina block at 1449 m/s (assuming axisymmetric target geometry and response). On comparison with experimental results obtained from the same test performed in the real world, they found that their simulation technique compared extremely well, particularly with cone cracks, lateral cracking and penetration depth.

Finite element techniques were employed by Haecker *et al.* (2005) to determine the elastic properties of cement paste at a microstructural level, with the most important factors being the correct representation of the porosity and solid bodies present and their associated elastic modulii. Considering the complexity of the microstructure of cement paste, a program called CEMHYD3D was employed, through which the composition of the cement pastes are determined by analysing digital images of the microstructure.

These are then output as a 3-dimensional microstructure model. The result from this is then input to a finite element modelling software called elas3d.f, which is an elastic solver for composite materials. The results output from the FE model could then be processed in order to gain the individual elastic modulii for the constituents of the paste, and in turn model the response of the cement paste under consideration. On comparison of the overall elastic modulus determined for the paste with experimentally derived values, the model predictions were good, but criticism was made of the CEMHYD3D software as the smallest unit size in the 3-dimensional models is one voxel (essentially a 3-dimensional pixel), and the smallest capillary size in cement paste is less than this. What has been shown is that by correctly representing the microstructure and applying the appropriate material properties to the different phases of material (coupled with the correct porosity distribution), the material properties of the whole can be determined.

A similar technique to that of Haecker *et al.* (2005) was used by Kim *et al.* (2006) for the study of tungsten carbide cobalt (WC-Co), utilising optical imaging microscopy (OIM) to evaluate the features of test specimen microstructures and creating these as finite element models in a software package called OOF. The orientation of the WC grains was determined according to the analysis made of the microstructure (four different grades of WC-Co were examined), but the resolution of the imaging was unable to determine the orientation of the Co grains so they were assumed to be isotropic. Each 2-dimensional model was meshed using between 180,000 and 210,000 elements, solutions obtained for stress and strain under different thermal conditions (the material properties of the grains were assumed to be constant at all temperatures), and the elastic modulii and fracture strength calculated. The results from the finite element models showed good trend agreement compared to the experimentally derived results (as also indicated in the previously described papers), but the values returned were lower than the real material. With the elastic modulus, this was attributed to the binder phase of the materials containing dissolved WC and Co which was not included in the FE model whereas the calculated fracture strength was within 6% of the measured value.

After validating the produced model, three hypothetical microstructures were developed using the Monte Carlo seeding method assuming the shape of the grains to be rectangular but containing the observed microstructural features (*e.g.* grain size

distribution and carbide volume fraction), and solved in OOF under the same conditions as the real microstructures. A number of model results were produced to examine the effects of altering several microstructural characteristics (such as size distribution and angularity of the grains) in order to provide information on how these features influence the elastic properties and the fracture strength that may be useful in the future manufacture of WC-Co for specific applications.

For graphites, the finite element modelling of the microstructure to gain a prediction of the strength and mechanical properties has taken a few different guises, with a notable amount of research taking place at the University of Manchester. Hall *et al.* (2002) used ABAQUS FE software to model a cracked single graphite crystal surrounded by binder material (see Figure 3.3.1). The idealised crystal was 2-dimensional, 1.5 μm wide by 6 μm long containing three internal cracks of thickness 0.025 μm and having a boundary thickness of 0.75 μm (the elastic modulus of which is set respective to weight loss). The single crystal displacement was analysed by cycling the irradiation temperature between 20ºC and 450ºC for a number of dose values, and the results through the centre of the model in the *x* and *y* directions recorded for determining the coefficient of thermal expansion.

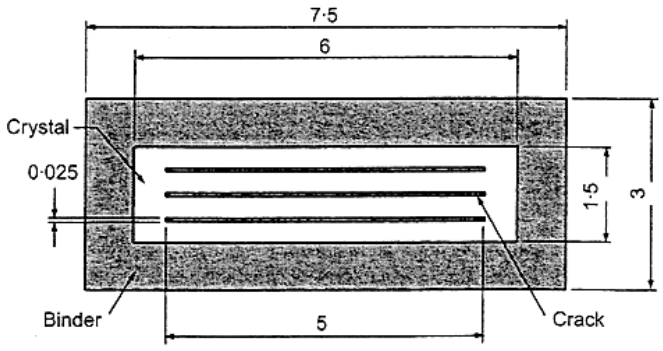

Figure 3.3.1 – Hall et al. (2002) single crystal for graphite FE model.

A FORTRAN subroutine called UMAT provides the single crystal properties and the constitutive relationships to ABAQUS during the solution procedure of the analysis. The initial results showed the expansion of the crystal to be inline with the expected behaviour of irradiated highly orientated pyrolytic graphite. On retrieving positive results, the approach was expanded to model a larger polycrystalline structure by stacking the single crystals at random with included solid binder sections and porosity. The orientation of the single crystals was also set at randomly determined horizontal or

vertical directions. For the polycrystalline model, two simulations were performed; one at 0% weight loss, the other at 30% weight loss. The dimensional change in the horizontal direction exhibited a similar turnaround (*i.e.* the polycrystal initially shrank, then turned back on itself and began to expand) to that observed in needle-coke graphites. In the vertical direction the model shrank at lower doses, then expanded with as the dose increased for the 0% weight loss. At 30% weight loss exhibited similar behaviour, but did not start to shrink until the dose at which the 0% weight loss model started to turnaround was reached. Calculating the apparent mean CTE showed that the model did not match the behaviour currently known for the effect of radiolytic oxidation on the coefficient of thermal expansion. Indeed, the work performed by Hacker (2001) modelled the dimensional change of the single crystal and the effect on CTE due to irradiation much more closely.

Further work on this model by Hall *et al.* (2006) was carried out to refine the approach and produce more accurate results for the prediction of irradiation induced property changes. The greatest change to the model was that of the definition of the single crystal, the number of cracks in the centre of the single crystal was reduced to two and the dimensions increased to those shown in Figure 3.3.2. The filler particle was also applied to the irradiated properties of highly orientated pyrolytic graphite, and the binder those of Gilsocarbon graphite. The single crystal FE model was solved in the same way as previously to provide input parameters for the next stage, the polycrystalline model.

The polycrystalline model (Figure 3.3.3) was also constructed and loaded in the same way as the previous work, though as well as orientating the filler particles at 0º and 90º, some were placed randomly at 45º and 135º. For the solution, the improved model was analysed at 450ºC, 600ºC, 1200ºC and 1500ºC. The results for dimensional change fell within the experimental data range, showing an improved prediction of the behaviour of the model. For Young's modulus, the FE results were close to the experimental data at the lower temperatures (450ºC and 600ºC), but the model slightly under predicted the change and did not correspond to the experimental data for the higher temperatures. What was shown with the refinement of the model is that a more thorough consideration of the initial setup of the model has yielded results that are closer to experimentally derived values and that there is evidence to show that this is a valid approach.

However, the lack of prediction for the higher temperature models could be caused by the single crystal model still not be a true representation of the material under scrutiny, in that HOPG is being examined but properties for Gilsocarbon are being used as inputs for the binder phase. Also, only the dimensional change and Young's modulus are being considered (not CTE in this refined model); if the model were designed to represent other material parameters too it may produce more favourable results.

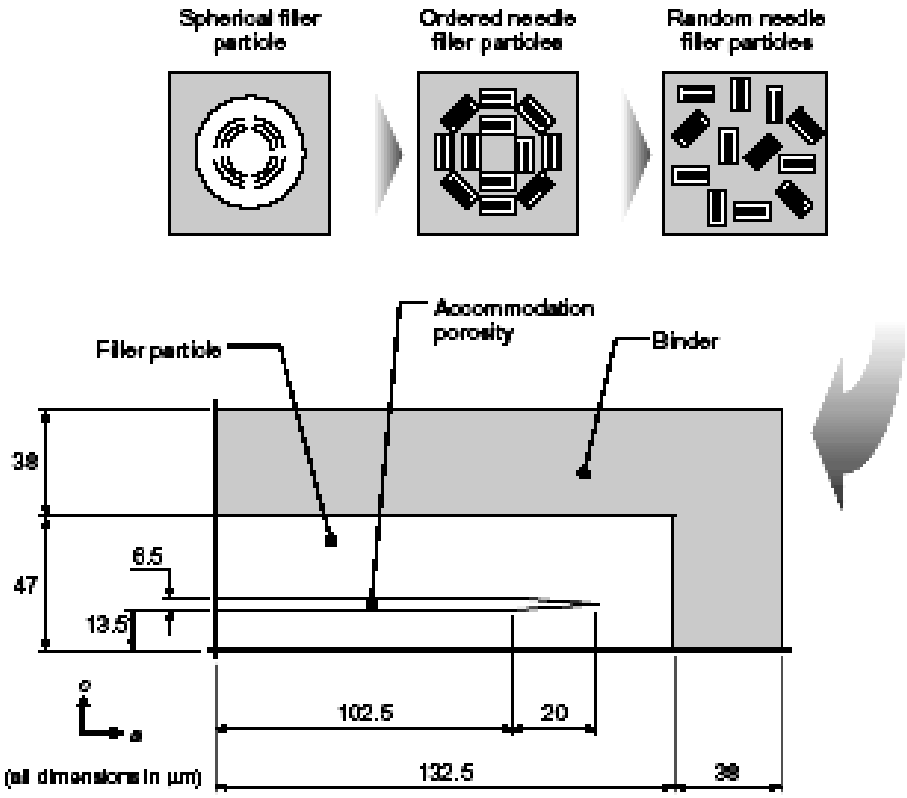

Figure 3.3.2 – Hall et al. (2002) revised single crystal model.

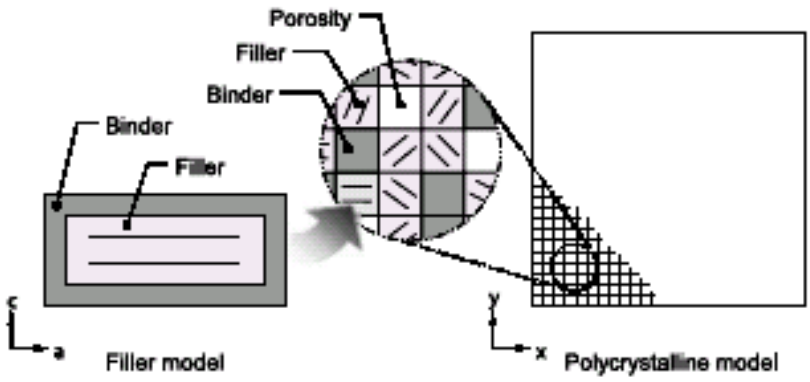

Figure 3.3.3 – Hall et al.(2002) polycrystalline graphite FE model.

Berre *et al.* (2006) also created FE models from microstructural images. X-ray tomography is used to obtain images of the 3-dimensional microstructure of Gilsocarbon graphite which are analysed by the image processing software ScanIP that segregates the image into the requisite filler, binder and porosity through the user defining threshold values for the greyscale image. In a greyscale image, the microstructural features of graphite can be determined by the shade of black or grey displayed, typically the black areas are porosity and varying shades of grey represent the filler and binder. Through image processing the features of interest can be separated out without the need for the user to define each individual area. The output from ScanIP is then processed by ScanFE that builds a voxel-based mesh of tetrahedral and hexahedral elements to fit the 3-dimensional structure which can then by analysed in by an FE package, in this instance ABAQUS (shown in Figure 3.3.4). Tensile loading was applied in the *x*, *y* and *z* directions and the Young's modulus calculated for several different porosity values ranging from 0% to 45% to simulate weight loss. The material input data for a single crystal was determined by nano-indentation tests. Additionally, the tensile strength at differing porosities was determined.

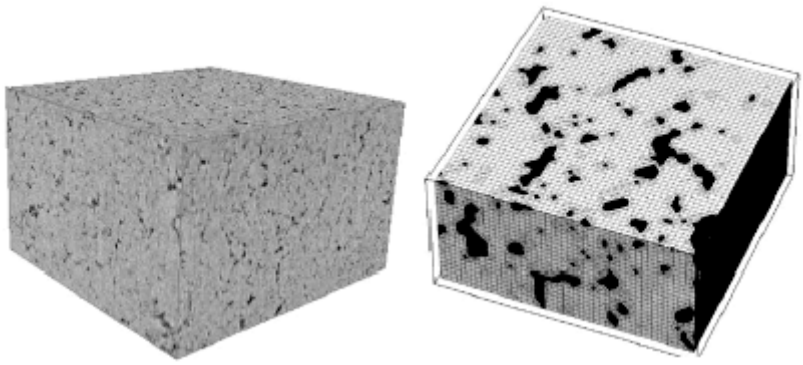

Figure 3.3.4 – X-Ray tomography image of Gilsocarbon graphite (left) and the meshed model for finite element analysis (right).

The results for the model were compared to theoretical values based on the Knudsen law (Equation 3.3.1) for Young's modulus based on the fraction of porosity, and experimentally derived values by Brocklehurst and Adam (1983) who performed mechanical tests of graphite subjected to weight loss.

$$E = E_{(\eta=0)} e^{-b\eta}$$ Equation [3.3.1]

where E is the Young's modulus, η is the porosity ratio, and b is a constant determined by experimental values (determined as 2.6 by Brocklehurst and Adam (1984)). It was found that the overall trend for the calculated Young's modulus followed that predicted by the Knudsen law, with the values being higher in the x and y directions, but were almost identical for the z direction. Unfortunately, the comparison to experimental was unfavourable, with the calculated Young's modulus being overestimated. It was suggested that this was due to the random distribution of porosities observed in graphites, but this could also be because the filler and binder were considered to be the same material as the image analysis could not distinguish between the two phases. The tensile data collected showed a decrease in stress in the material as weight loss increases but there was no experimental data available to compare these results to. On verifying the model results by increasing the mesh density, it was found that increasing the mesh density gave very different values to those obtained originally. Further work is planned to improve the model as finding the correct balance between the size of the area to analysed, a suitable mesh density and the inclusion of the important microstructural features is currently difficult. It could be suggested that further development of the image analysis to include the distinction between filler and binder phases is also required, as the elastic properties of the two are not the same.

Pandolfi *et al.* (2006) developed a method of simulating and analysing failure within a fine structured material through the application of what they term a recursive faulting model. By assuming a microstructure is essentially sections of elastic material joined together by faults, a series of equilibrium equations were developed to describe the behaviour of the material over time as stress is applied to the system, taking into account the energy required to cause crack propagation, the orientation of the crack, the scale of the microstructure, friction present within the system, and the potential relaxation of strain energy as a crack grows. Once developed, the initial model can be repeated through the use of the recursive function inherent in C and C++ software. This allows multiple faults to be constructed within a model to represent the structure of a brittle material. The finite element equations define a module that can be used as an input to FEA software when modelling structural components and also randomly

assigns the fault location and orientation. To validate the approach taken, FEA modelling of dynamic multi-axial compression experiments on sintered A1N took place. Having a large amount of data available enabled the authors to construct models replicating the conditions of the experiments, incorporate the measured material properties and implement their recursive faulting model. When viewing the comparison of axial stress versus axial strain of the experimental testing and finite element modelling, it is apparent that the recursive faulting model does produce similar, if not exact, results. The model tends to underestimate the stress at low strains and overestimates the stress at high strains, but the overall trend follows closely. However, the authors note that the model results are comparable under conditions that cause distributed damage (*i.e.* a large number of small cracks are present), but under conditions such as tensile loading where there are a small number of cracks and a specific fracture energy per unit area is required to cause failure the model cannot be used.

So far the modelling of microstructures has been discussed, but the development of finite element analysis came about with the need to study the structural response of components under different loading conditions. Blackburn and Ford (1996) modelled impact on reactor core components due to seismic loading. By fully evaluating the system as a whole under seismic loading the best approximation of the acting forces could be made, and the model constructed with these in mind. ABAQUS was again used to construct the model and simulate the reaction of two fuel bricks in contact being impacted by a third with the results compared to experimental data. Unirradiated mechanical properties of Gilsocarbon graphite were assumed and 2-dimensional linear plane strain elements used to mesh the model. The predicted response of the finite element model did not reflect that observed experimentally and was attributed primarily to the model being insufficiently constrained and therefore not damping the motion of the model. The inclusion of non linear properties would naturally reduce the motion of the model as more energy would be absorbed through the components due to the formation of cracks and material damage. Once again, the lack of a suitable description of the microstructure of graphite (or any heterogeneous microstructure) to be employed in finite element analysis has caused the production of results that, while useful, are not a complete prediction of how the components would behave.

Blackburn and Ford (1996) referred to a paper by Ahmed (1987) that studied the dynamic response of AGR core bricks under seismic loading with a custom non linear analysis program called AGRCOR. Ahmed (1987) gained input data for his model from a mechanical testing programme for use with AGRCOR, which is specifically designed to analyse uniform columns and layers of bricks that are defined as rigid bodies separated by spring and damper elements. The majority of the paper is concerned with the testing programme with little being mentioned of how the model was constructed or solved. However, it appears that the results gained from the model were produced by trial and error selection of the input parameters obtained from the experiments, with the input parameters used being the ones that produced the result closest to the measured value. This seems like a valid approach in order to study the effect of varying structural conditions (*e.g.* removing components to simulate failure) during an earthquake, but only a general impression of the response of the system can be gained from this as the model is based on the data it is being validated against.

Many studies of the interaction between reactor core components have taken place, a series of which were undertaken at the University of Bath. Taylor *et al.* (1997) completed a feasibility study into whether it was possible (at the time) to kinematically model a Magnox reactor core. By constructing a 2-dimensional model of core components (based on dimensional data obtained from Magnox Electric Plc for the Oldbury power station), the interaction between: i) a single key and the two surrounding keyway roots in the moderator bricks; ii) the centre of a fuel channel; iii) the centre key, could be modelled. All three constructed models are depicted in Figure 3.3.5. Using material properties for the parallel direction of PGA graphite (as only 2-dimensions were being considered), the models of each component were constructed and analysed in ABAQUS. Displacements equivalent to those noted in a reactor core were applied to the surfaces of the outlying components to cause contact between the components and the resultant stresses determined. This estimated displacement of 0.8 mm showed no contact to occur between the components as the distances between each component was greater than that, and therefore no results were obtained. To demonstrate the principle, a greater displacement was applied and generalised stress patterns determined, but these are not representative of the actual forces due to displacement of core components.

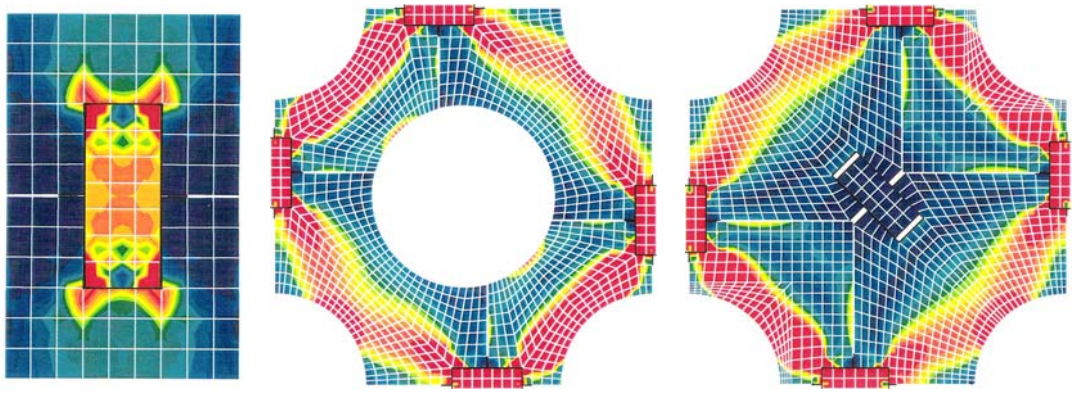

Figure 3.3.5 – (from left) i) key and keyway root model; ii) fuel channel model; iii) centre key model, Taylor et al. (1997).

Clift *et al.* (1997) created a linear elastic model to study the indentation of trepanned graphite specimens. Defining contact surfaces to represent the indenter and the graphite material, an impact analysis was performed with real values for elasticity for graphite obtained from the Haysham II reactor. The initial linear elastic analysis compared badly with experimental data, with the FE model value for maximum load being almost 20 times greater. As this was thought to be due to graphite not exhibiting linear elastic behaviour for this particular test (and that initially the model was solid material containing no porosity), non linear material properties present in the ABAQUS library were employed to further the analysis. The only applicable model was that of porous elasticity that also proved to give a value for the maximum load far in excess of the measured value though the value was less than half the original model, demonstrating the effect of porosity on the bulk material. The study was continued with the porous elastic model to investigate the effect of specimen thickness on maximum load, but as the values were far greater than experimentally derived it is difficult to see how these could be of use. This case again highlights the need for a definition of the microstructure of graphite in order to perform a valid structural analysis of the material.

Warner *et al.* (1998) furthered this work based on the fact that the initial models were built as unit cells with the aim of tessellating them together to examine the structural response of large sections of reactor core. To build a 3 unit cell by 3 unit cell model, the individual unit cells were connected by joining coinciding nodes together, and surface contact defined that, at the solution stage, determines if two surfaces are touching and develops the appropriate force between the two. If contact does occur then it becomes a case of impact analysis rather than static analysis and the ABAQUS

program calculates this separately, increasing solution times. Figure 3.3.6 shows the 3 x 3 unit cell model constructed for the static analysis.

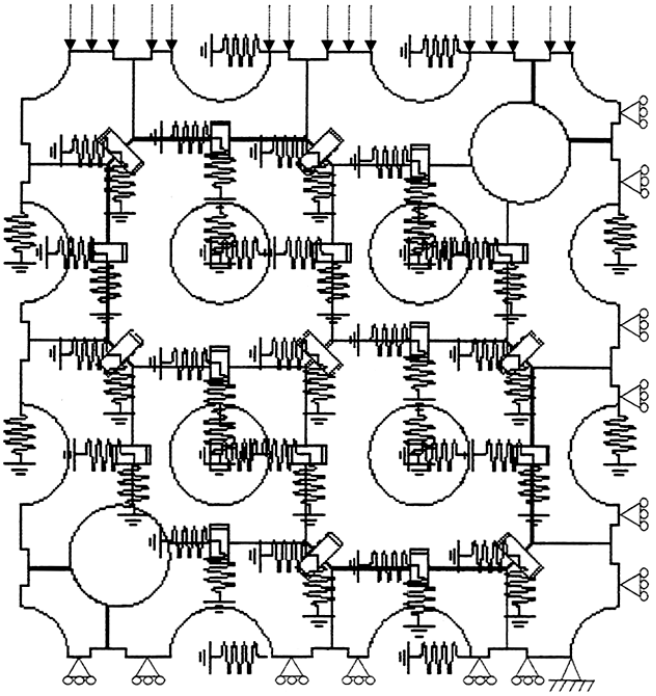

Figure 3.3.6 – 3 x 3 unit cell model of Magnox reactor core, Warner et al. (1998).

The model was displaced on the top surface (1 mm displacement in negative *y* direction), constrained in the *x* direction on the right hand edge, constrained in the *y* direction on the bottom edge, and the left hand edge left free to move in either direction. The first solution of the model failed to give a result as the keys had not been constrained correctly and were seen to 'rattle' in the keyways as their motion could not be determined by the software. By applying friction to the surfaces this was reduced. Upon running the complete model it was found that the result did not correspond to that anticipated, and that the 1 mm displacement on the outer surface only displaced the second row of unit cells 0.1 mm (0.5 mm was expected). Realistic loading was not transferred to the whole of the model. Although no significant result was obtained, the authors continued with the modelling process by simulating a cracked brick within the centre of the model, this produced no significant change in the result, though this could be the case as it is observed currently that single cracked bricks have no immediate impact on the functionality of the core as a whole. But as the model was not being displaced correctly this was the expected result.

Even though the 3 x 3 unit cell model had not solved correctly and the displacement problem had not been rectified, a larger 9 x 9 unit cell model was produced and placed under the same simulation conditions. This analysis failed after the initial displacement of 0.1 mm was applied, and the study ended at this stage. What can be gained from this is that there is most likely an error in the setting of the boundary conditions that have prevented the model behaving in a more realistic manner. From the images of the actual construction of the models and knowledge of FEA it is most likely that the contact surface definitions were causing the errors in transferring the displacement to the rest of the model, though no stress or strain distribution plots were included that could verify this and without detailed examination of the process of modelling, meshing and boundary condition setting there can be no suggested corrections. In terms of a feasibility study, it has shown that the modelling of a nuclear reactor core is not a simple matter, and that it is not just a case of producing a correct microstructural representation in order to gain a valid and useful result.

Looking at structural integrity from another point of view, Fok (1997) used ABAQUS to 2-dimensionally model the effects of brick failures within a reactor core. Half the core was modelled (with symmetry imposed along the centre in order to cut solution time) with the bricks set as rigid bodies separated by non linear elements that simulate the contact between components (unlike the analysis by Warner *et al.* (1997)). A FORTRAN based pre-processor called AGRIGID (developed by McLachlan (1996)) created the input files for the model and also randomly determined which of the structural components had failed. The displacement of the core bricks was defined by applying a load to the model in the *x* direction and allowing the components to move freely against one another. For the study to produce useful information, two analyses were performed; one with pessimistic core properties (brick shrinkage was at a maximum and key to keyway gaps were at a minimum with negligible shear resistance), and one with more representative shear resistance to reflect the actual behaviour of the core components. The analyses showed primarily that as the core life progresses and the number of failed bricks increases, the more displacement of the bricks takes place with them no longer fully separated by the keying system (*i.e.* brick to brick contact occurs). A secondary observation was that the forces acting on the keys are determined by the surrounding components and the number of failed bricks present. The difference between the two models showed that increasing the shear resistance causes a decrease

of the displacement of the bricks. Fok successfully demonstrated that a 2-dimensional model of a full reactor core is possible, and further work was planned to expand this to 3-dimensions.

A further study of the theoretical cracking of AGR core components was performed by Mar *et al.* (2002) on behalf of British Energy Generation Ltd. The purpose was to review the current techniques available and to investigate the potential application of concrete modelling methods for graphite. Graphite and concrete have some significant similarities:

- Both are a two phase material with aggregate particles surrounded by a matrix of chemically identical material;
- Concrete and graphite both contain porosity, the distribution of which effects the bulk material properties;
- Both materials exhibit shrinkage with age, though in the case of graphite this is caused by radiolytic oxidation, whereas with concrete this is due to the hydration of the cement paste;
- Graphite and concrete are classed as quasi-brittle materials, and both fail by similar fracture mechanisms (microcracking).

Using a finite element analysis program, DIANA, developed for the civil engineering sector and particularly suited to crack modelling, Mar *et al.* (2002) performed a number of analyses to predict failure in graphite due to either smeared or discrete cracks. Smeared crack models work on the principle that cracking is a fundamental part of the material behaviour, and are defined by two types: fixed (crack orientation is fixed) and rotating (crack orientation coincides with the principal stress direction). Discrete crack models view cracks as geometrical discontinuities that are represented by interface elements with their own unique properties. DIANA features the function that ABAQUS user defined material model subroutines can be incorporated, enabling the existing graphite UMAT produced by British Energy Generation Ltd. to be used.

Analyses of 3-point flexural (both unnotched and notched specimens), compact tension specimens and cracking due to the turnaround effect were performed using both the smeared and discrete crack approaches. 8-noded plane stress elements were used for

each 2-dimensional model in conjunction with standard unirradiated Gilsocarbon graphite material properties. Additionally, crack dilatancy and graphite lattice modelling were included to study the feasibility of applying these crack prediction techniques to graphite. These latter two techniques require microstructural data as an input and, at the time of writing, only those for concrete were incorporated in DIANA. Their inclusion was purely to demonstrate other approaches to crack modelling. As stated previously, this investigation was solely for analysing currently available FE techniques and their applicability to graphite, the model results produced were not used to predict graphite behaviour, but were used to demonstrate that the DIANA finite element analysis software could potentially be used in that fashion. It appears that the most suitable approach is a combination of the smeared and discrete crack models, as each individually has drawbacks that prevent it from being used on its own, *e.g.* the discrete crack model requires prior knowledge of the exact location of existing cracks and the smeared crack model results are dependent on element size. Once again, FEA has been shown as being of great benefit for the analysis of graphite structures, however, development is still needed to provide a complete package that would be enable it to be used as an effective tool for analysis.

One of the most recent finite element studies on the deformation of reactor core components was performed by He and Gotts (2005) using the computational fluid dynamics code FEAT (Finite Element Analysis Toolbox) to investigate the effect of a distorted moderator channel on the heat flow through the components. FEAT differs from other FE programs in that rather than constructing a solid model with a pre-processor and then meshing the model to divide it into elements, a 2-dimensional mesh of elements is used as a starting point and the geometry manipulated to the shape of the structure being analysed. Recognising the complexities involved in modelling a whole reactor core, He and Gotts simplified the analysis by scrutinising just one moderator channel and omitting the fine details that were unlikely to affect the heat flow through the fuel channel. They created models that were essentially just hollowed out cylinders (to represent the brick) with an annular insert (to represent the sleeve, see Figure 3.3.7), with one model having no distortion of the fuel sleeve and the others having varying degrees of distortion, so that the fuel sleeve wall bows towards the inner wall of the channel up to a maximum distortion where both are in contact. Standard thermal properties of AGR core graphite were used.

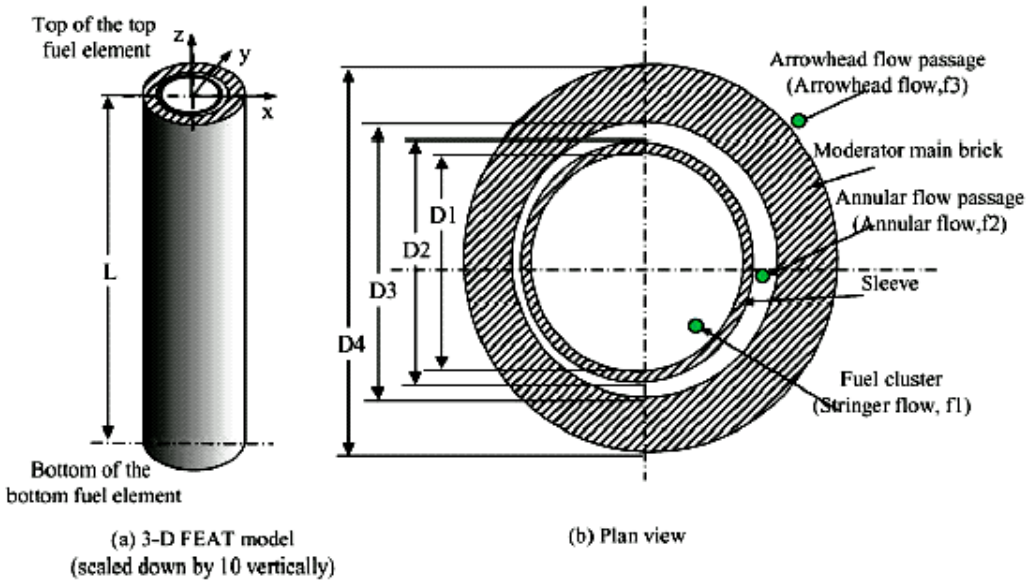

Figure 3.3.7 – Schematic representation of the fuel channel model (He and Gotts, 2005).

Where this study differs from the majority of the others discussed is the thorough consideration of boundary conditions and how they should be achieved to correctly model distortion of the moderator channel. Modelling reactor core behaviour tends to be based on a complex model with simplified material properties and applied forces (or even complex models with complex forces acting upon the structures), whereas they simplified the model but applied realistic forces and environmental conditions. At the time of writing there were no complete physical studies on this phenomenon to compare data with, although results from other research could be pooled to gain an indication of what should occur. The models determined a significant increase in the temperature through the walls of the fuel sleeve and the core brick (60ºC and 70ºC, respectively) where they come into contact if a maximum distortion has occurred, but concluded that this would have no detrimental effect on the integrity of the core as a whole.

In terms of other applications for graphite, Buch (1976) developed a mechanical behaviour model for graphite with a view to using the material for the nose tips of aerospace re-entry missile systems. Graphite is an ideal candidate for this application due to its mechanical properties, particularly its thermal resistance. Buch observed that the available statistical models for the prediction of failure in graphite do not relate fracture to the microstructure, and so developed a model for the tensile failure of polycrystalline graphite based only on microstructural fracture. Starting with an idealised microstructure that contained no pores, the model was constructed of cubic

particles to represent the grains that were bonded together to form the bulk material. By assuming that each particle contained a plane of weakness and that fracture was a progressive phenomenon as described by fracture mechanics (as covered in Chapter 2.3 – Fracture Mechanics and Fractography), a series of equations were developed to determine the theoretical fracture of this idealised material. A computer program was written for the purpose of solving these equations, with increments in stress level being applied to the model and the probability of failure of each grain calculated. At each stress level, the probability of a critical flaw being formed from a number of microcracks was also determined, and hence, the probability of model failure.

The next step was to add porosity into the model and was achieved by randomly setting grains as being pre-cracked; using the assumption that porosity is equivalent to a cleaved grain as it has no strength in any direction. A function to represent the probability that a grain site is a pore was derived and added to the computer program. Further to this, the probability of failure at a grain boundary and the random orientation of the grains were also included to give as complete a definition as possible of the microstructural mechanisms during fracture. Though only comparing the predictions from the model to ATJ graphite, the output stress and strain data matched those obtained experimentally very well as did the results for failure stress with increasing volume. The purpose of the model was to logically approach the failure of graphite in microstructural terms rather than fitting an empirically derived expression to test data, and in this Buch succeeded for graphite used in aerospace applications.

3.4 Summary

The preceding two chapters have detailed some of the literature available on graphite properties, structure, analysis techniques and utilisation. In addition to these areas, they have also touched on the large amount of papers and reports available on finite element analysis techniques and the theory of fracture mechanics. It is clear that although there is a wealth of information available, no single defined solution to the objectives stated in the opening chapter exists.

The literature review provides guidance on the potentially successful approaches to take, and importantly gives concepts and data that can be used to validate the results of both the proposed modelling and testing programmes. Of particular reference to the testing programme are Brocklehurst's (1977) testing of small scale graphite specimens, and Sakai and Brandt's (1993) review of notched test specimen geometries. This will aid greatly in both the development of the test specimens and in the validation of the test results. Further to this, the application of fracture mechanics in the form of correctly interpreting the testing programme results will be key to producing a valid data set for comparison to the conceptual model. Both Griffith (1921) and Irwin (1958) will provide the basis for the derivation of the equations required for correct calculation of the material fracture properties.

In terms of the modelling programme and the information gained, it is clear that Hacker's (2001) application of abstraction to the study of the co-efficient of thermal expansion was particularly successful, which suggests that this is a valid approach to take in modelling the effect of specimen size on strength. The application of physical graphite data to a computer model was successfully achieved by Hall *et al.* (2002) through the modelling of the cracked single graphite crystal, showing that the inclusion of more complex material properties can now be handled by current computer systems and software. Additionally, Rodriguez *et al.* (1986) have demonstrated the ability to use automated microstructure generation to mimic the structure found in the real world material. However, as with any computer modelling, it is essential that all input parameters are considered fully and deemed appropriate in order to gain useful results.

Whilst the above mentioned papers and theses are not the only literature that will be taken into account throughout the course of this thesis, they provide solid starting points from which to develop both a comprehensive testing programme and conceptual model to examine the issues of scale in the nuclear graphites.

Part B: Design and construction of a conceptual FEA model and its predictions

Chapter 4 - Conceptual Modelling

The previous three chapters have given details on the objectives of the thesis, the history and manufacture of graphite, and the fracture and prediction of failure of different types of graphite through numerical, experimental and finite element analyses. The information obtained on the microstructural features and mechanical properties from the literature have assisted in the development and implementation of a finite element model that bases itself on the analysis of the graphite microstructure under stress and not just the component as a whole.

4.1 Model Development

Modelling techniques are currently available for the failure analysis of graphite, which generally comprise of a component being constructed within finite element analysis software, with the application of standard graphite material properties used to indicate how the component would behave. However, no model/method at this time includes the complexities of the microstructure of graphite and so this offers a possible route to understand the apparent random arrangement of its constituents.

The process of abstraction and associated modelling techniques has been used successfully in other fields as well as in understanding polygranular graphite better. The process of abstraction involves simplifying a complex system to its basic, most important components or in other words using the principle of separating out important features from other less important ones. Hacker (2001) demonstrated that abstraction could be used successfully to model complex behaviour related to the coefficient of thermal expansion (CTE). In this study, the "balls in the box" approach was used to simulate the interaction of spherical graphitic particles when heated and thereby

generating a dilation curve from which a value of the CTE could be determined. The study was also able to use the dimensional change theory proposed by Neighbour (2000) to predict, and for the first time with some remarkable closeness, the change in CTE with increasing neutron fluence. In the same way, this process of simplifying a complex system to its basic, most important components can be used to generate an abstract model of the graphite microstructure with the random representation of flaw size distributions to understand how material properties such as strength may change with volume. To demonstrate the initial thought processes involved in outlining the direction of this new approach using abstract techniques, Figure 4.1.1 is a 'rich' picture highlighting key areas for investigation.

Selecting an appropriate technique for modelling is of great importance, but so is selecting the appropriate software to perform the analyses. An initial appraisal of the various possible numerical analysis routes suggested finite element analysis to be the most appropriate, and in particular ANSYS (based on prior experience).

The thought process of abstracting the microstructure to its simplest form involved initially considering just the main two individual particle types, binder and filler. These particles could be manually placed, at random, within a pre-determined structure to generate a microstructure mimicking that of Gilsocarbon graphite. Figure 4.1.2 shows the particles initially modelled as 2-dimensional squares, and were used to illustrate the size of the two different particles and the various packing arrangements within the confines of the outer shape. The selection of square particles would aid in the use of FEA software because to perform FEA and produce accurate results there must be a uniform mesh (distribution of elements) throughout the model (the fine detail of the FE analysis will be discussed in greater detail later in this chapter). Square particles enabled the use of a very even element distribution due to the simplicity of the shape.

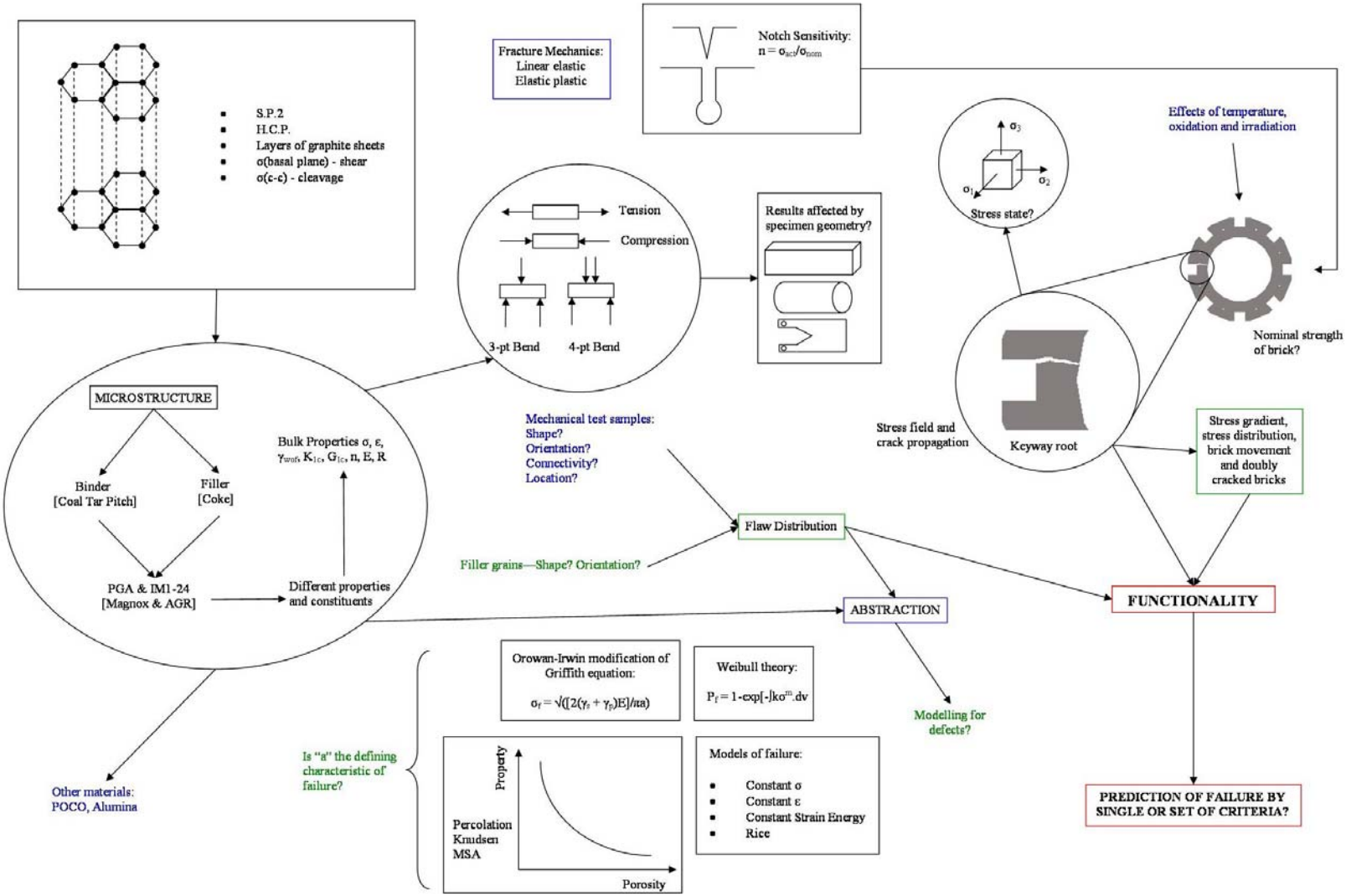

Figure 4.1.1 – Rich picture produced at the planning stages to focus the direction of the research.

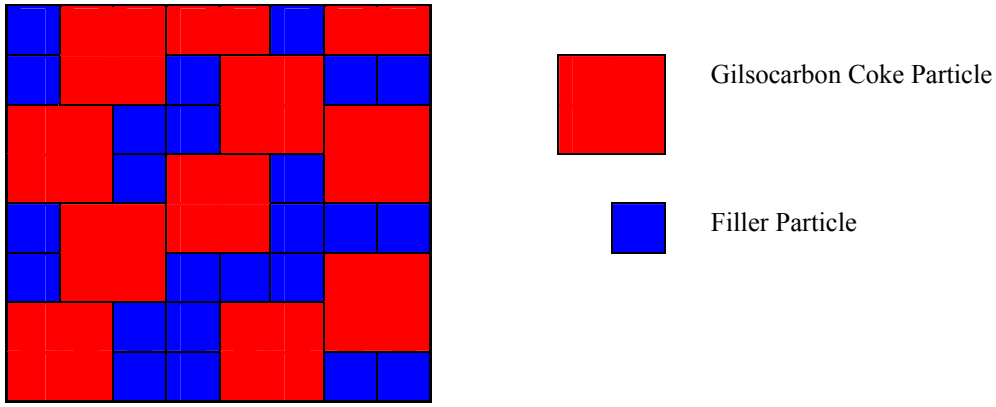

Figure 4.1.2 –Square particle abstract model for microstructure of graphite.

However, this simple model does not take into account the porosity of graphite as no provision for spaces between the particles was made at this early stage. Creating a random grid of particles and assigning each square (or element) a material property dependent on which particle it is representing would enable the first simple analyses to be performed quickly and easily before moving on to the next step, but there would be no merit in modelling the interaction of particles without pores being present. Thus, the next step from here was to incorporate elements that represent porosity to include flaws and defects within the material as shown in Figure 4.1.3. Through leaving sections of the model clear, the presence of voids can be created and the inclusion of porosity within the structure begins.

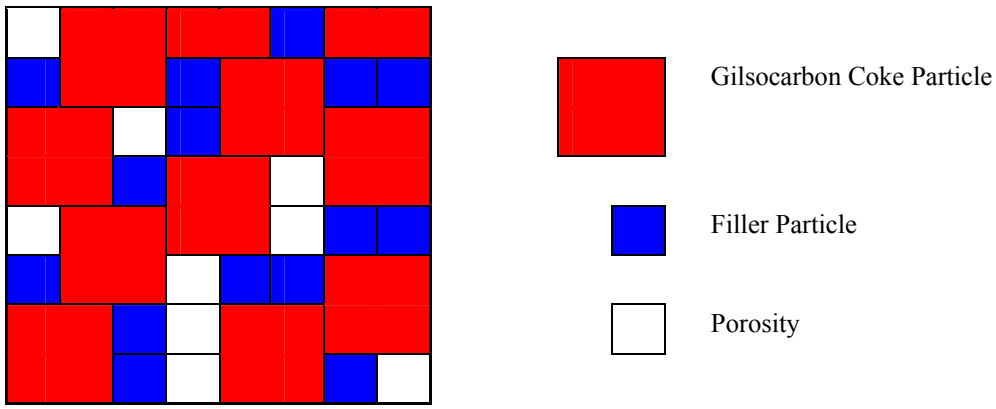

Figure 4.1.3 – Inclusion of porosity in the square particle abstract model.

At this stage, the abstract model contains all the fundamental elements of the microstructure and through simply increasing the size of the model and the number of

particles within it, would provide an easy solution by FEA. However, the ultimate aim is to model the microstructure of graphite (and potentially any ceramic material) as accurately as possible, and thus it becomes apparent that square particles represented a far too simple model.

As shown in Figure 4.1.4, increasing the complexity of the model through modelling spherical coke and Gilsocarbon particles would allow a more accurate model of the microstructure, but would then be negating the concept of abstraction. This "balls in the box" approach (so named due to it representing the random arrangement of particles as if it were balls being dropped into a container and allowing them to settle naturally) would prove to be too complex to model in any great detail at this stage in time, given present computer processing power. A good compromise between simplification and complexity is that of using hexagons to represent the filler, binder and porosity, and from here the microstructural model could be built and analysed.

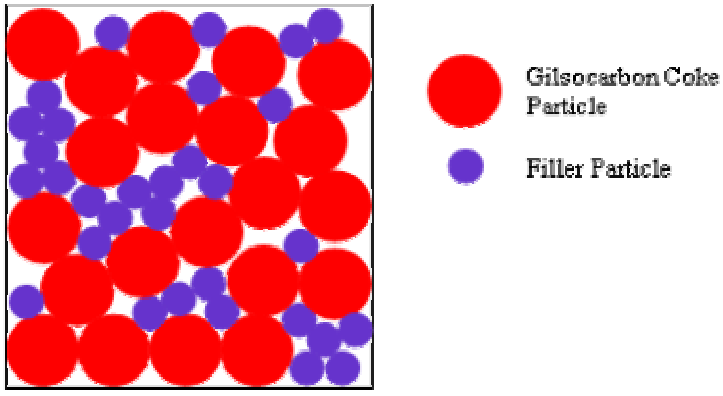

Figure 4.1.4 – Modelling of spherical particles ("balls in the box"), Rodriguez et. al. (1986).

4.2 Model Design

Having selected a method of abstracting the microstructure of graphite in order to develop a model to examine the relationship between scale and material parameters, the first model was built and consisted of a 2-dimensional FEA, simply arranged with hexagons representing filler, binder and porosity. The initial work was undertaken by Auckett (2003) who determined that the approach, assuming that the single crystals and

pores were all hexagonally shaped, was valid as shown in Figure 4.2.1. This approach allowed the tessellation of each of the elements with ease without over complicating the model. An arrangement of six hexagons around a single pore was set as the basic building block for the models (known as the basic structural unit or BSU) which could, of course, be employed in the production of any size of model by simple replication. Through using individual hexagons in the model to denote the single crystals, different material properties could be assigned to each specific hexagon in order to represent the differing crystal orientations or in the case of a pore, a null value. In the smallest models, *e.g.,* the single BSU model, this could be done manually by selecting individual areas at random and applying the appropriate property. This method, whilst valid for building the models and defining the material properties, would prove to be very time consuming and as such, a different solution to this problem needed to be found.

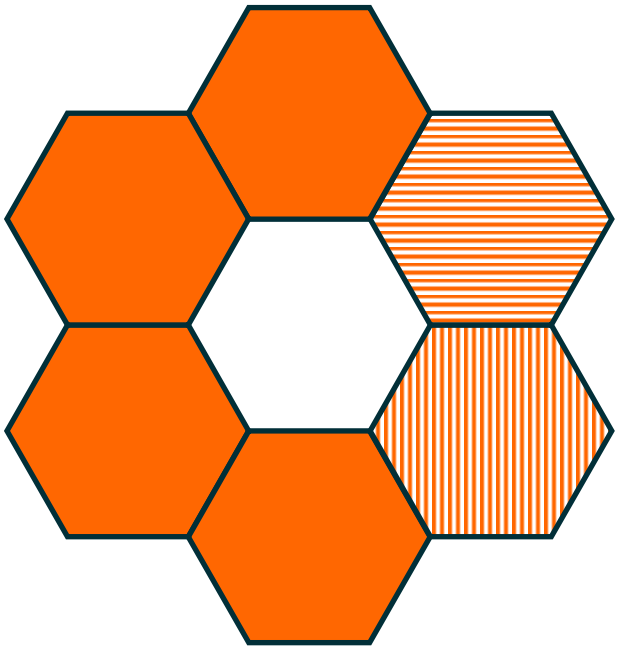

Figure 4.2.1 - An illustration of the basic structural unit (BSU) used in the development of the abstract model. Crystal orientation is denoted by the horizontal and vertical bars (the central hexagon is considered to be a pore).

The ideal solution to these particular problems was to automate the tasks of generating the model and assigning the material properties to sections of the model at random. Two programs were written in C++ code (see Appendix B) to automate these tasks, principally:

1. A Model Generator - an executable file that generates an ANSYS format .log file, which when read by the ANSYS software builds an array of hexagons that represent the simplified version of the graphite microstructure complete with pores;
2. A Material Setter - an executable file that generates an ANSYS format .log file that sets the material properties of the model at random to give a simple representation of the two crystal orientations with a section of graphite.

The model generator prompts the user to input a filename for the log file that is to be created, then asks for the scale of the model (*i.e.* the overall size of the model). Once completed, a log file is generated that contains the commands that ANSYS requires to build the model.

For the material setter, the user is requested to input a filename, the number of volumes (or areas) present in the model and which type it actually is (volume or area). The created file can then be read by ANSYS to set the material properties of the model, and randomly set half of the volumes/areas to one material property, leaving the rest set to a different material property which represents the different constituents in the microstructure, *e.g.* crystal orientations. The model generator was used to create a file for a model containing 100 BSU, as shown in Figure 4.2.2, where only one material type and porosity is represented, and the required sections to build a square model. The material setter was used to generate a file that set the material properties of the model to those specified in Table 4.2.1 in the first iteration using single crystal values for Young's modulus (1=a-axis and 2=c-axis) and generic values for Poisson's ratio and density. It is important to recognise here that the values used are to some extent arbitrary since the main purpose initially is to demonstrate the methodology.

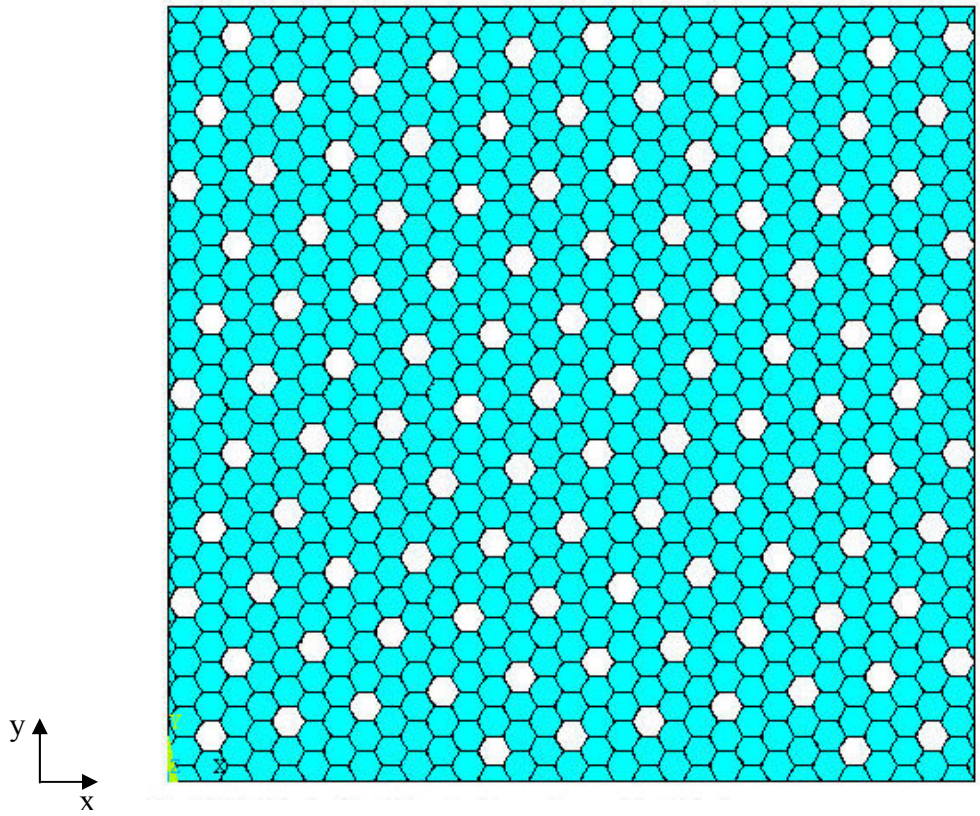

Figure 4.2.2 - 100 BSU model with uniform pore distribution throughout produced by the model generator program (the white spaces represent the pore distribution).

	Young's modulus (Pa)	**Poisson's Ratio**	**Density (kg/m^3)**
Material 1	3.64 x 10^{10}	0.2	2200
Material 2	100 x 10^{10}	0.2	2200

Table 4.2.1 - Material properties set by the material setter program.

Further, the file created by the model generator is used by ANSYS to build the model by defining all the key-points required, joining these key-points together with lines, extruding the resultant model by 1 unit in the z-direction (by default, although this can be set to any desired value) and finally gluing all the areas/volumes together. The log file also defines the element type to be used in the analysis, initially the element SOLID92 was used, a ten-noded tetrahedral 3-dimensional element (discussed in more detail later). On reading the material setter file into ANSYS, the values for the two material properties used to represent the "filler" and "binder" phases are applied to the BSU configuration, as illustrated by Figure 4.2.3, before the model is used for any analysis.

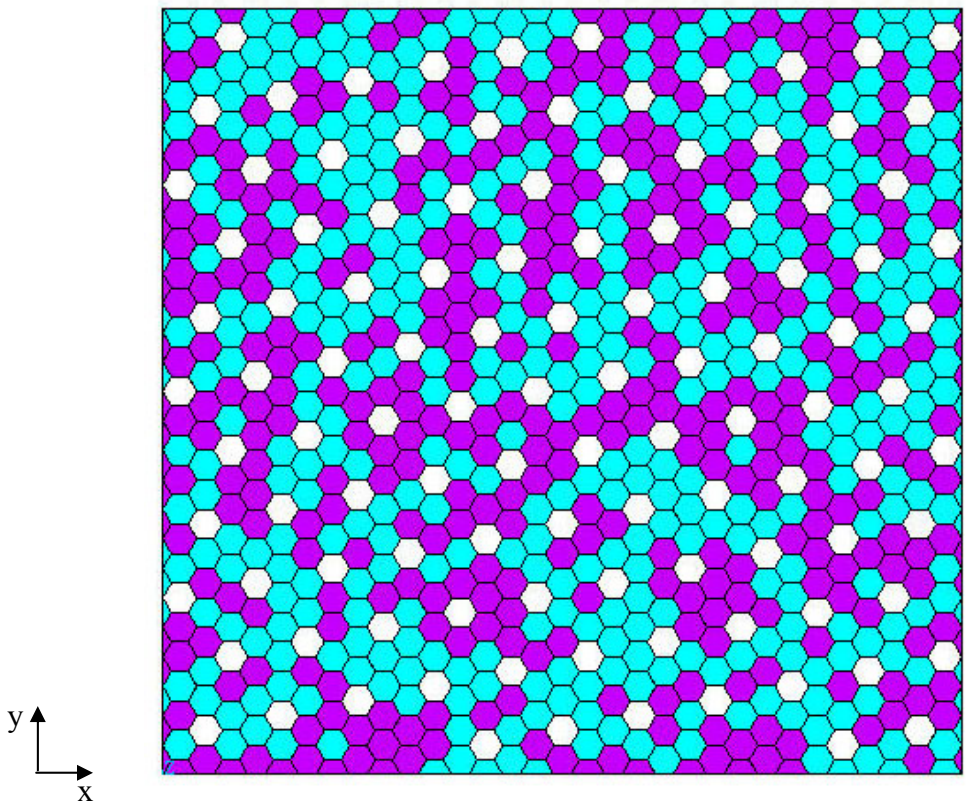

Figure 4.2.3 – Distribution of material properties within the 100 BSU model. The purple hexagons represent the filler Gilsocarbon particles, the light blue hexagons represent the binder coal tar pitch.

The generated model is meshed with the just the default mesh options, with the exception that the number of elements on each line is limited to one. This step causes ANSYS to insert one element for each side of the hexagons representing the particles in the model and, in turn, provides a uniform mesh of elements across the model giving the best compromise between mesh density and accuracy. The relevant loads and displacements are then applied. In this instance, the left hand edge is fixed (no displacement allowed) in the x-direction and the bottom edge of the model is fixed in the y- and z- directions. A displacement of one quarter of the total model height is applied to the top surface in the positive y-direction (in tension) and to instigate a stress state before being solved by ANSYS. Upon the solution, many different parameters regarding the stress and strain states can be examined. For this study the following maximum values were recorded, and plots of the results produced:

- the total displacement of the nodes;
- von Mises stress;
- von Mises strain;

- 1st Principal Stress;
- 1st Principal Strain;
- Strain Energy;
- Stress Intensity.

An example of an output for the von Mises stress through 100 BSU uniform pore distribution model is presented in Figure 4.2.4. Plotting these material parameters against the number of BSU's in the model (analogous to volume) would give an initial indication of how the strength (and other properties) might vary with the model size, which (as per the literature reviewed) would be expected to increase with the model size up to a given point, then decline.

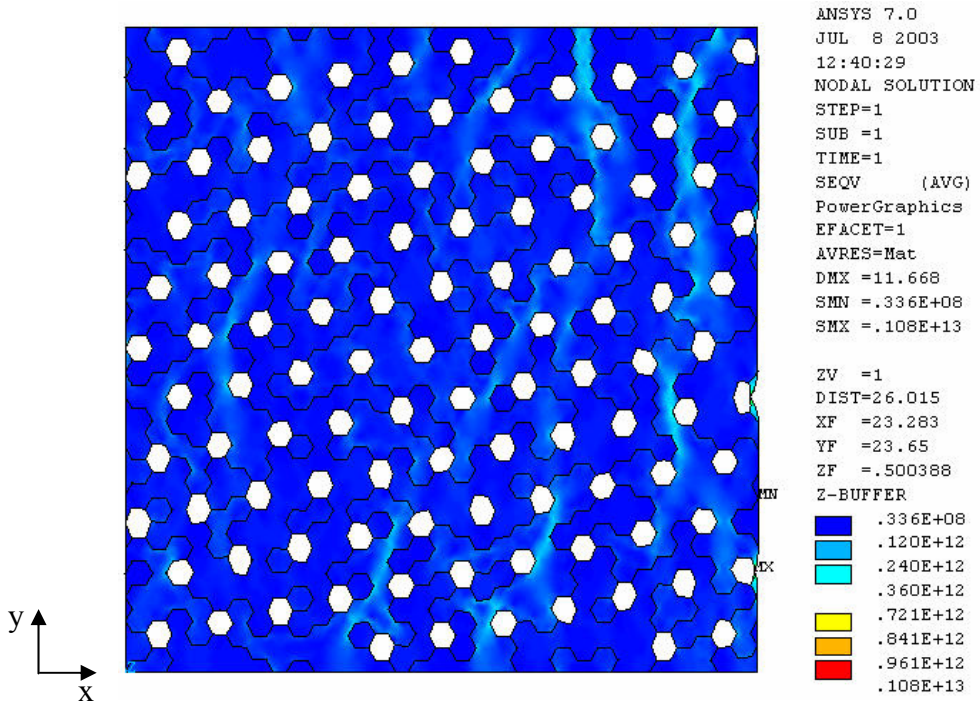

Figure 4.2.4 – von Mises stress distribution through solved 100 BSU model. Maximum and minimum stresses are located at edges of pores where the "material" is thickest and thinnest, respectively (represented by MX and MN).

Clearly, the amount and the distribution of porosity will alter the theoretical strength and therefore the next step in developing the methodology was to expand the model further through the introduction of a random pore distribution. By altering the model generator source code, its function was changed to enable it to randomly distribute the pores at a pre-defined porosity. In order to validate the approach with earlier models, a porosity value of 13 % was initially used (equivalent to even pore distribution) before

moving to a 20% porosity (a more typical value for nuclear graphites). Figure 4.2.5 depicts an example model generated with a random pore distribution.

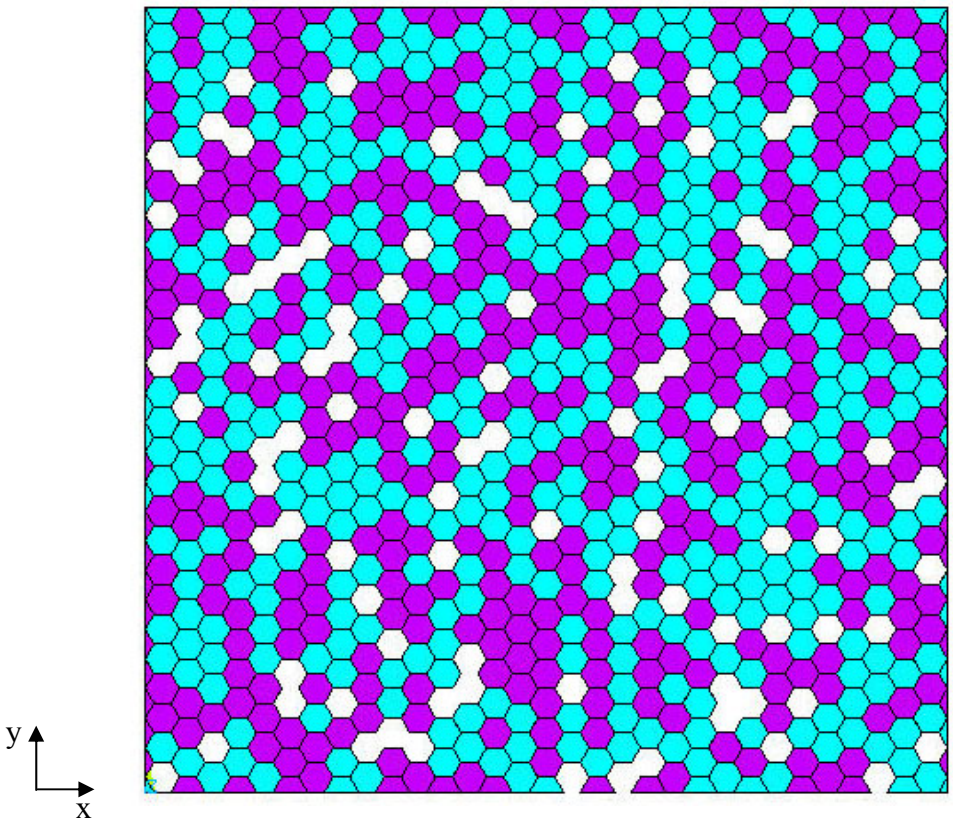

Figure 4.2.5 – Distribution of material properties within the 100 BSU model with the inclusion of the randomly generated pore structure. Again, the purple hexagons represent the filler Gilsocarbon particles and the light blue hexagons represent the binder coal tar pitch.

Upon the generation of a random pore distribution model, it became apparent that the models are no longer defined by a BSU, and therefore the methodology evolved to increase flexibility by defining the models by the number of whole units (hexagons) along two orthogonal edges, *e.g.* the model shown in Figure 4.2.5 would be 31 x 28. Models of size 5 x 5 units, 10 x 10 units and 20 x 20 units (see Figures 4.2.6, 4.2.7 and 4.2.8, respectively) were generated with a 20 % porosity value, read by ANSYS and then solved in order to examine the relationship between the size, pore distribution, crystal orientation, stress and strain. Each model had six iterations of its size generated giving six unique pore and material distributions for investigation; that is, for each configuration a mean and standard deviation was obtained. Further model sizes of 40 x 40 units, 50 x 50 units and 80 x 80 units could be analysed to obtain a larger catalogue of results to evaluate any scale/parameter relationship.

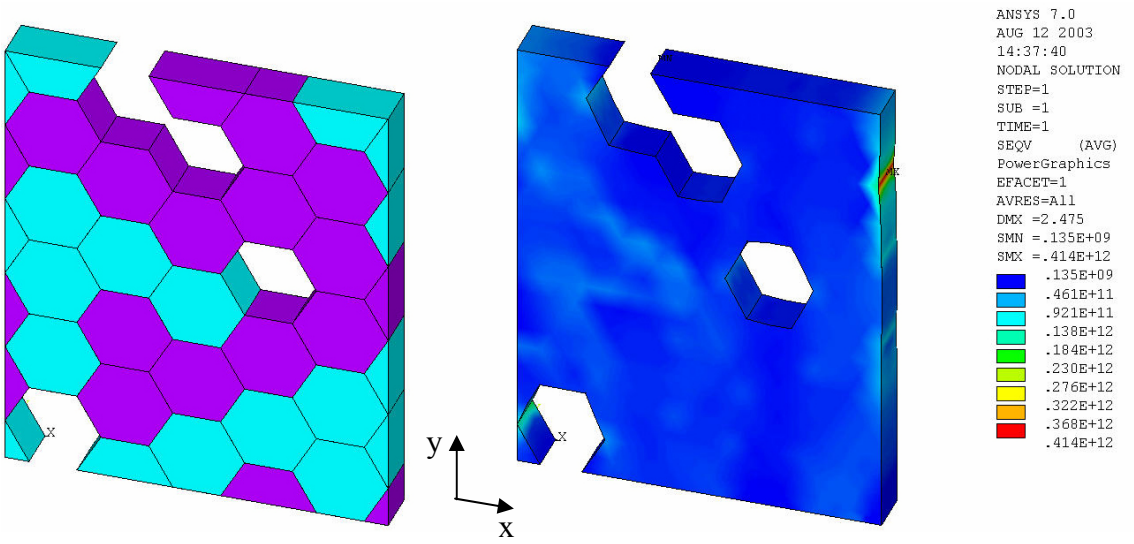

Figure 4.2.6 – Distribution of material properties and resulting von Mises stress output for the 5 x 5 unit model.

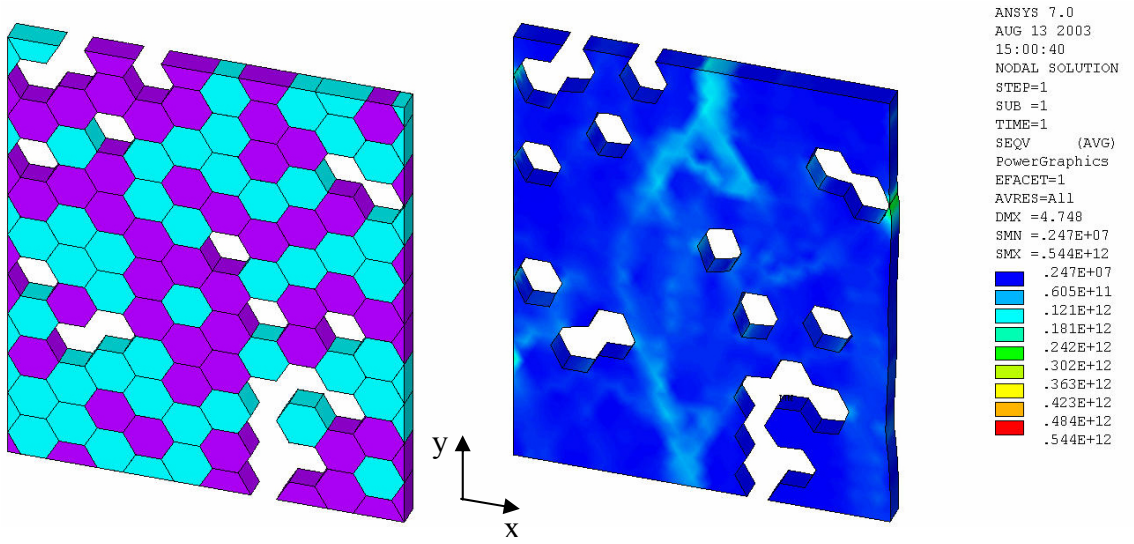

Figure 4.2.7 – Distribution of material properties and resulting von Mises stress output for the 10 x 10 unit model.

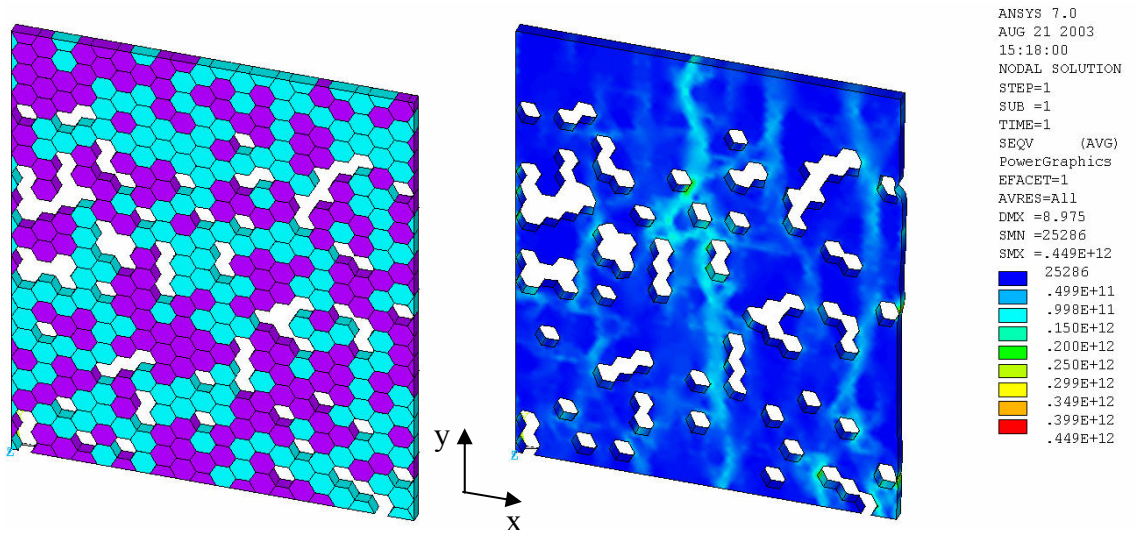

Figure 4.2.8 – Distribution of material properties and resulting von Mises stress output for the 20 x 20 unit model.

4.3 Model Refinement

On consideration of the previous work for the development of an abstract model for the microstructure of graphite, it was known that the model produced at this stage was not a fully correct representation. Further questions needed to be asked and answered before a final workable model could be produced.

What does the model represent?

The model is made up from an array of hexagons which can have material properties applied to them depending on what the model is required to represent. In this instance the model is a simplified representation of the microstructure of polygranular graphite, using the hexagons to represent both the filler and binder phases of the structure, and the absence of hexagons to represent pores. Although the model has a thickness of one unit creating a 3-D image, it is essentially a 2-D analysis that is performed on the system under the condition of plane strain (plane strain elements can be used to model solid components that can be idealised as long (infinite) prisms). The element mesh represents a cross section through the prism and it is assumed that the strain normal to the plane of the section is zero (NAFEMS, 1994).

What should the material properties be?

Two sets of material properties are used in the model, one to represent material 01 (the binder phase, coal tar pitch), and one to represent material 02 (the filler particles, Gilsocarbon). If material 01 is considered to be a randomly orientated mosaic of equi-axed "single" crystallites and it is known that the material is isotropic, then the Young's modulus can be considered to be 692 GPa (Neighbour, 2004) and the density 2260 kg/m^3 (Brocklehurst, 1977). Poisson's ratio can be determined through the utilising the equation:

$$\nu = 0.24(1 - 0.58P) \qquad \text{Equation [4.3.1]}$$

where P is the porosity.

This gives a value for Poisson's ratio of graphite at a given porosity, P (Maruyama, 1995); in this case that value is 0.24. However, Maruyama's equation relates to graphites commonly used by the Japanese nuclear industry, whereas this section is aiming to set material properties for graphites used in the United Kingdom and therefore, this equation must be altered accordingly. It is known that ν for IM1-24 is 0.2 at a porosity of 20.12 %, rearranging the above equation to re-evaluate the constant (given as 0.24 in Equation 4.3.1) gives:

$$\frac{\nu}{1 - 0.58P} = constant \qquad \text{Equation [4.3.2]}$$

Working through this equation results in a constant value of 0.226 (or 0.23). The equation can now be rewritten as:

$$\nu = 0.23(1 - 0.58P) \qquad \text{Equation [4.3.3]}$$

which produces a value of 0.23 for the Poisson's ratio of material 01.

Material 02 can be considered to have properties similar to a fully dense polygranular graphite. However, it is known that Gilsocarbon filler particles contain calcination cracks (formed during the calcination process), and hence have an inherent porosity of

their own. Determining the percentage porosity of the Gilsocarbon particles was achieved through selecting typical Gilsocarbon particles from a number of micrographs of IM1-24 graphite and, by image analysis, comparing the amount of solid material to the amount of porosity within the particle. In detail, this was done, by extracting the particles from the micrographs using Adobe Photoshop CS, it was possible to produce a reading of the number of pixels within the whole particle image. To highlight the difference between solid and porous areas, each image was first sharpened up and then treated with the threshold function. The threshold function converts the image to black and white based on a user input value. This value determines the threshold point at which any pixel lighter then the value becomes white and any pixel darker than the value becomes black (Figure 4.3.1). The porous areas could then be selected and the number of pixels counted. From a range of Gilsocarbon particles analysed, a value of 15.203% was obtained as the average amount of porosity within a filler particle.

Figure 4.3.1 – Comparison of original Gilsocarbon particle image to threshold produced image. The green background was chosen because this colour does not occur naturally in graphite and therefore would not be picked up by any of the automatic selection tools incorporated into Adobe Photoshop CS.

This value allowed the calculation of the density, ρ, as 1849 kg/m^3 (from an initial value of 2180 kg/m^3) based on a rule of mixtures. In general terms, the rule of mixtures can be described by:

$$X = X_s(1-P) + X_P P \qquad \text{Equation [4.3.4]}$$

where, X is the material property, X_s is the solid material property, P is the porosity and X_p is the property of the pore phase (usually zero). Calculating the Poisson's ratio for the model inputs was more demanding as Poisson's ratio values for hexagonal close packed (HCP) materials are typically 0.30 to 0.38, and it is suggested that Poisson's ratio is unaffected by porosity (Theocaris, 1994). However, using υ=0.50 for the solid material value (the ideal value for a material that undergoes no net volume change) as the input for the rule of mixtures returned a value of 0.42, which appears high. It is expected that this is not the value to use as the assumption that zero porosity Gilsocarbon particles are perfectly inelastic is not correct. A more appropriate value would be that of 0.33 (obtained by taking the average Poisson's ratio of several HCP materials (Theocaris, 1994)).

For the Young's modulus value, it is possible to use the extrapolation of the Knudsen equation (Knudsen, 1962):

$$E = E_0 \exp(-bx) \qquad \text{Equation [4.3.5]}$$

where E = Young's modulus at a given porosity, E_0 = Young's modulus of original material, b = property porosity dependence value, x = material porosity. From this the Young's modulus can be calculated. Using E = 10.89 GPa (Nuclear Electric, 1996), b = 3.6 (Rice, 1998) and x = 0.15203 (obtained through measuring the average Gilsocarbon particle porosity), Young's modulus at zero porosity is given as 18.82 GPa.

The finalised material properties to be used in modelling the microstructure of IM1-24 graphite can be seen in Table 4.3.2.

	Material 01	**Material 02**
Young's modulus (GPa)	692	18.82
Density (kg/m^3)	2260	1849
Poisson's ratio	0.23	0.33

Table 4.3.2 – Finalised material properties for the FEA model of the graphite microstructure.

Is the model structurally sound?

Other than determining the most appropriate material properties to use, consideration was given to the overall structure of the model, with regards to the make-up of the base, top surface and edges; the dimensionality (2-dimensions or 3-dimensions and model size); and the placement of the boundary conditions. Although some useful results had been obtained from the initial modelling concept, the concentration of maximum values for the stress and strain at the edges of the model was a concern. They were thought to be brought about mainly due to the essentially zero thickness of the material where adjoining triangles were connected by a node (illustrated in Figure 4.2.6). This effect would not be seen in a real graphite component as at a microscopic level graphite does not have smooth edges (see Chapter 6.2 – Microscopy). Therefore it was not actually necessary for these to be used within the model (the initial purpose was to allow fixation). Thus, the model generator C++ code was altered to disable them in the build process simply by omitting the lines of code.

As the size of the models was increased to 80 x 80 units, it became apparent that to really examine what happens to the microstructure when loaded at different sizes it would be necessary to produce models larger than this. As would be reasonably expected, constructing, meshing and solving these larger models requires more computing power as the complexity of them increases. By doubling the unit size of a model it effectively quadruples the number of nodes and calculations to be performed. To this end, analysing 3-dimensional models became impractical as current computational ability would restrict the maximum size of model. To counter this and to allow the investigation of larger models, the decision was made to make the models 2-dimensional and adjust the sizes to be examined accordingly.

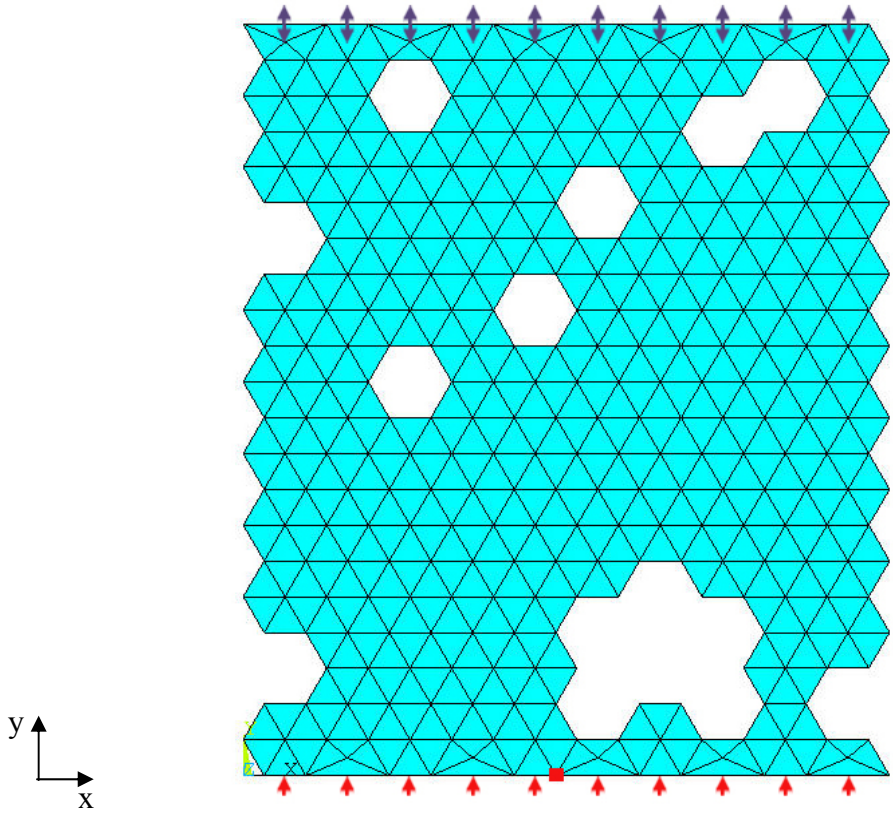

Figure 4.3.2 – Constraints applied to each model. Red colouring indicates a fixed point, purple colouring indicates a displacement (0.2 % model height for tension, 2 % model height for compression). This is an example 10 x 10 unit model in 2-dimensions.

The model unit sizes chosen to be analysed were:

- 5 x 5;
- 10 x 10;
- 20 x 20;
- 30 x 30;
- 100 x 100;
- 200 x 200;
- 400 x 400.

It is possible to see that by choosing to model in 2-dimensions, the maximum size of model to be investigated was greatly increased. In order to ensure that this change to the model would not detract from the initial modelling already performed, several of the previous 3-dimensional models were re-solved as 2-dimensional and although the numerical values obtained were different (though still arbitrary at this stage) the stress,

strain and displacement patterns were almost identical. Through changing the dimensionality of the model a new element had to be selected, the PLANE42 element was chosen (a 4-noded, rectangular or triangular 2-dimensional element).

With the removal of the edge effects and the change to 2-dimensions the boundary conditions also had to be revised. As the models are to be examined in pure tension and compression, fixing the model along the left hand edge would prevent any natural contraction of the model taking place, which would also produce an adverse effect on the right hand edge as the nodes along this side would register greater movement in the negative x-direction than would be expected. However, providing stability to the model is still very important for realistic (if not numerically accurate) results to be produced. Therefore, each model had one keypoint fixed in all degrees of freedom at the centre of its base to ensure that it was not permitted to move other then in the desired plane. To simulate the model in tension and compression, the upper and lower lines were selected and the appropriate constraints/displacements applied. The lower surface was fixed in the y-direction, whilst the upper surface was displaced by 0.2 % of the model height in the positive y-direction (for tension), and by 2 % in the negative y-direction (for compression).

The values of 0.2 % and 2 % were selected as it is widely accepted that at 0.2 % strain, a specimen of graphite will fail in tension, and at 2 % strain a specimen will fail in compression (with tensile strain failure being between 0.1% and 0.3% at room temperature (Reynolds, 1968)). Figure 4.3.2 illustrates these constraints and also shows the finalised structure of the model once the changes to the format had been applied.

The element types used in the initial model (SOLID92) and in the finalised model (PLANE42) are both packaged with the ANSYS software. As stated previously, SOLID92 is a 3-dimensional 10-noded element (shown in Figure 4.3.3) and PLANE42 is a 2-dimensional 4-noded element (shown in Figure 4.3.4), and both are suited for use in analysing stress and strain within a given structure. The SOLID92 element has a quadratic displacement behaviour, three degrees of freedom at each node and is particularly suited to models that require irregular meshes due to its shape being able to tessellate well. It is capable of modelling large displacements, stresses and strains. The PLANE42 element is primarily used to model the behaviour of 2-dimensional solid

structures and can be used for examining plane stress and plane strain, or as an axisymmetric element. There are two degrees of freedom at each node of the 4 nodes and the element has two shape options, quadratic or triangular (ANSYS 7.0 Help Documentation, 2002). For the microstructural modelling here, the triangular shape was selected in order to obtain the most uniform mesh possible.

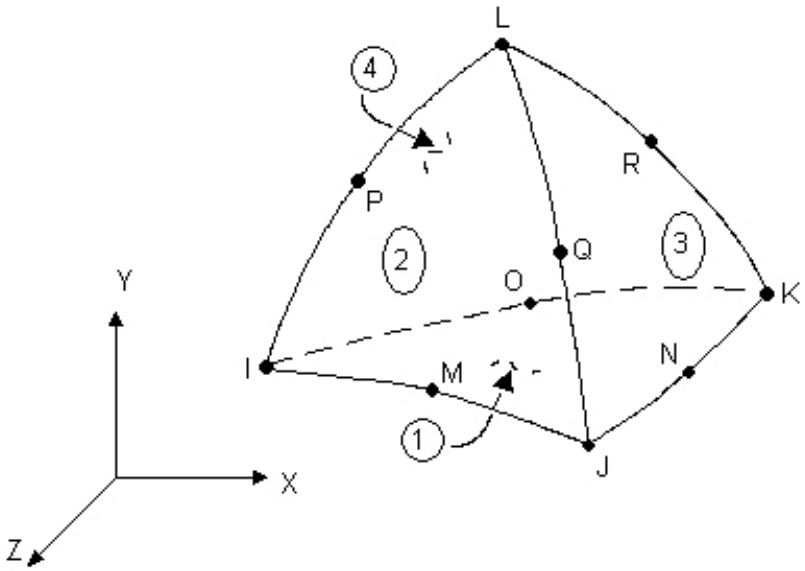

Figure 4.3.3 – Graphical representation of the SOLID92 element used within ANSYS.

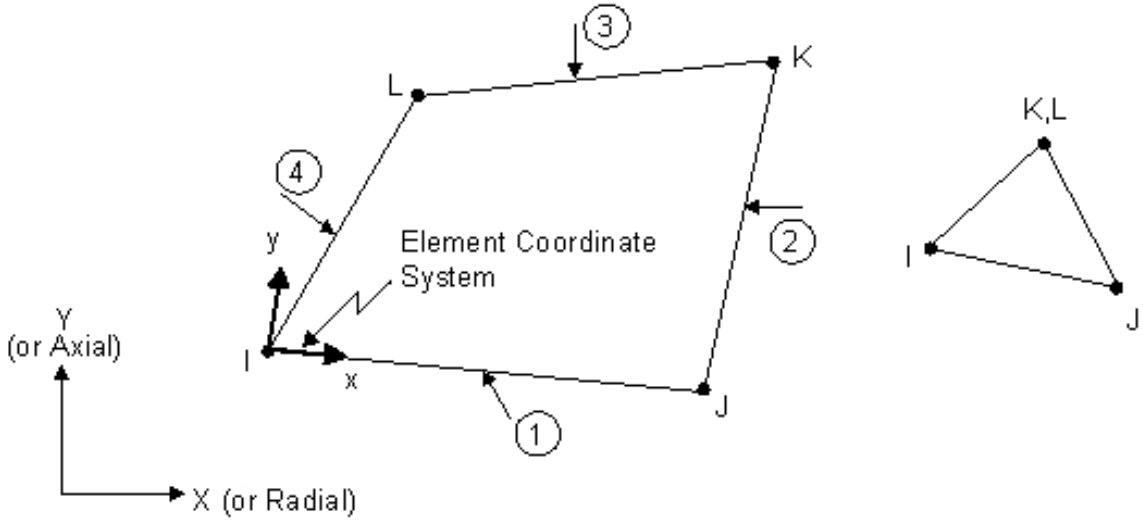

Figure 4.3.4 – Graphical representation of the PLANE42 element used within ANSYS.

As the ultimate aim of the model is to analyse a component under plane strain conditions the element types selected are the most suitable choice for this, whether it be 2- or 3-dimensional.

4.4 Computational Issues and the Modelling Programme

For the building, loading and solving of the initial models, any modern computer running Windows software as its operating system could be used. However, as the model was altered and the sizes to be analysed increased, it rapidly became apparent that a standard desktop machine was not sufficient for the task.

A Dell dual-processor (Intel Xeon 2.4 GHz) with 4GB RAM was used to perform the modelling on as this would prove to have the processing power to manage the large amount of calculations involved in determining the reactions of the nodes within the model (typically, a 100 x 100 unit model will contain approximately 240,000 nodes), and solve the model in a reasonable time frame.

The setup of each model could take from 5 minutes for the smallest to approximately 48 hours for the largest, this being due to the process of gluing the hexagons to form the model. ANSYS' capability at gluing areas together appeared to be limited to allowing only 5000 areas to be glued at any one time, and this process taking 40 minutes. With the larger models containing in excess of 40,000 areas the process of building the models could be very time consuming and user intensive (ANSYS requiring user input to determine which areas to glue together next). However, once setup correctly the solutions took very little time (typically less than 2 minutes), and each result appeared to be consistent with the previous model size and iteration of the current size.

4.5 Summary

This chapter outlines the logical development of an abstract FEA model. Confirmation that the models were set up correctly and the correct mesh and constraints had been applied was gained by achieving expected solutions. With the approach to producing an abstract model of the graphite microstructure assumed to be the most suitable, the modelling programme was undertaken and the results reported in Chapter 5 – Modelling Predictions.

Chapter 5 - Modelling Predictions

This chapter presents the results from the model developed in Chapter 4 – Conceptual Modelling using the finite element analysis software ANSYS, with the subsequent calculations to determine the simulated material properties, and comments on the features and effects observed in the models under tension and compression, based upon the assumptions made regarding the inherent material properties and the models constraints.

5.1 Predicted Model Results

For each of the model sizes to be analysed, the Model Generator and Material Setter programs were employed to produce an ANSYS compatible log file that would build the appropriate model in the finite element analysis software. A step-by-step instruction on how these files were used with ANSYS, and how the models were setup is included in Appendix B and shall not be covered in detail here. However, there was an exception to this procedure. It was discovered that as the models approached the largest sizes, the software was unable to process the information required to 'glue' the hexagons together so that they would all be considered as a single solid in preparation for the analysis. The model generator program created each hexagon as a single area, and it transpired that the software was unable to process more than 5000 areas at any one time, so the 100 x 100, 200 x 200 and 400 x 400 models had to be glued manually. This involved selecting the areas to be glued in sequence once the model was loaded into ANSYS. In the case of the 100 x 100 models, selecting the areas in the bottom half of the model and gluing, then selecting the areas in the top half of the model and gluing, ensuring there was an overlap so that the areas were fully joined. For the 200 x 200 models, the areas had to be glued in sections starting at the bottom and selecting fewer than 5000 areas for

the operation, then moving up the model, overlapping the glued sections to ensure all the areas were joined.

The 400 x 400 models proved to be extremely difficult to glue in this way as the display of the hexagons on the computer screen was too small, and accurate gluing was near impossible using the previous technique. Due to time constraints it was decided that to produce the 400 x 400 models, previously produced 200 x 200 models would be used that were copied and reflected in both the x-axis and y-axis and then glued along the joins. This would have the effect of producing a semi-random microstructure that would be conducive to the analysis, but would not yield as ideal results as were sought. The effect of the time constraint and the selection of method for creating the 400 x 400 models meant that only two 400 x 400 models could be generated.

With exception of the 400 x 400 models, 8 models were generated for each size, and these models were analysed under tension and compression under the loading strains detailed in Chapter 4 – Conceptual Modelling. After solving for the given loading condition the following results were recorded from ANSYS:

- von Mises stress;
- von Mises strain;
- 1st Principal Stress;
- 1st Principal Strain;
- Nodal Displacement;
- Stress Intensity;
- Strain Energy.

The maximum values were recorded from the software and plots of the property distributions through the models were output to image files. As there were in total 100 models being analysed and 10 output images for each model, for ease of presentation only a few examples for the models are shown. All output images for each individual model size and loading condition with numerical results can be viewed on the CD-ROM (Appendix D) under the folder ANSYS\Results Files.

Figures 5.1.1 and 5.1.2 show examples of the material property distribution and mesh density for each of the model sizes, respectively. The images are not to scale but represent the views that are seen in ANSYS. It is clear from these images that at the larger model sizes it is very difficult to visually analyse the pore and material distributions in the model. However, as the model sizes increase they become more representative of a cross-sectional view of a ceramic microstructure. Note: for ease of presentation the 400 x 400 models have been excluded (see CD-ROM, Appendix D).

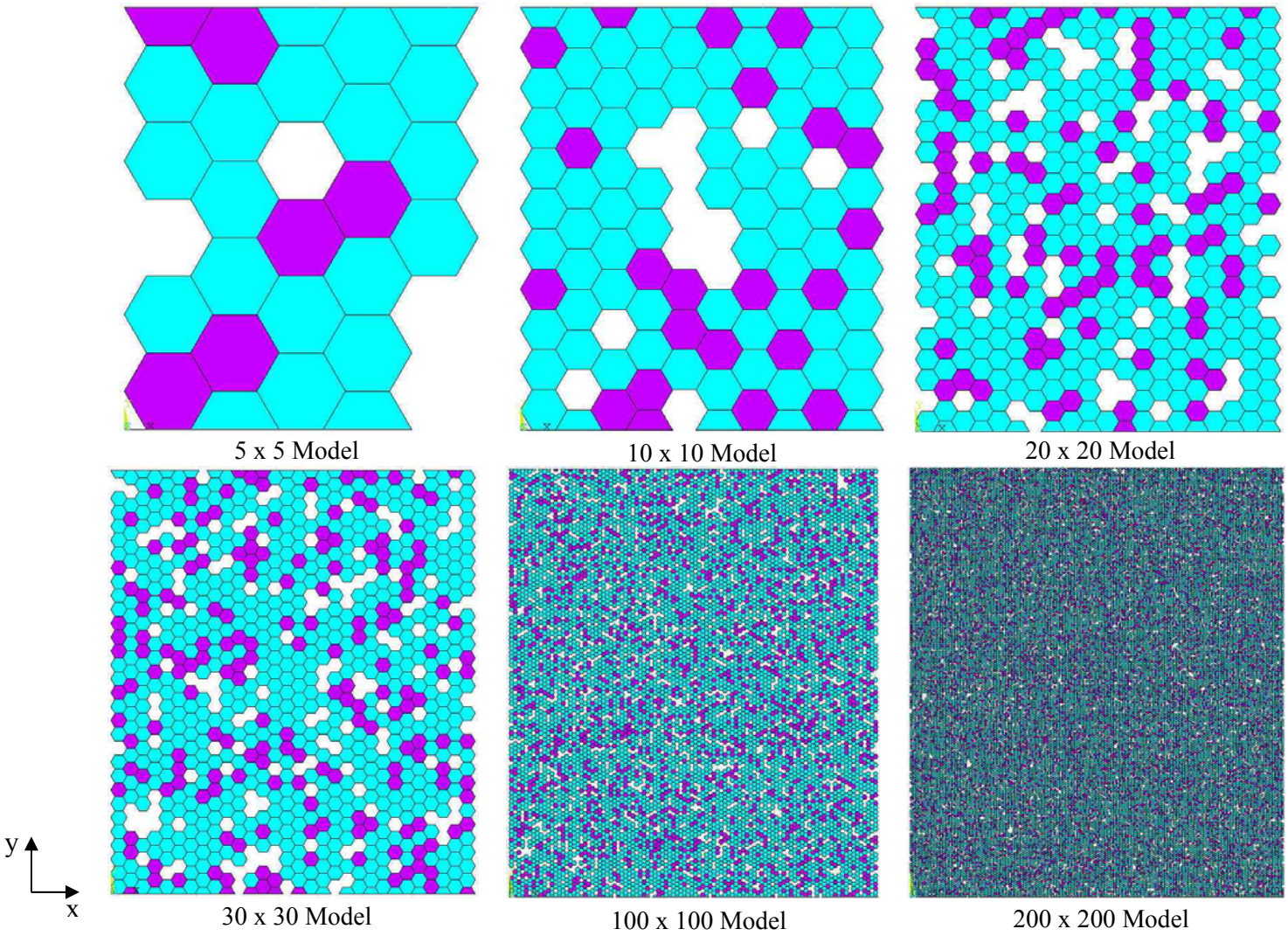

Figure 5.1.1 – Material property distribution examples for all model sizes.

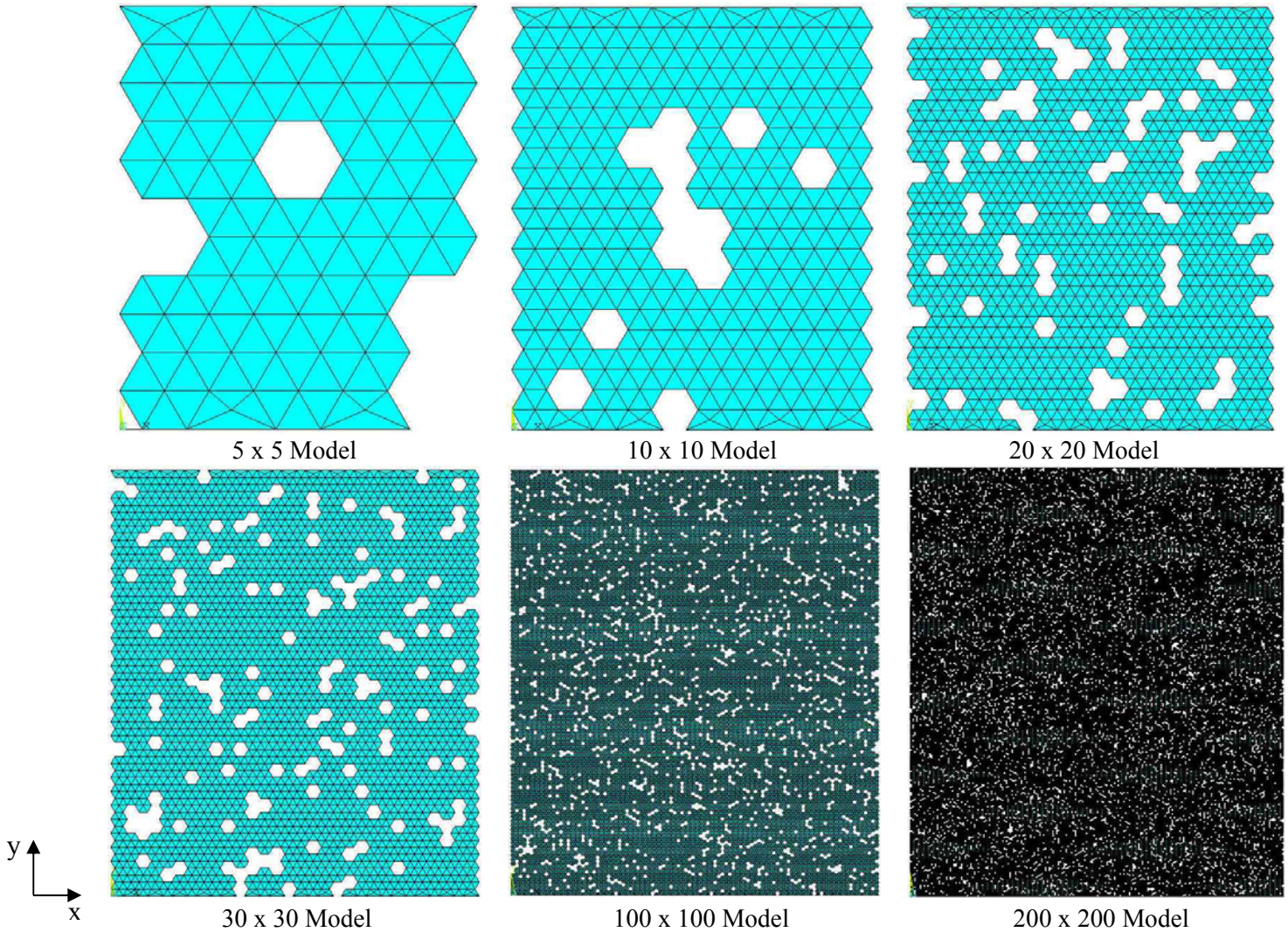

Figure 5.1.2 – Mesh density examples for all model sizes.

Figures 5.1.1 and 5.1.2 depict the initial model setup before any solutions were obtained. Once the model was solved the numerical data for the models was recorded and the mean and standard deviation for each model size calculated, as shown in Tables 5.1.1 and 5.1.2 which show the results for the models in tension and compression, respectively.

The values for the von Mises stress, von Mises strain, 1st principal stress and 1st principal strain are all taken as maximum values from the analysis. To gain a more meaningful value of the stress and the strain within the models it was necessary to perform some additional calculations using ANSYS. Within ANSYS all data obtained for the reactions within the elements during an analysis is stored in an element table. These tables can be accessed after the solution has been gained and calculations performed on the data held within them. To calculate the average stress and average strain (both von Mises and 1st principal) within each model the following equations were used:

$$\sigma_{Average} = \frac{\sum(\sigma_{Element} \times A_{Element})}{A_{Total}} \qquad \text{Equation [5.1.1]}$$

$$\varepsilon_{Average} = \frac{\sum(\varepsilon_{Element} \times A_{Element})}{A_{Total}} \qquad \text{Equation [5.1.2]}$$

where σ is the von Mises stress, ε is the von Mises strain and A is the area. From these values it is possible to calculate the secant Young's modulus for each model size. The following tables detail the numerical values obtained from ANSYS for the given properties, with the value displayed being the average over each model size, σ being the standard deviation from the mean in each instance and YM being the Young's modulus. All distance units are arbitrary but 1 unit can be assumed to equal 1 mm for the purpose of the results.

Model Size	Max. von Mises Stress (Pa)	σ	Max. von Mises Strain	σ	Max. Displace-ment (mm)	σ	Max. Stress Intensity (Pa)	σ	Max. Strain Energy (J/m^3)	σ	Max. 1st Principal Stress (Pa)	σ
5 x 5	1.34E+09	6.18E+08	1.22E-02	2.79E-03	2.06E-02	1.38E-03	1.43E+09	5.93E+08	8.46E+05	3.43E+05	1.36E+09	6.06E+08
10 x 10	1.89E+09	1.87E+08	1.72E-02	2.73E-03	3.94E-02	3.11E-03	2.10E+09	1.89E+08	1.40E+06	3.03E+05	1.95E+09	2.35E+08
20 x 20	2.06E+09	3.55E+08	2.48E-02	3.32E-03	7.63E-02	4.77E-03	2.34E+09	3.52E+08	1.96E+06	3.76E+05	2.20E+09	4.09E+08
30 x 30	2.15E+09	3.15E+08	2.71E-02	3.88E-03	1.22E-01	3.46E-02	2.47E+09	4.65E+08	2.44E+06	7.95E+05	2.29E+09	3.23E+08
100 x 100	2.61E+09	3.39E+08	3.91E-02	6.89E-03	3.53E-01	3.43E-03	2.84E+09	4.36E+08	4.81E+06	1.54E+06	2.73E+09	3.91E+08
200 x 200	2.68E+09	1.75E+08	4.15E-02	3.59E-03	7.24E-01	2.60E-02	3.06E+09	2.38E+08	5.23E+06	1.15E+06	2.84E+09	1.42E+08
400 x 400	2.88E+09	1.91E+08	4.47E-02	9.20E-04	1.40E+00	1.41E-03	3.30E+09	1.20E+08	5.97E+06	2.12E+04	3.00E+09	1.98E+08

Model Size	Max. 1st Principal Strain	σ	Secant 1st Principal YM (Pa)	σ	Mean 1st Principal Stress (Pa)	σ	Mean 1st Principal Strain	σ	Mean Secant 1st Principal YM (Pa)	σ
5 x 5	9.28E-03	2.15E-03	1.55E+11	8.00E+10	4.49E+08	1.97E+08	1.82E-03	2.08E-04	2.43E+11	9.96E+10
10 x 10	1.31E-02	2.07E-03	1.52E+11	2.93E+10	5.08E+08	1.17E+08	1.66E-03	1.74E-04	3.04E+11	5.00E+10
20 x 20	1.89E-02	2.47E-03	1.18E+11	2.62E+10	3.91E+08	6.77E+07	1.61E-03	1.29E-04	2.42E+11	2.79E+10
30 x 30	2.07E-02	2.99E-03	1.12E+11	2.02E+10	3.70E+08	5.55E+07	1.46E-03	2.08E-04	2.59E+11	6.44E+10
100 x 100	2.98E-02	5.17E-03	9.46E+10	2.39E+10	3.55E+08	1.20E+07	1.55E-03	2.24E-05	2.29E+11	6.17E+09
200 x 200	3.17E-02	2.81E-03	9.03E+10	1.03E+10	3.58E+08	6.51E+06	1.57E-03	1.18E-05	2.28E+11	3.12E+09
400 x 400	3.40E-02	3.93E-04	8.83E+10	4.81E+09	3.57E+08	3.90E+05	1.56E-03	1.11E-05	2.29E+11	1.88E+09

Table 5.1.1 – Numerical modelling results for tensile loading.

Model Size	Max. von Mises Stress (Pa)	σ	Max. von Mises Strain	σ	Max. Displace-Ment (mm)	σ	Max. Stress Intensity (Pa)	σ	Max. Strain Energy (J/m^3)	σ	Max. 1st Principal Stress (Pa)	σ
5 x 5	1.34E+10	6.18E+09	1.22E-01	2.79E-02	2.06E-01	1.38E-02	1.03E+10	7.71E+09	6.11E+07	5.01E+07	2.55E+09	1.45E+09
10 x 10	1.89E+10	1.87E+09	1.72E-01	2.73E-02	3.94E-01	3.11E-02	1.65E+10	9.12E+09	1.07E+08	7.16E+07	5.54E+09	1.36E+09
20 x 20	2.06E+10	3.55E+09	2.48E-01	3.32E-02	7.63E-01	4.77E-02	1.84E+10	1.04E+10	1.47E+08	9.66E+07	8.03E+09	2.06E+09
30 x 30	2.15E+10	3.15E+09	2.71E-01	3.88E-02	1.10E+00	1.87E-02	1.93E+10	1.14E+10	1.93E+08	1.40E+08	9.24E+09	2.59E+09
100 x 100	2.61E+10	3.39E+09	3.91E-01	6.89E-02	3.54E+00	2.90E-02	2.84E+10	4.36E+09	4.81E+08	1.54E+08	1.21E+10	1.44E+09
200 x 200	2.68E+10	1.75E+09	4.15E-01	3.60E-02	7.07E+00	1.19E-01	3.06E+10	2.38E+09	5.23E+08	1.16E+08	1.29E+10	1.49E+09
400 x 400	2.88E+10	1.91E+09	4.47E-01	9.20E-03	1.40E+01	1.20E-02	3.30E+10	1.20E+09	5.97E+08	2.12E+06	1.51E+10	1.56E+09

Model Size	Max. 1st Principal Strain	σ	Secant 1st Principal YM (Pa)	σ	Mean 1st Principal Stress (Pa)	σ	Mean 1st Principal Strain	σ	Mean Secant 1st Principal YM (Pa)	σ
5 x 5	3.78E-02	7.58E-03	6.78E+10	3.38E+10	4.83E+08	2.10E+08	8.45E-03	1.86E-03	5.71E+10	2.16E+10
10 x 10	5.76E-02	1.20E-02	1.00E+11	3.57E+10	7.06E+08	5.21E+07	8.07E-03	1.07E-03	8.83E+10	9.67E+09
20 x 20	7.65E-02	6.81E-03	1.05E+11	2.58E+10	7.05E+08	7.40E+07	7.60E-03	4.84E-04	9.27E+10	4.73E+09
30 x 30	9.45E-02	1.53E-02	9.80E+10	2.34E+10	6.08E+08	2.27E+08	6.86E-03	2.49E-03	8.85E+10	5.51E+09
100 x 100	1.31E-01	2.21E-02	9.51E+10	2.07E+10	7.48E+08	1.25E+07	7.98E-03	9.07E-05	9.37E+10	1.26E+09
200 x 200	1.53E-01	2.26E-02	8.55E+10	1.53E+10	7.58E+08	8.81E+06	8.09E-03	4.91E-05	9.38E+10	9.62E+08
400 x 400	1.79E-01	2.36E-02	8.57E+10	2.00E+10	7.62E+08	4.88E+06	8.07E-03	4.27E-05	9.44E+10	1.10E+09

Figure 5.1.2 – Numerical modelling results for compressive loading.

After initial viewing of the results it was clear that the von Mises results were displaying identical stress and strain distributions through each of the models, with the numerical results being only a factor of 10 different under tension and compression, which is not ideal for gaining meaningful data from the models. ANSYS calculates the von Mises stress through:

$$\sigma_e = \left(\frac{1}{2} \left[\{\sigma_1 - \sigma_2\}^2 + \{\sigma_2 - \sigma_3\}^2 + \{\sigma_3 - \sigma_1\}^2 \right] \right)^{1/2} \qquad \text{Equation [5.1.3]}$$

where σ_e is the von Mises (or equivalent) stress and σ_1, σ_2 and σ_3 are the stresses in the *x*-, *y*- and *z*-directions, respectively. This can also be expressed as:

$$\sigma_e = \left(\frac{1}{2} \left[\{\sigma_x - \sigma_y\}^2 + \{\sigma_y - \sigma_z\}^2 + \{\sigma_z - \sigma_x\}^2 + 6\{\sigma_{xy}{}^2 + \sigma_{yz}{}^2 + \sigma_{xz}{}^2\} \right] \right)^{1/2}$$

Equation [5.1.4]

In terms of the predictions made by the tension and compression models, only the *x*- and *y*-directions are considered, implying that the $\{\sigma_2 - \sigma_3\}$ and $\{\sigma_3 - \sigma_1\}$ terms do not provide a truly accurate value for the stress within the models as the stress in the *z*-direction is effectively zero. Similarly, for the von Mises strain:

$$\varepsilon_e = \frac{1}{1+\nu'} \left(\frac{1}{2} \left[\{\varepsilon_1 - \varepsilon_2\}^2 + \{\varepsilon_2 - \varepsilon_3\}^2 + \{\varepsilon_3 - \varepsilon_1\}^2 \right] \right)^{1/2} \qquad \text{Equation [5.1.5]}$$

where ε_e is the von Mises (or equivalent) strain, ε_1, ε_2 and ε_3 are the strains in the *x*-, *y*- and *z*-directions, respectively. Again, the $\{\varepsilon_2 - \varepsilon_3\}$ and $\{\varepsilon_3 - \varepsilon_1\}$ terms are not a true representation for the models due to the zero strain in the *z*-direction. For the calculation of the stress intensity, σ_I, the maximum value is determined through the evaluation of:

$$\sigma_I = MAX\left(|\sigma_1 - \sigma_2|, |\sigma_2 - \sigma_3|, |\sigma_3 - \sigma_1| \right) \qquad \text{Equation [5.1.6]}$$

The strain energy, E_e^{PO}, is calculated by:

$$E_e^{PO} = \frac{1}{2}\{U_e\}^T([K_e]+[S_e])\{U_e\} \qquad \text{Equation [5.1.7]}$$

where $\{U_e\}$ is a time derivative of the element degree of freedom vector, $[K_e]$ is the element stiffness matrix, and $[S_e]$ element stress stiffness matrix (ANSYS 7.0 Help Documentation, 2002).

Insight into the model behaviour with increasing size was gained through plotting the numerical results for the stresses and strains obtained by ANSYS (those shown in Tables 5.1.1 and 5.1.2) against the increase in model size, and can be seen in the following series of graphs. All trendlines are fitted to the data using a software program XLFit that employs non-linear regression analysis to determine the optimum curve. In all cases for the tensile results the highest R^2 value determined by XLFit was used, for the compressive results the same model selected by XLFit for the tensile results was used, providing that the R^2 value was near the determined best fit. All trendlines are intended as guide for the eye of the reader rather than an expression of the relationship between model size and measured material property, and as such the complex equations are not displayed. As with the numerical results, the model dimensions are arbitrary but can be assumed to be in mm for the purposes of presentation.

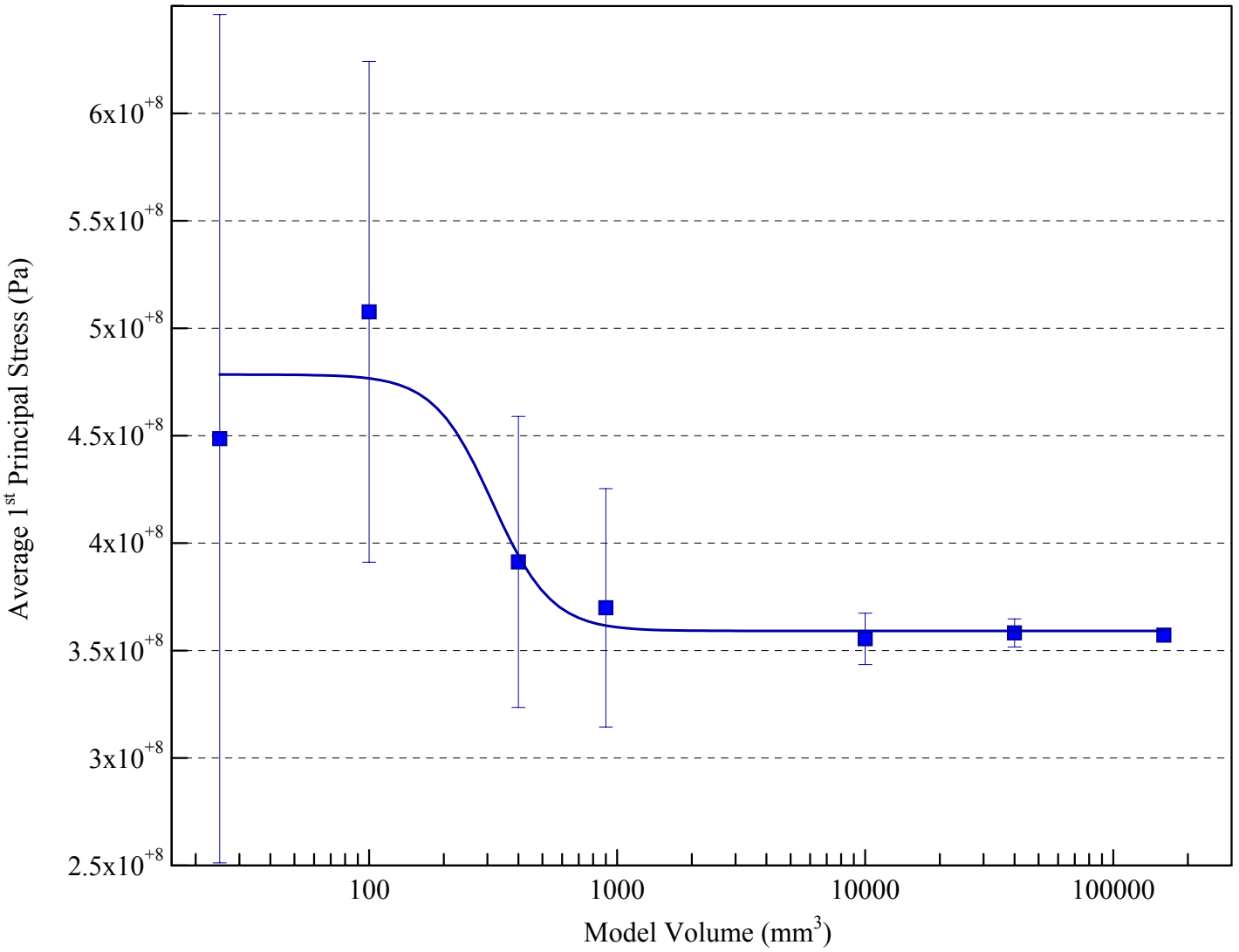

Graph 5.1.1 – Plot of average 1st principal stress under tensile loading against increasing model size.

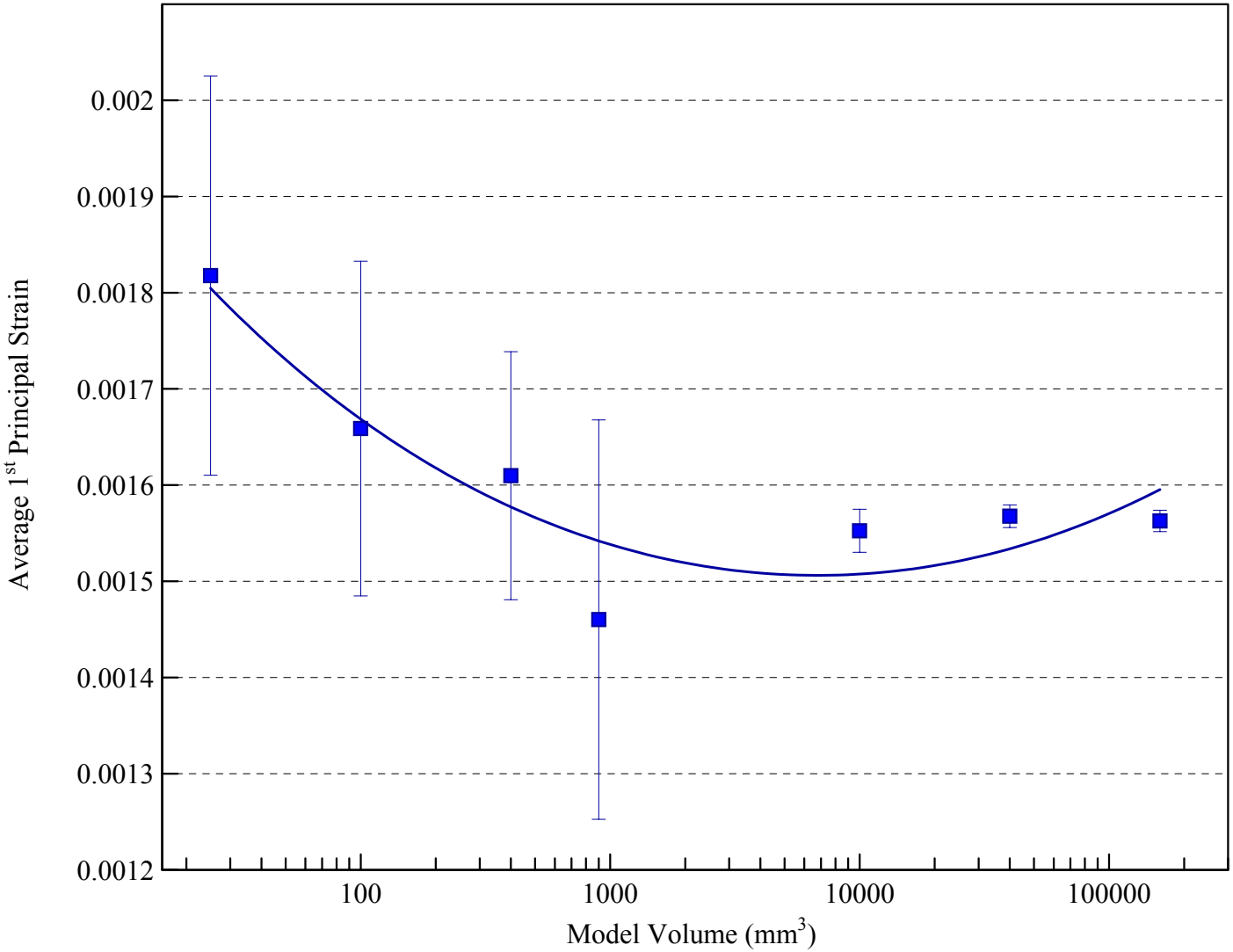

Graph 5.1.2 – Plot of average 1st principal strain under tensile loading against increasing model size.

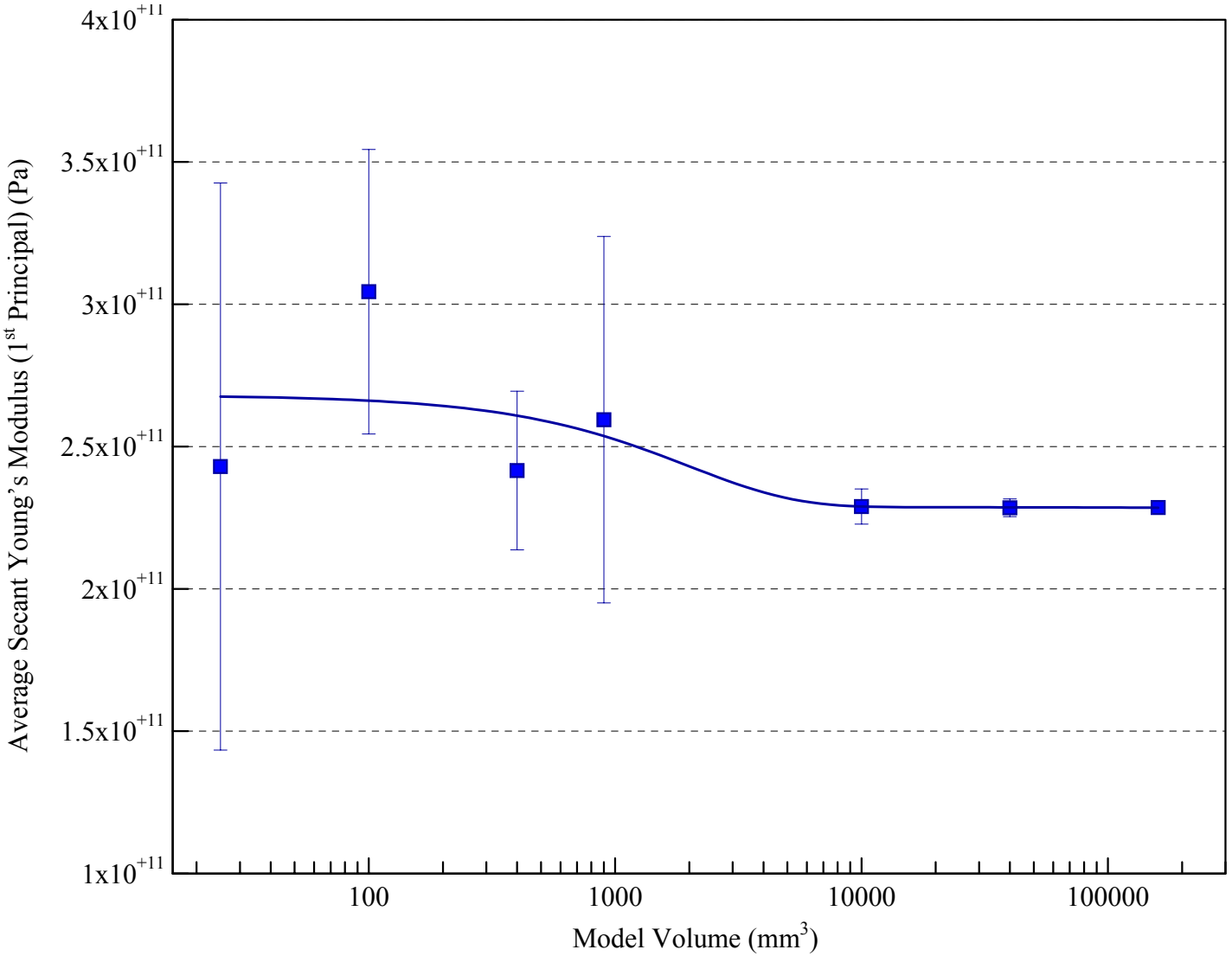

Graph 5.1.3 – Plot of average 1st principal secant Young's modulus under tensile loading against model size.

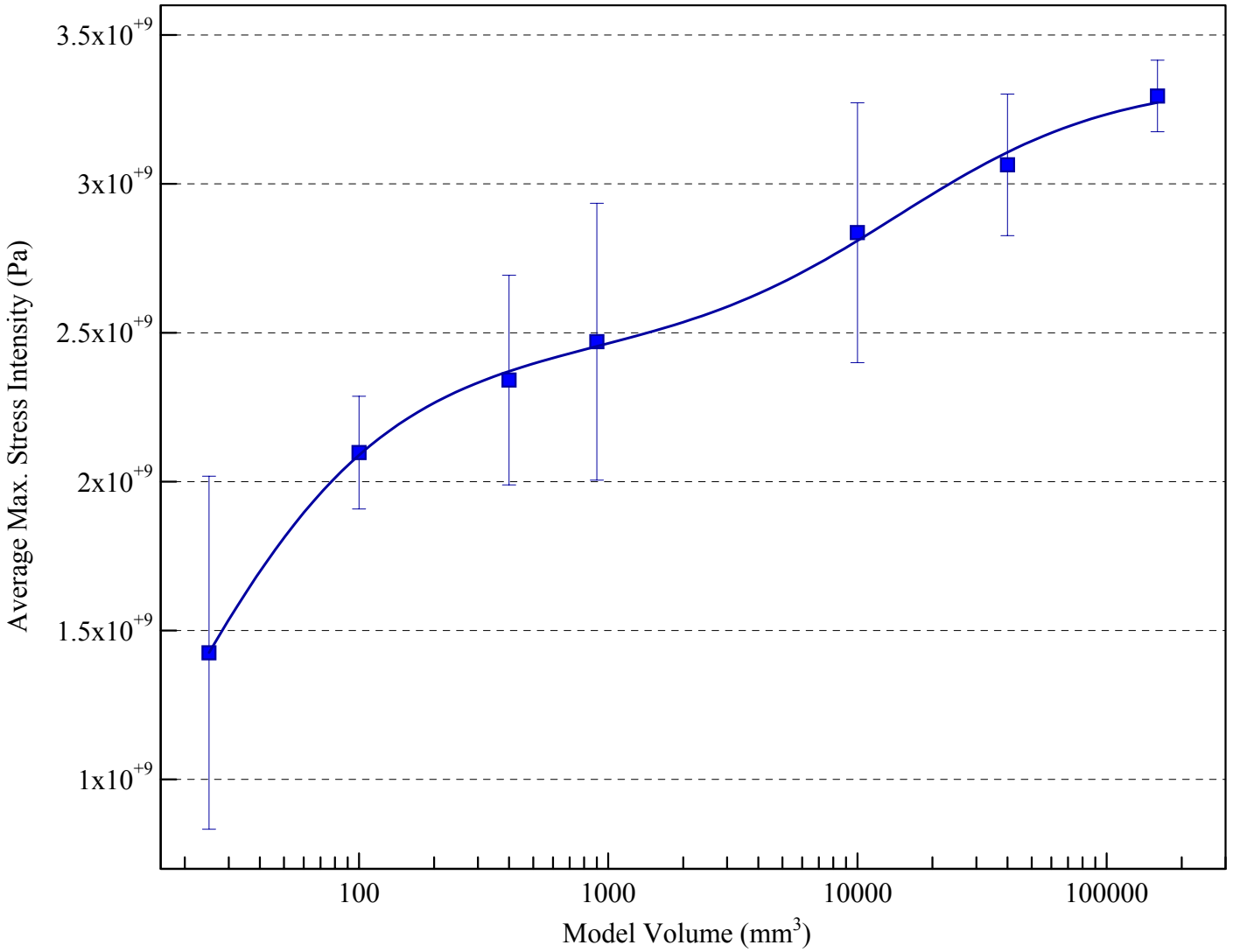

Graph 5.1.4 – Plot of average maximum stress intensity under tensile loading against increasing model size.

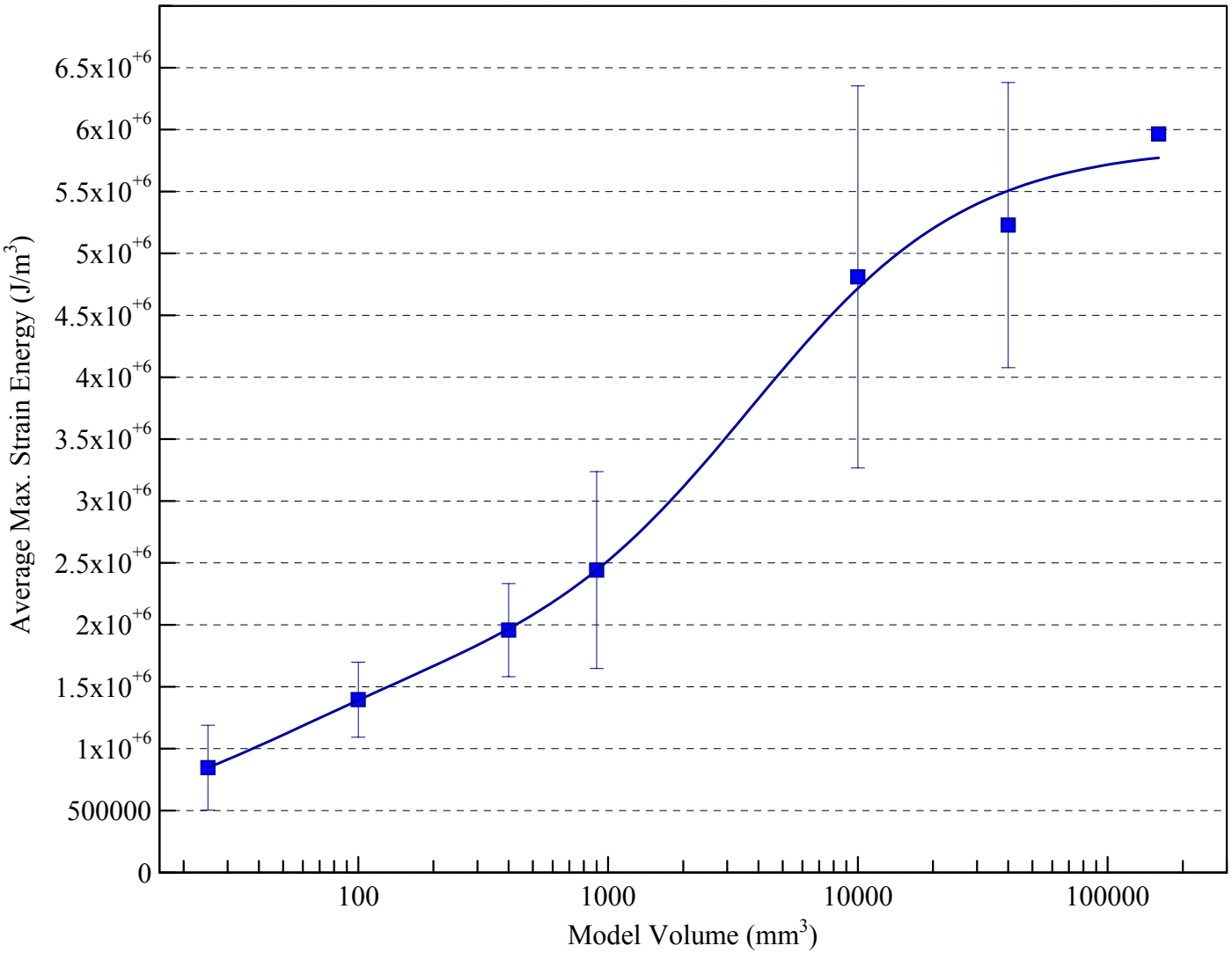

Graph 5.1.5 – Plot of average maximum strain energy under tensile loading against increasing model size.

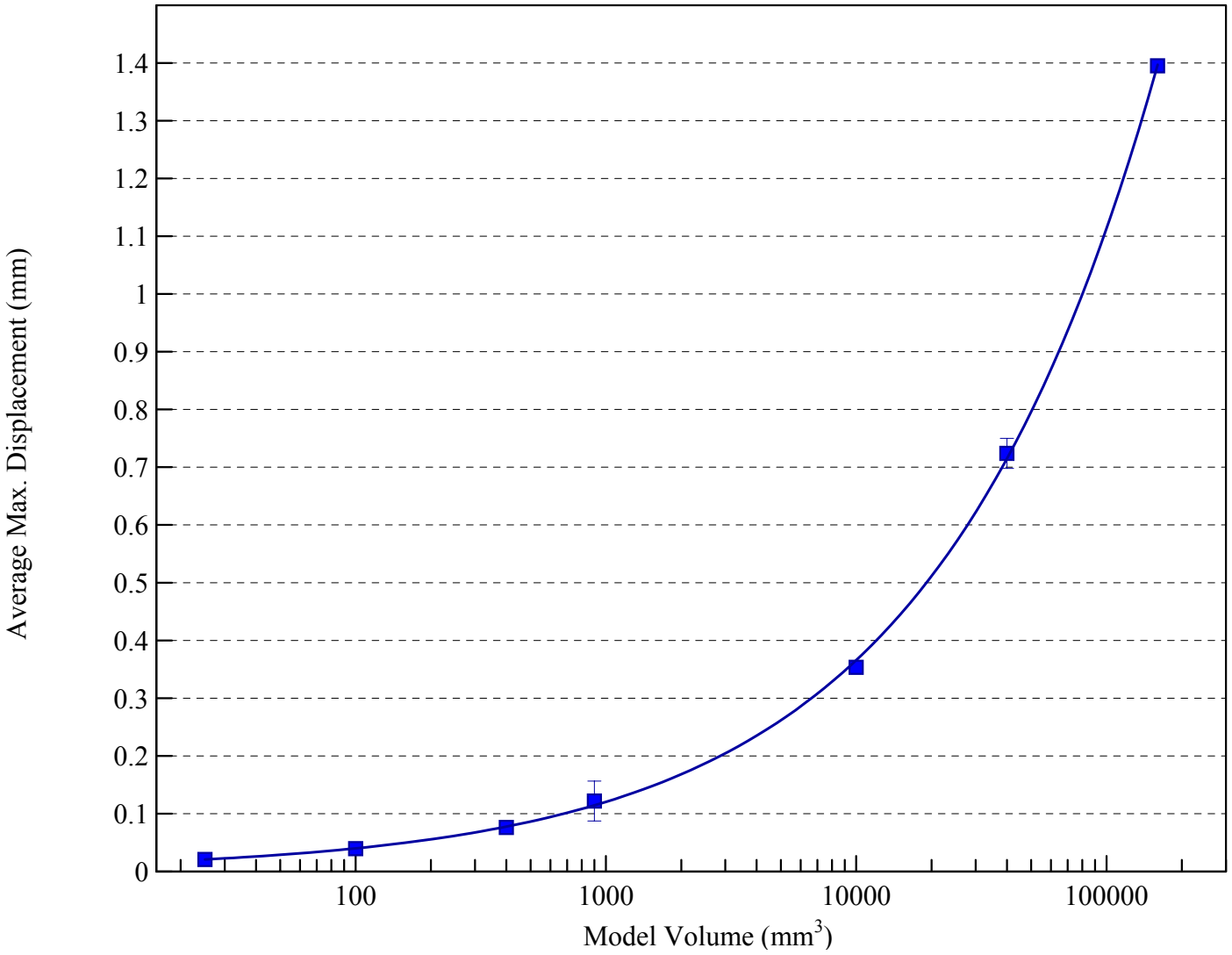

Graph 5.1.6 – Plot of average displacement under tensile loading against increasing model size.

The plots of the models under tensile loading show a number of different features. Graph 5.1.1 depicts an increasing 1st principal stress with increasing model size initially, which then decreases with the trend beginning to plateau as the larger model sizes are reached. This suggests that the models are predicting that at small sizes a higher average stress is present at the given displacement which reduces as the model size increases. The effect of the average 1st principal stress levelling off for the largest three model sizes implies that as more bulk material is present, more strain is required to raise the internal stress.

The plot showing the change in 1st principal strain (Graph 5.1.2) with model size has an initially decreasing average strain through the models up to the 30 x 30 model size, after which the average strain within the models increases. The average 1st principal strain calculated over all the model sizes under tension is 0.0016 (or approximately 0.2%) which is to be expected as the model has been displaced by 0.2% of its overall height. The average von Mises strain predicted by the models is 0.0022, closer to the percentage strain the model has been subject to.

On plotting the secant 1st principal Young's modulus it can be seen from Graph 5.1.3 that there is very little variation in the values obtained from each of the model sizes. The prediction would be consistent with the material as the elastic modulus should be a constant property. However, the value predicted is not consistent with the Young's modulus value for IM1-24 graphite.

For both the calculated maximum stress intensity and strain energy (Graphs 5.1.4 and 5.1.5 respectively), the values increase steadily as the model size increases, both to be expected with the increased displacement of the models. The increased displacements can be seen clearly in Graph 5.1.6 and is taken from the predictions as the node that has been displaced the furthest distance through the *x*- and *y*-directions. Although the models are displaced by a fixed value, the largest vector displacement in the model can be greater than this due to the additional horizontal movement of the elements when the loads are applied.

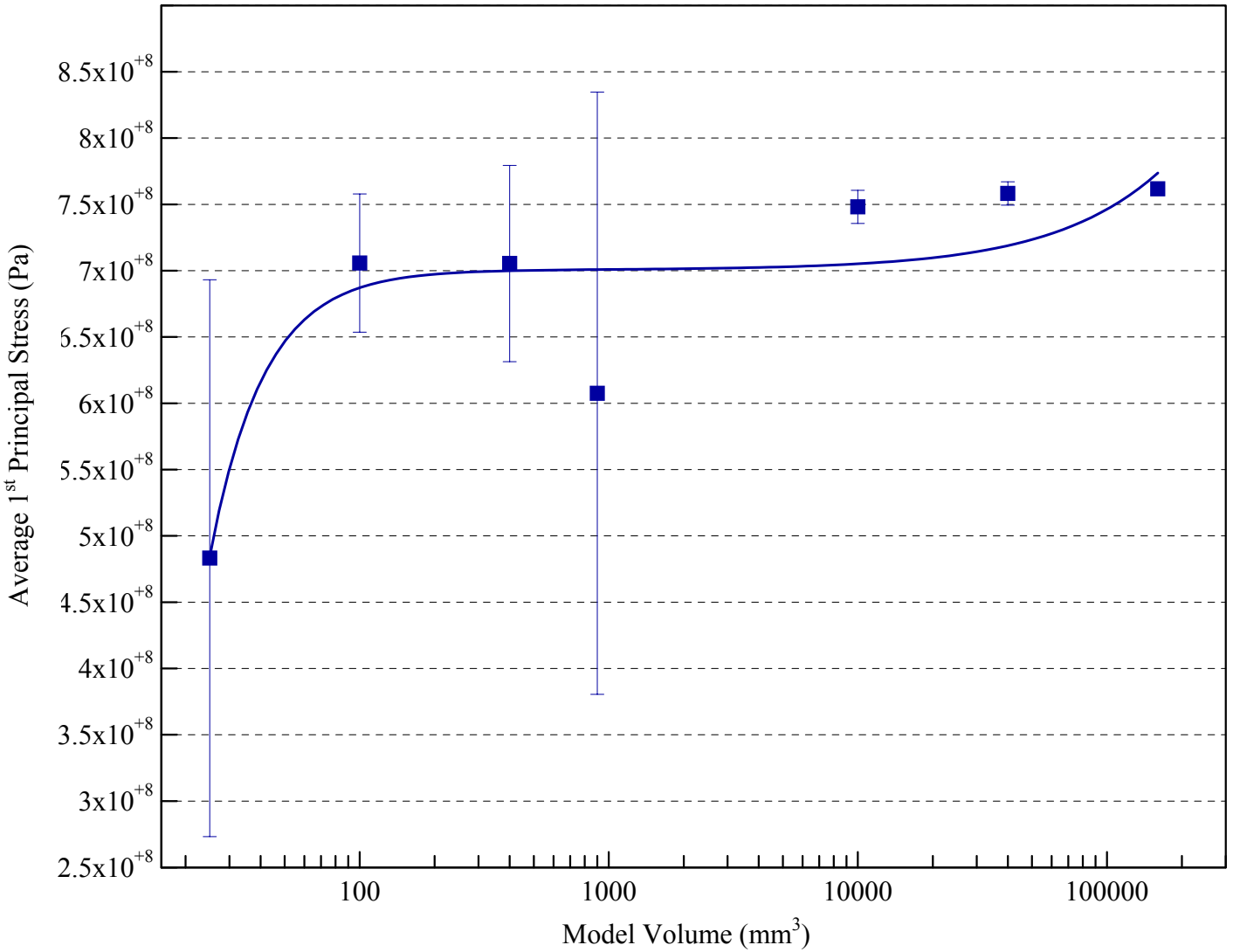

Graph 5.1.7 – Plot of average 1st principal stress under compressive loading against increasing model size.

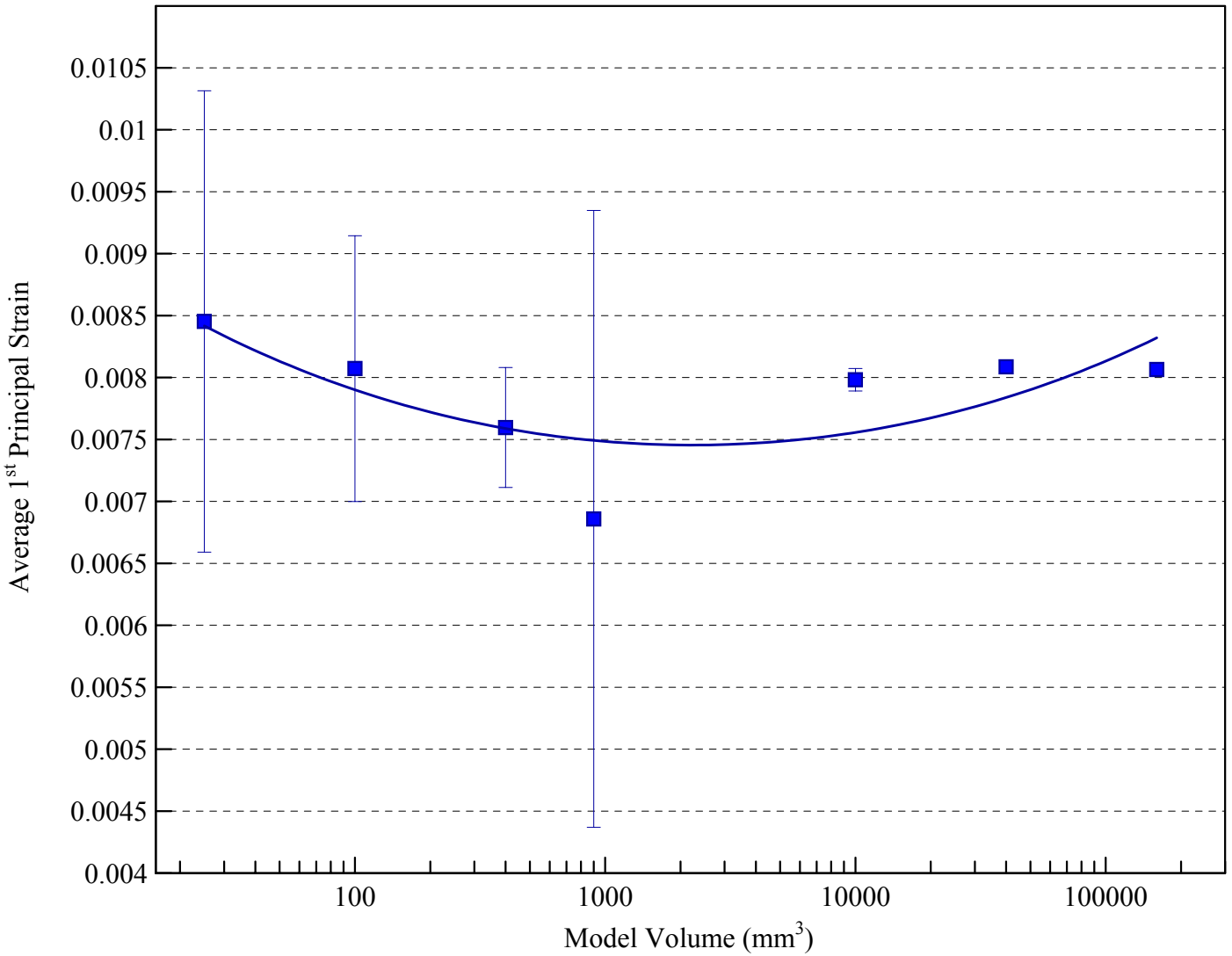

Graph 5.1.8 – Plot of average 1st principal strain under compressive loading with increasing model size.

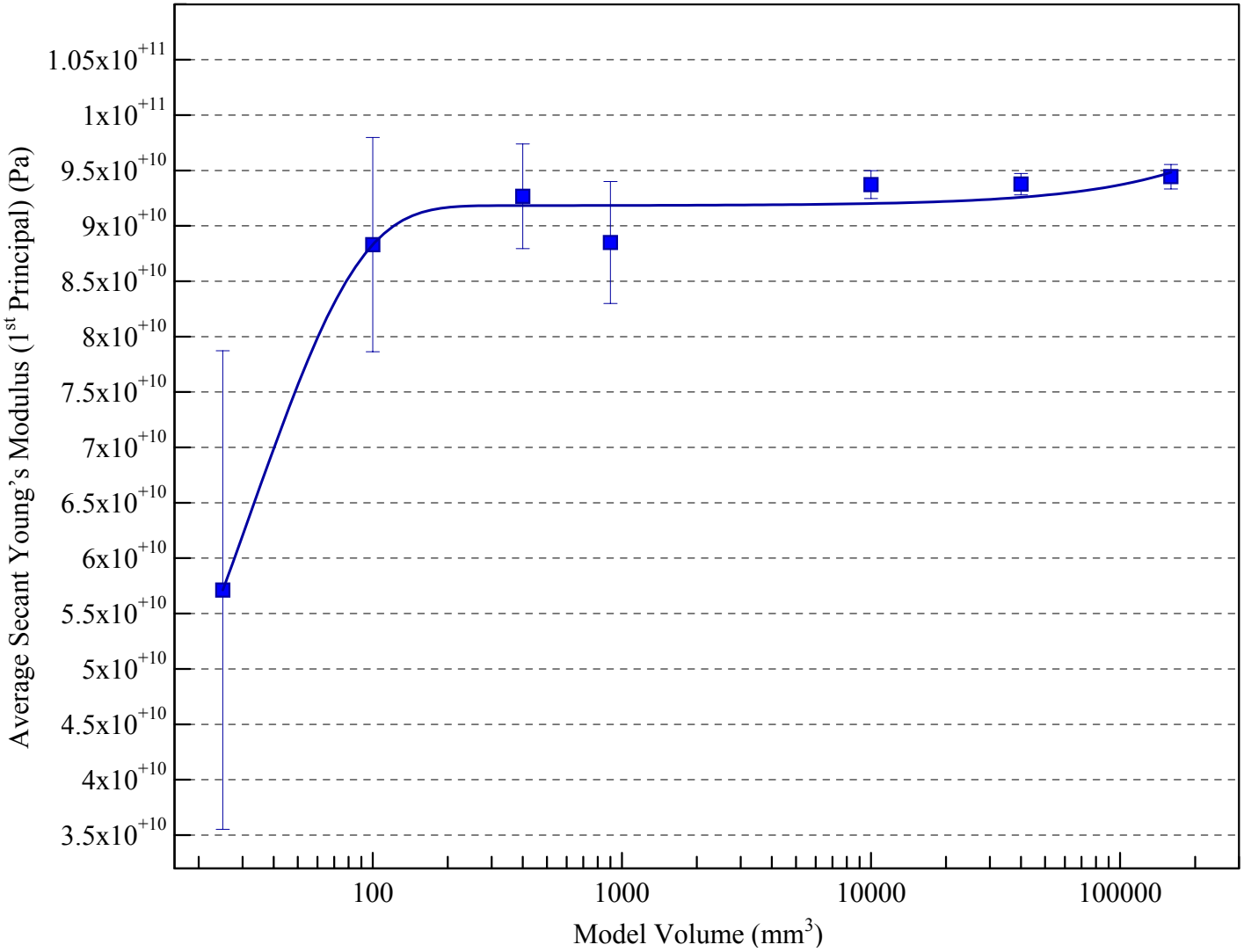

Graph 5.1.9 – Plot of average 1st principal secant Young's modulus under compressive loading against increasing model size.

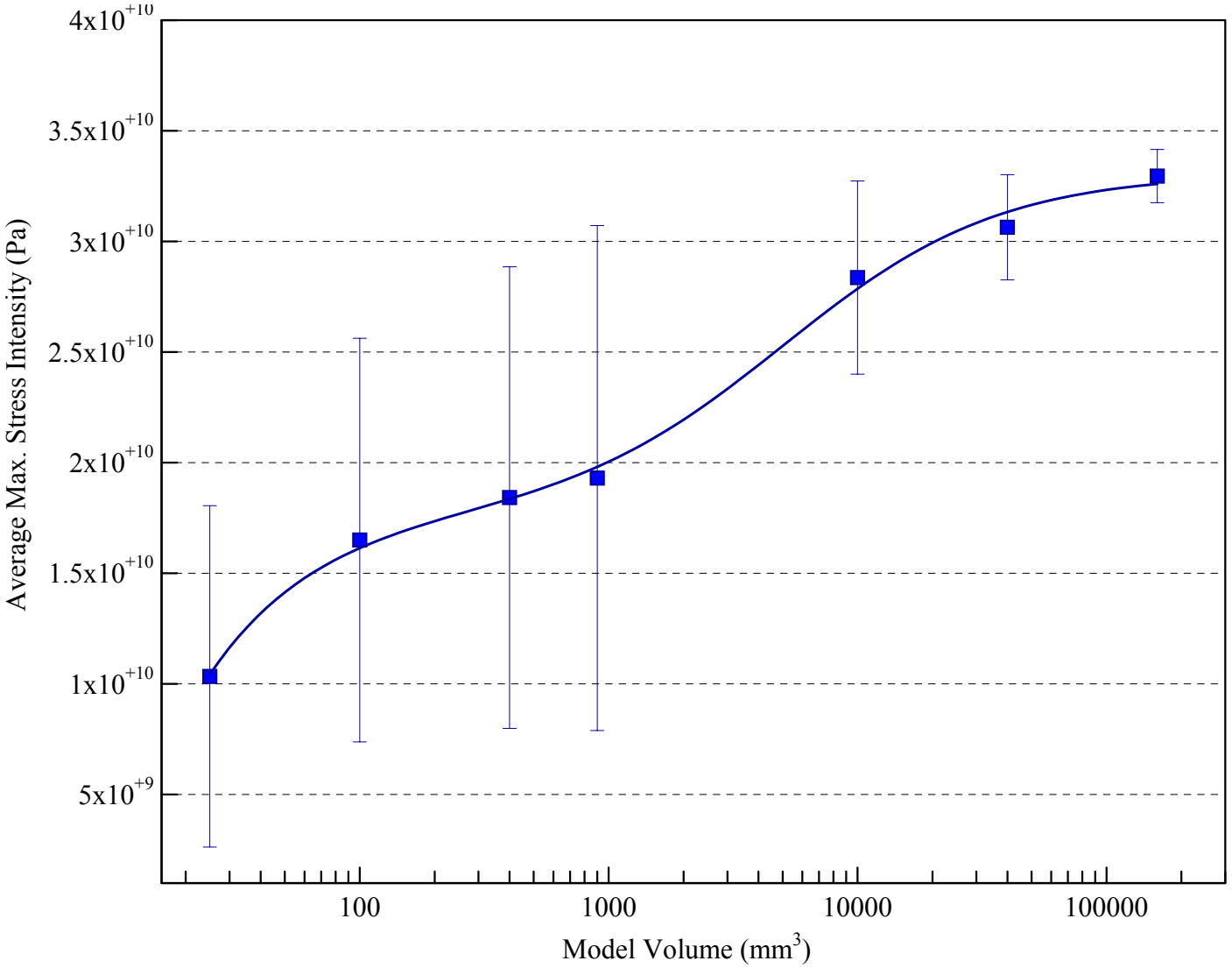

Graph 5.1.10 – Plot of average maximum stress intensity under compressive loading against increasing model size.

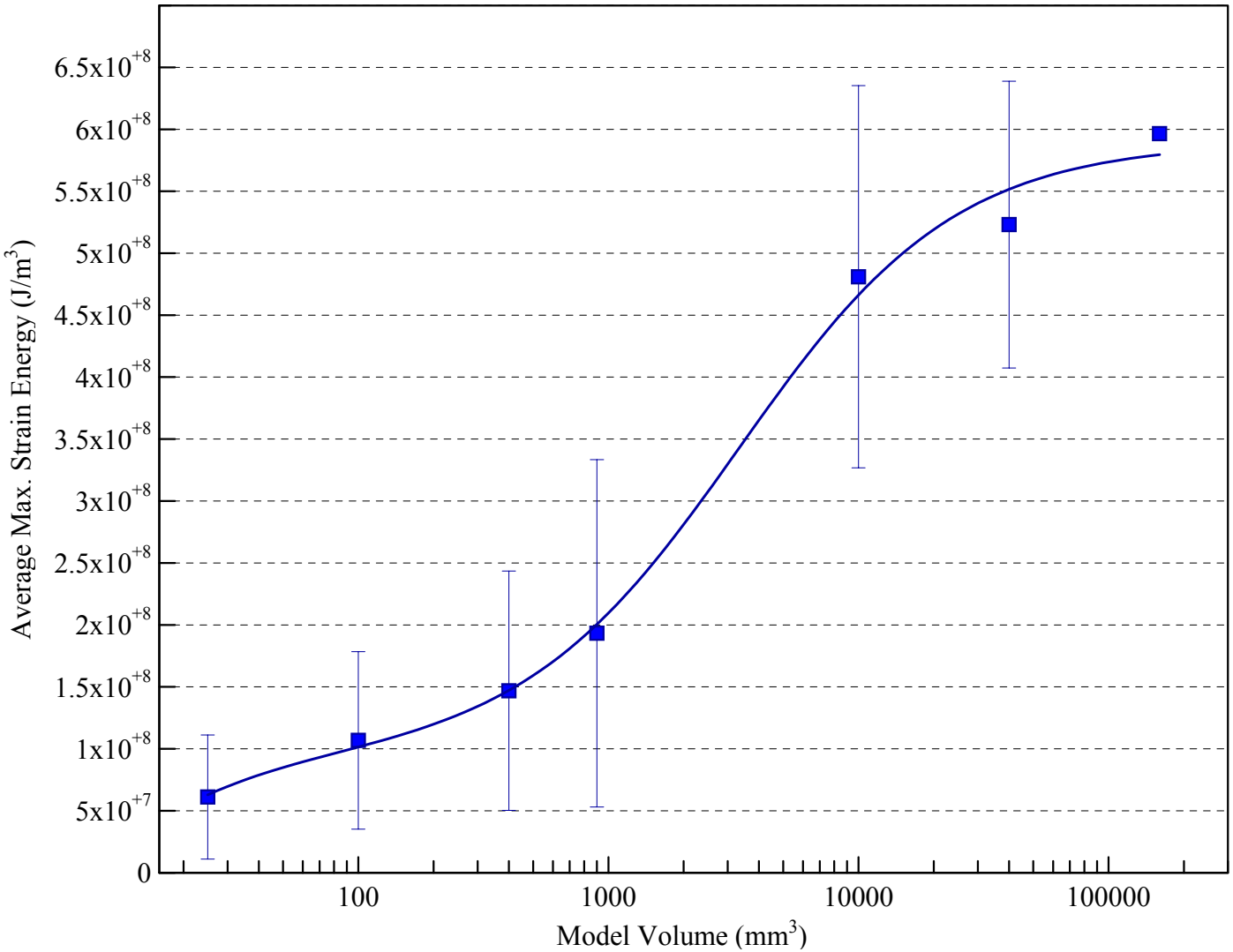

Graph 5.1.11 – Plot of average maximum strain energy under compressive loading against increasing model size.

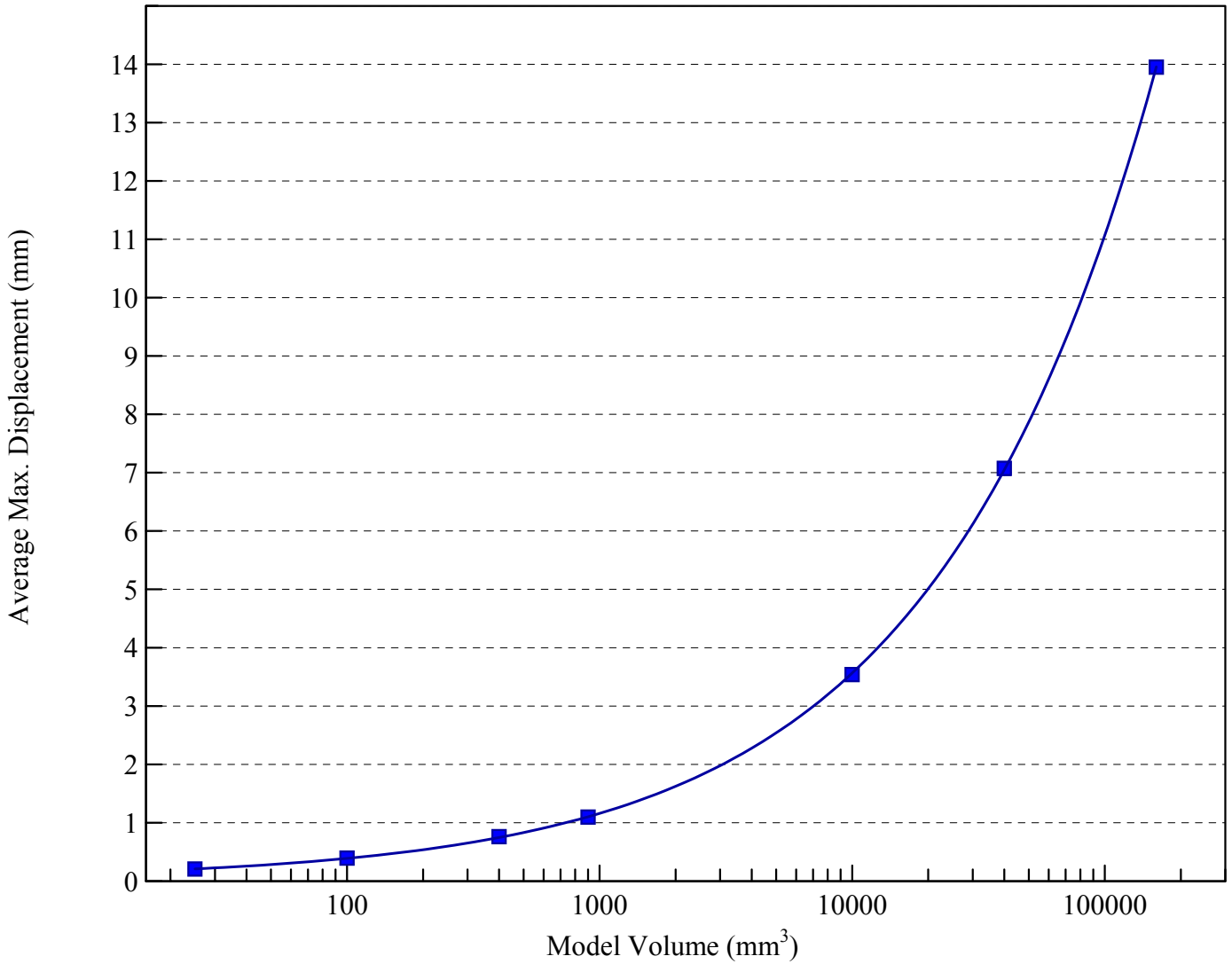

Graph 5.1.12 – Plot of average displacement under compressive loading against increasing model size.

Graphs 5.1.7 to 5.1.12 show the same properties plotted against model size as the tensile loading, but for compressive loading. Typically, they display the same characteristics but with different predicted values. Graph 5.1.7 for the average 1st principal strain under compression appears different to that under tension, but this is due to the fact that the stress values for compression have not been plotted as negative values (as the loading is applied in the negative *x*-direction).

The main difference between the two sets of results occurs with the determination of the secant Young's modulus. The average elastic modulus value is almost constant for all model sizes, with the exception of the 5 x 5 model size where the calculated value is much lower. Further interpretation of the predictions made by the conceptual models is discussed in Part C – Discussion, Conclusions and Further Work.

5.2 Modelling Observations

To graphically demonstrate what these values mean in relation to the models being analysed, the following figures compare the results for the same model being analysed under tension and compression (5 x 5 model number 03). In all the figures, red indicates the maximum value and dark blue indicates the minimum value, with graduated colours defining the values between. Figure 5.2.1 depicts both the tensile and compressive von Mises stress.

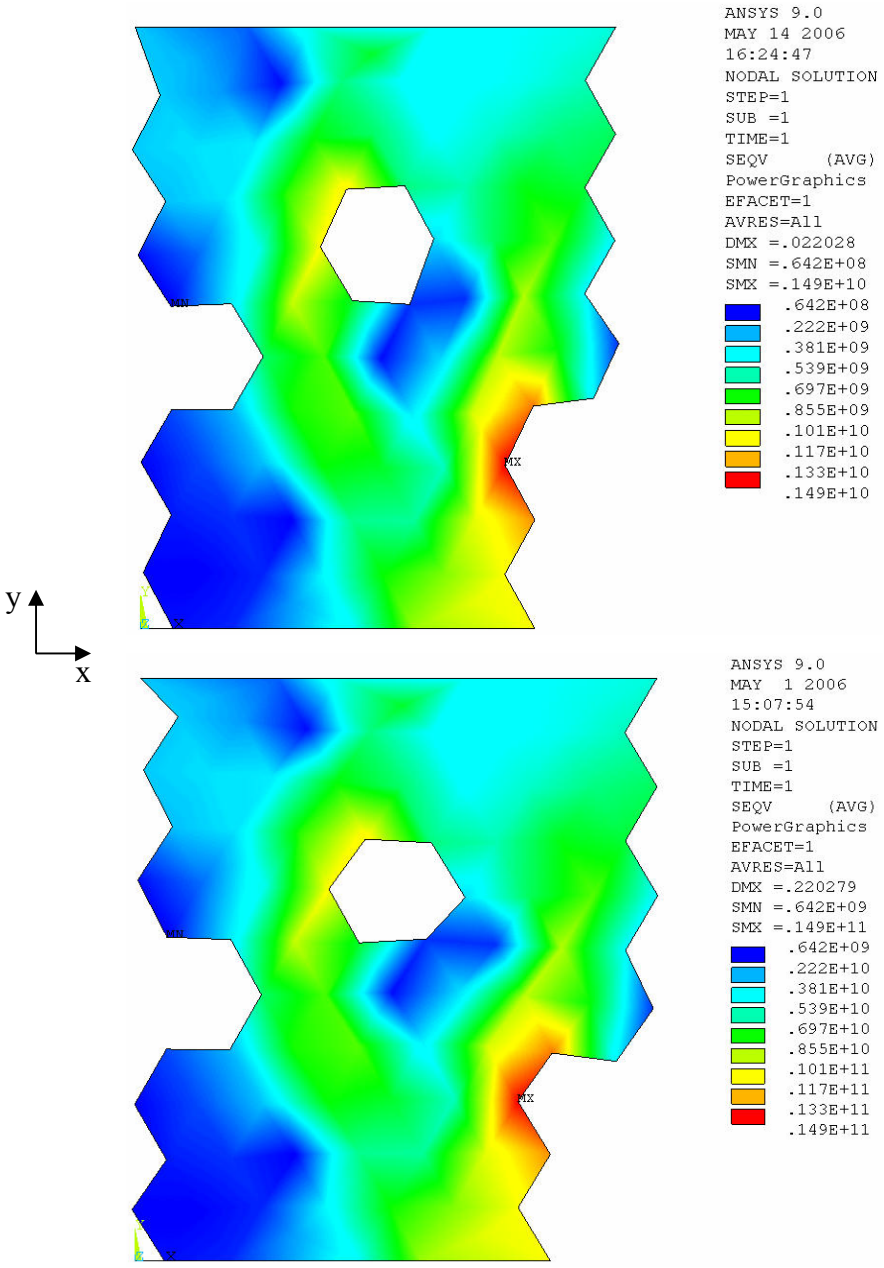

Figure 5.2.1 – Comparison of the von Mises stress result for a 5 x 5 model in tension and compression.

It is immediately noticeable that both models have almost identical stress distributions, with the maximum stress being recorded on the lower right hand side of the model. This higher concentration of stress occurs in a region of pure binder material at the edge of a large pore (in relation to the rest of the model). The von Mises strain is shown in figure 5.2.2.

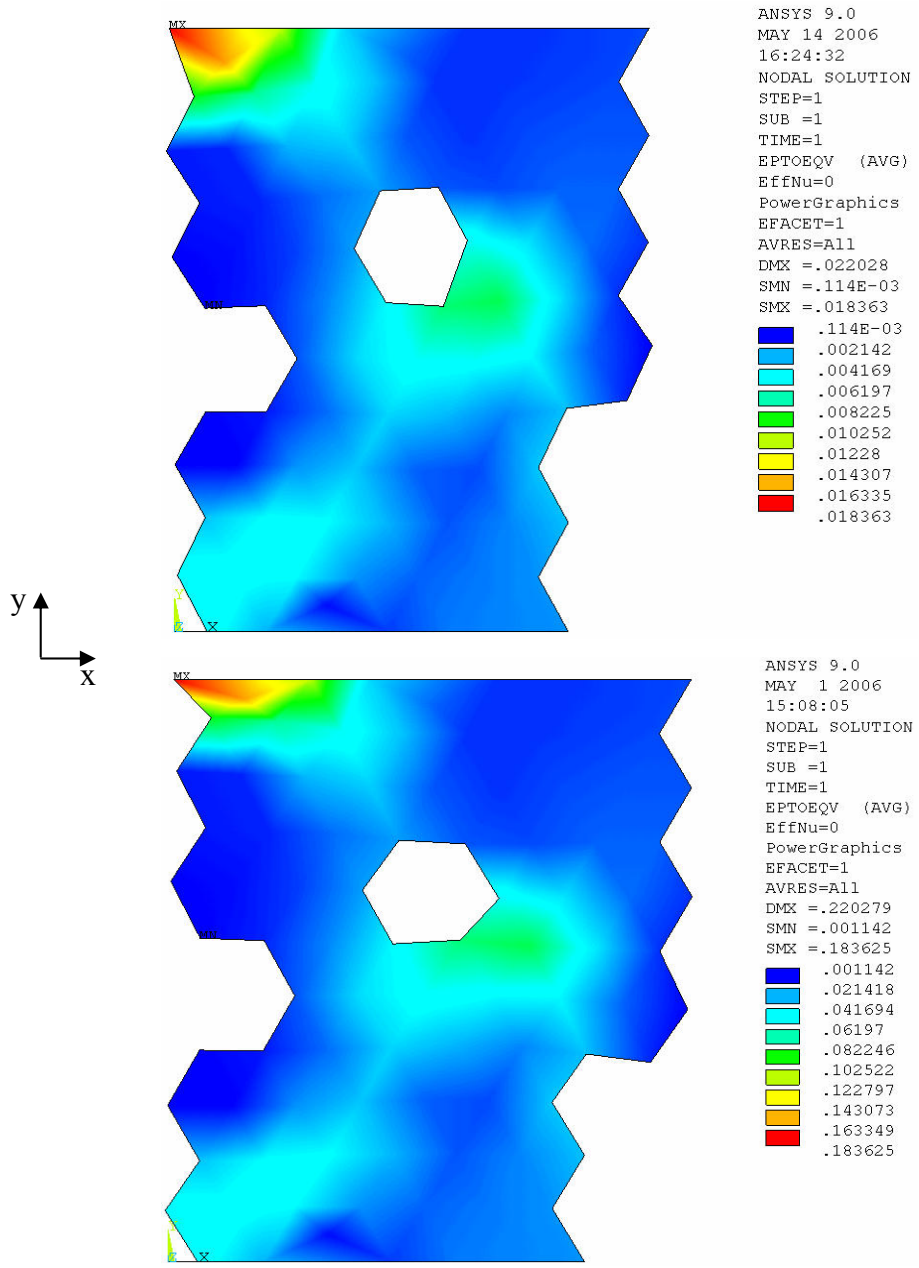

Figure 5.2.2 – Comparison of the von Mises strain result for a 5 x 5 model in tension and compression.

Again, the concentrations of strain are very similar with the highest value occurring in the top left hand corner of the model. The point at which the maximum strain value occurs is predominantly filler material, and is part of the region where the displacement constraint was set (*i.e.* the tensile/compressive force is acting upon the upper surface). The total displacement of the model is shown in Figure 5.2.3.

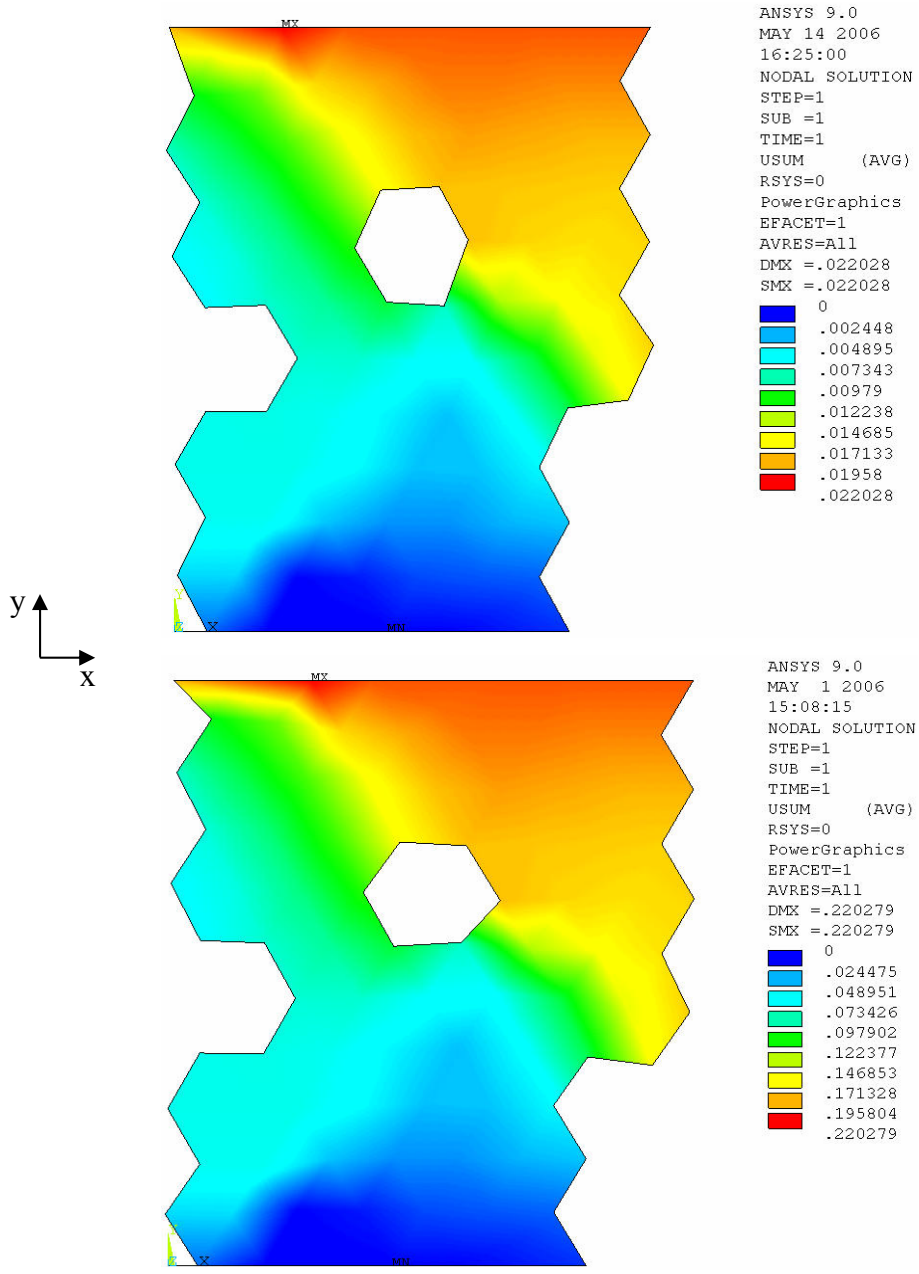

Figure 5.2.3 – Comparison of the displacement of a 5 x 5 model under tension and compression.

As would be expected for this output, the maximum and minimum displacements occur on the loaded and fixed surfaces respectively. What cannot be seen from these images alone is that the areas of maximum displacement are sections made up purely of binder material, and the sections with reduced displacement are those that contain filler material. This indicates that the stiffer of the two materials is arresting the displacement of the areas and preventing a uniform displacement through the models.

As with the previous figures, it can be seen that the pore in the centre (and those at the edges) have distorted in an elastic fashion with the respective load. It is worth reminding at this point that the loads are 0.2% strain in tension and 2% strain in compression, which if these were real material specimens they would have been expected to fail at or before this point. The finite element software does not calculate cracking and failure of the models in this case and therefore all the individual elements behave as if there are elastic for the purpose of displaying the results. Figures 5.2.4 and 5.2.5 show the stress intensity and the strain energy through the same models as before.

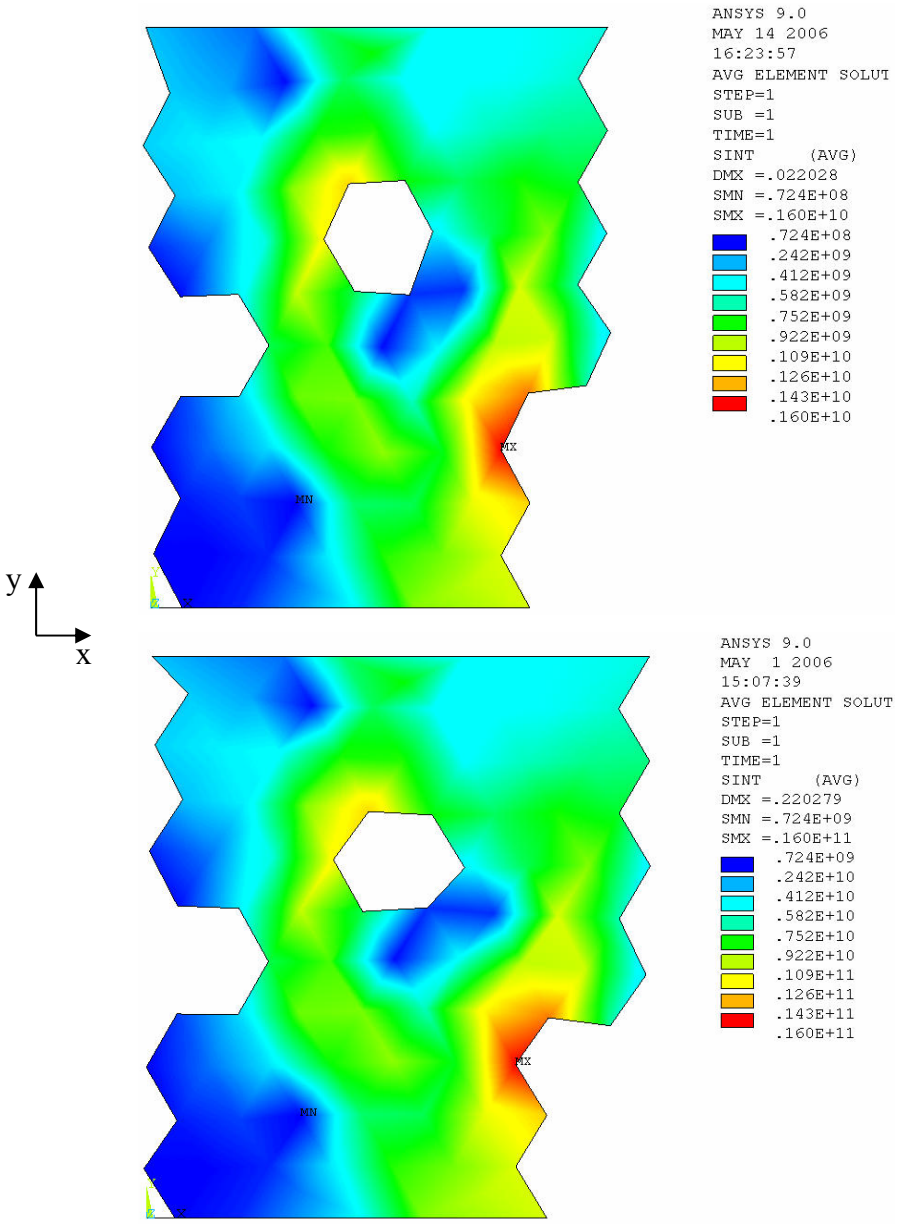

Figure 5.2.4 – Comparison of the stress intensity of a 5 x 5 model under tension and compression.

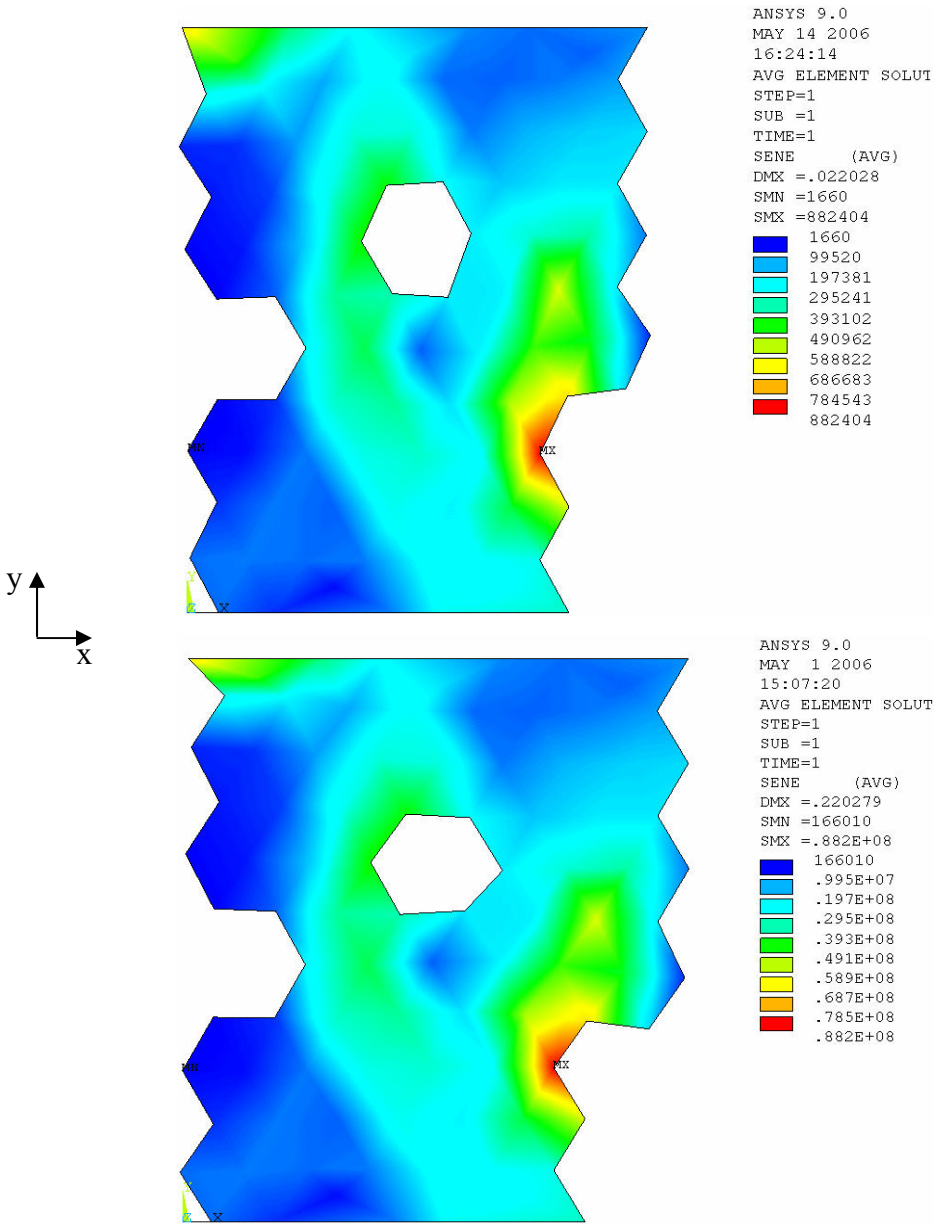

Figure 5.2.5 – Comparison of the strain energy of a 5 x 5 model under tension and compression.

As with figure 5.2.1, the same patterns can be seen in both the tension and compression models for the stress intensity. For the higher stress regions, binder is the predominant material, for the higher strain regions, filler is the predominant material. However, the strain energy shows a slightly different picture to that of figure 5.2.2. There is a higher concentration of strain in the upper left hand corner where the filler particles are present, but the maximum strain energy occurs at the point where there is a larger concentration of binder and a large pore area. Figures 5.2.6 and 5.2.7 are the 1st principal stress and strain (the stress and strain acting in the direction of the applied force, which in all these cases is vertically in the y-direction).

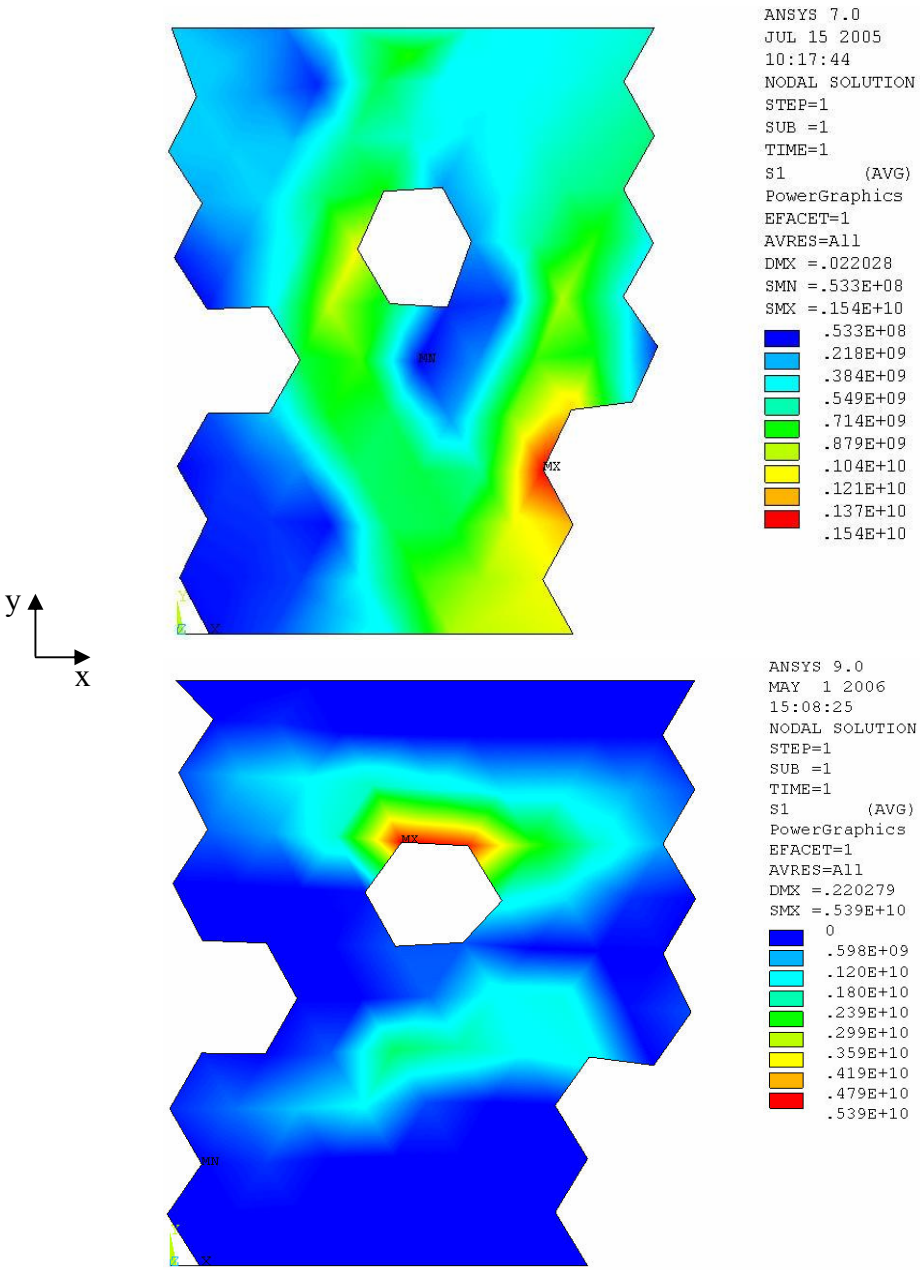

Figure 5.2.6 – Comparison of the 1st principal stress of a 5 x 5 model under tension and compression.

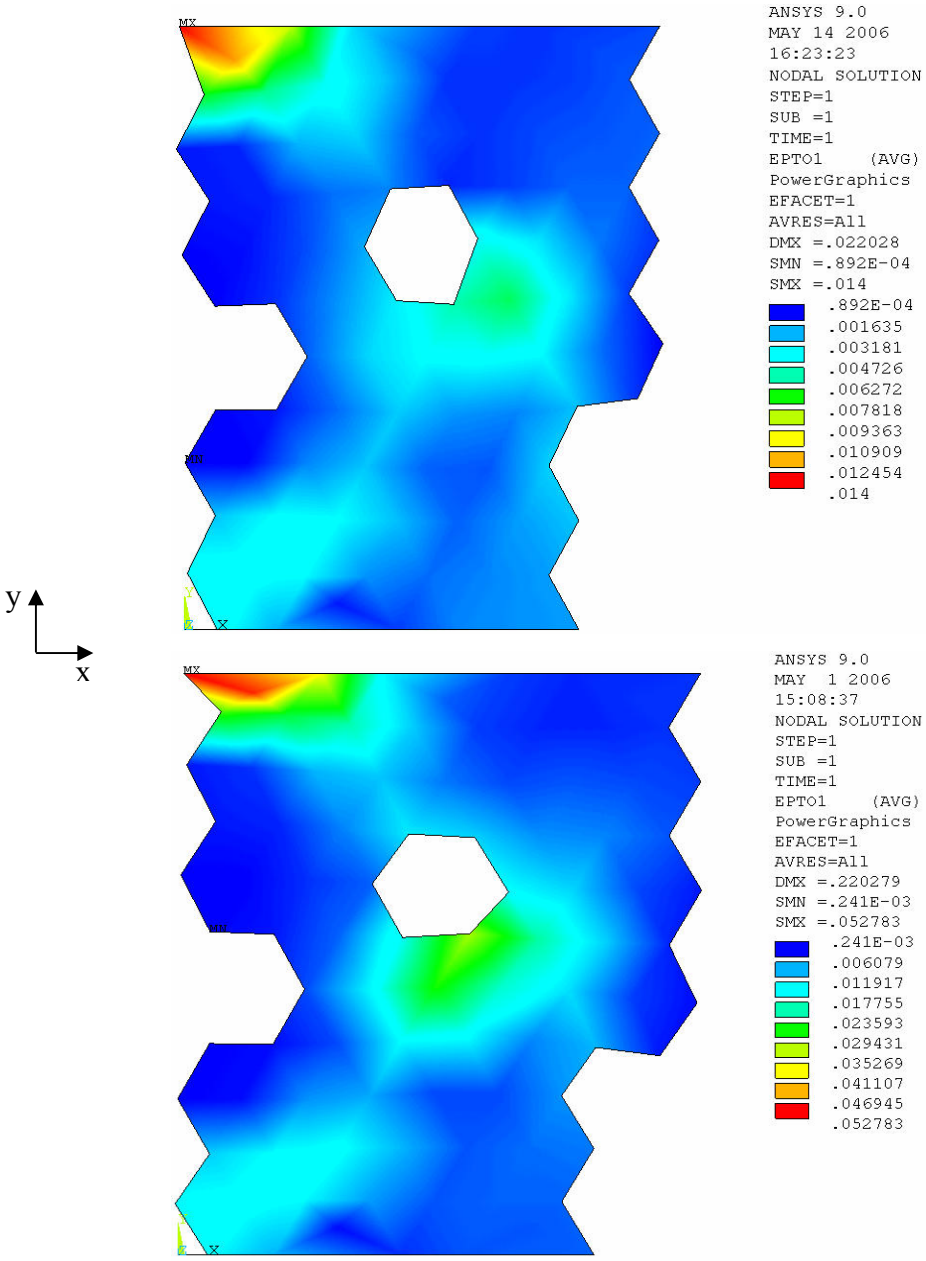

Figure 5.2.7 – Comparison of the 1st principal strain of a 5 x 5 model under tension and compression.

Figure 5.2.7 for the 1st principal strain shows a very similar trend to all the other images, strain distributions that look remarkably similar. But the images in Figure 5.2.6 for the 1st principal stress show markedly different stress distributions to those seen previously. Under tension the stress in the y-direction is focussed at the edge of the large pore in the lower right hand corner of the model, but under compression the stress is shown to be concentrated at the top of the pore in the centre of the model. Although in different locations, the maximum stress for both is still in regions containing mainly binder material. As the number of predictions obtained was numerous, a selection of one

example from each of the analysed model sizes can be seen in Appendix C that detail the same observations as the previous figures, and the full results can be viewed on the CD-ROM Appendix D.

One of the limitations of the predictions made is that ANSYS considers the materials to be elastic in their behaviour, even though all the material properties are those of a brittle material. Figure 5.2.8 depicts the displacement of one of the 30 x 30 models under compression compared to the original shape. It is clear to see that many of the pores in the model have been compressed as the displacement is applied, an effect that a real graphite would not undergo. Although this is not a strict representation of graphite microstructural behaviour, the models are considered to be abstract and the predictions made are not altogether inaccurate.

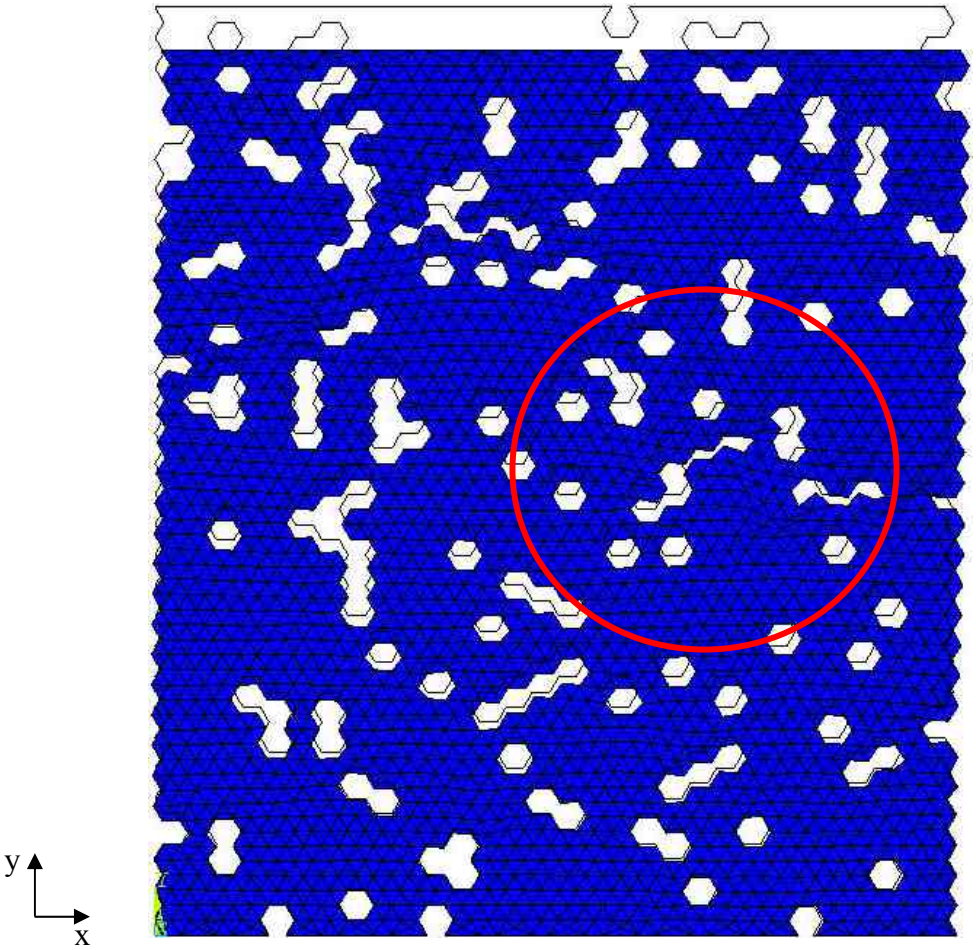

Figure 5.2.8 – Deformed shape of a 30 x 30 model under compressive loading.

The compressing (and stretching, in the case of tensile loading) of the pores and the constituent particles appears greater than is actually the case as the output images from the software exaggerates the displacement to graphically show the movement of the entire model. In the above example, the model was displaced by 2% of the overall height, but the output image displays a compression of approximately 5%. The values taken directly from the program are not adjusted in any way.

On generating the models, observations of the porosity distribution were made to study the origination of conglomerations of pores and the development of pore chains. At all model sizes up to 30 x 30 this was a relatively simple task of counting the number of pores connected and plotting the frequency of occurrence against the size of the pore chain. At the 100 x 100 model size, the ability to count the number of pores connected through any normal visual means became limited due to the number of pores present (approximately 1700 in each model). The pore distributions were able to be measured in much the same way as the porosity of graphite determination detailed in Chapter 4 – Conceptual Modelling, through the use of image analysis. However, there were limitations on analysing the distributions of the models larger than this (200 x 200 and 400 x 400) due to the conversion of the hexagonal forms of the particles and pores to square pixels on the output images. The distributions of the larger models could not be determined precisely at this stage, but the data obtained from the smaller models can be considered indicative for all model sizes. Graph 5.2.1 shows the porosity distribution for examples of the 5 x 5 to 30 x 30 models, whilst Graph 5.2.2 shows the porosity distribution for an example of the 100 x 100 model. These are plotted on separate graphs as the increase in the number of pores for the 100 x 100 model causes the distributions for the smaller sizes not to be seen when plotted together.

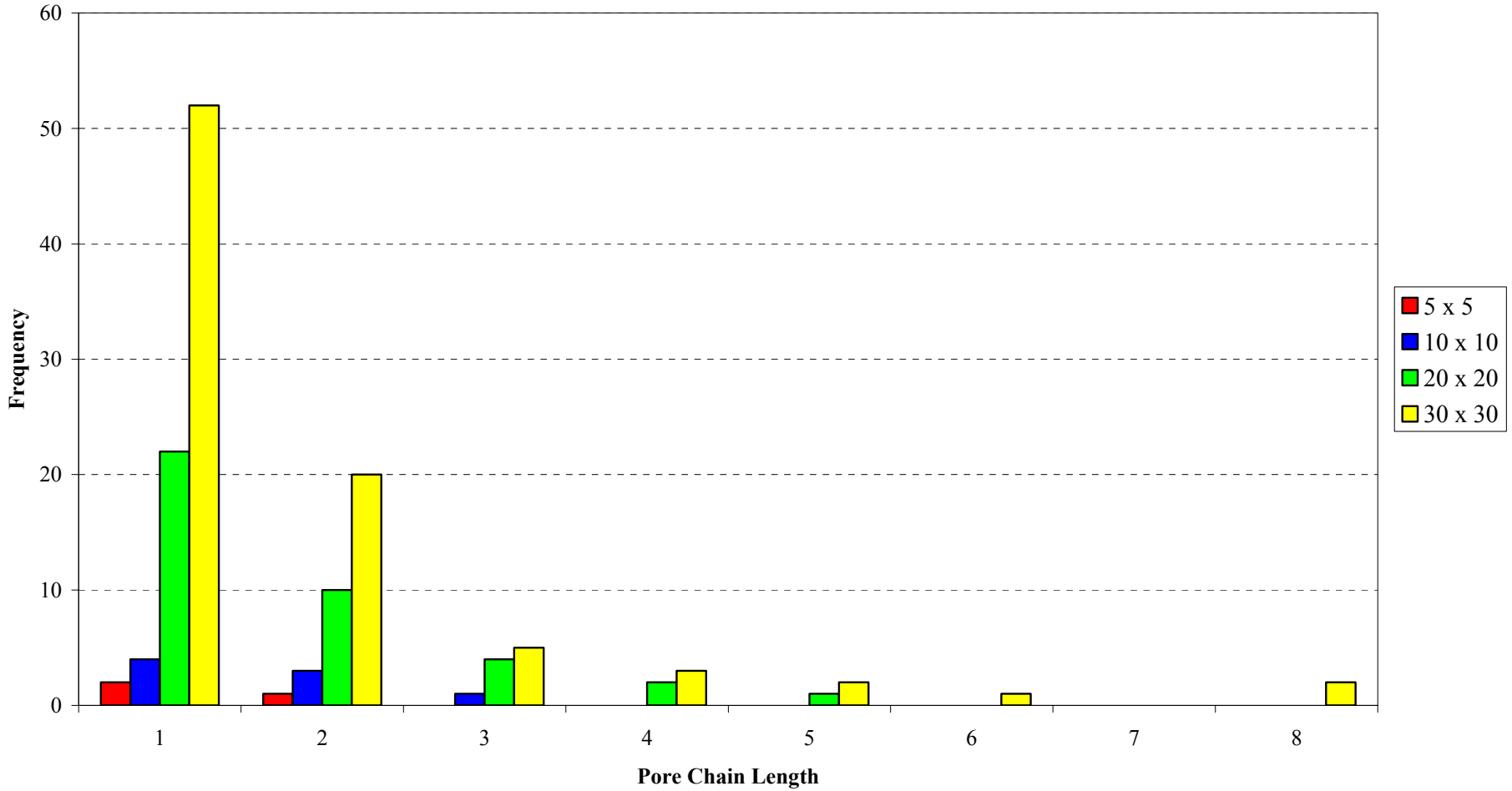

Graph 5.2.1 – Pore chain frequency examples for the 5 x 5 to 30 x 30 models.

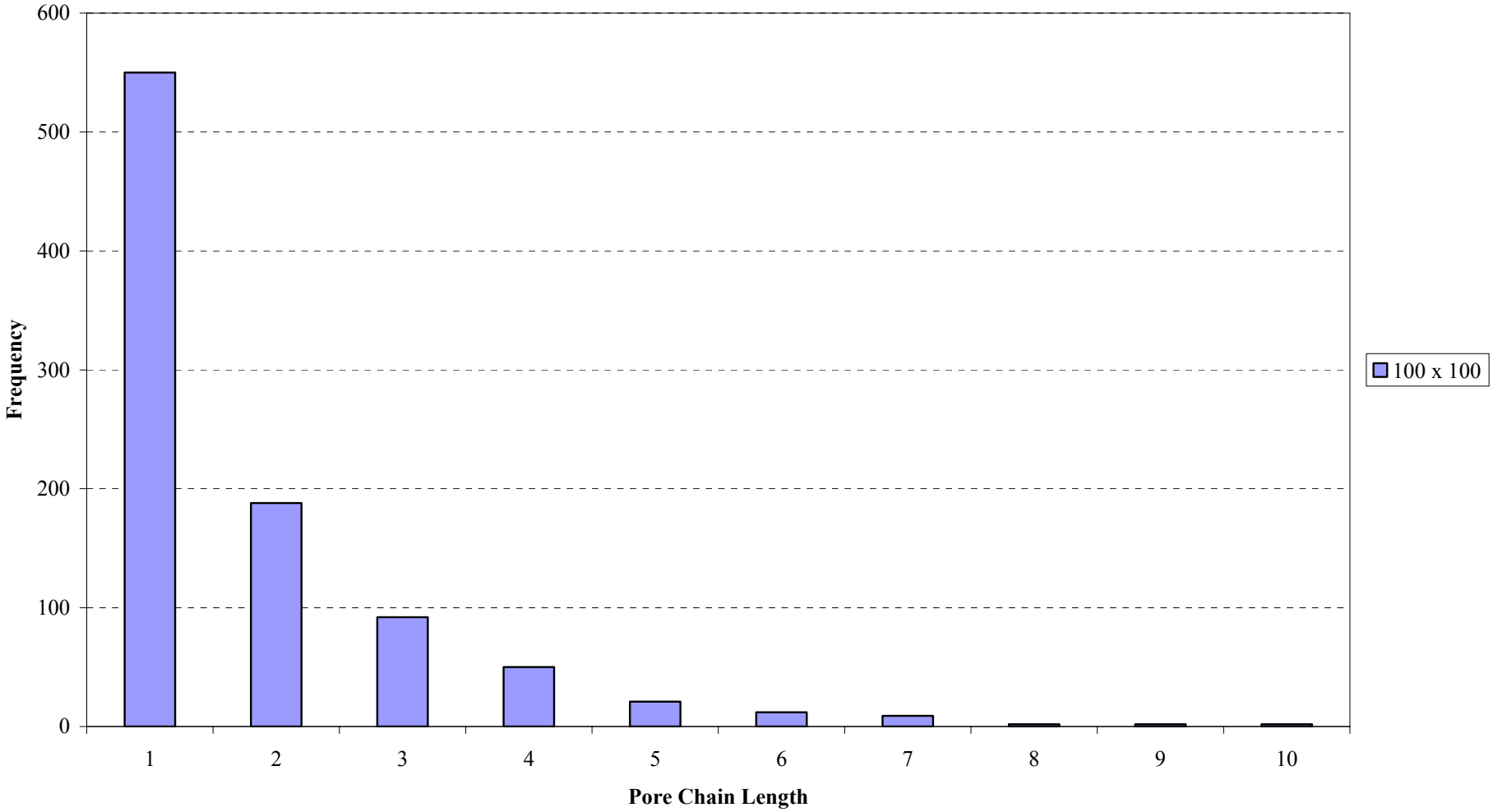

Graph 5.2.2 – Pore chain frequency example for the 100 x 100 model.

From the previous two graphs it is clear that all the models analysed have a very similar pore chain distribution. The largest occurrence within the models is of single pores which constitute approximately one third of the total number of pores. As the size of the pore chain increases, the frequency decreases with the pore chain lengths equating to approximately the same percentage of the total number of pores present for each model size (see Table 5.2.1 for count of the number of pore chains, and Table 5.2.2 for the percentage of total pores present in the model).

Number of Pore Chains		**Model Size**				
		100 x 100	30 x 30	20 x 20	10 x 10	5 x 5
Pore Chain Length	1	550	52	22	4	2
	2	188	20	10	3	1
	3	92	5	4	1	-
	4	50	3	2	-	-
	5	21	2	1	-	-
	6	12	1	-	-	-
	7	9	-	-	-	-
	8	2	2	-	-	-
	9	2	-	-	-	-
	10	2	-	-	-	-

Table 5.2.1 – Count of the number of pore chains within example models.

Percentage of Total Number of Pores		**Model Size**				
		100 x 100	30 x 30	20 x 20	10 x 10	5 x 5
Pore Chain Length	1	32%	34%	33%	31%	50%
	2	22%	26%	30%	46%	50%
	3	16%	10%	18%	23%	-
	4	12%	8%	12%	-	-
	5	6%	7%	7%	-	-
	6	4%	4%	-	-	-
	7	4%	-	-	-	-
	8	1%	11%	-	-	-
	9	1%	-	-	-	-
	10	1%	-	-	-	-

Table 5.2.2 – Percentage that the pore chains contribute to the total number of pores within the example models.

It would be expected that as the model sizes increase, the larger pore chains would increase in number, but would not necessarily contribute a higher percentage of the overall porosity of the model. It should also be noted that from the images displayed previously and from those in Appendices C and E that the larger pore chains do not always denote the regions of highest stress or strain and may not be the defining factor that leads to failure with in graphite.

5.3 Modelling Summary

This chapter has discussed the results, both numerical and graphical, obtained through the modelling programme. It is apparent from the numerical results that the values obtained for the considered material properties are significantly larger than those for real world graphite, *e.g.* in the case of the secant Young's modulus in tension it is approximately 20 times greater, and there is no easily defined relationship between the model properties and model size. However, whilst the numerical results are not representative of the real values, the models are not fully representative of real size components (*i.e.* square models with no thickness), and as such at this early stage of modelling the disparity is not too great a concern.

The graphical results are much more promising with each output indicating the effect the loading condition has on the bulk material. With particular reference to the stress and strain, it is currently assumed that failure of graphite occurs at the largest flaw in the material, usually at a pore or a grain boundary. The models indicate that failure is not necessarily linked to the largest flaw, and cracking may initiate in regions where there are a large conglomeration of smaller pores, stiffer binder material and fewer filler particles.

The results observed and the predictions obtained through the conceptual modelling of the graphite microstructure are further explored in Chapter 8 – Discussion where the data obtained from the mechanical testing programme and the existing literature are used to validate the models and highlight any areas of weakness.

Part C: Development and performance of an experimental programme

Chapter 6 - Experimental Details

The purpose of the testing programme was to provide sets of data that could be used to validate the results obtained from the conceptual modelling of the graphite microstructure. Although information of this nature is available from a variety of sources, none that were investigated were suitable for the needs of this work. Furthermore, the benefits of directly performing the experiments allows the operator to fully observe the process and study all the minute details that may not necessarily be reported by others, gaining an much better insight into the behaviour of the materials concerned.

The following chapter is a detailed examination of the materials used in the mechanical testing programme, and the methods utilised in performing the experimental programme. The chapter covers the design of the experiments and equipment, microscopy, experimental methods, and the relevant key equations.

6.1 Design of the Experiments, Specimens and Equipment

To develop a structured testing programme the Design of Experiments technique was employed. Design of Experiments (DoE) is a practice in which a systematic approach is taken to investigate a system or process. The technique allows the maximum information to be gained whilst minimising the resources to be used.

Traditionally “one change at a time” testing programmes have been employed. This method has the experimenter changing one of the input variables during the testing programme, as and when it seems appropriate, to take the investigation in the required direction. However, this technique has many drawbacks, not least that the effect of

changing one variable and discovering its response does not indicate if that response is solely influenced by the one variable, *i.e.* would changing another variable greatly alter the result, or produce the same result?

By developing a series of structured tests, planned changes can be made that allow the measurement of the effects of an input variable on the output of the system. DoE enables the experimenter to plan for all the possible dependencies within the system and examine them individually, as well as together. It also prescribes what information is needed to assess the individual variables, reducing the amount of unnecessary testing through determining the length, size and number of the experiments in advance (thequalityportal.com, 2005).

For the development of the experimental programme for this research project it was necessary to begin with the determination of the specimen sizes. As it was required that tests were to be performed on small scale samples, a size of 3 mm x 3 mm x 10 mm was chosen as the starting point for the selection of specimen geometries (as it is known that British Energy Generation Ltd use a standard specimen size of 6 mm x 6 mm x 19 mm for their testing purposes, it was needed to be smaller than this). Taking this initial specimen size and incorporating the British Energy standard test specimen size, it was possible to build a matrix for the required sample dimensions with regarding to studying the effect of altering volume, length and cross-sectional area (see Table 6.1.1).

Specimen Type	Volume	Length	Cross-Sectional Area	Specimen Size (mm)
A	V	L	A	3 x 3 x 10
B	$7.6V$	$1.9L$	$4A$	6 x 6 x 19
C	$10V$	$4L$	$2.5A$	4.74 x 4.74 x 40
D	$20V$	$5L$	$4A$	6 x 6 x 50
E	$100V$	$10L$	$10A$	9.49 x 9.49 x 100
F	$160.4V$	$4L$	$40.1A$	19 x 19 x 40

Table 6.1.1 – Matrix of specimen geometries.

It can be seen from the matrix that it is not simply a matter of just doubling the specimen dimension in accordance with the previous one (*e.g.* L, $2L$, $4L$ etc), the sizes are selected so that the effects of each individual property can be examined independently of the others, or in conjunction with them. For instance, does the increase

in volume solely influence the response of the specimen? Or is the cross-sectional area important as well? This selection of specimen sizes allows for the investigation of the effect of geometry as well as individual scale.

But, why limit the samples to the smallest and largest sizes shown in Table 6.1.1? Brocklehurst's work indicated that at small sample volumes the results were not representative of the microstructure. That is, the typical filler particle diameter in IM1-24 graphite is widely taken as being ~ 0.5 mm, if the specimen size is too small then very few particles would be present (if any at all) in a given cross-section, and a valid test result would not be produced as it would not be indicative of the material as a whole. Conversely, as also demonstrated by Brocklehurst's research, if the specimen exceeds a given size the overall strength is reduced due to the higher probability of a critical flaw being present (also the basis of Weibull's theory). As this particular aspect of the study is concerned with providing validation data, there is no cause to examine what the resultant effect of greatly increased specimen size is.

An additional consideration in the selection of sample sizes and their limiting factors is the ability to machine components. Although large samples can be manufactured with relative ease, small samples are not as easy to produce. A specimen size smaller than 3 mm x 3 mm x 10 mm would be not be easy to manufacture without fracturing during the machining process and would be too costly due to the increased care needed to produce a usable specimen.

Having determined the required specimen dimensions it was necessary to produce working drawings for the manufacturing process. As all the specimens were simple geometric shapes (cuboids) this was not a difficult task. However, a number of the specimens were to be notched in order to examine the effect of scale on the work of fracture and critical stress intensity (K_{IC}).

The single edged notched bend bar (SENB, see Figure 6.1.1) type specimen was selected for the 3-point and 4-point flexural tests, heavily influenced by the geometric shape of the unnotched samples. The advantages of this type of specimen over others (such as the CT, Compact Tension, specimen) are that it is a simple geometry for the ease of machining and there is a minimal amount of waste material in comparison with

others. It does have a disadvantage in that there is difficulty in obtaining subcritical crack growth data due to the relatively unstable mode of crack propagation, and R-curve measurements. However, neither of these features are to be investigated in this study and therefore have no impact on the selection of the SENB specimen type.

The notch geometry is critical in obtaining a valid K_{IC} from the experiment and for this, the notch length *a* and the depth *B* should not be less than:

$$2.5\left(\frac{K_{IC}}{\sigma_Y}\right)^2 \qquad \text{Equation [6.1.1]}$$

where σ_Y is the 0.2 % proof stress of the material under the test conditions. Alternatively, the calculation of the ratio of yield strength (σ_{YS}) to the Young's modulus (E) can be used to determine a suitable specimen size. Data tables for the selection of specimen width and crack length depending on this figure can be found in BS 5447:1977, and the calculations relevant to this study can be found in Chapter 6.4 – Key Equations.

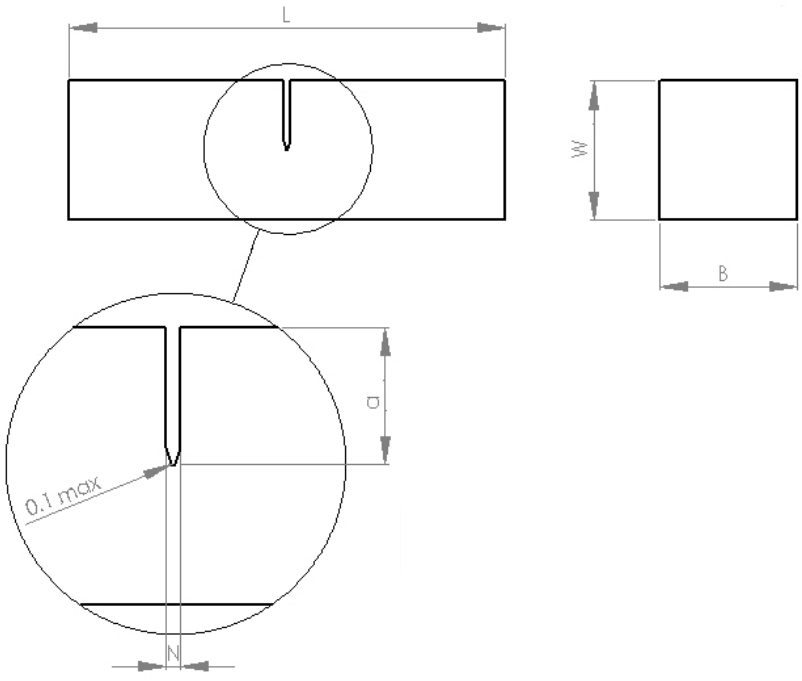

Figure 6.1.1 – The single edged notched bend bar (SENB). L is the loading span, W is the width, B is the depth, a is the notch length and N is the notch width. The maximum allowed notch tip radius 0.1 mm.

A notch of width 0.3 mm was chosen for all sample sizes, with the notch depth set at:

$$a = \frac{W}{2} \qquad \text{Equation [6.1.2]}$$

effectively half the sample width. Each notch was to be machined so that the notch tip radius was 0.05 mm to promote crack initiation through the centre of the specimen. Examples of the design of the unnotched and notched specimens are shown in Figures 6.1.2 and 6.1.3 respectively. Note that the images shown are rendered interpretations of the designs to depict the overall shape of the specimens, produced by Solidworks Education Edition CAD package in which all the design work was performed. All working drawings for the design of the specimen types (both notched and unnotched) can be seen on the CD-ROM Appendix D.

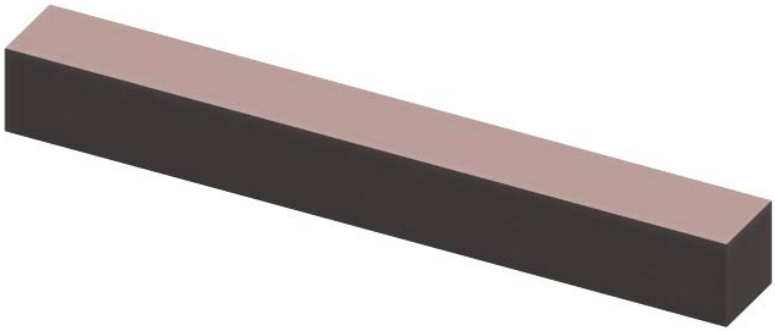

Figure 6.1.2 – Solidworks rendering of the 4.74 mm x 4.74 mm x 40 mm specimen (unnotched).

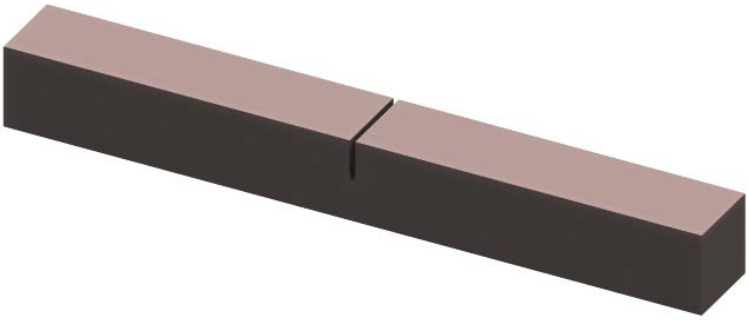

Figure 6.1.3 – Solidworks rendering of the 4.74 mm x 4.74 mm x 40 mm specimen (notched).

It was already known that IM1-24 graphite was going to be the choice material for the testing programme, and the matrix of sample sizes was developed for that purpose. However, a reference material was required for comparison to the obtained results.

The reference material ideally was to be a ceramic with similar properties to those of IM1-24 graphite, but with a more homogenous microstructure so as to provide data that could be used as a control set. This reference data could be used when comparing the modelling programme results to the testing programme to indicate whether the models were providing results analogous to a material with a random microstructure. Initially, a form of rock was considered (such as limestone or sandstone) but was quickly discarded as being inappropriate due to the difficulty involved in manufacturing the specimens, and the significant difference in material properties and microstructure.

Using the required microstructure as a basis, the optimal solution appeared to be to acquire a technical ceramic to the specifications needed. Materials such as aluminium oxide (alumina), boron nitride or pyrophillite would suit the purposes, and investigation into the material properties, availability and cost was undertaken. Table 3.3.1 gives a comparison of the basic material properties of interest for these three potential reference materials.

Material	**Density (g/cm^3)**	**Porosity (%)**	**Compressive Strength (MPa)**	**Hardness**
Alumina (Al_2O_3)	3.5	0	2×10^6 -2.25 x 10^6	1650 (Vickers)
Boron Nitride (BeO)	1.92	2.84	143	13.79 – 18.95 kg/mm
Pyrophillite	Not available	2.88	105	5 (Mohs)

Table 6.1.2 – Potential reference material properties (data obtained from Precision Ceramics, 2003).

After reviewing the data gathered in the potential reference materials, requests for quotes were sent to the companies that manufactured these products for the production of the test specimens. The responses that were returned were not favourable as the cost of producing these materials at the sizes and quantities required would have exceeded

the project budget by some way, and unfortunately the skills to accurately manufacture these materials in-house were not available, therefore an alternate solution had to be found.

This came in the form of a fine grained graphite produced by the SGL Carbon Group. R4340 is a speciality graphite produced by the company and has similar properties to IM1-24 graphite but with a more homogenous microstructure (this can be seen in Figure 6.1.4). The material is commercially available and relatively inexpensive, and a deciding factor was the SGL Carbon Group could also machine the required IM1-24 samples, reducing the cost through requesting a larger order.

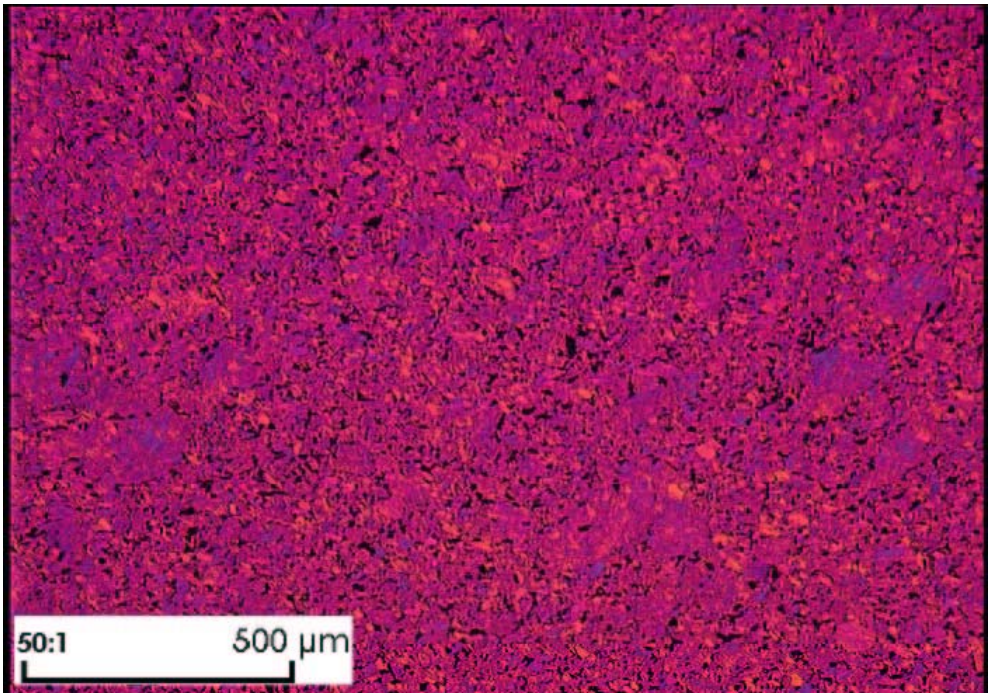

Figure 6.1.4 – Polarised light micrograph of the microstructure of R4340 graphite, provided by the SGL Carbon Group. Density ~1.72 g/cm3, porosity ~ 15 %, compressive strength ~ 92 MPa.

For determining the number of samples required, the matrix designed through DoE needed to be consulted. Six specimen sizes were required, and three different tests were to be performed on each specimen size, compression tests, 3-point flexural tests and 4-point flexural tests. To produce representative sets of data, a minimum of six specimens for each specimen size and each test must used in order to gain the mean and standard

deviation. It was decided that ten specimens for each size should be produced. This would have meant the production of 180 samples in total.

In the interests of gaining as much data as possible, a further criterion was added, testing notched samples under 3-point and 4-point flexural conditions. This would add another 120 specimens, meaning 300 would be required in total for each material and giving 600 individual test specimens (details of sample design were described earlier in this chapter). The most convenient method of having the specimens prepared was to ship the bulk IM1-24 graphite (supplied by British Energy) to the SGL Carbon Group for machining, and at the same time the R4340 graphite specimens would be manufactured. Additional instructions were sent with the bulk material to ensure the most suitable specimens for testing could be produced:

- No sample identification or orientation to be marked on the specimens
- The surface finish should be 0.8 μm or better where the grain structure permits
- Ensure production of sharp edges and parallel sides
- Dimensional tolerance is to +/- 0.1 mm
- All machining to be done under "clean conditions" as normal for nuclear graphite requirements
- All material to be suitably packed and protected from moisture and other contaminates during transportation

All machining work was completed by SGL Carbon with the exception of notching the largest sized specimens (*F*, the 19 mm x 19 mm x 40 mm samples) for both material types, as they were unable to notch to a depth of 9.5 mm in their workshops. As this was a required element for the testing programme a solution had to be sought in-house (detailed in Chapter 6.2 - Microscopy).

For the three different types of tests set in the programme, only the compression test had the equipment required readily available in that compression platens were supplied with the tensile test machine. For the 3-point and 4-point flexural tests, the apparatus needed to be designed and manufactured. Through examining existing designs and the

consideration of what was expected of the equipment to perform the tests accurately and efficiently a specification could be drawn up.

Due to the variation in sample sizes a fixed size flexural test rig would not be suitable as it is required to accommodate samples from 10 mm in length to 100 mm in length, and have the ability to support the appropriate load spans (*e.g.* a 10 mm length 3-point flexural sample has a load span of 5 mm, whereas a 100 mm length 3-point flexural specimen has a load span of 50 mm). The test rig should also be capable of ensuring that each sample is horizontal throughout the duration of the test to ensure a uniform load across it, this in particular applies to the 4-point flexural tests. The whole rig must be able to withstand the load required to fracture the toughest samples, and preferably this should be 50 kN as this is the limit of the tensile testing machine. In addition to withstanding this maximum load it should also be able to tolerate repeated loading.

The testing rig should also be easy to operate in that any alteration of the load span or the changing of parts must be simple and relatively quick primarily due to the number of tests that are to be performed. Ideally it should be operable by any individual, but as this is a specialised rig for a predetermined testing programme run by one person, this is not essential. As little maintenance as possible should be undertaken on the finished rig, and it should also be safe when maintenance is undertaken, such as no sharp edges or sections that can cause harm. Additionally, future experimental work that may be performed on it should be catered for where possible (*e.g.* increased sample sizes or specimens differing in geometry from the ones laid out here).

Taking this brief specification into account and knowing what was needed from the rig, the design took the form as follows.

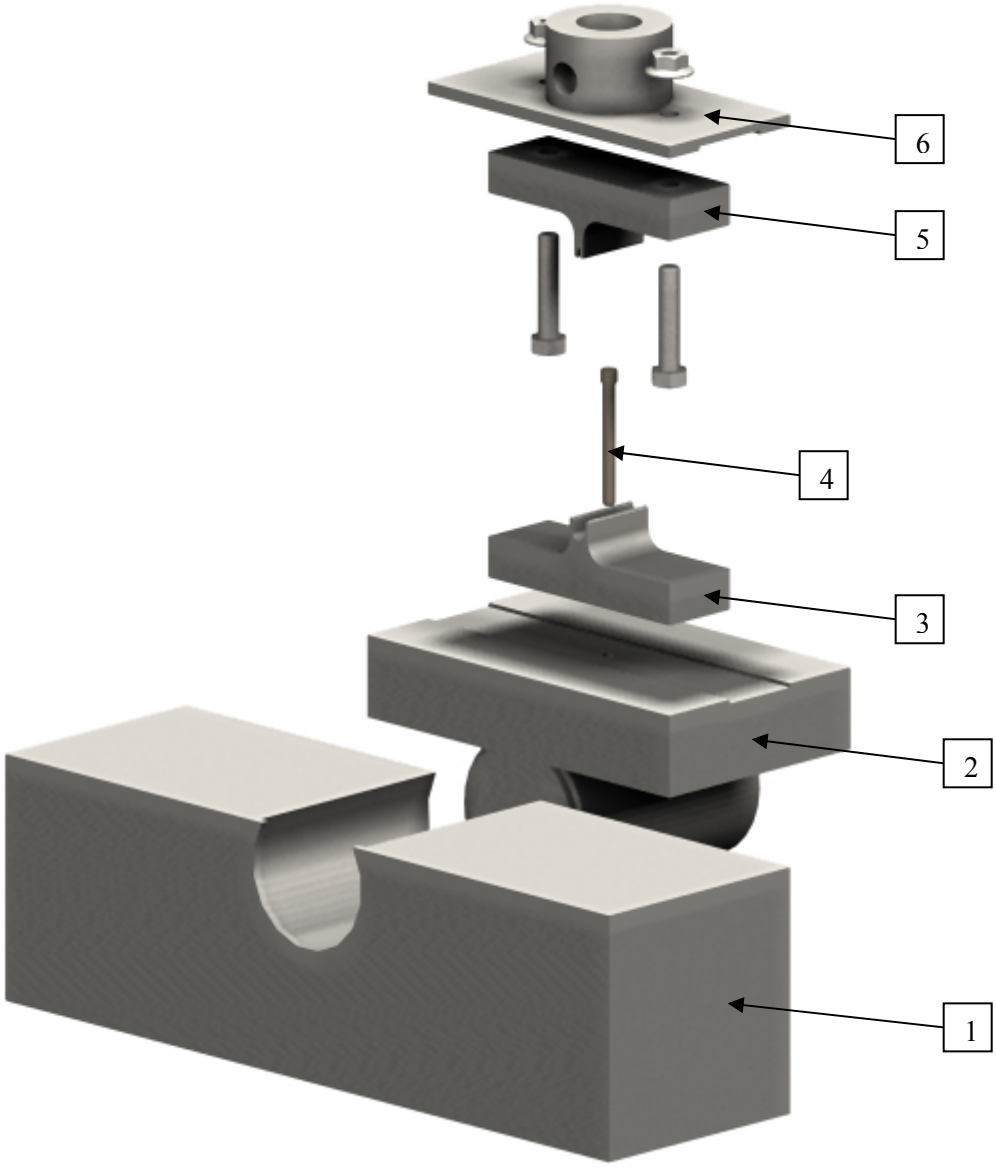

Figure 6.1.5 – Small specimen flexural test rig, exploded view. Rendered image produced in Solidworks Education Edition.

Figure 6.1.5 depicts the design for the 3-point flexural test rig which is constructed from essentially six individual components:

1. The base – this is the component that is located centrally on the bed of the tensile test machine and provides stability for the whole rig. It is machined from a solid block of mild steel to ensure rigidity and its dimensions allow it to fit comfortably within the confines of the tensile test machine (images of this are shown in Chapter 6.3 – Experimental Methods).

2. Auto-levelling mechanism – through creating a cylindrical joint for connection to the base, a mechanism is formed that causes the rig to level itself and maintain a uniform load across the test specimen when the test is in progress. The section can be easily disconnected from the base and replaced with an alternative component for the larger samples. The channel cut into the surface of this piece allows easy location of the next component and prevents any lateral movement of the section of the test rig.
3. Specimen support – an interchangeable component that works in conjunction with the one above it to apply the loads for the 3-point and 4-point flexural tests. This component is machined to a specific size for an individual small scale specimen (the one depicted is for the 3 mm x 3 mm x 10 mm 4-point flexural test specimens). Once the specimens become greater than 50 mm in length an alternate method of support is used (detailed later in this section).
4. Locating pin – this is a simple pin that locks the specimen support and locates it in the centre of the test rig.
5. Load applicator – this is another interchangeable component, its dimensions determined by the specimen size to be tested. It is fixed into the grooved section above through the use of two bolts which keep it securely fixed and centrally located (further detail on parts 3 and 5 of the rig follows this section).
6. Load cell connector – this connects directly to the load cell of the tensile test machine. It was designed to be relatively light weight as it was to be used for the flexural testing of the smaller specimens, and therefore would be connected to a more appropriate load cell (there were three different types of load cell available, 2.5 kN, 5kN and 50 kN) for the test being performed.

Several different sized specimen support and load applicators were designed to hold the smaller sized samples as all specimens below 50 mm in length could not be supported and loaded correctly on the larger scale rig (in accordance with the specifications for 3-point and 4-point flexural testing). An example of the 3-point flexural test specimen support and load applicator is shown in Figure 6.1.6. The tips of the "knife-edges" (the points of contact for the loading of the specimens) were created as radii to give a point contact with the specimen and not distribute the load over a larger than necessary area.

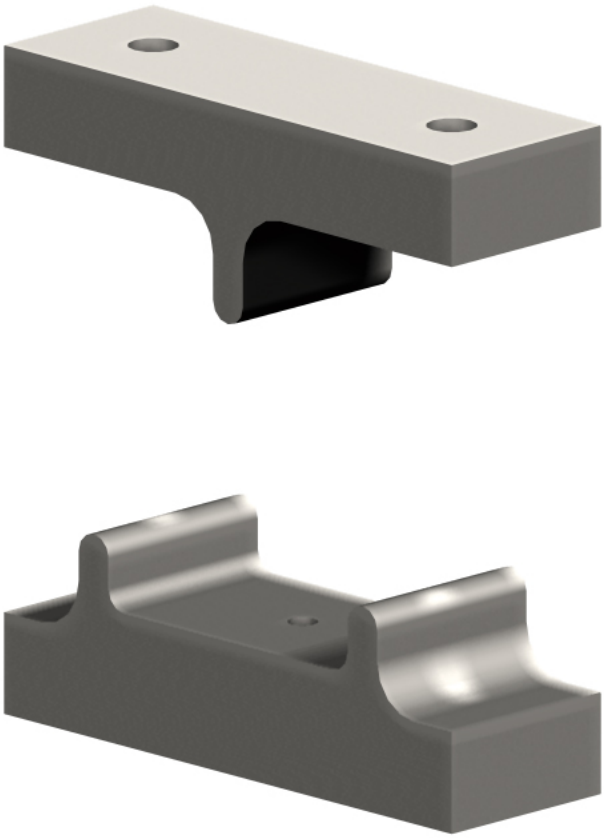

Figure 6.1.6 – Example 3-point flexural test specimen support and load applicator. This particular example is for a 40 mm length sample.

For the larger test specimens, a different approach to the design of the rig was required. An adjustable rig capable of accommodating more than one size of specimen was preferred as it would reduce the amount of time taken for the set up of the equipment between tests. Figure 6.1.7 shows the design for the lower section of the adjustable test rig. It can be seen that the base is the same as the previous rig, but connected to this is a platform with an adjustable span mechanism. Through simply rotating the handle and the incorporation of clockwise and anti-clockwise threads, the span can be increased or decreased accordingly. The specimen supports themselves are rollers mounted on top of this mechanism, and are free to rotate providing minimal contact with the sample during the testing process. Figure 6.1.8 shows the upper section of this design, and it is the same mechanism and construction as the lower section, with the exception that it connects directly to the load cell (it can only be connected to the 50 kN load cell due to the weight of the device).

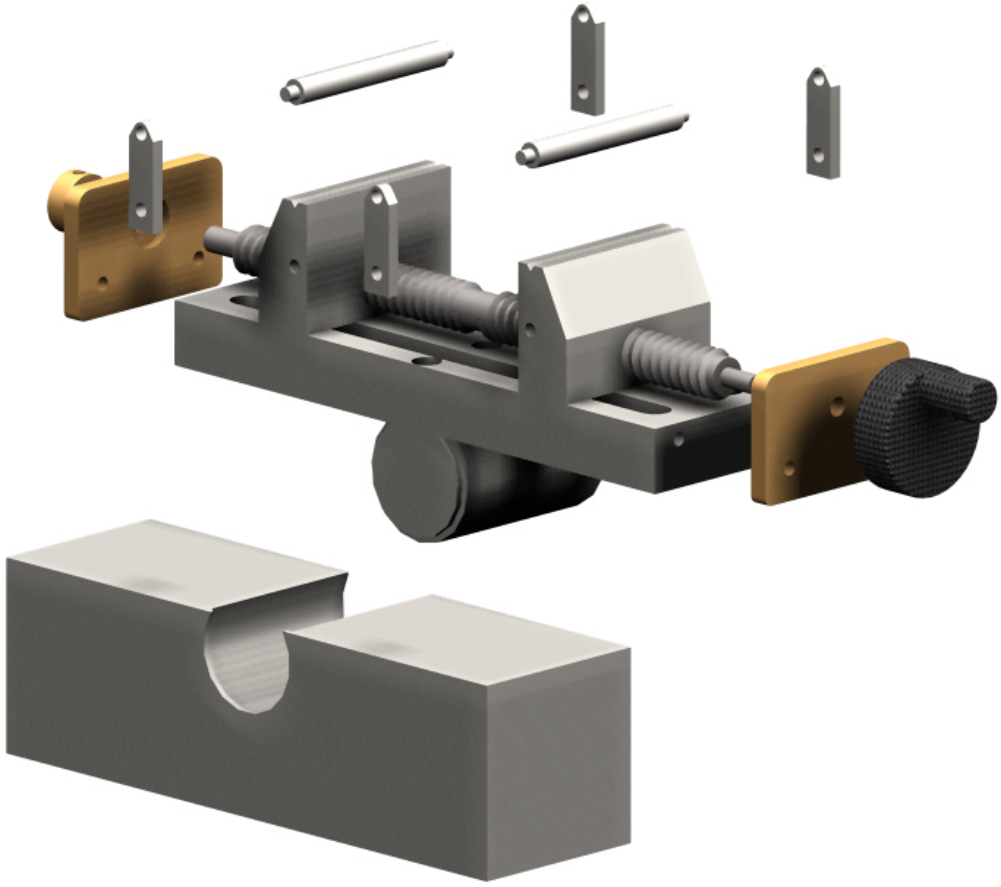

Figure 6.1.7 – Adjustable flexural test rig, lower section exploded view. It can be utilised for both 3-point and 4-point flexural tests for samples greater that 50 mm in length.

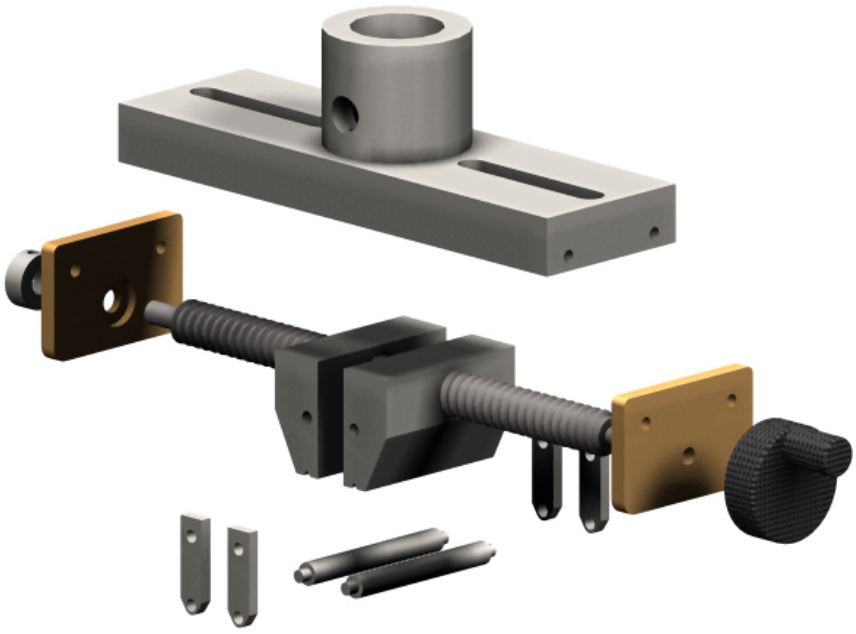

Figure 6.1.8 – Adjustable flexural test rig, upper section exploded view. This can only be used for 4-point flexural tests for samples greater than 50 mm in length.

A combination of the lower section of the adjustable flexural test rig and the upper section of the smaller test rig could be used for the 3-point flexural testing of the samples greater than 50 mm in length. And indeed, the rig was designed so that the interchangeable components allow for the successful testing of the various specimens sizes determined by the DoE matrix. Figure 6.1.9 is a rendered image simulating the adjustable 4-point flexural rig performing a test on a 9.49 mm x 9.49 mm x 100 mm sample to indicate how the finished product would appear.

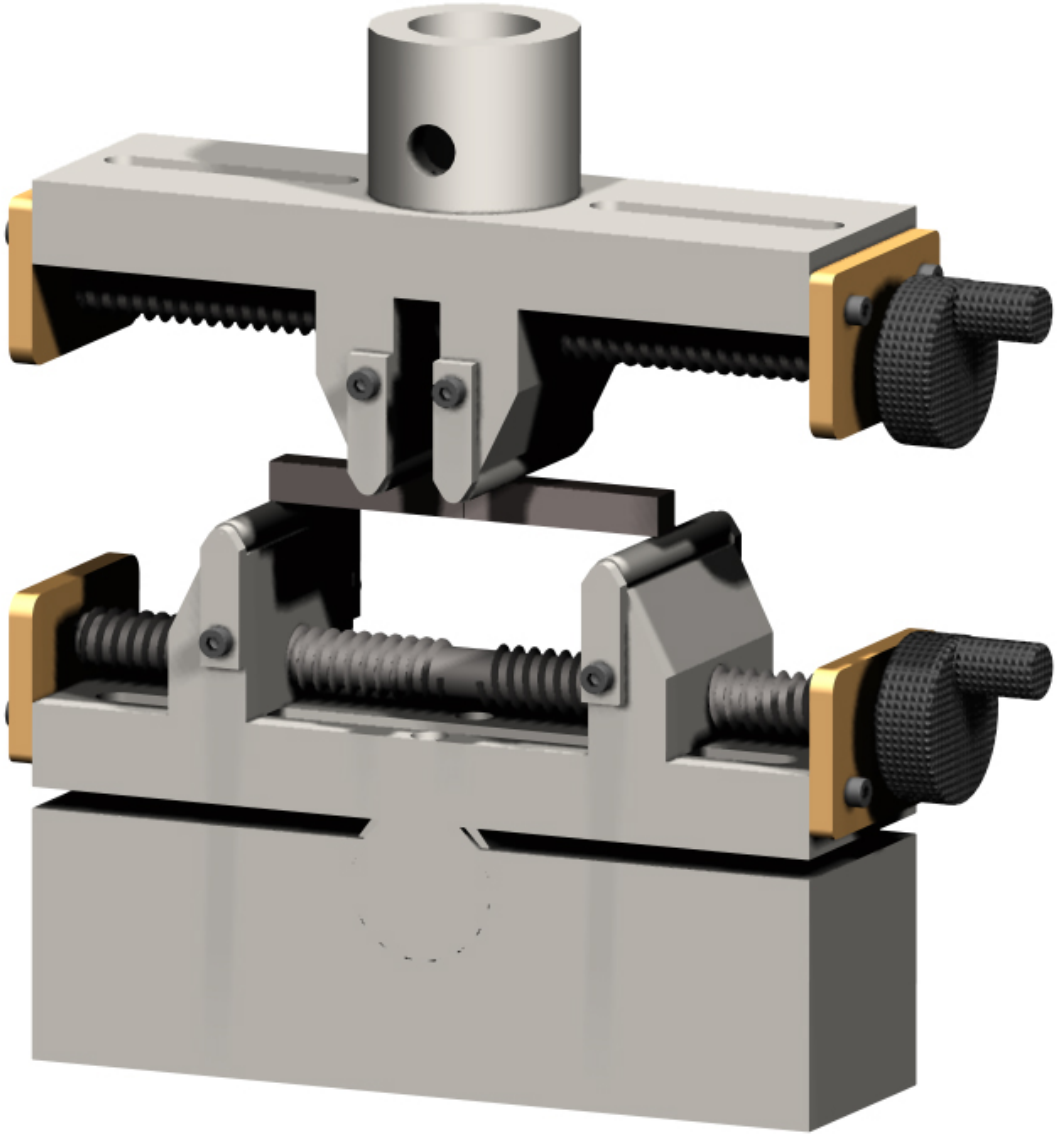

Figure 6.1.9 – Solidworks rendered image of the finished adjustable 4-point flexural rig design including graphite specimen.

Manufacture of the test rig and components was performed in-house at minimal cost and with a production time of approximately 6 weeks. The material selected for the majority of components of the rig was mild steel as it was available in abundance within the machine shop and is suitable for the needs of the equipment and the experimentation. The exceptions in material selection were for the end plates that hold the adjustable span mechanism in place, brass was selected for this due to its lower friction coefficient, and plastic handles were purchased to fit the device as it was more cost effective than manufacturing them. All working drawings for the design of the test rig and its components can be seen on the CD-ROM Appendix D.

6.2 Microscopy

In order to understand the structure of the materials being tested, a number of examinations were made, beginning with a standard optical analysis of the microstructure of both R4340 and IM1-24 graphite. Fractured specimens were taken from the testing programme and reused for the microscopic examination, with both graphites having transverse and longitudinal samples prepared.

The samples for both graphite types were prepared for examination using a procedure based on the Struers methodology for graphite specimens. Initially the samples were cleaned by being placed in an ultrasonic bath for a short time in order to remove any loose particles from the surface of the pores, and were then dried in an oven at 60º C. The IM1-24 graphite specimens were simply set in epoxy resin prior to the polishing process, whereas the R4340 samples were vacuum impregnated. To ensure the resin penetrated the graphite fully, a low viscosity epoxy resin with a long curing time was mixed with the hardener and the mixture out gassed with the samples in a vacuum chamber for approximately two hours. Once the impregnation was complete the specimens were placed in a steel chamber that was pressurised to between two and three bar, which has the effect of ingressing the resin further into the samples. The resin was fully cured after 24 hours and then the samples were then ground and polished in accordance with the method detailed in Table 6.2.1.

Stage	Surface	Lubricant	Abrasive Size	Time	Force	Speed	Rotation
Coarse/ Planar Grinding	SiC Paper	Water	1200 Grit SiC	Until Plane	3lbs per sample	240 rpm	Comp
Fine Grinding	SiC Paper	Water	2400 Grit SiC	2 mins	3lbs per sample	240 rpm	Comp
Coarse Polishing	Chemotextile Cloth	-	3um Diamond Suspension	5 mins	3lbs per sample	120 rpm	Comp
Fine Polishing	Imperial Napped Cloth	-	1um Diamond Suspension	1 min	3lbs per sample	120 rpm	Comp
Final Polishing	Imperial Napped Cloth	-	0.1um Colloidal Silica	30 secs	2.5lbs per sample	120 rpm	Cont

Table 6.2.1 – Sample grinding and polishing procedure.

As outlined in Table 6.2.1, there are five stages in total that the prepared specimens undergo to be polished for microscopic examination. Planar grinding is used to ensure the sample surface is level and the rotation of the SiC paper is complementary to that of the specimen (*i.e.* they are both rotating in the same direction). Fine grinding follows this to smooth the surface in preparation for the polishing process. For graphite, the polishing process consists of three stages, each using a specific cloth with an abrasive solution applied. The first two stages use a diamond suspension solution and are performed, again, complimentary to the rotation of the specimen. The final stage employs a silica solution that is softer than the diamond solution and provides the final polish of the specimen surface. The polishing disc with the attached napped cloth is rotated contrary to the specimen in this stage (*i.e.* in the opposite direction of rotation). All polishing processes were performed on a Beuhlar Metaserv Motapol 12.

For the inspection of the prepared samples, a Nikon Optiphot-2 optical microscope equipped with 5 x, 10 x, 20 x, 50 x, and 100 x magnification lenses connected to a JVC TK-1280E camera was used. The specimens were mounted on glass slides using a custom designed rig that ensured the surface to be viewed was parallel to the microscope table. A Sony DKR-700P minidisc recorder was connected to the camera to save the images. The following images (Figures 6.2.1 to 6.2.9) are micrographs taken

during the examination of the two graphite materials. The main features of the microstructure of IM1-24 graphite can be seen here, those being the spherical Gilsocarbon particles situated within a binder phase that contains a pore network. The Gilsocarbon particles are situated at random throughout the material and vary (though not greatly) in size and shape. These particles contain closed pores (*i.e.* they are not connected to the pore network in the binder) that are formed during the calcination process and are the result of volumetric shrinkage of the bulk material. Surrounding the Gilsocarbon particles is the coal tar pitch used as the binder, which contains an open pore network that is formed by the release of volatiles during the baking process. Mrozowski (1954) postulated that the globular pores present in the binder are connected by shrinkage cracks formed as the material cools and contracts after graphitisation. The size, shape and connectivity of the porosity is dependent on the volatiles being released and as such has no distinct pattern to it and cannot be controlled or defined to any suitable degree.

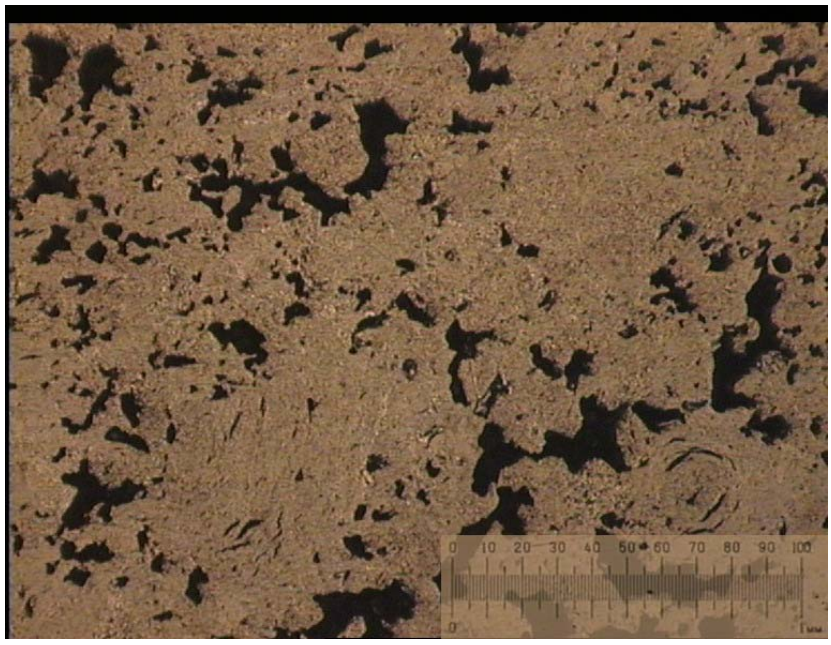

Figure 6.2.1 – Micrograph of an IM1-24 graphite specimen showing pore distribution and variation in pore size.

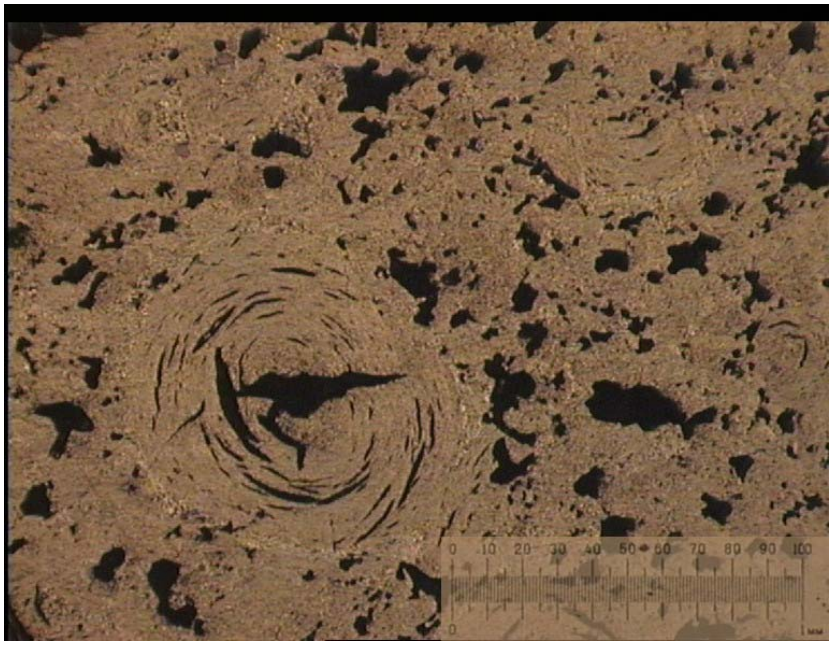

Figure 6.2.2 – Micrograph of an IM1-24 graphite specimen showing an example of a Gilsocarbon particle containing substantial porosity and Mrozowski cracks.

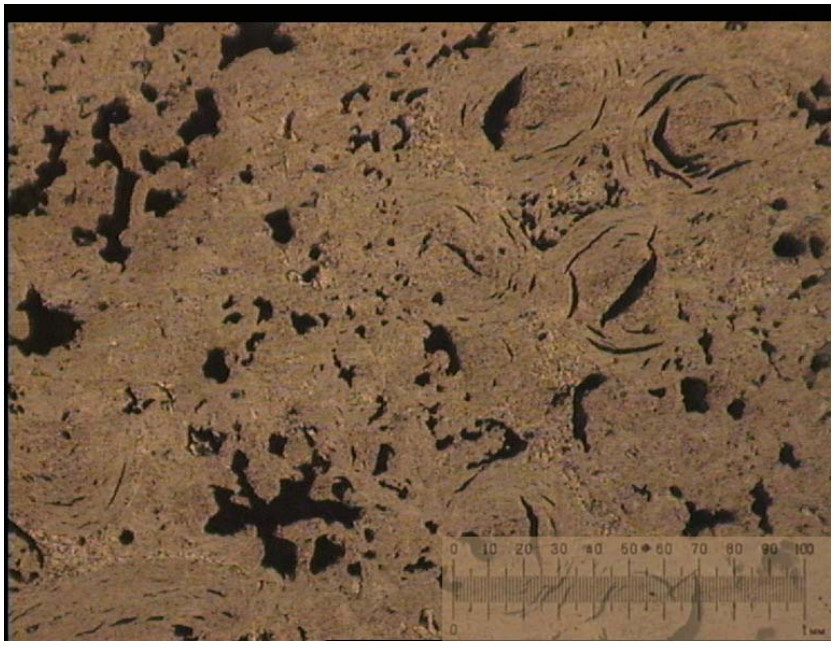

Figure 6.2.3 – Micrograph of an IM1-24 graphite specimen showing an example of a cluster of Gilsocarbon particles and their distribution through the material.

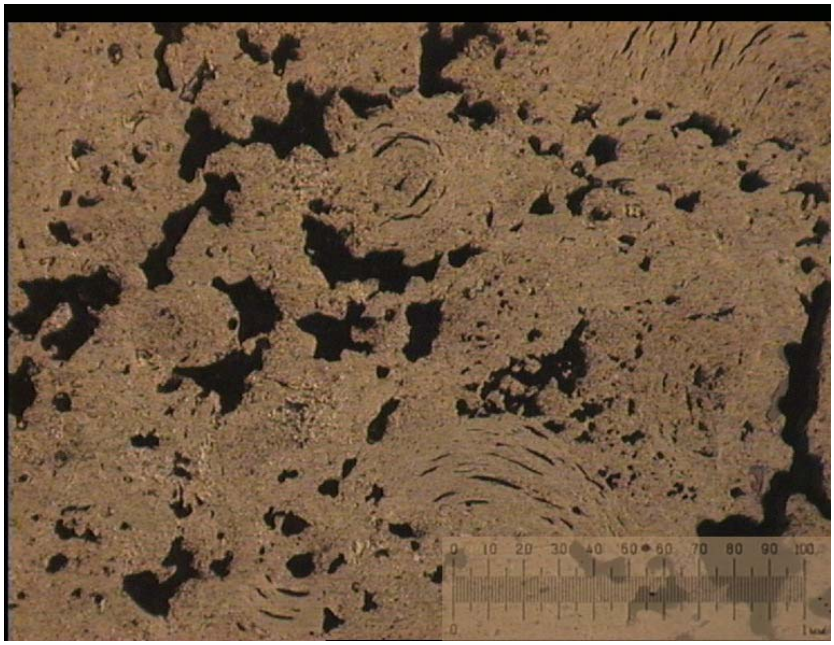

Figure 6.2.4 – Micrograph of an IM1-24 graphite specimen showing an example of large pores surrounding a small Gilsocarbon particle.

The structure of the R4340 graphite is very different to that of the IM1-24 even though they are essentially produced in the same way. As it is a much finer grained material (the smaller particles facilitating the ease with which volatiles are released via the fine pore network developed during the isostatic moulding of this graphite), the pore structure is not as prevalent. It also uses a different carbon filler particle that is much smaller in size that the Gilsocarbon particles and appear to be semi-elliptical in shape. The specific material used is unknown as SGL Carbon did not divulge this. Once again, it is difficult to precisely define the structure of any graphite, and Figure 6.2.6 shows this in that an unusually large pore is present in the sample being observed. As this was the only example seen in the structure it is almost impossible to quantify how often this occurs, but it is assumed that this is an abnormality and that the microstructure is generally considered to be homogenous compared to IM1-24.

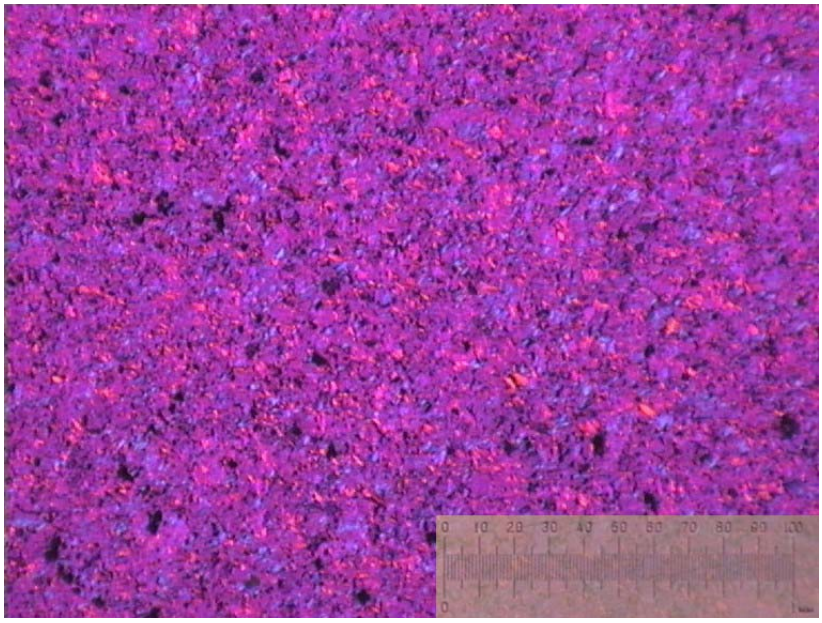

Figure 6.2.5 – R4340 graphite under polarised light illustrating the microstructure of the material.

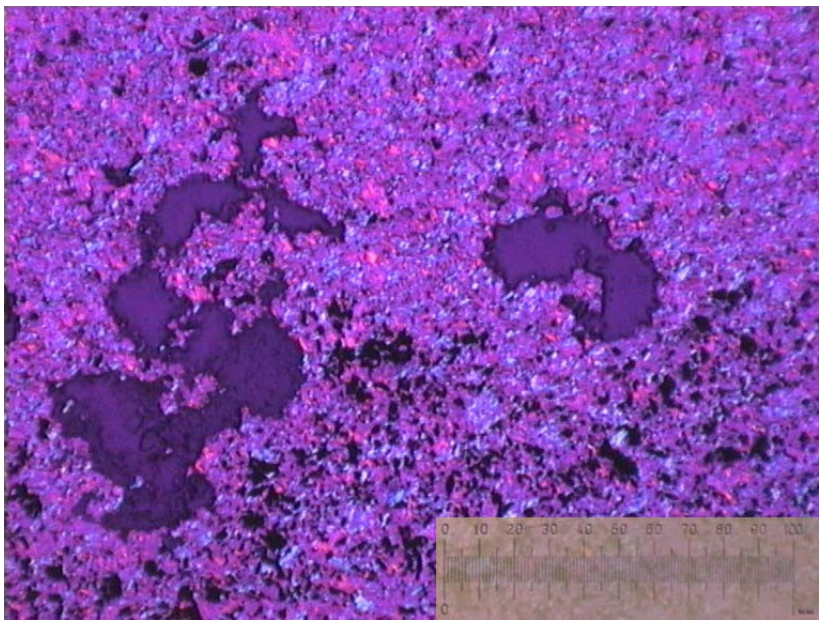

Figure 6.2.6 – R4340 graphite under polarised light depicting an abnormally large pore structure (in comparison with other specimens).

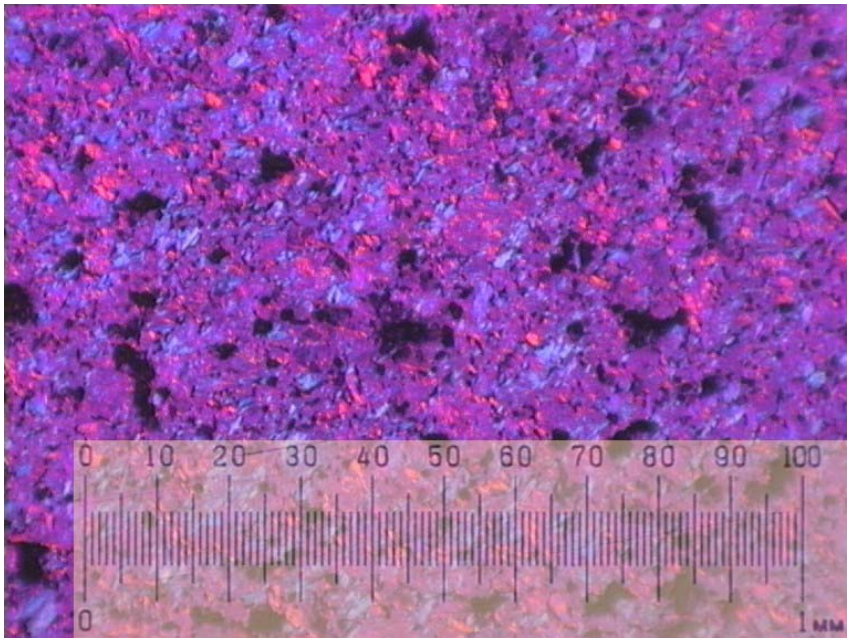

Figure 6.2.7 – R4340 graphite under polarised light illustrating the pore size relative to the grain size.

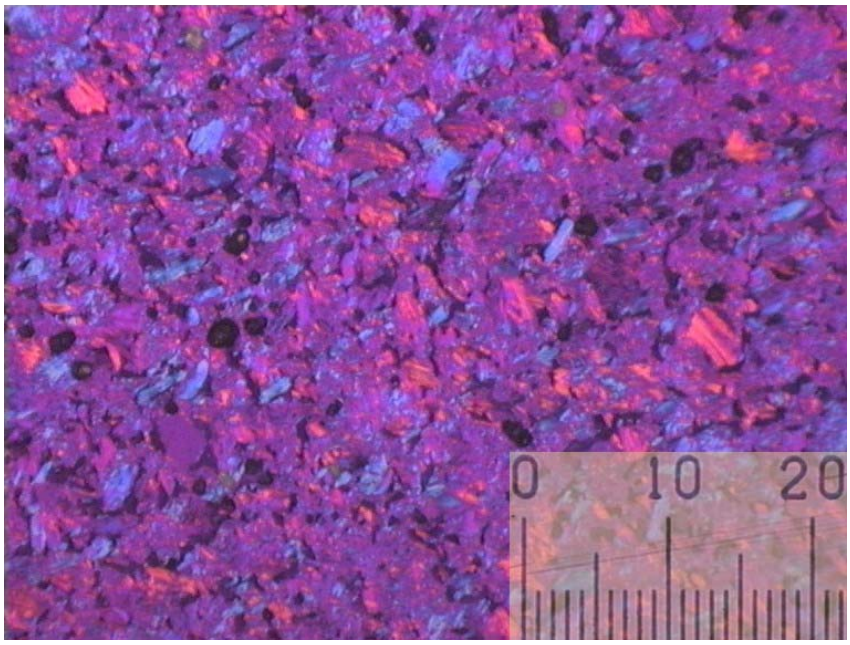

Figure 6.2.8 – R4340 graphite under polarised light showing the arrangement of the grains within the microstructure.

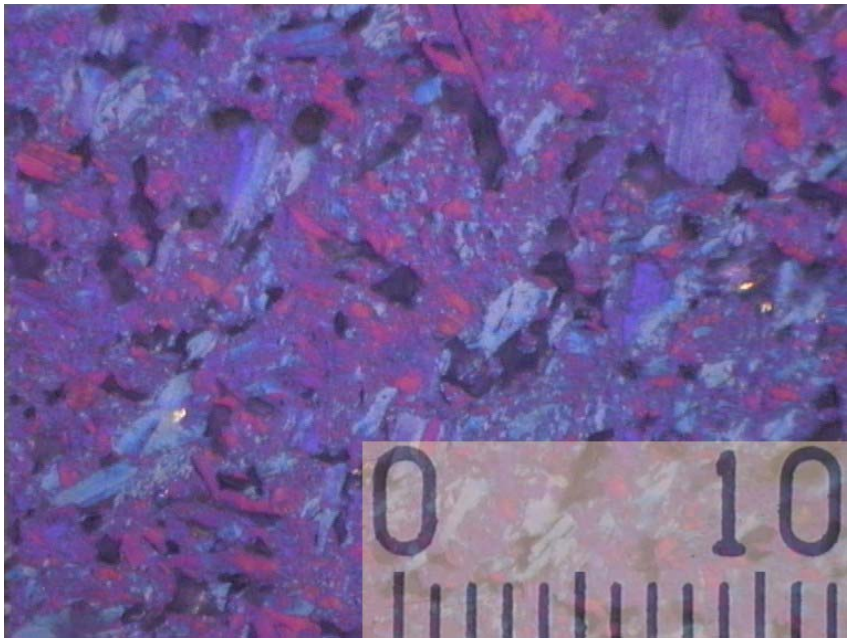

Figure 6.2.9 – R4340 graphite under polarised light showing a highly magnified image of the grains.

In addition to the optical microscopy, samples of the two types of graphite were viewed with a Cambridge S200 scanning electron microscope (SEM) which was connected to a Link analytical QX2000 X-ray analyser that enables a compound breakdown of the substances that constitute the specimens being examined. This was primarily done in order to accurately examine the notches present in half of the 3- and 4-point flexural test specimens to ensure they had been produced correctly and would provide the desired result.

Figures 6.2.10 to 6.2.13 are typical examples of the images recorded during this inspection and depict the profile of the notches machined into the specimens.

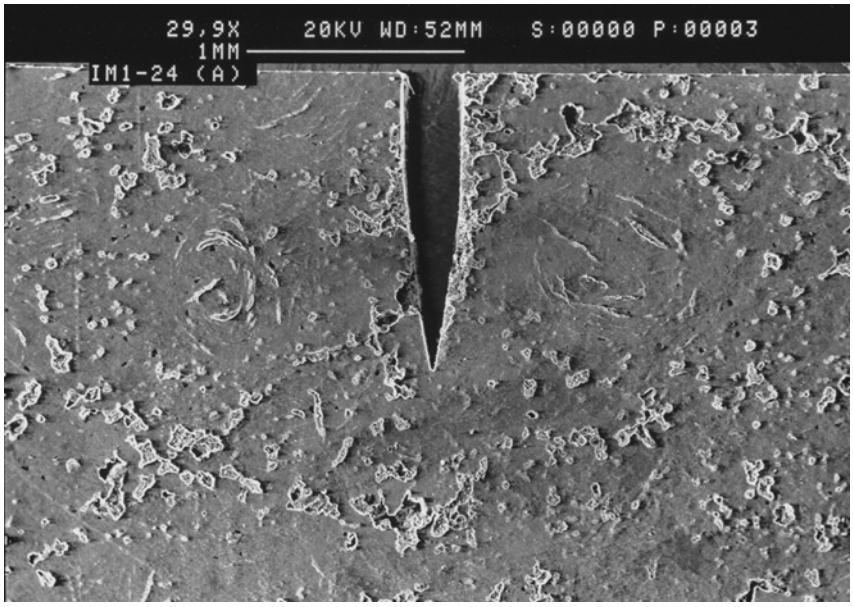

Figure 6.2.10 – IM1-24 graphite, *A* specimen (3 mm x 3 mm x 10 mm) notch.

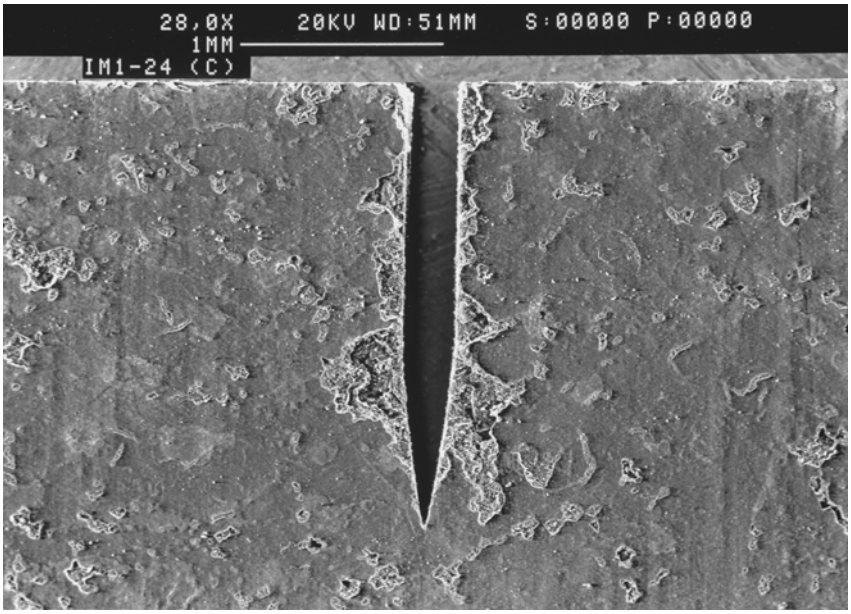

Figure 6.2.11 – IM1-24 graphite, *C* specimen (4.74 mm x 4.74 mm x 40 mm) notch.

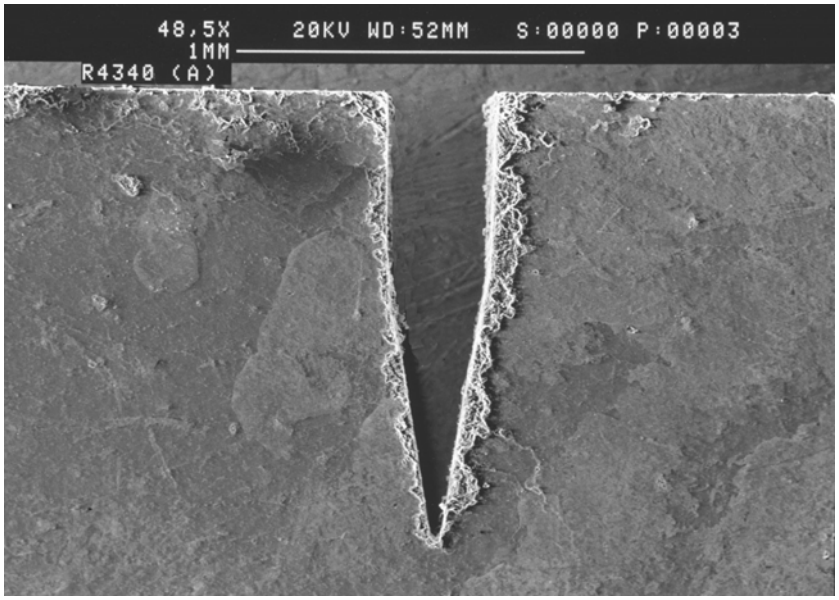

Figure 6.2.12 – R4340 graphite, *A* specimen (3 mm x 3 mm x 10 mm) notch.

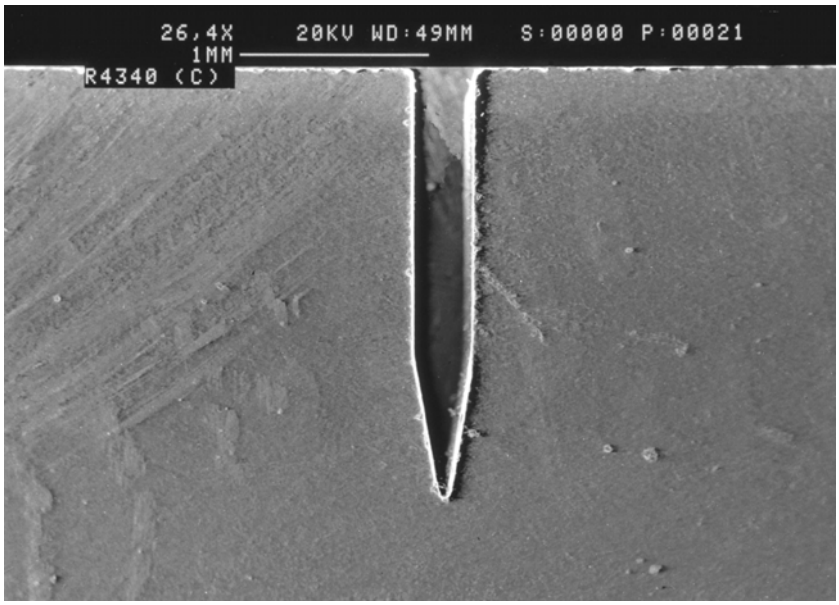

Figure 6.2.13 – R4340 graphite, *C* specimen (4.74 mm x 4.74 mm x 40 mm) notch.

It is apparent on comparison of the two types of graphite from both the optical and scanning electron microscopy that they differ greatly in their appearance and their microstructure. The R4340 graphite is a much finer grained material than the IM1-24 graphite, having an almost "glassy" finish to the surface when viewed in normal light. Although it is easier to machine and produces more sharply defined edges than the IM1-24 graphite, it can be seen from Figures 6.2.12 and 6.2.13 that some damage is caused

to the exterior of the material during the notching process. However, the notching process of the IM1-24 graphite causes much more damage to the surface of the material, but it is not known at this time how this can be avoided due to the small size of the specimens and the nature of the microstructure. An interesting observation (in Figure 6.2.10) is that the Gilsocarbon particles that can be seen clearly at the surface of the graphite (which are typically < 0.5 mm) appear to be not much smaller than the depth of the notch. This image highlights the small scale of the samples being used in the testing programme, and the difficulty in gaining a true value of material strength at this scale as it is not wholly representative of the bulk material.

The notches were cut into specimen sizes *A* to *E* for both types of graphite by SGL Carbon during the manufacture process. A 0.3 mm thick slitting saw blade was profiled in order to produce the tip of the notch, and all notches were cut to half the depth of the specimen. SGL Carbon were unable to cut notches into the size *F* samples (19 mm x 19 mm x 40 mm) stating that their equipment was unable to perform the task. The remaining samples were notched in the University of Hulls' engineering workshop using the same technique as SGL Carbon, but with a 0.6 mm thick profiled slitting saw. Several other methods for cutting the notches were tried first in order to maintain the same notch width for all the specimens however, the correct geometry of the notch tip could not be achieved and a compromise had to be reached. Figure 6.2.14 and 6.2.15 depict notches cut by spark erosion and through using a saw to cut to the required depth before attempting to profile the notch tip with a razor blade, and display the inaccuracy that would be inherent in the flexural testing as neither produces the required notch profile.

Comparing these with the notches cut with the 0.6 mm profiled slitting saw (Figures 6.2.16 and 6.2.17) it is clear that this was the optimal method for creating the required geometry. However, it can be seen that creating a perfect notch tip in IM1-24 graphite is very difficult due to particles of Gilsocarbon being extracted during the cutting process as can be seen at the notch tip in Figure 6.2.16, leaving an uneven section of material at this point. It should be noted that this image is not of an actual test specimen, but is waste material used for practice to create the notch profile, and the damage either side of the notch represent markings to ensure the notch is perpendicular to the horizontal axis.

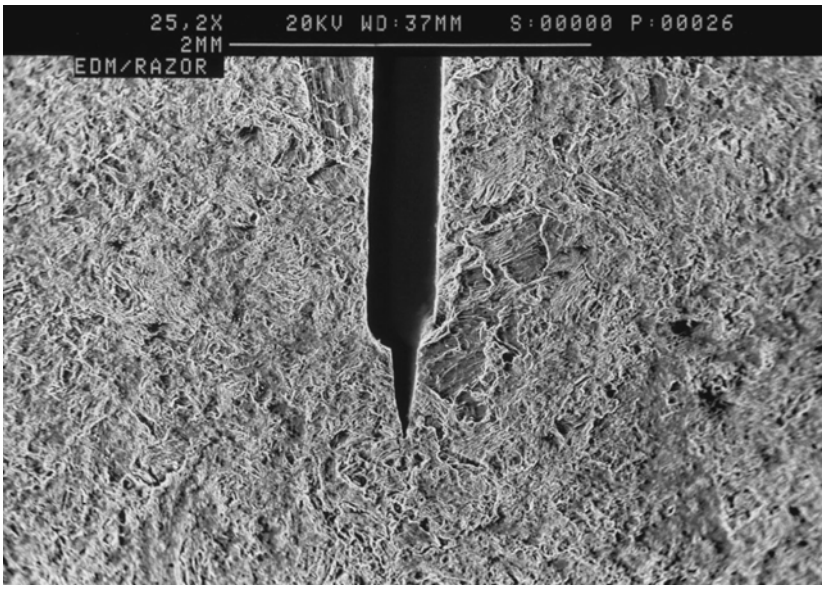

Figure 6.2.14 – Spark erosion cut notch with razor sharpening of the tip.

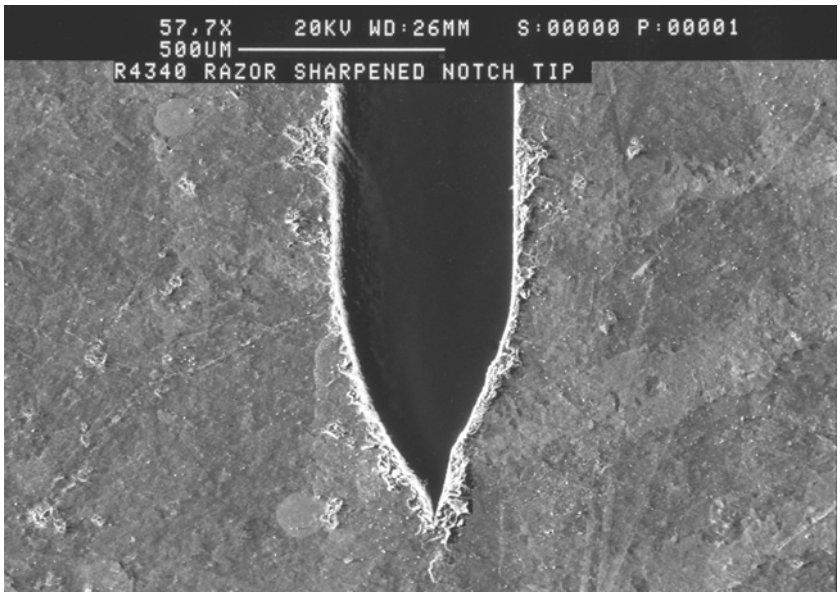

Figure 6.2.15 – Saw cut notch with razor sharpening of the tip.

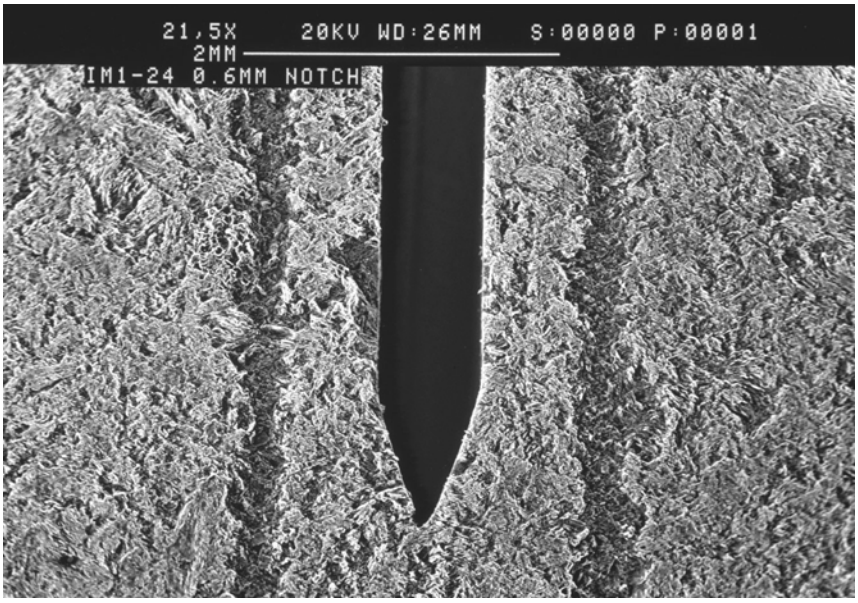

Figure 6.2.16 – *F* specimen notch tip created with a 0.6 mm profiled slitting saw. Filler particle extraction is observed at the notch tip.

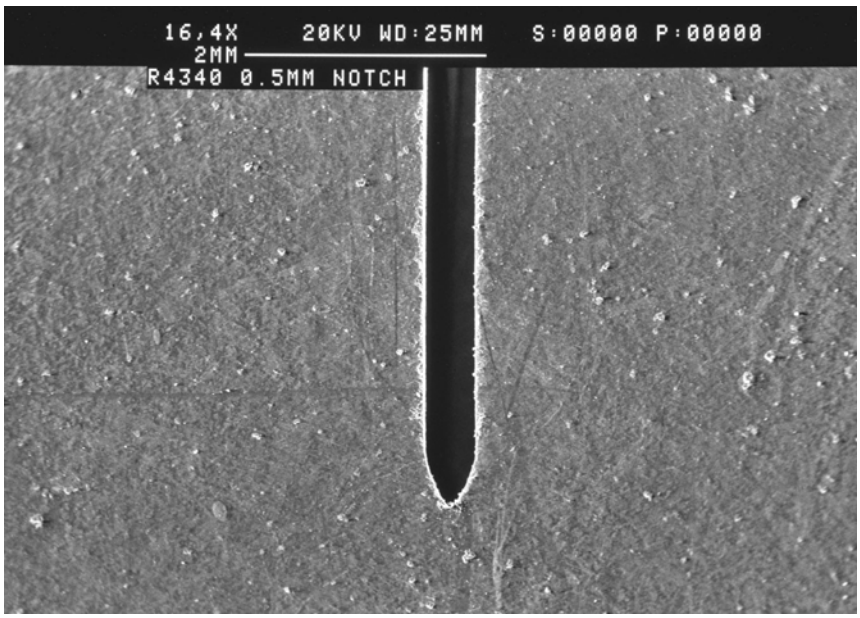

Figure 6.2.17 – *F* specimen notch created with 0.6 mm profiled slitting saw.

The testing programme required a reference material so that the trend observed for the IM1-24 graphite could be compared to another material with a homogeneous microstructure that would then enable any effects attributed to the material (or otherwise) to be quickly identified. That is, the effect of scale for the graphite specimen studied can be normalised against a reference material. Should the need arise, the behaviour of related graphites and other materials can be evaluated at a later date.

6.3 Experimental Methods

In order to complete the mechanical testing programme, six hundred samples of differing geometries were tested to destruction in several ways:

- Compression
- 3-point flexural (notched and unnotched)
- 4-point flexural (notched and unnotched)

This allowed the collection of a large amount of data to be used as validation for the abstract modelling of the microstructure of graphite. It also acted as a further investigation into the behaviour of graphite as specimen size is increased to expand the information available in this area. The following is a summary of the results obtained from the testing programme for IM1-24 and R4340 graphites.

On the completion of the manufacture of the testing rig and receipt of the graphite specimens the experimental programme could begin in earnest. The first step was to catalogue the dimensions of each of the specimens for both types of graphite by measuring the length, width, height and weight of each. Every specimen was given a reference number, *e.g.* the 3 mm x 3 mm x 10 mm *A* IM1-24 specimens were given the reference *A01*, *A02*,…,*A10*; whilst the same size for the R4340 were given the reference *RA01*, *RA02*,…,*RA03*. Using digital Vernier callipers, three measurements were taken of the required dimension and the average calculated which would be used later in the determination of the material properties. Additionally, the volume and density were calculated for each individual specimen. The measurements taken are included for reference on the CD-ROM in Appendix D (IM1-24 Test Specimen Dimension.xls and R4340 Test Specimen Dimension.xls).

Once the dimensions of the specimens had been recorded the testing of each specimen under the required conditions could be performed. The equipment employed for the testing programme was a UKAS certified Lloyd Instruments EZ50 universal materials testing machine with an RS232 data acquisition link to a desktop PC using Nexygen (with the accompanying Ondio plug-in) software. The setup of the testing machine and

attached PC is shown in Figure 6.3.1. Nexygen software is Lloyd Instruments own test control and data processing system and is written specifically to work with their range of test machines, whereas Ondio is the plug-in for the software which allows the user to design and control tests specific to their requirements. The software facilitated very accurate control of the test through specifying the type of test being performed and setting conditions for the end of the test, in all cases reported on here the test was deemed to end with sample failure which was determined by Nexygen as when the current load was less than 10 % of the maximum recorded value. In addition to the control, the software also enabled accurate recording of the load and deflection data of the specimens during the tests, as well as providing a graphical display of the load/displacement curve as the test progressed that enabled the user to better observe the response of the material under loading.

Figure 6.3.1 – Lloyd Instruments EZ50 universal testing machine with data acquisition PC.

The three types of experiment being performed were standard compression, 3-pt flexural and 4-pt flexural tests. The platens used for the compression tests were supplied by Lloyd instruments with the EZ50 machine and were attached to the system via a 50 kN load cell, the selection of which was due to the expected high value of load to cause the failure of the specimens, and that the physical weight of the platens negated the use of the other load cells. Figure 6.3.2 depicts the setup of the compression test with a 3 mm x 3 mm x 10 mm specimen.

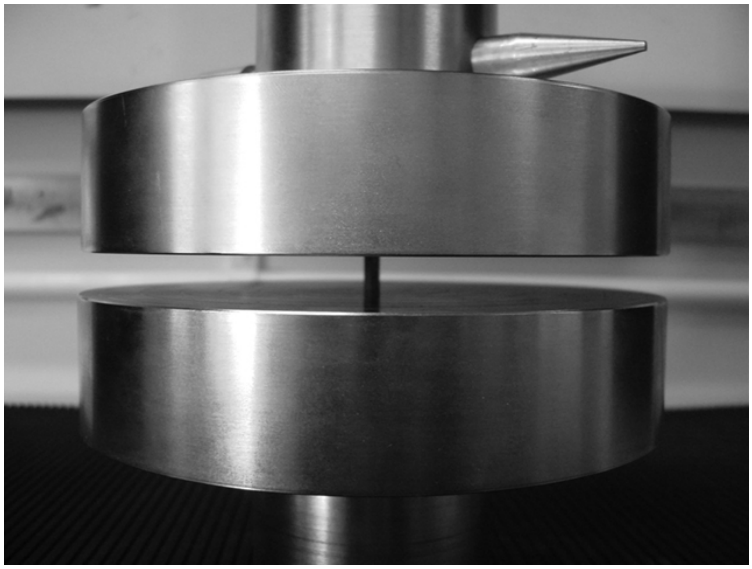

Figure 6.3.2 – 3 mm x 3 mm x 10 mm specimen compression test setup.

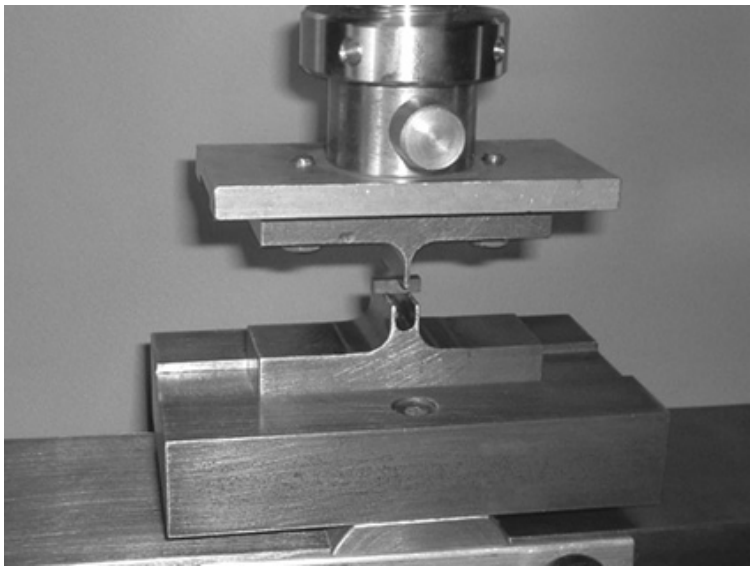

Figure 6.3.3 – 3 mm x 3 mm x 10 mm specimen 3-pt flexural test configuration.

For the 3-pt flexural tests, a number of configurations for the test setup were used. The adjustable test rig reported on in the previous chapter had been designed and manufactured, but the smallest specimen sizes could not be tested accurately on this. For specimen lengths under 50 mm, the interchangeable small scale supports were used with the upper load applicator attached to a 5 kN load cell. For the specimens of length equal to and greater than 50 mm, the adjustable support was used in conjunction with the 3-pt load applicator and 5 kN load cell. An example of the small scale specimen setup can be seen in Figure 6.3.3.

As with the 3-pt flexural tests, it was necessary to use a number of setup configurations to accommodate the differing specimen dimensions. As previously, for specimens less than 50 mm in length the small scale supports and load applicator were utilised with the 5 kN load cell. For the specimens equal to and greater than 50 mm in length, the adjustable test rig was used with the upper section connected to the testing machine via the 50 kN load cell (due to the weight of this section). This can be seen in Figure 6.3.4.

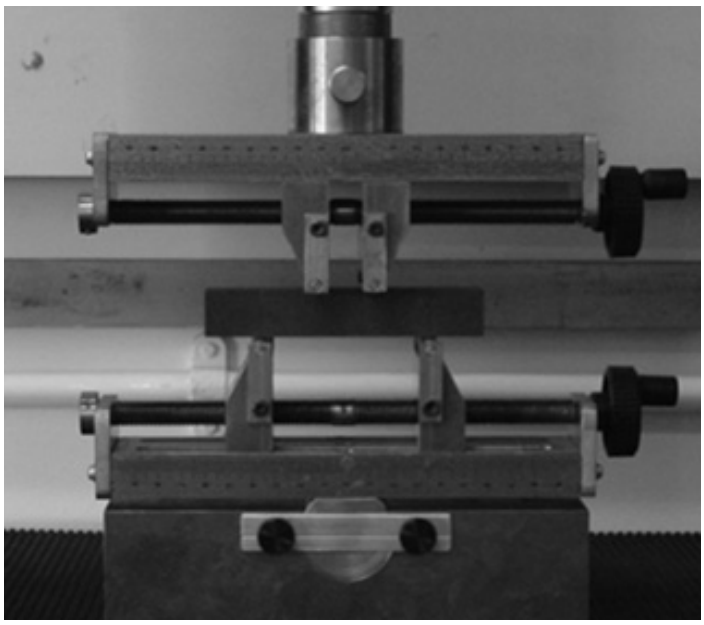

Figure 6.3.4 – 4-pt flexural test setup for specimens equal to and greater than 50 mm in length.

Although different types of setup were employed for testing the selection of specimen sizes, the executions of the tests were kept constant. The specimens were placed in the appropriate rig for the test (with the span being fixed for the tests with the adjustable rig) and the upper platen or applicator moved into contact with the upper surface of the specimen, ensuring that no load was applied before the start of the test. The Nexygen control system is able to register loads to less than 0.01 N, and therefore it was possible to ensure there was no significant loading prior to the test. The primary outputs from Nexygen are the load and deflection values for the duration of the test, with these being zeroed once the correct setup has been obtained. However, there was some fluctuation of the deflection reading prior to the commencement of testing depending on which load cell was being used, +/- 0.05 mm for the 50 kN load cell, +/- 0.03 mm for the 5 kN load cell. This fluctuation could not be eliminated unless a very small load was applied to the specimen, but as the loads required for failure were very small (especially in the case of the notched flexural specimens) this was unwise, and the fluctuation was deemed

acceptable as it did not interfere with the readings taken once the test started (*i.e.* maximum load and deflection were unaffected). A crosshead speed of 0.5 mm/min was defined for all tests. Once ready to begin the software requests the dimensions of the test specimen and takes control of the experiment until completion, upon which it will calculate the necessary parameters (such as compressive or flexural strength) based on the readings taken.

The information for each test was saved as a Nexygen specific batch file and the load/deflection curves printed. Although the automatic calculation of results is useful for the analysis, especially for the maximum load/deflection values, there were some functions Nexygen could not perform and, as such, raw data text files were produced for the notched specimen tests in order to calculate further parameters. The raw data is simply the load/displacement values given at set timed intervals through the test, with the user specifying the number of data points required. Graph 6.3.1 shows an example load/deflection curve created from one of the raw data files. The negative displacement values are due to the fluctuation mentioned previously and the movement of the crosshead before coming into full contact with the surface of the specimen. The software accounts for this in the report of the maximum values recorded (in that it will calculate the maximum displacement from the initial displacement value rather then from zero).

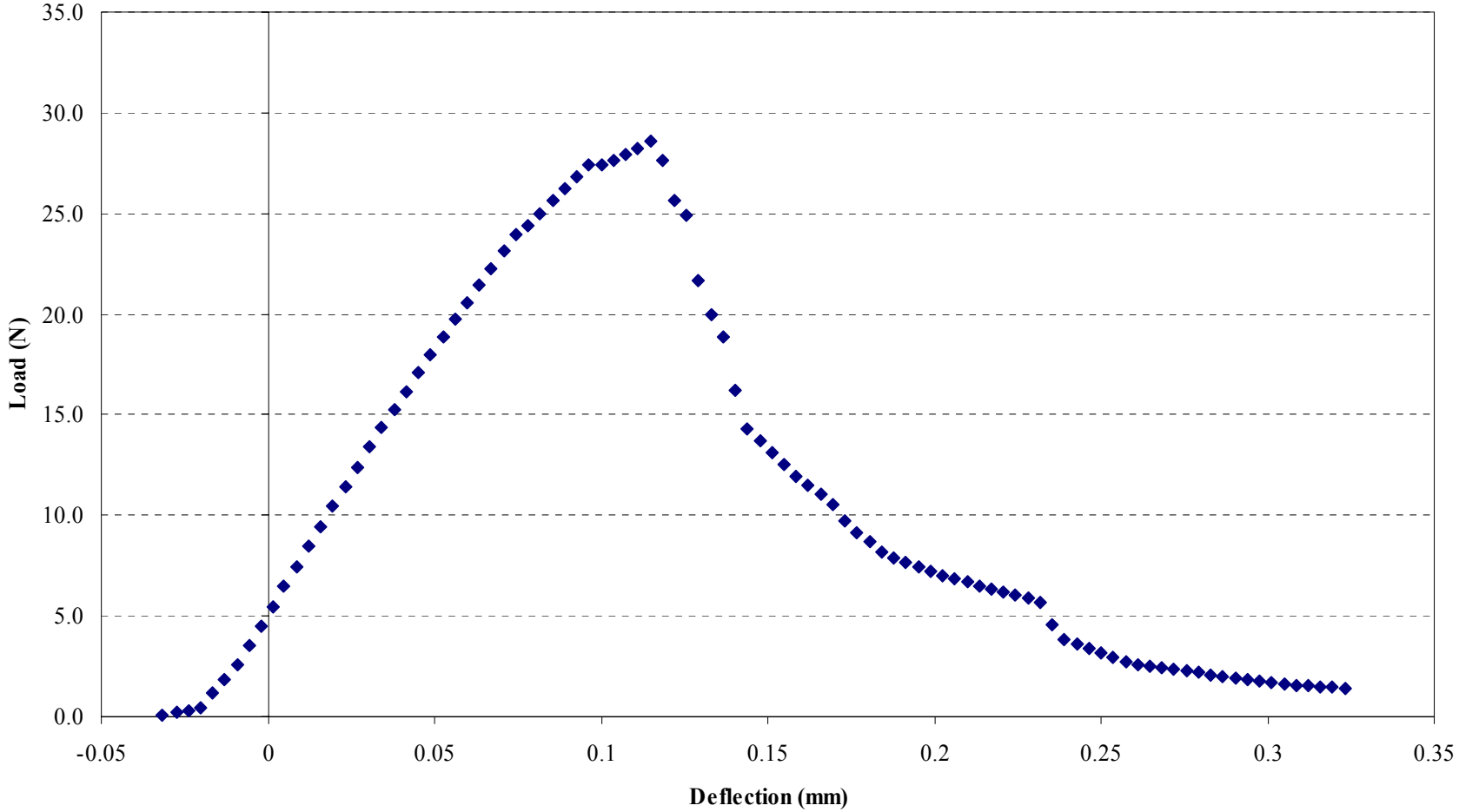

Graph 6.3.1 – Example load/deflection plot produced from the raw data from Nexygen (notched IM1-24 graphite, 4.74 mm x 4.74 mm x 40 mm, 4-pt flexural).

6.4 Key Equations

For processing the experimental data, the following calculations and information were used to for interpreting the results. The compressive strength was calculated using:

$$S_c = \frac{W_{\max}}{A_{\min}} \qquad \text{Equation [6.4.1]}$$

where W is the load and A is the cross-sectional area (ASTM C695).

For both the unnotched 3-pt flexural tests the following load spans were used, with the notch depths being associated to the notched version of the specimen:

Specimen Size	Notch Depth (mm)	Span (mm)
A	1.500	5.000
B	3.000	10.000
C	2.370	27.500
D	3.000	36.000
E	4.745	50.000
F	9.500	27.500

Table 6.4.1 – Notch depth and load span for the 3-pt flexural tests.

Similarly, for the 4-pt flexural tests:

Specimen Size	Notch Depth (mm)	Lower Span (mm)	Upper Span (mm)
A	1.500	2.00	5.00
B	3.000	4.00	10.00
C	2.370	10.00	27.50
D	3.000	12.00	36.00
E	4.745	20.00	60.00
F	9.500	10.00	27.50

Table 6.4.2 – Notch depth and load spans for the 4-pt flexural tests.

To calculate the additional parameters for the 3-pt flexural tests (stress, strain and Young's modulus of bending) the following equations were used:

$$\sigma = \frac{3WL}{2bh^2} \qquad \text{Equation [6.4.2]}$$

$$\varepsilon = \frac{6hD}{L^2} \qquad \text{Equation [6.4.3]}$$

$$E = \frac{WL^3}{4Dbh^3} \qquad \text{Equation [6.4.4]}$$

where L is the load span, b is the specimen width, h is the specimen depth and D is the deflection. The maximum values for the stress and strain were gained by using the values for the maximum load and maximum deflection, respectively.

For the 4-pt flexural tests, these equations become:

$$\sigma = \frac{3W(L_O - L_I)}{2bh^2} \qquad \text{Equation [6.4.5]}$$

$$\varepsilon = \frac{12hD}{2L_O{}^2 - L_I{}^2 + 2L_O L_I} \qquad \text{Equation [6.4.6]}$$

$$E = \frac{(W/D)(L_O - L_I)(2L_O{}^2 - L_I{}^2 + 2L_O L_I)}{8bh^3} \qquad \text{Equation [6.4.7]}$$

where L_O is the lower (or outer) span and L_I is the upper (or inner) span. The bending moment, M, calculations for both 3-pt and 4-pt flexural are the same:

$$M = \frac{¼Wg}{½L} \qquad \text{Equation [6.4.8]}$$

where g is gravity. Both the 3-point and 4-point flexural strengths are calculated using:

$$S_f = \frac{WL}{bd^2} \qquad \text{Equation [6.4.9a]}$$

where d is the thickness of the specimen, and Equation 6.4.9a is valid as long as the fracture occurs within the stressed volume between the load bearing supports and the test duration is greater than 5 seconds (ASTM C651, 1977). This equation is only applicable for load spans that are two thirds the length of the specimen. For load spans that are one half that of the specimen length, Equation 6.4.9b should be used:

$$S_f = \frac{3WL}{4bd^2} \qquad \text{Equation [6.4.9b]}$$

For the notched specimens the nominal stress required calculation:

$$\sigma_{(nom)} = \frac{3WL}{(b-a)^2 h} \qquad \text{Equation [6.4.10]}$$

where L is now the distance between the centre loading point and the outer support, and a is the notch depth. And for the 4-pt flexural tests this converts to:

$$\sigma_{(nom)} = \frac{3W(L_O - L_I)}{(b-a)^2 h} \qquad \text{Equation [6.4.11]}$$

The work of fracture here is determined as the work done (the area under the load/deflection curve) in creating the two fracture surfaces. The work done in this instance was calculated using a software program called Maths Helper Plus that had the facility to analyse complex shapes and determine the area. Using the raw data files from Nexygen and neglecting any data points after the maximum load had been reached (assuming that failure of the specimen occurred at this point), the data points were imported into the program and the area calculated and recorded. The work of fracture was calculated by dividing the work done by the fracture surface area. However, the effective surface energy, γ_F, was calculated using:

$$\gamma_F = \frac{U}{2b(h-a)} \qquad \text{Equation [6.4.12]}$$

where U is the work done (or energy under the load/displacement curve). The plane strain critical stress intensity factor (K_{Ic}) calculation was performed using the technique put forward by Brown and Strawley (1969). They suggested that for notched beams under 3-pt or 4-pt flexural loading:

$$K_{Ic} = Y = \frac{6Ma^{1/2}}{bh^2} \qquad \text{Equation [6.4.13]}$$

where M is the bending moment. This can also be expressed as:

$$Y = \frac{K_{Ic}bh^2}{6Ma^{1/2}} \qquad \text{Equation [6.4.14]}$$

and manipulated to become:

$$K_{Ic} = \frac{Y}{b\left(\frac{h^2}{6M\sqrt{e_i}}\right)} \qquad \text{Equation [6.4.15]}$$

where e_i is the effective notch depth and Y is given by:

$$Y = A_0 + A_1\left(\frac{a}{w}\right) + A_2\left(\frac{a}{W}\right)^2 + A_3\left(\frac{a}{W}\right)^3 + A_4\left(\frac{a}{W}\right)^4 \qquad \text{Equation [6.4.16]}$$

where a/W is the notch to depth ratio and A_0 = 1.99, A_1 = -2.47, A_2 = 12.97, A_3 = -23.17, and A_4 = 24.80, with all values being constants for pure bending.

Considering Weibull (1939) as discussed in Chapter 3.2, σ_u (the stress below which the failure probability is zero) is difficult to determine with any precision, especially for brittle materials, and is usually set to equal zero. With this as the case, the survival probability can be expressed as:

$$P_S(V_0) = \exp\left[-\left(\frac{\sigma}{\sigma_0}\right)^m\right] \qquad \text{Equation [6.4.17]}$$

where $P_S(V_0)$ is the survival probability (*i.e.* the fraction of identical samples, each of volume V_0, which survive loading to a stress σ); σ_0 is the characteristic strength of the distribution (a constant); and m is the Weibull modulus. Figure 6.4.1 shows a graph generated to illustrate the probability of survival versus the failure stress with varying Weibull modulus values (nominal values were used for σ and $\sigma_0 = 1$).

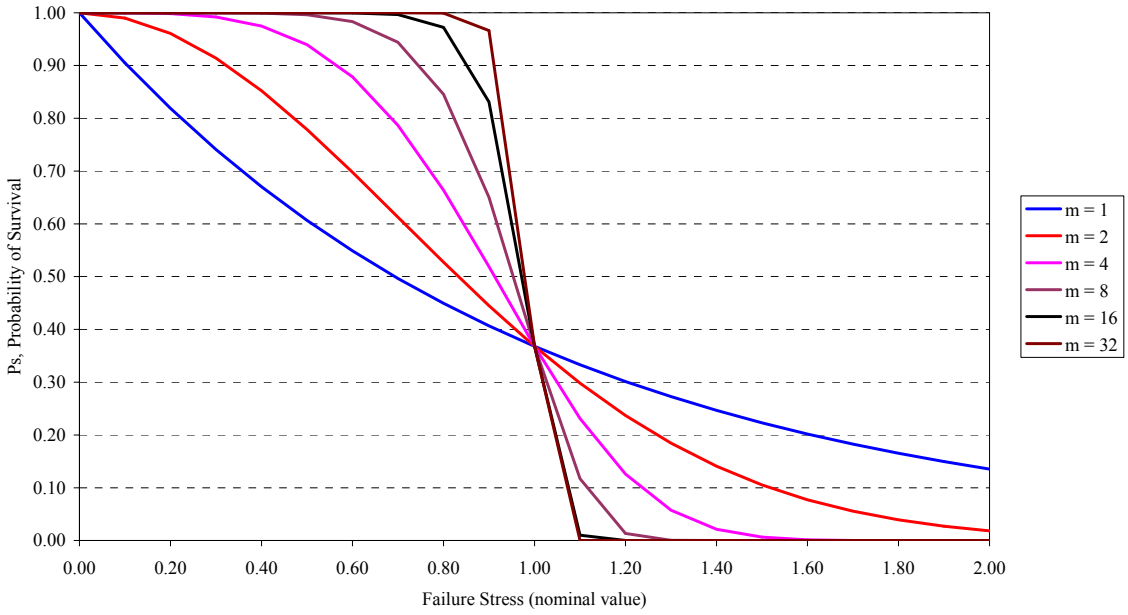

Graph 6.4.1 – Example of the effect of Weibull modulus on survival probability.

It is clear to see that with a higher Weibull modulus the material has a higher probability of failure over a lower stress range, *i.e.* when m is low, P_s reduces almost gently, when m is high, P_s reduces quite sharply. This shows that for materials with a low Weibull modulus, a large increase in stress does not necessarily mean the material will fail, whereas for materials with a high Weibull modulus, a small increase in stress can cause component failure.

Whilst it is not the intention to prove or disprove Weibull (1939), it is worth noting as many graphite studies have used Weibull as a guide when interpreting results (*e.g.* Brocklehurst (1974)).

6.5 Summary

Chapter 6 has detailed the development of a testing programme to comprehensively examine the affect of specimen size on the material properties of IM1-24 graphite and a reference graphite provided by SGL Carbon, R4340. The specimen type, quantities and sizes have been determined, and the key equations for the calculation of a number of material properties have been determined. In addition this, a 3-point and 4-point flexural test rig has been designed and manufactured that is capable of testing all the required specimen sizes. Issues arose in creating the notches in the largest volume specimen size (the 'F' size specimens). Several methods for producing the correct notch profile were investigated and each evaluated using scanning electron microscopy before selecting the most appropriate technique. In addition to the SEM examination, a number of samples of both types of graphite were examined under standard microscopy to identify the key microstructural features of each.

The results of the testing programme are detailed in the following section, Chapter 7 – Experimental Results.

Chapter 7 - Experimental Results

As detailed in Chapter 6 - Experimental Details, in order to complete the mechanical testing programme, six hundred samples of differing geometries were tested to destruction in several ways:

- Compression
- 3-point flexural (notched and unnotched)
- 4-point flexural (notched and unnotched)

This allowed the collection of a large amount of data to be used as validation for the abstract modelling of the microstructure of graphite. It also acted as a further investigation into the behaviour of graphite as specimen size is increased to expand the information available in this area. The following is a summary of the results obtained from the testing programme for IM1-24 and R4340 graphites.

7.1 Experimental Results

The following is a summary of the results obtained through the experimental programme. The results from the compression tests on the two types of graphite can be seen in Tables 7.1.1 and 7.1.2. The 3-pt flexural and 4-pt flexural results for the IM1-24 graphite can be seen in Tables 7.1.3 and 7.1.4, which are followed by the 3-pt flexural and 4-pt flexural results for the R4340 graphite in Tables 7.1.5 and 7.1.6. And finally, Tables 7.1.7 to 7.1.10 are the results for the notched IM1-24 and R4340 specimens. In each of the tables σ denotes the standard deviation across the ten specimens tested, and for easier reference the tests are colour coded: Compression tests are purple, 3-point flexural tests are blue and 4-point flexural tests are green.

Specimen Size	Maximum Load (N)	σ	Maximum Deflection (mm)	σ	Stress @ Max. Load (Pa)	σ	Strain @ Max. Deflection	σ	Young's Modulus (Pa)	σ	Compressive Strength (MPa)	σ
A	5.48E+02	47.551	0.319	0.056	6.02E+07	5.17E+06	0.032	5.55E-03	1.95E+09	4.06E+08	60.234	5.166
B	2.27E+03	131.242	0.569	0.030	6.30E+07	3.54E+06	0.030	1.59E-03	2.11E+09	1.38E+08	62.965	3.537
C	1.41E+03	48.922	0.811	0.052	6.27E+07	2.68E+06	0.020	1.29E-03	3.10E+09	9.62E+07	62.717	2.682
D	2.27E+03	75.281	0.999	0.036	6.31E+07	2.08E+06	0.020	7.20E-04	3.16E+09	1.13E+08	63.076	2.077
E	5.49E+03	154.140	1.703	0.059	6.04E+07	1.83E+06	0.017	5.90E-04	3.55E+09	1.13E+08	60.359	1.827
F	2.55E+04	962.270	1.831	0.057	7.07E+07	2.64E+06	0.046	1.42E-03	1.54E+09	5.11E+07	70.681	2.643

Table 7.1.1 – Summary of compression test results for IM1-24 graphite.

Specimen Size	Maximum Load (N)	σ	Maximum Deflection (mm)	σ	Stress @ Max. Load (Pa)	σ	Strain @ Max. Deflection	σ	Young's Modulus (Pa)	σ	Compressive Strength (MPa)	σ
A	9.44E+02	38.818	0.596	0.051	1.06E+08	4.45E+06	0.059	5.06E-03	1.79E+09	8.29E+07	105.804	4.447
B	3.34E+03	374.109	0.981	0.067	9.20E+07	1.05E+07	0.052	3.53E-03	1.80E+09	2.80E+08	92.040	10.472
C	1.95E+03	50.181	1.150	0.039	8.66E+07	2.26E+06	0.029	9.85E-04	3.02E+09	1.37E+08	86.584	2.265
D	3.26E+03	40.945	1.484	0.028	9.01E+07	1.07E+06	0.030	5.59E-04	3.04E+09	5.44E+07	90.134	1.068
E	5.85E+03	248.754	2.068	0.034	6.48E+07	2.72E+06	0.021	3.44E-04	3.13E+09	1.19E+08	64.774	2.724
F	3.13E+04	1230.235	2.295	0.077	8.66E+07	3.40E+06	0.057	1.92E-03	1.51E+09	3.65E+07	86.575	3.401

Table 7.1.2 – Summary of compression test results for R4340 graphite.

Sample Size	Maximum Load (N)	σ	Maximum Deflection (mm)	σ	Maximum Stress (Pa)	σ	Maximum Strain	σ	Young's Modulus (Pa)	σ	Bending Moment (N/m)	σ	Flexural Strength (Pa)	σ
A	163.505	27.824	0.175	0.036	4.47E+07	7.36E+06	0.127	0.026	3.55E+08	2.21E+07	1.002	0.171	2.23E+07	3.68E+06
B	550.762	71.611	0.459	0.042	3.82E+07	4.92E+06	0.166	0.015	2.30E+08	1.63E+07	6.754	0.878	1.91E+07	2.46E+06
C	82.330	5.547	0.209	0.012	3.18E+07	1.91E+06	0.008	0.000	4.04E+09	1.91E+08	2.776	0.187	2.12E+07	1.28E+06
D	123.502	11.601	0.250	0.019	3.10E+07	2.90E+06	0.007	0.001	4.47E+09	2.02E+08	5.452	0.512	2.06E+07	1.93E+06
E	313.018	37.237	0.328	0.029	2.73E+07	3.33E+06	0.007	0.001	3.65E+09	2.03E+08	19.192	2.283	1.37E+07	1.67E+06
F	5960.593	272.746	1.766	0.063	2.61E+07	1.19E+06	0.503	0.018	5.18E+07	2.22E+06	146.184	6.689	2.39E+07	1.09E+06

Table 7.1.3 – Summary of 3-pt flexural test results for unnotched IM1-24 graphite.

Sample Size	Maximum Load (N)	σ	Maximum Deflection (mm)	σ	Maximum Stress (Pa)	σ	Maximum Strain	σ	Young's Modulus (Pa)	σ	Bending Moment (N/m)	σ	Flexural Strength (Pa)	σ
A	213.161	43.549	0.182	0.039	3.52E+07	7.16E+06	0.100	0.021	3.57E+08	3.86E+07	1.307	0.267	2.93E+07	5.96E+06
B	730.264	76.613	0.381	0.035	3.04E+07	3.19E+06	0.104	0.010	2.92E+08	1.14E+07	8.955	0.939	2.53E+07	2.66E+06
C	116.046	23.378	0.181	0.033	2.86E+07	5.68E+06	0.005	0.001	5.44E+09	4.54E+08	3.913	0.788	3.00E+07	5.95E+06
D	165.840	17.582	0.225	0.026	2.77E+07	2.91E+06	0.005	0.001	5.68E+09	2.97E+08	7.321	0.776	2.77E+07	2.91E+06
E	341.874	28.142	0.432	0.029	2.39E+07	1.97E+06	0.005	0.000	4.45E+09	1.50E+08	25.153	2.071	2.39E+07	1.97E+06
F	7608.208	492.573	1.649	0.089	2.33E+07	1.52E+06	0.245	0.013	9.51E+07	2.85E+06	223.910	14.496	3.06E+07	1.99E+06

Table 7.1.4 – Summary of 4-pt flexural test results for unnotched IM1-24 graphite.

Sample Size	Maximum Load (N)	σ	Maximum Deflection (mm)	σ	Maximum Stress (Pa)	σ	Maximum Strain	σ	Young's Modulus (Pa)	σ	Bending Moment (N/m)	σ	Flexural Strength (Pa)	σ
A	266.110	17.647	0.245	0.019	7.42E+07	5.07E+06	0.177	0.014	4.20E+08	1.16E+07	1.632	0.108	3.71E+07	2.54E+06
B	834.671	100.482	0.498	0.038	5.77E+07	6.93E+06	0.180	0.014	3.20E+08	1.45E+07	10.235	1.232	2.88E+07	3.46E+06
C	141.676	8.765	0.304	0.032	5.36E+07	3.27E+06	0.012	0.001	4.53E+09	3.37E+08	4.691	0.290	3.64E+07	2.22E+06
D	259.178	8.548	0.465	0.021	6.43E+07	2.12E+06	0.013	0.001	4.97E+09	1.23E+08	11.441	0.377	4.29E+07	1.42E+06
E	563.982	31.531	0.611	0.022	4.89E+07	2.72E+06	0.014	0.001	3.50E+09	9.71E+07	34.579	1.933	2.45E+07	1.36E+06
F	5748.702	346.087	1.692	0.113	3.39E+07	1.93E+06	0.265	0.018	1.28E+08	8.10E+06	190.332	10.886	2.30E+07	1.31E+06

Table 7.1.5 – Summary of 3-pt flexural test results for unnotched R4340 graphite.

Sample Size	Maximum Load (N)	σ	Maximum Deflection (mm)	σ	Maximum Stress (Pa)	σ	Maximum Strain	σ	Young's Modulus (Pa)	σ	Bending Moment (N/m)	σ	Flexural Strength (Pa)	σ
A	362.117	16.143	0.264	0.010	6.08E+07	2.44E+06	0.144	0.006	4.24E+08	1.18E+07	2.220	0.099	5.07E+07	2.71E+06
B	1146.395	107.334	0.577	0.026	4.75E+07	4.38E+06	0.158	0.007	3.00E+08	1.74E+07	14.058	1.316	3.95E+07	3.65E+06
C	206.860	14.387	0.387	0.046	4.93E+07	3.35E+06	0.012	0.001	4.30E+09	6.30E+08	6.849	0.476	5.32E+07	3.61E+06
D	358.273	18.492	0.486	0.016	5.92E+07	2.97E+06	0.011	0.000	5.59E+09	1.90E+08	15.816	0.816	5.92E+07	2.97E+06
E	613.796	42.990	0.759	0.040	4.26E+07	2.99E+06	0.009	0.000	4.52E+09	1.80E+08	45.160	3.163	3.20E+07	2.24E+06
F	9726.850	1213.292	2.065	0.186	2.99E+07	3.37E+06	0.302	0.042	9.98E+07	9.71E+06	288.935	30.276	3.89E+07	4.85E+06

Table 7.1.6 – Summary of 4-pt flexural test results for unnotched R4340 graphite.

Specimen Size	Volume (m^3)	σ	Density (kg/m^3)	σ	Maximum Load (N)	σ	Maximum Deflection (mm)	σ	Nominal Stress @ Maximum Load (Pa)	σ
A	9.20E-08	5.03E-10	1728.865	38.756	50.423	7.832	0.0658	0.0045	5.32E+07	8.18E+06
B	6.81E-07	1.53E-09	1771.797	26.439	122.644	13.154	0.1475	0.0122	3.43E+07	3.94E+06
C	9.02E-07	4.32E-09	1792.506	12.908	21.089	1.639	0.0858	0.0105	3.25E+07	2.54E+06
D	1.80E-06	4.95E-09	1775.635	33.862	27.263	1.425	0.1023	0.0079	2.74E+07	1.42E+06
E	9.06E-06	1.84E-08	1747.140	27.496	72.066	3.419	0.1954	0.0142	2.50E+07	1.21E+06
F	1.44E-05	8.59E-09	1775.067	15.614	1190.691	54.401	0.7319	0.0133	2.86E+07	1.29E+06

Specimen Size	Work Done (J)	σ	Work of Fracture (J/m)	σ	γf, Effective Surface Energy (J/m^2)	σ	Bending Moment (N/m)	σ	K_{Ic}, Critical Stress Intensity Factor ($N/m^{3/2}$)	σ
A	0.00206	0.00047	443.100	98.760	221.550	49.380	0.309	0.048	4.37E+06	6.72E+05
B	0.00913	0.00185	509.783	105.329	254.891	52.665	1.504	0.161	3.90E+06	4.33E+05
C	0.00226	0.00023	200.630	19.927	100.315	9.963	0.711	0.055	3.30E+06	2.57E+05
D	0.00385	0.00061	214.197	34.591	107.098	17.295	1.204	0.063	3.11E+06	1.61E+05
E	0.01118	0.00088	246.283	19.610	123.142	9.805	4.419	0.210	3.59E+06	1.74E+05
F	0.02726	0.00146	151.067	8.070	75.533	4.035	40.152	1.835	5.80E+06	2.64E+05

Table 7.1.7 – Summary of 3-pt flexural test results for notched IM1-24 graphite.

Specimen Size	Volume (m^3)	σ	Density (kg/m^3)	σ	Maximum Load (N)	σ	Maximum Deflection (mm)	σ	Nominal Stress @ Maximum Load (Pa)	σ
A	9.18E-08	1.92E-10	1721.513	37.961	73.955	7.478	0.0875	0.008	3.64E+04	3.68E+03
B	6.83E-07	1.61E-09	1745.235	40.373	193.323	23.472	0.2298	0.023	4.85E+04	5.93E+03
C	9.04E-07	2.58E-09	1788.433	6.434	32.349	2.177	0.1077	0.013	3.76E+04	2.51E+03
D	1.80E-06	5.29E-09	1777.365	22.707	40.295	4.151	0.1277	0.011	4.04E+04	4.17E+03
E	9.06E-06	1.81E-08	1776.275	29.244	84.775	6.315	0.2617	0.017	5.63E+04	4.23E+03
F	1.44E-05	8.89E-09	1772.222	34.431	1802.282	172.150	0.8472	0.042	1.32E+05	1.26E+04

Specimen Size	Work Done (J)	σ	Work of Fracture (J/m)	σ	γf, Effective Surface Energy (J/m^2)	σ	Bending Moment (N/m)	σ	K_{Ic}, Critical Stress Intensity Factor ($N/m^{3/2}$)	σ
A	0.00344	0.00054	743.850	115.756	371.925	57.878	0.453	0.046	7.10E+06	6.95E+05
B	0.02119	0.00398	1180.478	224.144	590.239	112.072	2.371	0.288	6.79E+06	8.40E+05
C	0.00298	0.00040	263.366	36.193	131.683	18.096	1.091	0.073	5.56E+06	3.70E+05
D	0.00405	0.00038	225.211	20.906	112.606	10.453	1.779	0.183	5.08E+06	5.25E+05
E	0.01300	0.00135	285.734	29.786	142.867	14.893	6.237	0.465	5.60E+06	4.22E+05
F	0.05103	0.00804	282.641	44.597	141.321	22.299	60.776	5.805	9.72E+06	9.31E+05

Table 7.1.8 – Summary of 4-pt flexural test results for notched IM1-24 graphite.

Specimen Size	Volume (m^3)	σ	Density (kg/m^3)	σ	Maximum Load (N)	σ	Maximum Deflection (mm)	σ	Nominal Stress @ Maximum Load (Pa)	σ
A	9.00E-08	4.80E-10	1765.582	8.711	28.552	13.107	0.0382	0.0146	3.20E+07	1.45E+07
B	6.88E-07	1.50E-09	1743.400	16.317	100.929	7.269	0.1284	0.0046	2.77E+07	1.98E+06
C	9.00E-07	2.79E-09	1744.260	2.528	15.637	0.982	0.0640	0.0033	2.38E+07	1.48E+06
D	1.81E-06	2.72E-09	1769.304	2.085	24.211	2.701	0.0889	0.0063	2.39E+07	2.70E+06
E	9.05E-06	1.08E-08	1748.051	8.909	54.920	2.202	0.1431	0.0041	1.91E+07	7.76E+05
F	1.45E-05	7.81E-09	1731.714	8.337	874.577	74.022	0.6277	0.0233	2.10E+07	1.77E+06

Specimen Size	Work Done (J)	σ	Work of Fracture (J/m)	σ	γf, Effective Surface Energy (J/m^2)	σ	Bending Moment (N/m)	σ	K_{Ic}, Critical Stress Intensity Factor ($N/m^{3/2}$)	σ	Flexural Strength (MPa)	σ
A	0.00080	0.00045	178.147	101.864	89.073	50.932	0.175	0.080	2.57E+06	1.18E+06	10.645	4.885
B	0.00625	0.00056	345.557	30.316	172.779	15.158	1.238	0.089	3.17E+06	2.24E+05	9.272	0.655
C	0.00111	0.00006	98.859	5.845	49.430	2.922	0.518	0.033	2.40E+06	1.54E+05	7.921	0.505
D	0.00198	0.00023	109.343	12.474	54.671	6.237	1.069	0.119	2.73E+06	3.03E+05	7.981	0.891
E	0.00555	0.00022	122.458	4.865	61.229	2.433	3.367	0.135	2.74E+06	1.12E+05	6.369	0.260
F	0.01677	0.00210	92.765	11.616	46.382	5.808	29.492	2.496	4.25E+06	3.60E+05	6.997	0.592

Table 7.1.9 – Summary of 3-pt flexural test results for notched R4340 graphite.

Specimen Size	Volume (m^3)	σ	Density (kg/m^3)	σ	Maximum Load (N)	σ	Maximum Deflection (mm)	σ	Nominal Stress @ Maximum Load (Pa)	σ
A	8.99E-08	5.90E-10	1755.596	16.321	53.548	19.729	0.0608	0.0191	2.69E+04	9.89E+03
B	6.89E-07	1.95E-09	1746.688	12.599	136.847	10.468	0.2103	0.0092	3.41E+04	2.56E+03
C	8.99E-07	1.99E-09	1745.288	3.905	24.855	1.159	0.0804	0.0039	2.82E+04	1.34E+03
D	1.81E-06	2.64E-09	1769.824	2.897	32.989	4.159	0.1030	0.0065	3.29E+04	4.17E+03
E	9.05E-06	9.55E-09	3327.369	4995.333	64.375	3.312	0.1768	0.0072	4.28E+04	2.20E+03
F	1.45E-05	6.90E-09	1741.229	11.074	1211.372	161.383	0.6838	0.0387	8.84E+04	1.18E+04

Specimen Size	Work Done (J)	σ	Work of Fracture (J/m)	σ	γf, Effective Surface Energy (J/m^2)	σ	Bending Moment (N/m)	σ	K_{Ic}, Critical Stress Intensity Factor ($N/m^{3/2}$)	σ	Flexural Strength (MPa)	σ
A	1.94E-03	0.00115	432.838	257.274	216.419	128.637	0.328	0.121	5.32E+06	1.96E+06	19.981	7.331
B	1.20E-02	0.00153	663.450	83.453	331.725	41.726	1.678	0.128	4.76E+06	3.54E+05	12.554	0.924
C	1.45E-03	0.00015	128.806	13.322	64.403	6.661	0.823	0.038	4.23E+06	2.00E+05	12.593	0.611
D	2.26E-03	0.00033	124.302	18.253	62.151	9.126	1.456	0.184	4.12E+06	5.21E+05	10.894	1.388
E	6.19E-03	0.00028	136.730	6.101	68.365	3.051	4.736	0.244	4.27E+06	2.19E+05	8.970	0.460
F	2.61E-02	0.00521	144.144	28.787	72.072	14.394	40.850	5.442	6.52E+06	8.67E+05	9.689	1.287

Table 7.1.10 – Summary of 4-pt flexural test results for notched R4340 graphite.

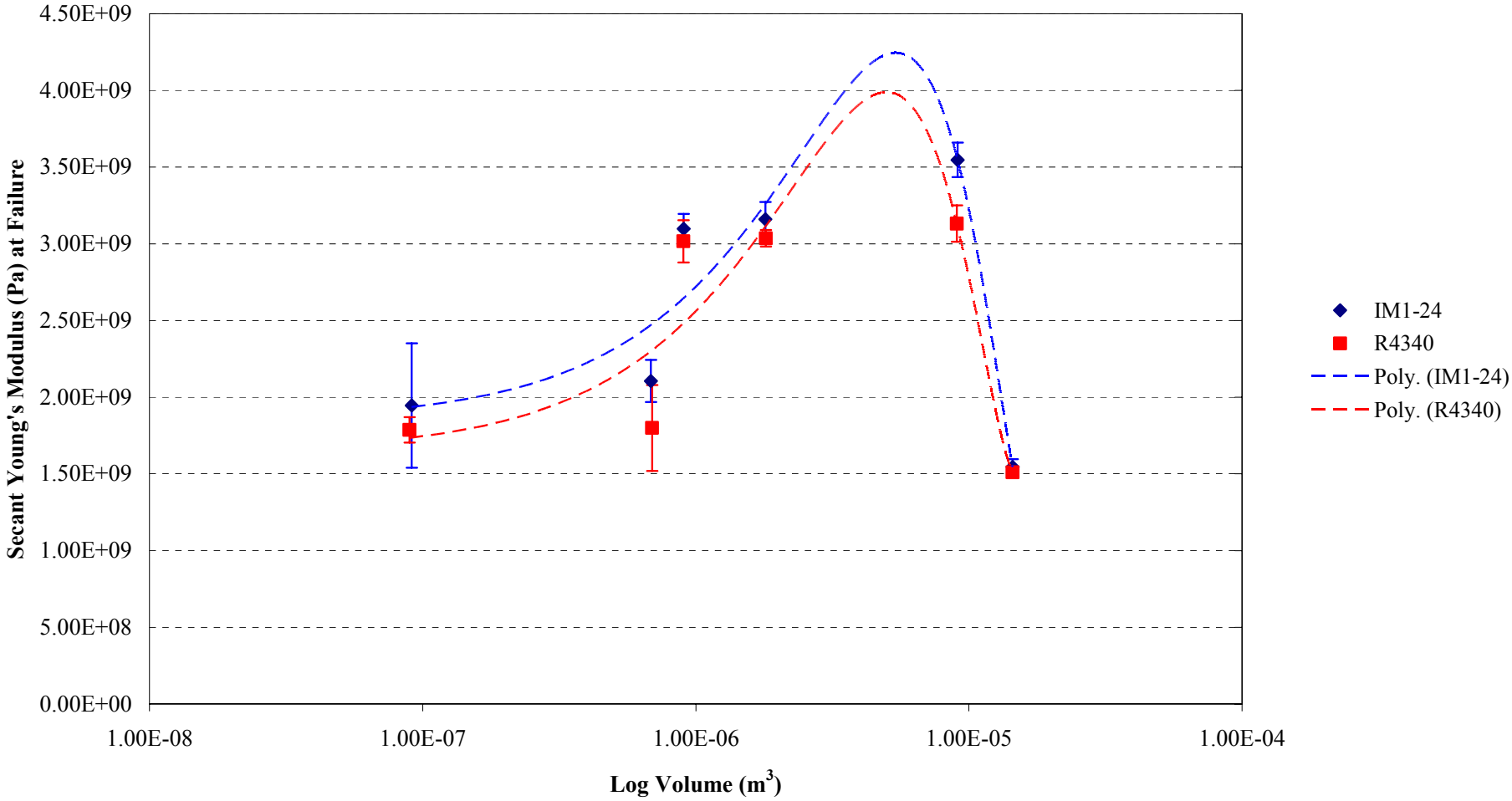

Graph 7.1.1 – Plot of volume versus secant Young's modulus at failure for IM1-24 and R4340 graphites under compression.

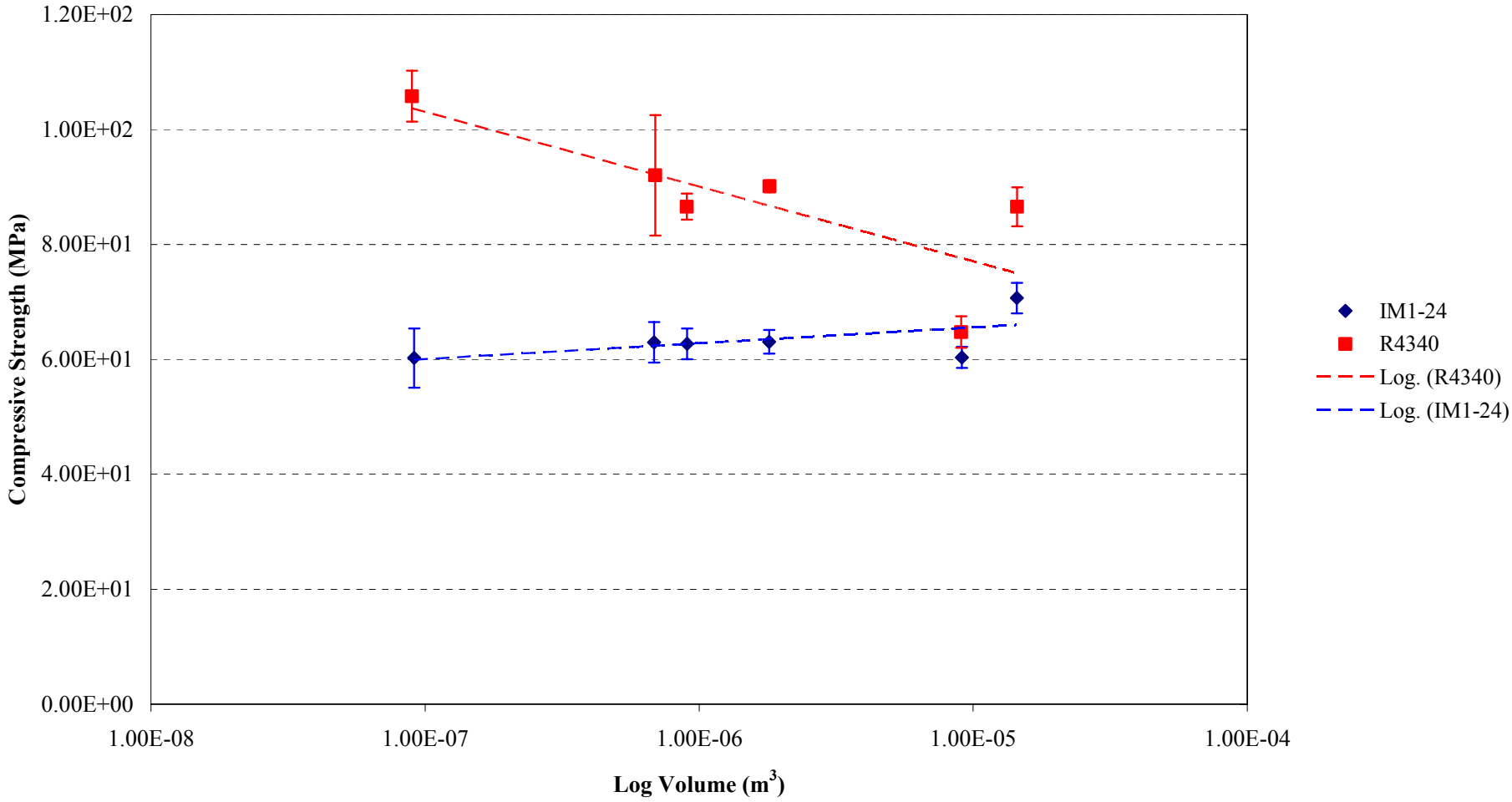

Graph 7.1.2 – Plot of volume versus compressive strength for IM1-24 and R4340 graphites under compression.

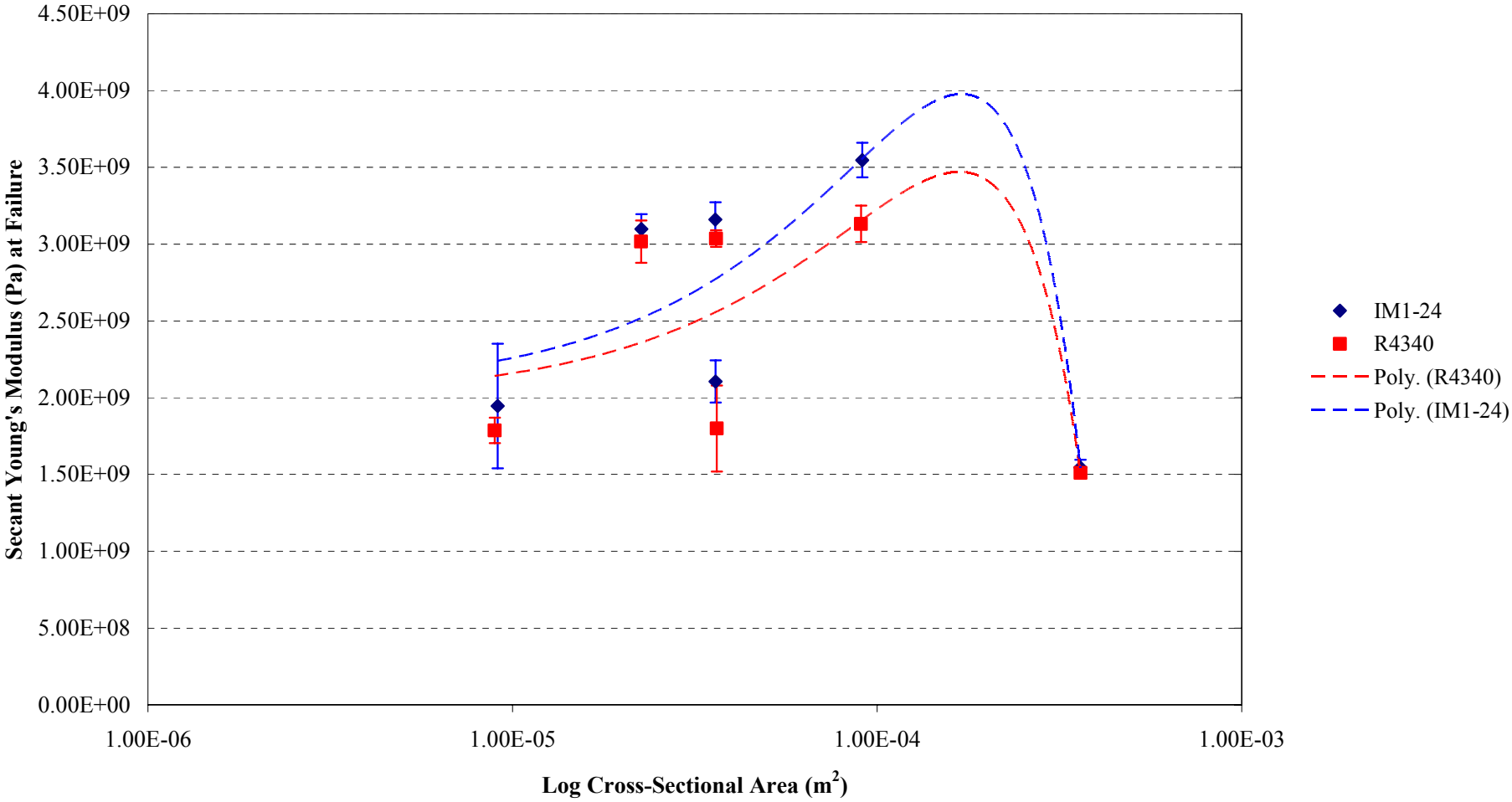

Graph 7.1.3 – Plot of cross-sectional area versus secant Young's Modulus at failure for IM1-24 and R4340 graphites under compression.

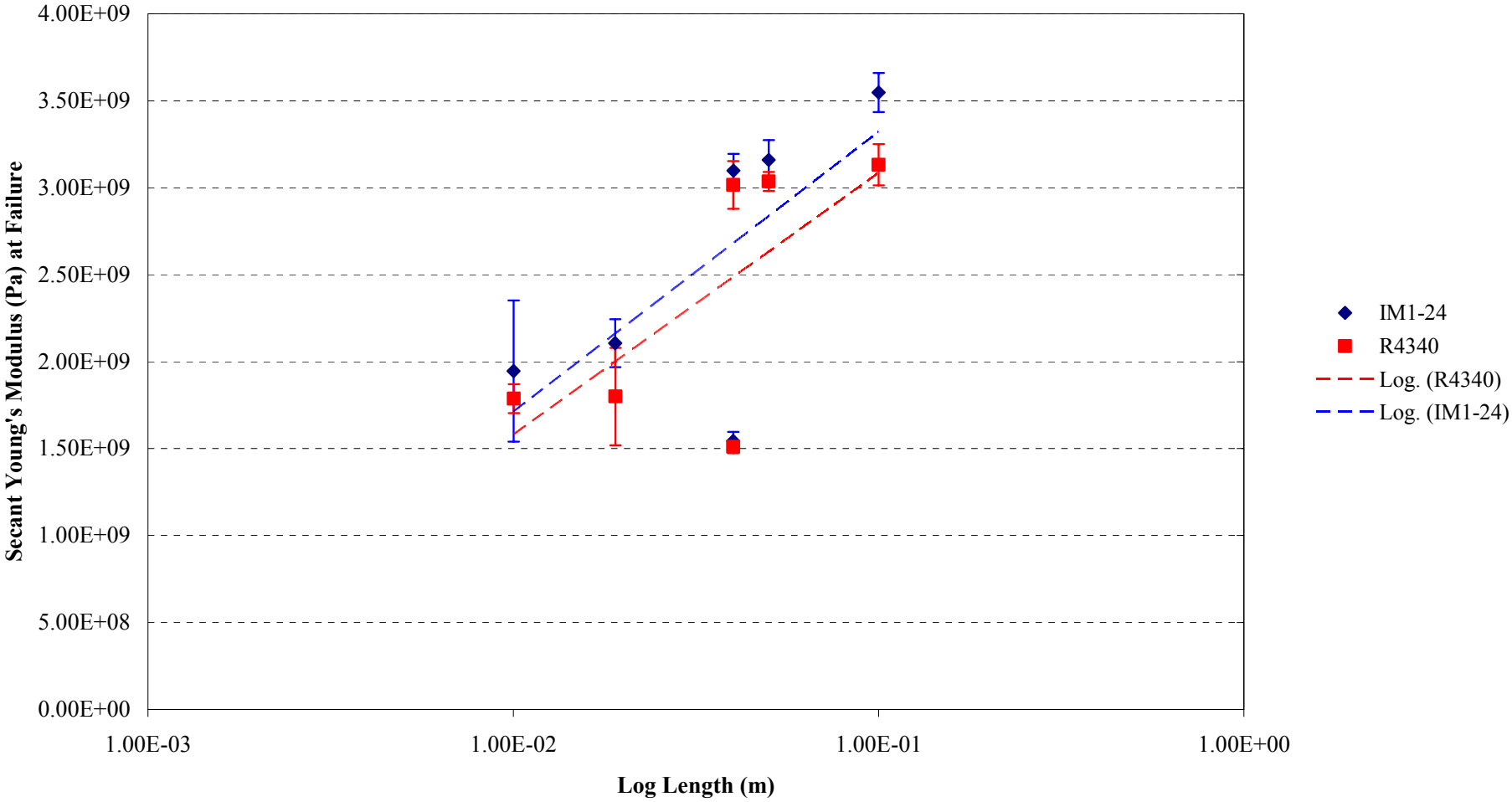

Graph 7.1.4 – Plot of length versus secant Young's modulus at failure for IM1-24 and R4340 graphites under compression.

Graphs 7.1.1 to 7.1.4 display a selection of the results obtained from the compression tests performed during the testing programme. In each of the graphs, and all subsequent graphs that follow, the trendlines displayed are intended as a guide for the eye of the reader rather than an expression of the relationship between specimen size and material property. For this reason no curve or line equations are displayed.

Comparing the values of the calculated Young's modulus under compression (graph 7.1.1); it can be observed that both the IM1-24 and R4340 graphites show a trend for increasing Young's modulus with increasing volume. However, when analysing the individual points on the graph it is clear that the geometry of the largest sized specimen causes it to have a significantly lower Young's modulus than the other specimens. Specimen sizes *A* to *E* all show an increase in elastic modulus which under the experimental conditions would be expected. As the specimen lengths were increased more flexure through the longitudinal axis was observed, indicating the materials behaving in a fractionally more elastic fashion. It can be seen that the IM1-24 graphite has a greater increase in Young's modulus than the R4340 graphite, though the trendlines for both materials are very similar.

With the compressive strength of the two materials, it can be seen that the IM1-24 graphite is stronger with increasing volume, and the R4340 is weaker with increasing volume (graph 7.1.2). Again, the largest volume specimen skews the results slightly due to the differing geometry. As the *F* size specimen has a greater cross-sectional area to length ratio than the other specimen sizes, it enables it to sustain a higher failure load and therefore appears to be a stronger specimen. If the two *F* specimen results were neglected for the time being, it is clear that as the volume of the specimens increases, the compressive strength decreases. The IM1-24 graphite initially increases in strength with the first step up in volume; from there it plateaus for the next three specimen sizes, and then reduces in strength as the longer specimens are tested. For the R4340 graphite, the smallest specimen size proves to be the strongest, but there is a small degree of variability in the strength as the specimen sizes increase. The difference in strength between the two materials highlights the more brittle nature of the R4340 graphite due to the more homogeneous microstructure.

To demonstrate the effect the cross-sectional area and length of the specimens on the various mechanical properties of the two materials, graphs 7.1.3 and 7.1.4 were produced. Graph 7.1.3 plots cross-sectional area against the secant Young's modulus at failure and displays a very similar spread of results to those seen in graph 7.1.1. Graph 7.1.4 plots the length versus stress at maximum load and observes an increase in secant Young's modulus as the length of the specimens increases, up to the *E* specimens. The *F* specimens once again do not follow the same pattern as the other sizes, in this instance due to their increased cross-sectional area. Interestingly, the R4340 graphite *F* specimens failed at approximately the same load as the *C* sized specimens, unlike the IM1-24 F sized specimens which all failed at higher stresses than the other sized samples. If the *F* specimen results are neglected for the IM1-24 graphite, as the specimen sizes increase the stress required to cause failure also increases up to a point between the *B* and *C* sized specimens, after this point the stress required to cause failure begins to reduce. Considering the same case for the R4340, the stress required to cause failure decreases with each increase in specimen size, though the *D* sized specimens slightly skew this.

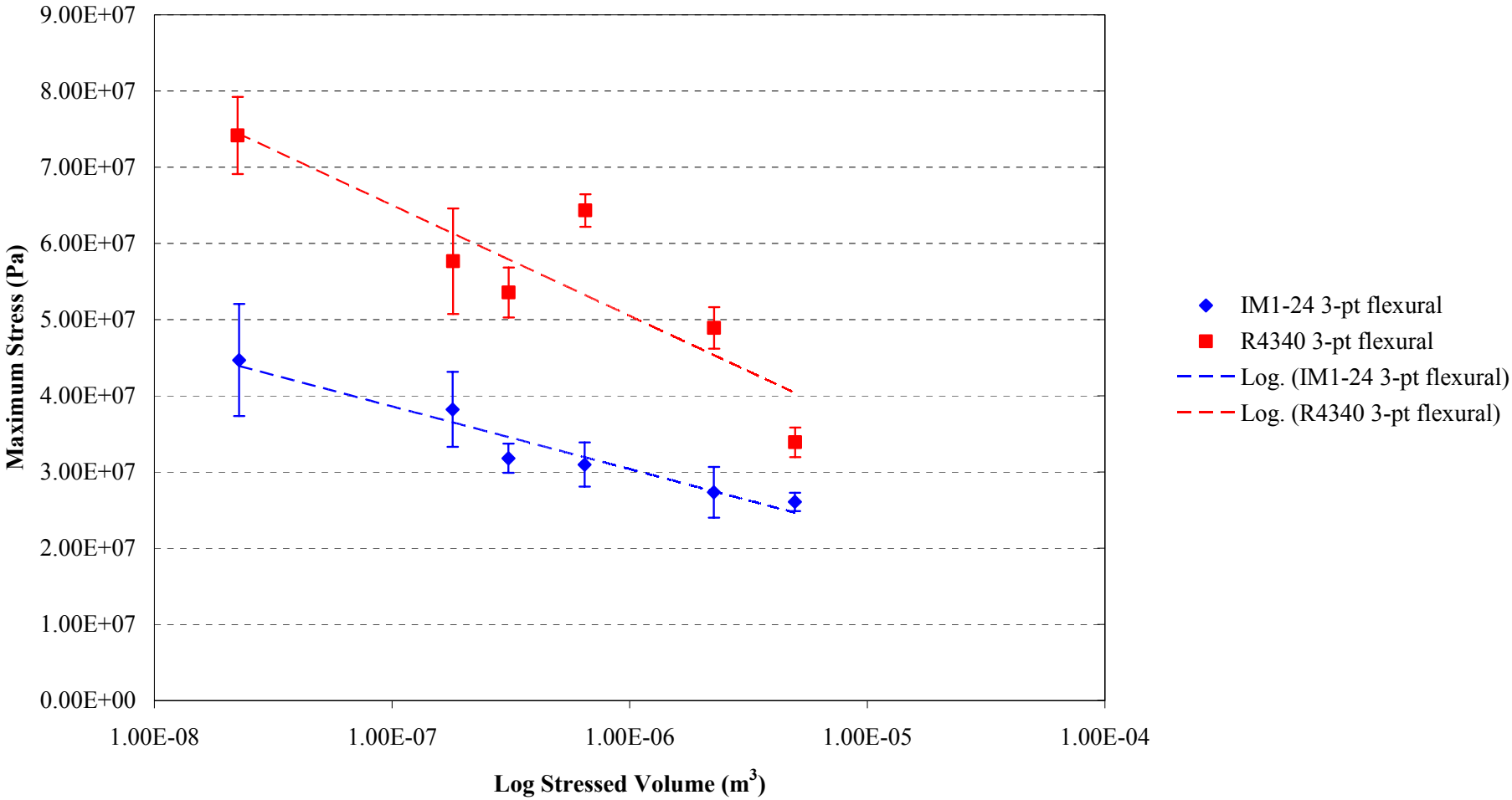

Graph 7.1.5 – Plot of volume versus maximum stress for unnotched IM1-24 and R4340 graphites under 3-pt flexural loading.

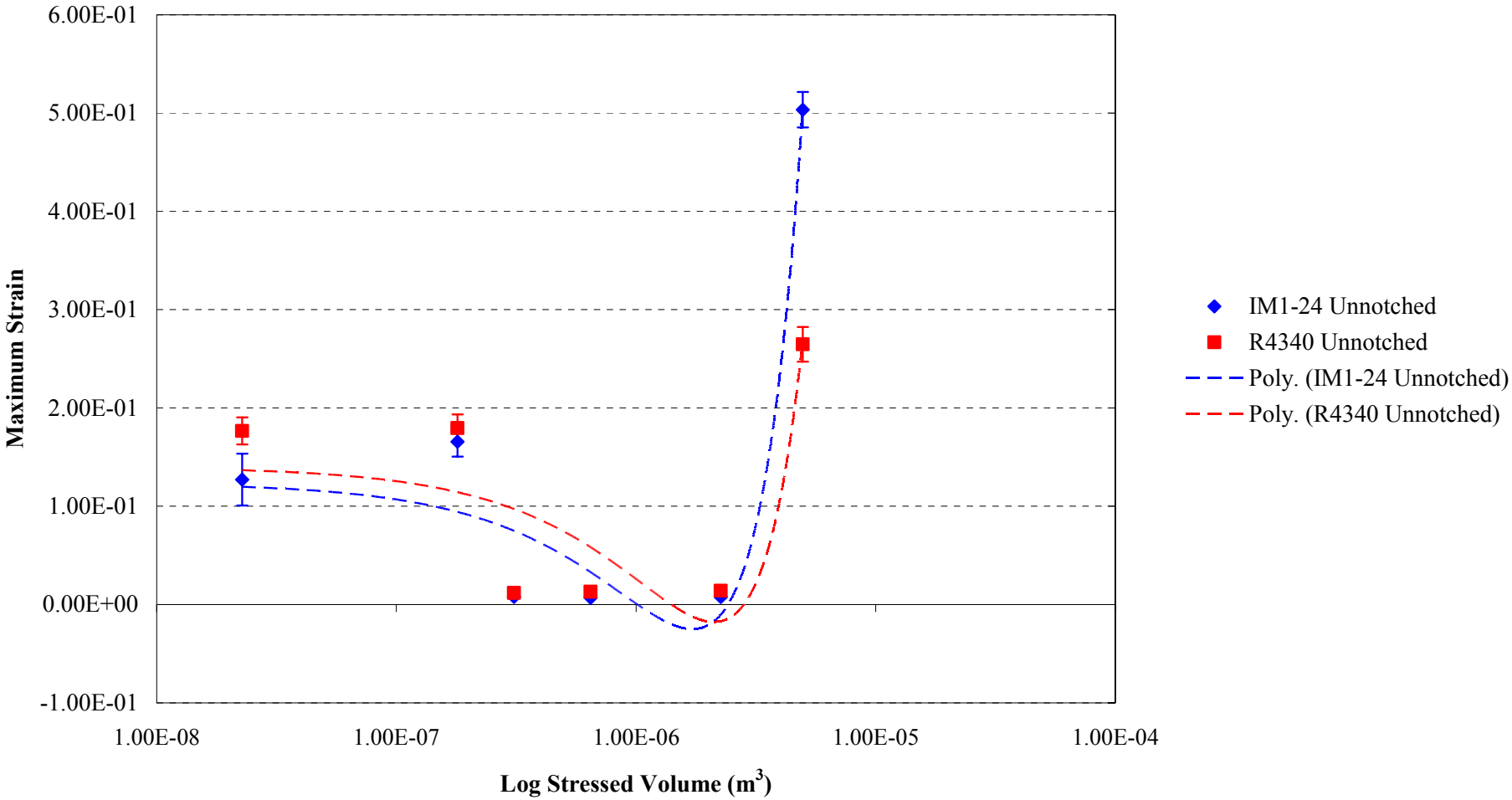

Graph 7.1.6 – Plot of volume versus maximum strain for unnotched IM1-24 and R4340 graphite under 3-pt flexural loading.

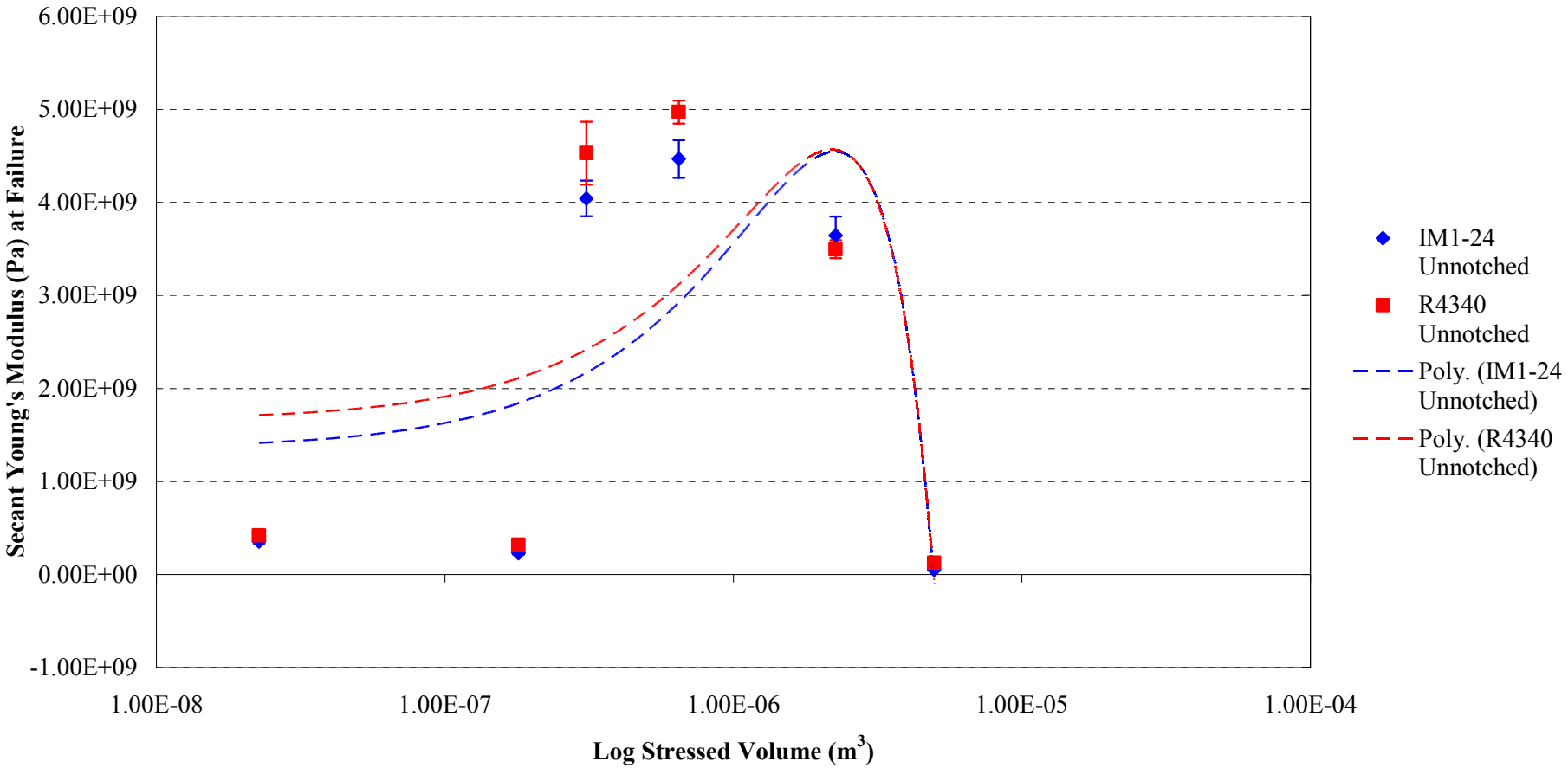

Graph 7.1.7 – Plot of volume versus secant Young's modulus at failure for unnotched IM1-24 and R4340 graphite under 3-pt flexural loading.

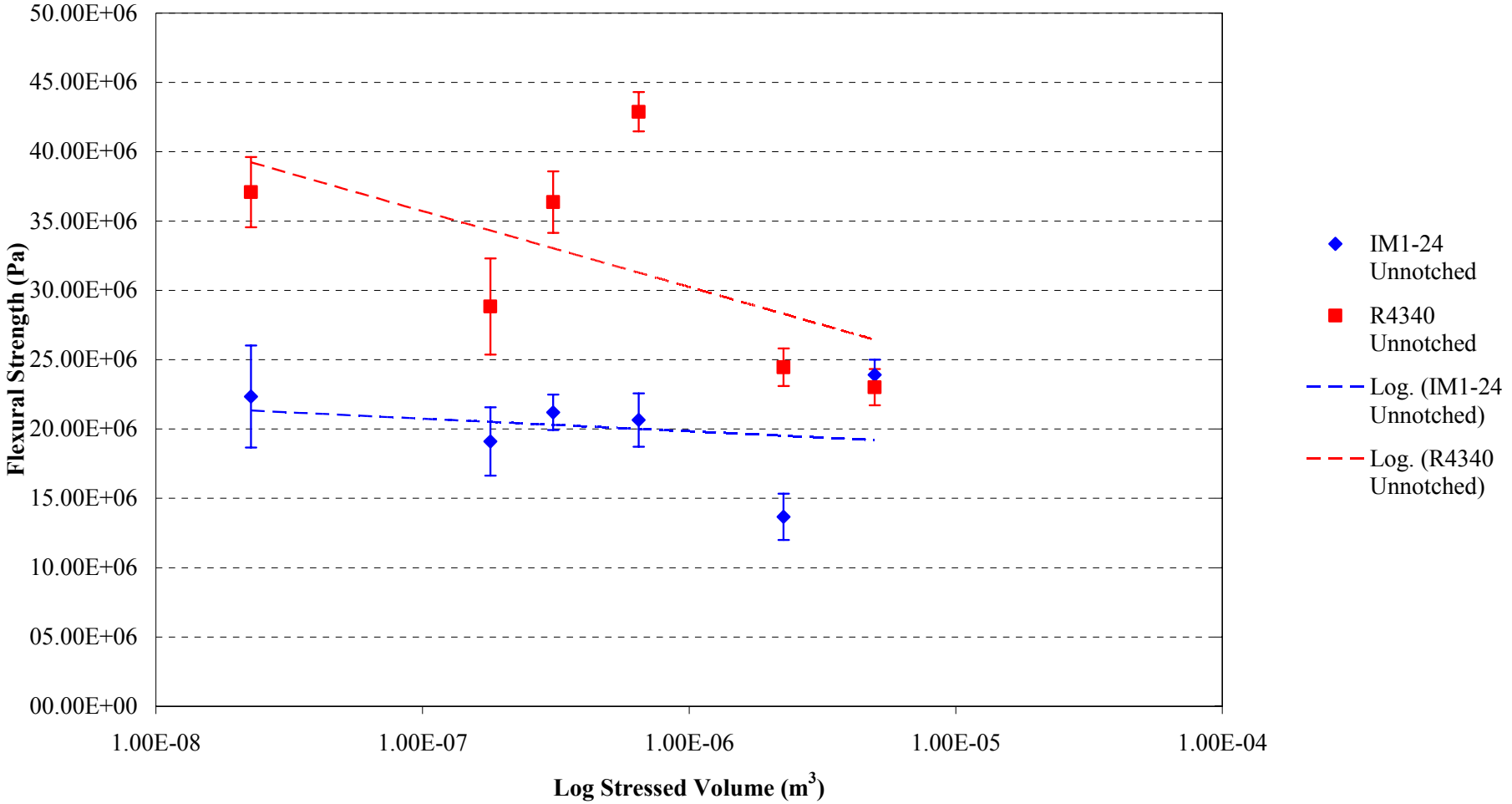

Graph 7.1.8 - Plot of volume versus flexural strength for unnotched IM1-24 and R4340 graphite under 3-point flexural loading.

The unnotched specimen 3-point flexural test results show a different picture to those of the compression tests. Examining the volume versus maximum stress result first (graph 7.1.5), it can be seen that for both IM1-24 and R4340 graphite, as the specimen size increases the maximum stress decreases, and both graphite types show a similar trend (though the R4340 has a slightly steeper decline and higher failure stress). Unlike the compression tests the unnotched *F* specimens do not appear to skew the results due to the difference in geometry to the other specimens, they follow the trend of increasing volume leading to a decrease in maximum stress at failure.

In contrast to the maximum stress, graph 7.1.6 plots the volume versus the maximum strain and shows an alternate picture of what is occurring with the materials. For both materials the strains are higher at the lower specimen sizes, and decrease with increasing volume. However, the largest specimen volume requires a much larger strain to initiate failure. For specimens *C*, *D* and *E* a much lower strain is measured, this could be attributed to the increased length of the specimens, causing a reduced rigidity that would enable failure to occur at lower loads. Indeed, a lower failure load for each of these specimens was recorded than for specimen sizes *A*, *B* and *F*.

This can be further seen in the plot of volume versus Young's modulus (graph 7.1.7). As the specimen sizes increase (and the length along which the load is spread) there is an increase in Young's modulus indicating a less elastic response in the materials. As the load span between the lower supports is increased there is a increase in the Young's modulus due to specimens *C*, *D* and *E* all having a higher length to width ratio than specimen sizes *A*, *B* and *F*. Due to the brittle behaviour of the materials the increased load span causes the materials to fail under a lower load and register a higher Young's modulus. Unsurprisingly, the *F* specimen sizes have the lowest length to width ratio and as such the lowest calculated Young's modulus. In the majority of the results the Young's modulus of the R4340 graphite is higher, indicating a more brittle response under 3-point flexural loading.

Plotting the volume versus flexural strength in graph 7.1.8 clearly shows that as the specimen volume increases, the flexural strength decreases with the R4340 graphite having a steeper decline in flexural strength with increasing specimen size. It is

interesting to note that for both types of graphite, the *F* specimen sizes have a very similar measured flexural strength.

The results for the 4-point flexural tests show a very similar trend to those for the 3-point flexural tests if the recorded values are not considered. Graph 7.1.9 shows that the maximum stress results are lower than those for the 3-point flexural tests, indicating more brittle behaviour as would be expected from the 4-point flexural tests due to the increased constraint on the specimens (two points of loading on the upper surface instead of one).

The maximum strain recorded at failure is different to that observed under 3-point loading due to the higher strain of the R4340 *F* specimens (graph 7.1.10). The trend observed under 4-point loading is more indicative of the results that should have been observed for the 3-point flexural tests, *i.e.* the R4340 graphite fails at a higher strain than the IM1-24 graphite as it has a closer packed, finer grained microstructure. As the *F* specimens skew the results, if they were neglected it is possible to see that with the increase in volume a lower strain is required to initiate failure.

Graph 7.1.11 shows that under 3-point flexural loading the Young's modulus of the R4340 graphite was the clearly higher than the IM1-24 graphite. However, under 4-point flexural loading there is very little difference between the two materials. Although the trend for how the Young's modulus is affected through the increase in volume is still the same, the values are different, with the 4-point flexural tests yielding a greater Young's modulus value than those of the 3-point flexural tests. This can be expected as mentioned earlier due to the increased inherent stiffness of the test conditions.

As observed with the Young's modulus results, the measured 4-point flexural strength values are higher than those of the 3-point flexural tests (graph 7.1.12), but again the trend is very similar (increasing the volume of the specimen reduces the flexural strength).

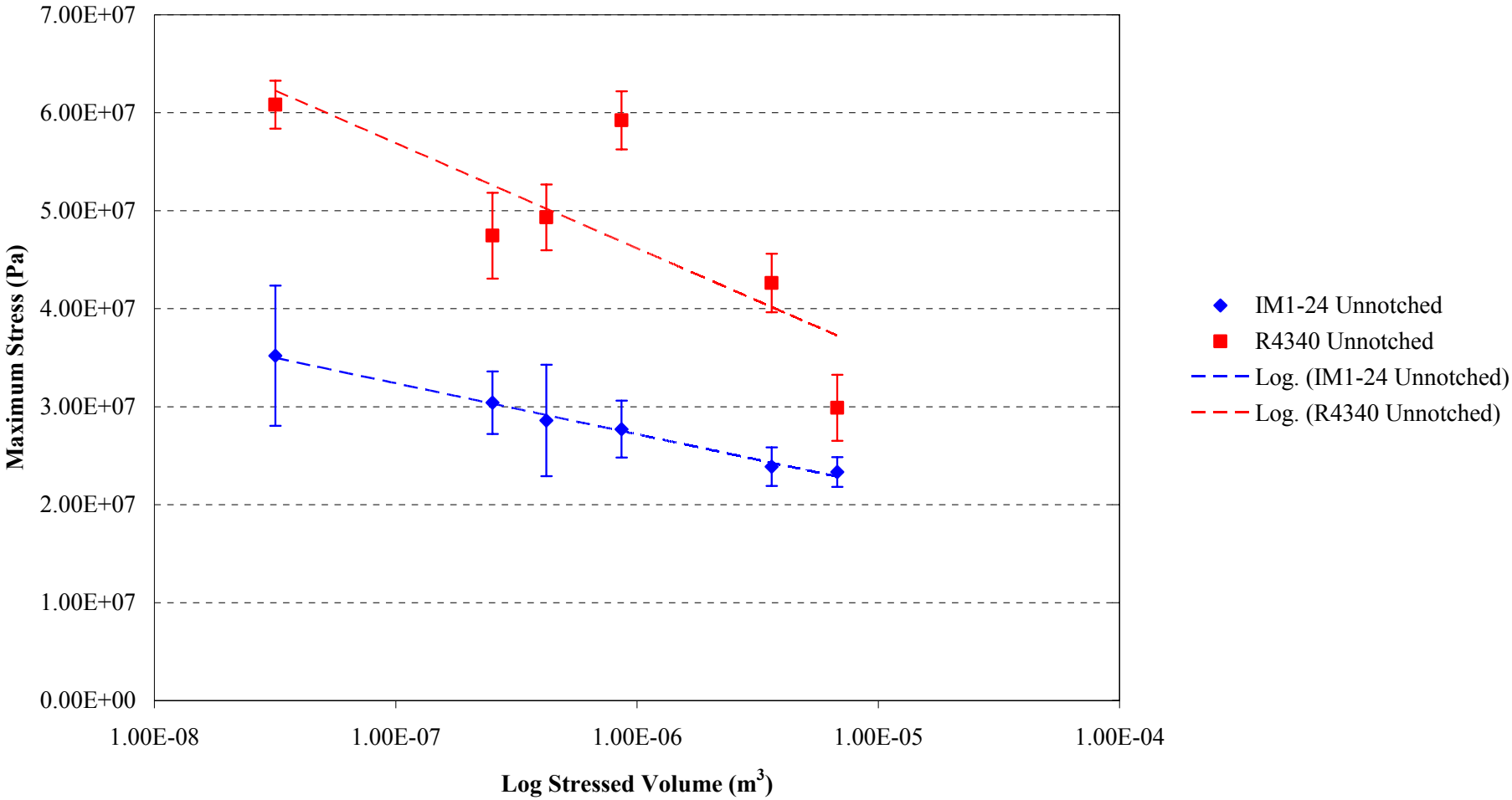

Graph 7.1.9 – Plot of volume versus maximum stress for unnotched IM1-24 and R4340 graphites under 4-pt flexural loading.

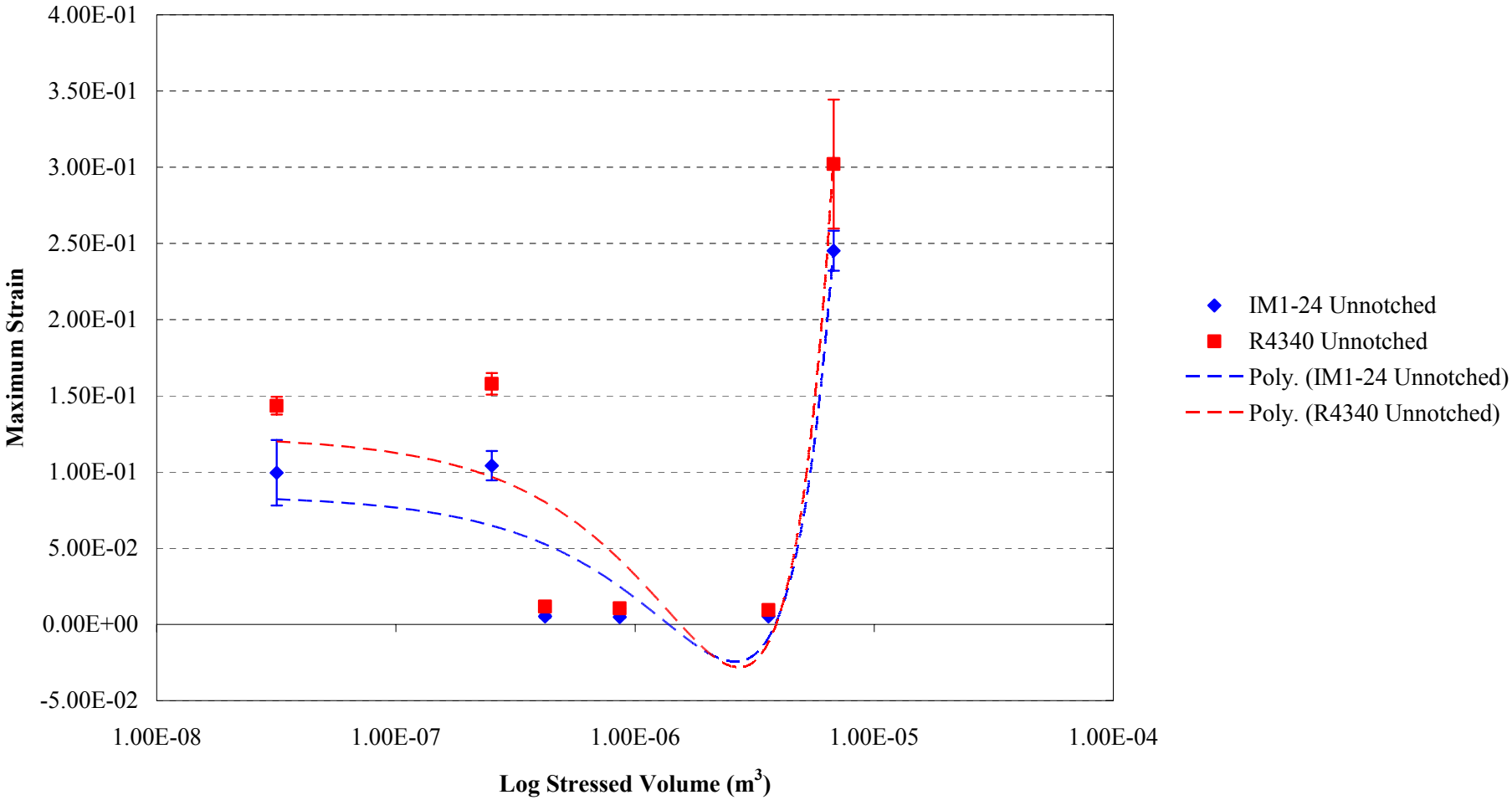

Graph 7.1.10 – Plot of volume vs. maximum strain for unnotched IM1-24 and R4340 graphite under 4-point flexural loading.

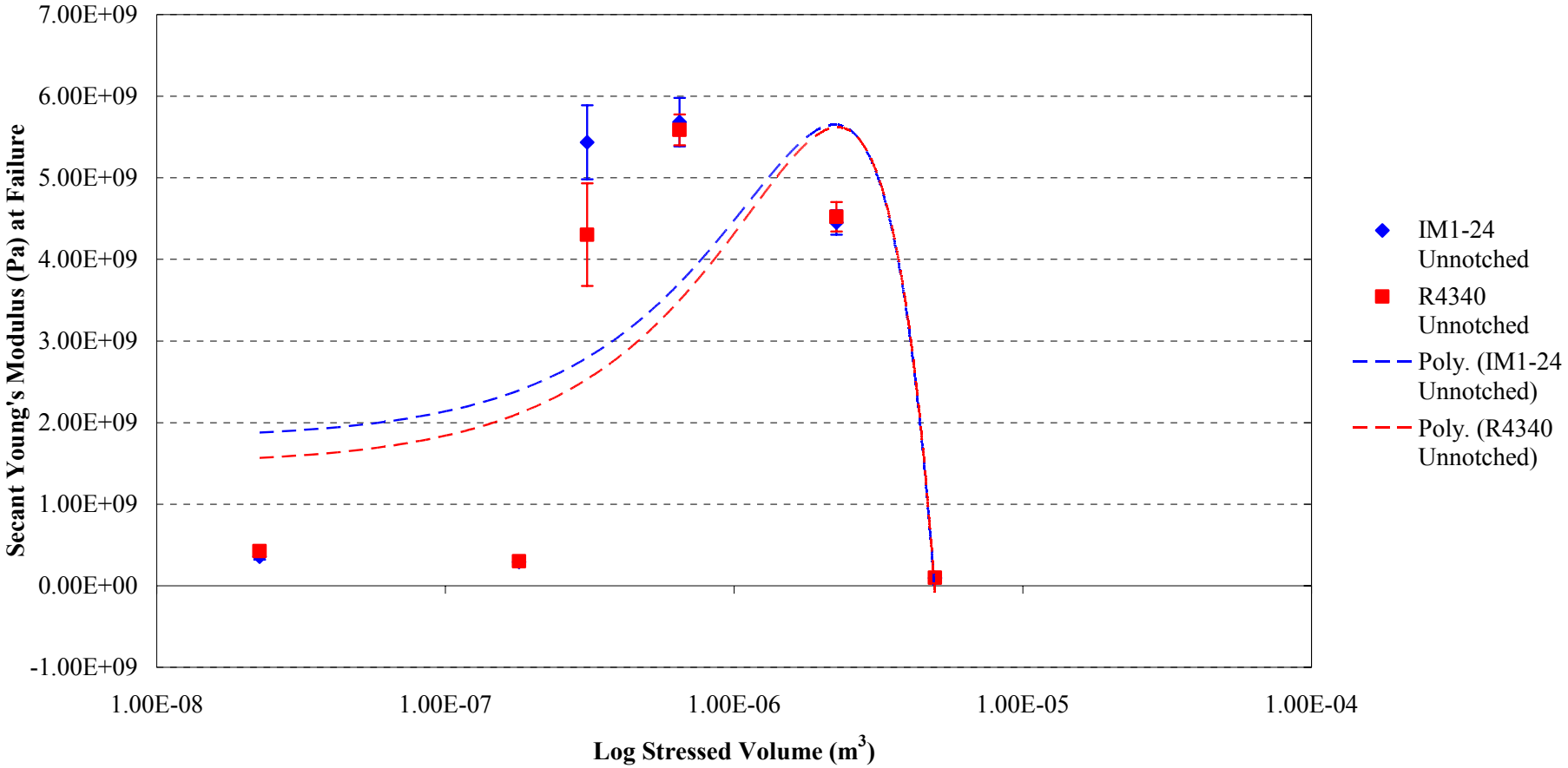

Graph 7.1.11 – Plot of volume versus secant Young's modulus at failure for unnotched IM1-24 and R4340 graphite under 4-point flexural loading.

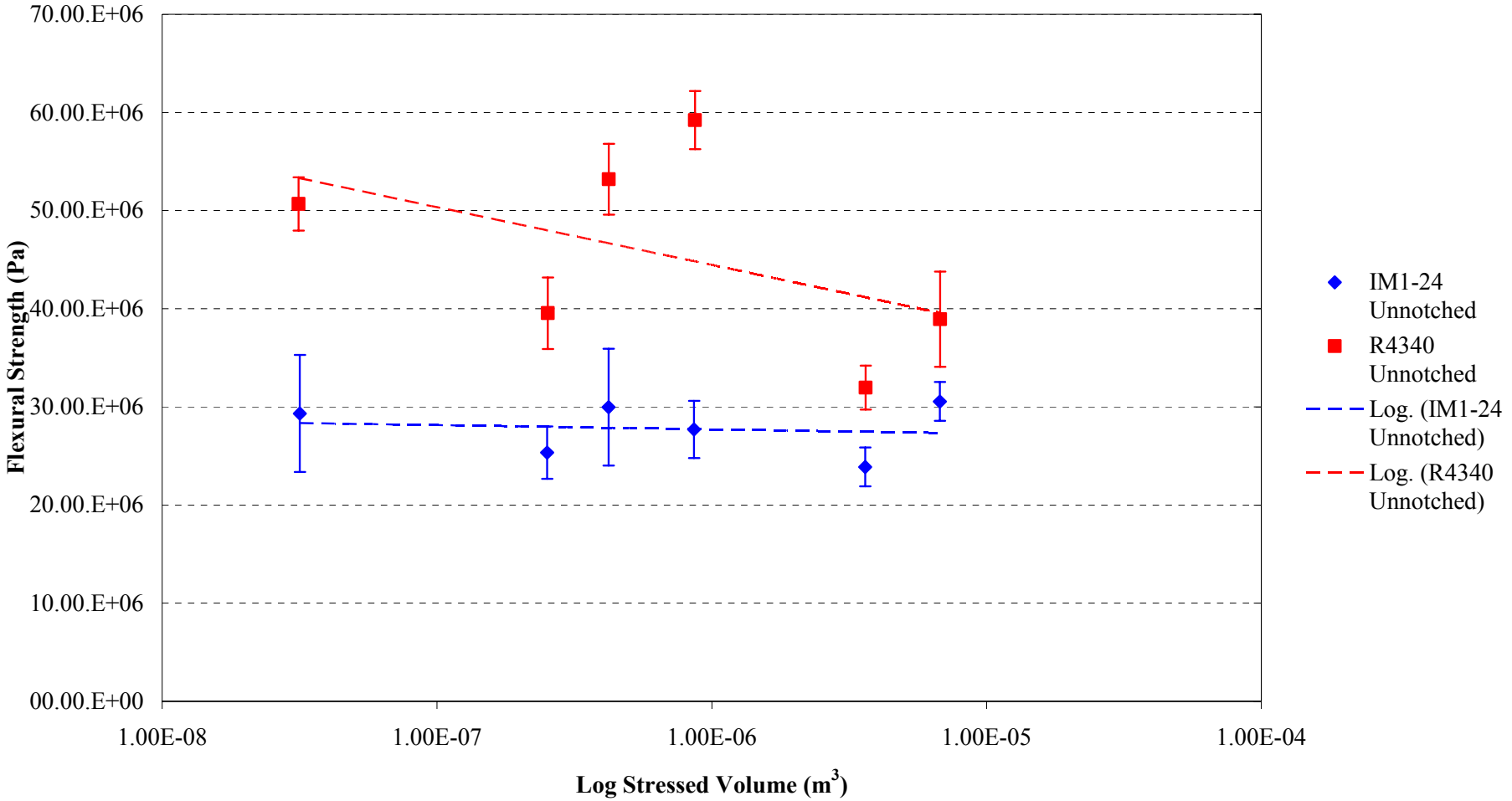

Graph 7.1.12 – Plot of volume versus flexural strength for unnotched IM1-24 and R4340 graphite under 4-point flexural loading.

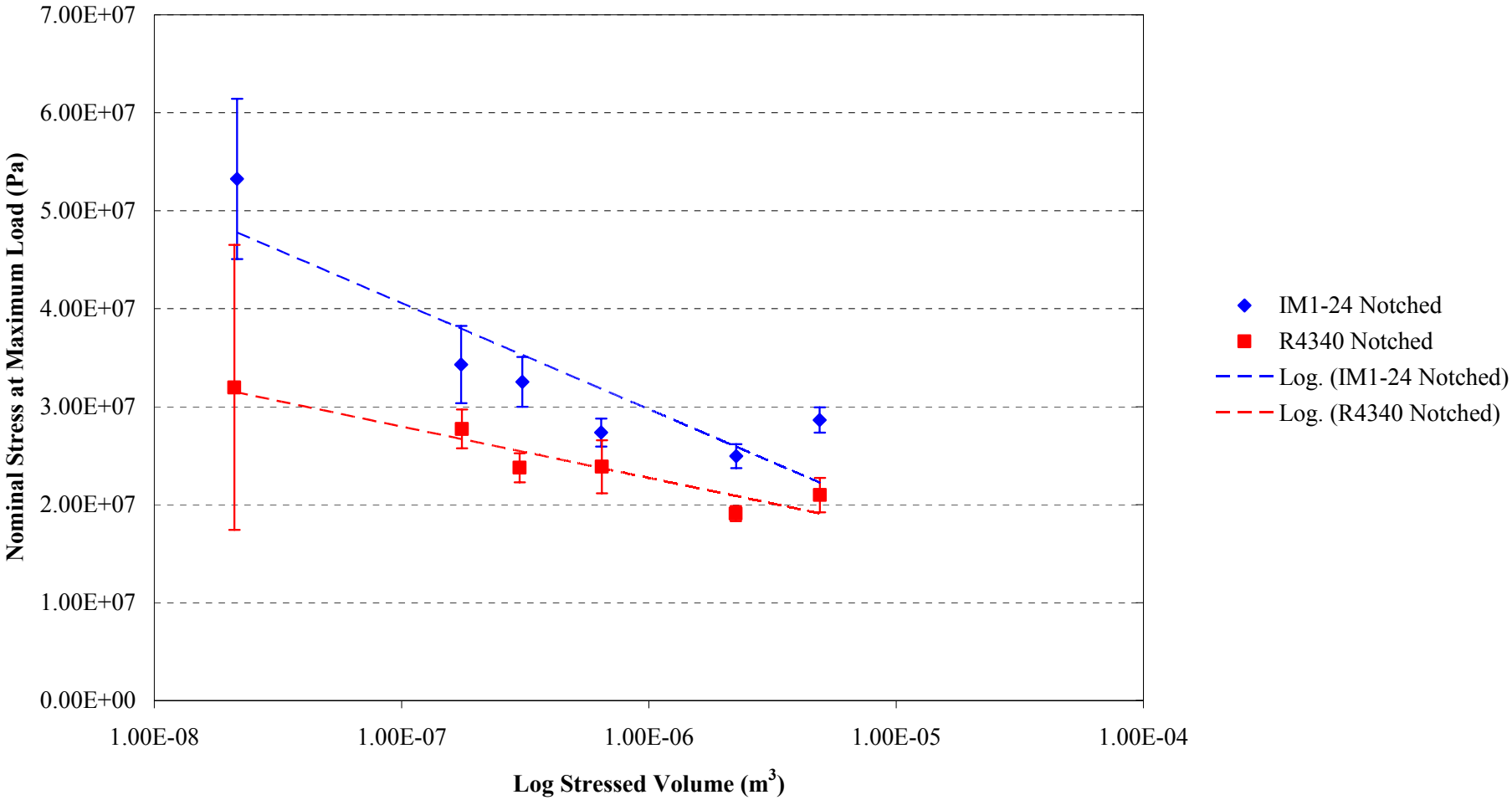

Graph 7.1.13 – Plot of volume versus nominal stress at maximum load for notched IM1-24 and R4340 graphites under 3-point flexural loading.

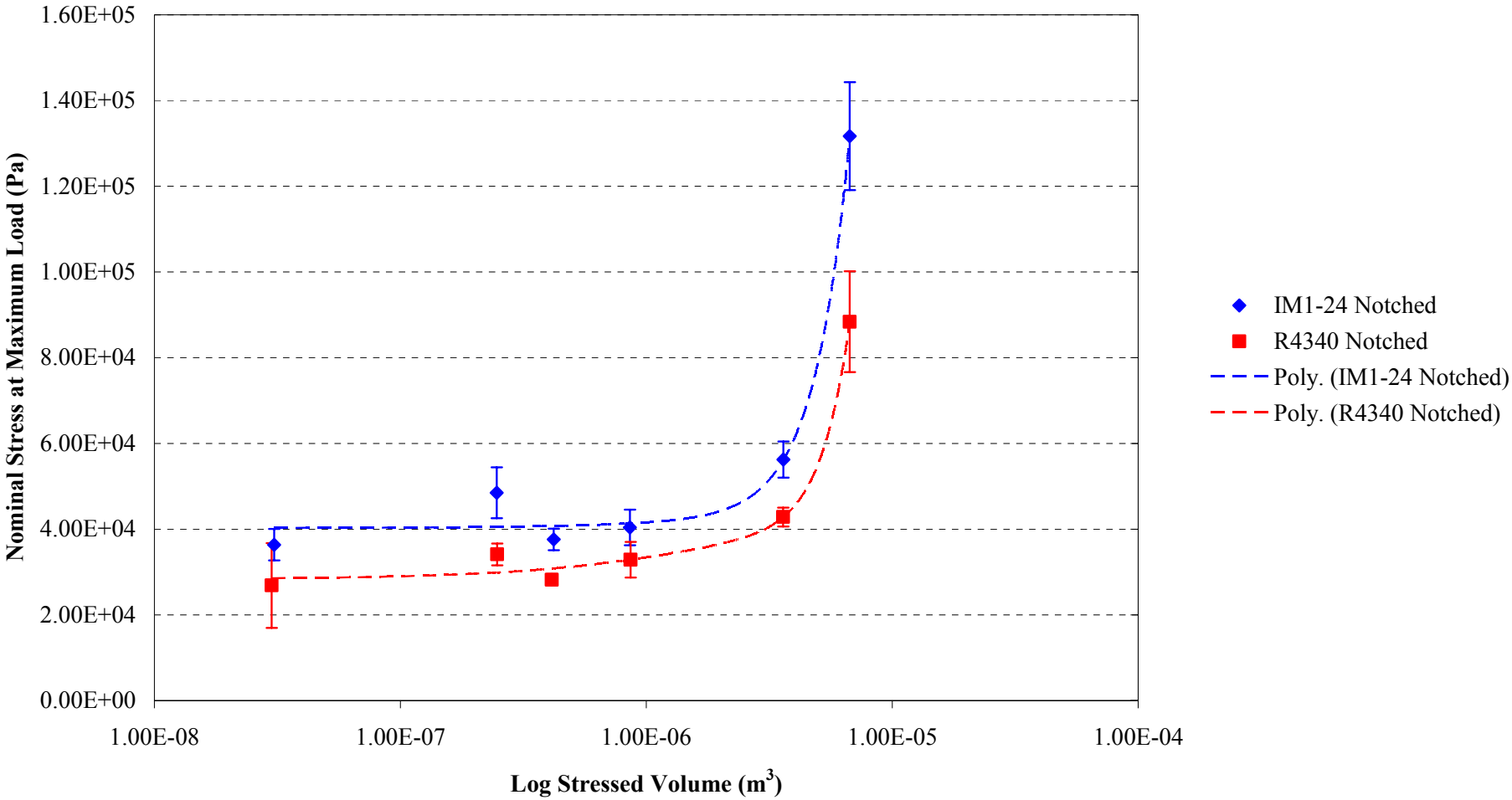

Graph 7.1.14 – Plot of volume versus nominal stress at maximum load for notched IM1-24 and R4340 graphites under 4-pt flexural loading.

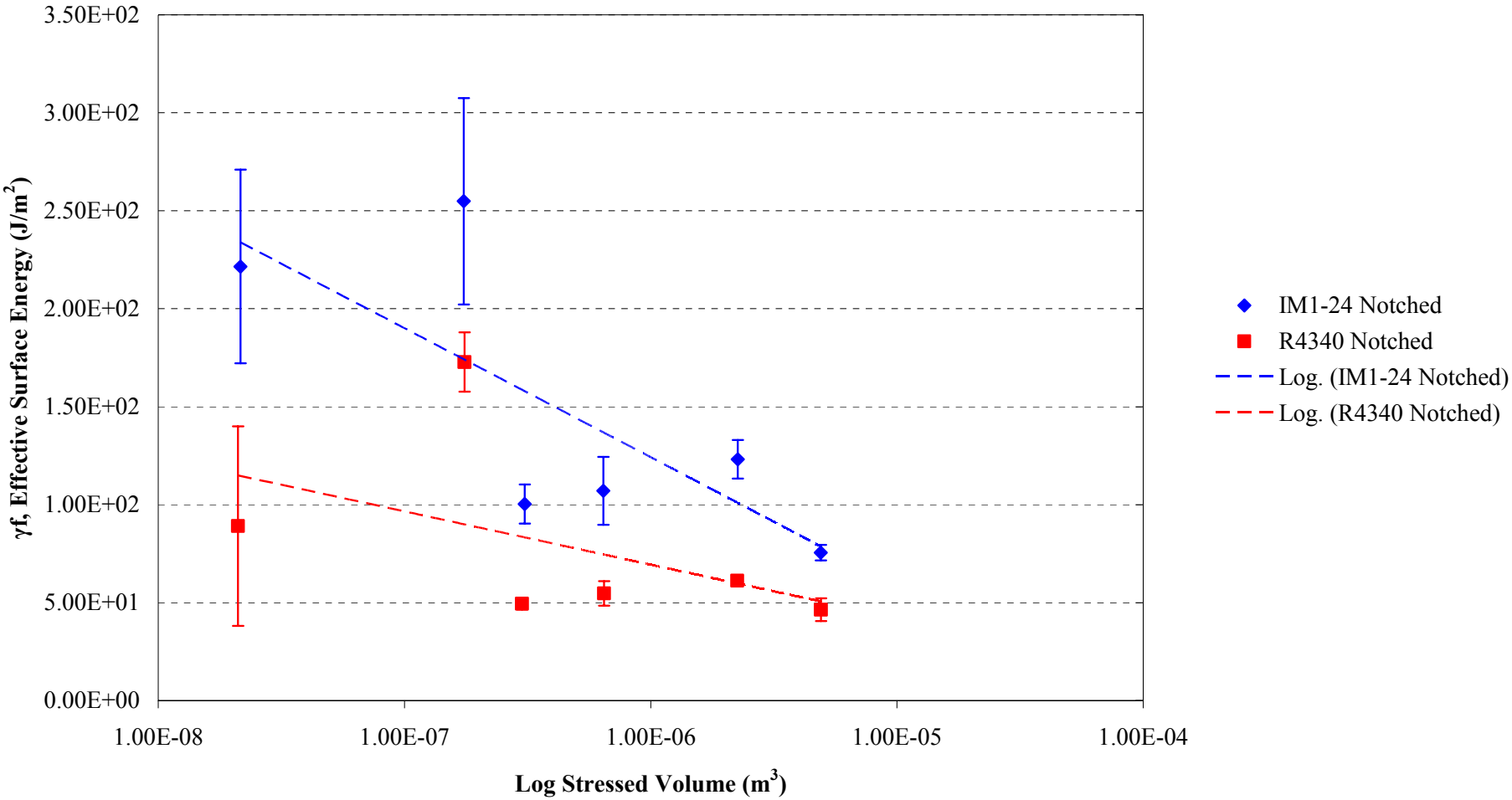

Graph 7.1.15 – Plot of volume versus effective surface energy for notched IM1-24 graphites under 3-pt flexural loading.

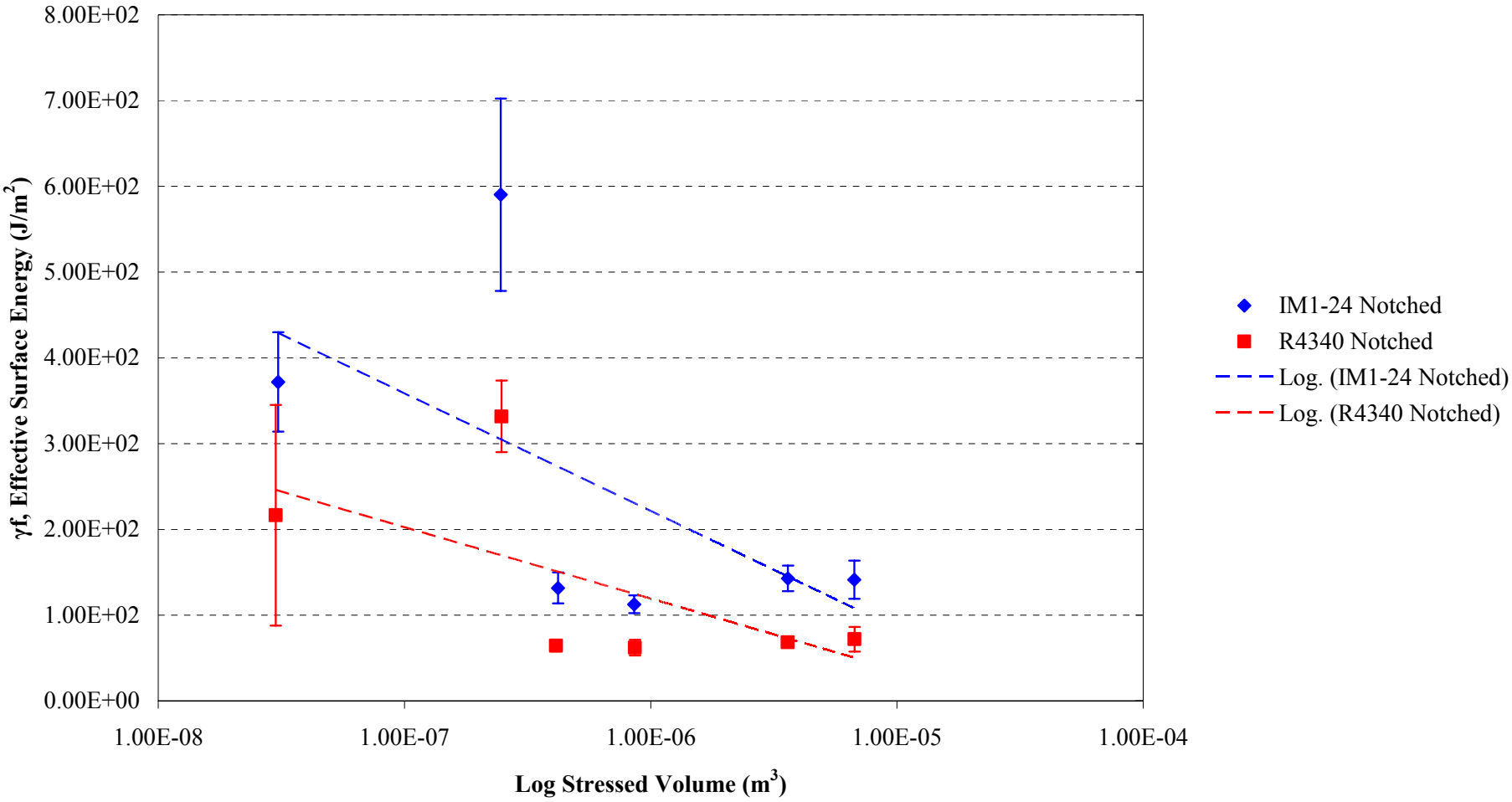

Graph 7.1.16 – Plot of volume versus effective surface energy for notched IM1-24 graphites under 4-pt flexural loading.

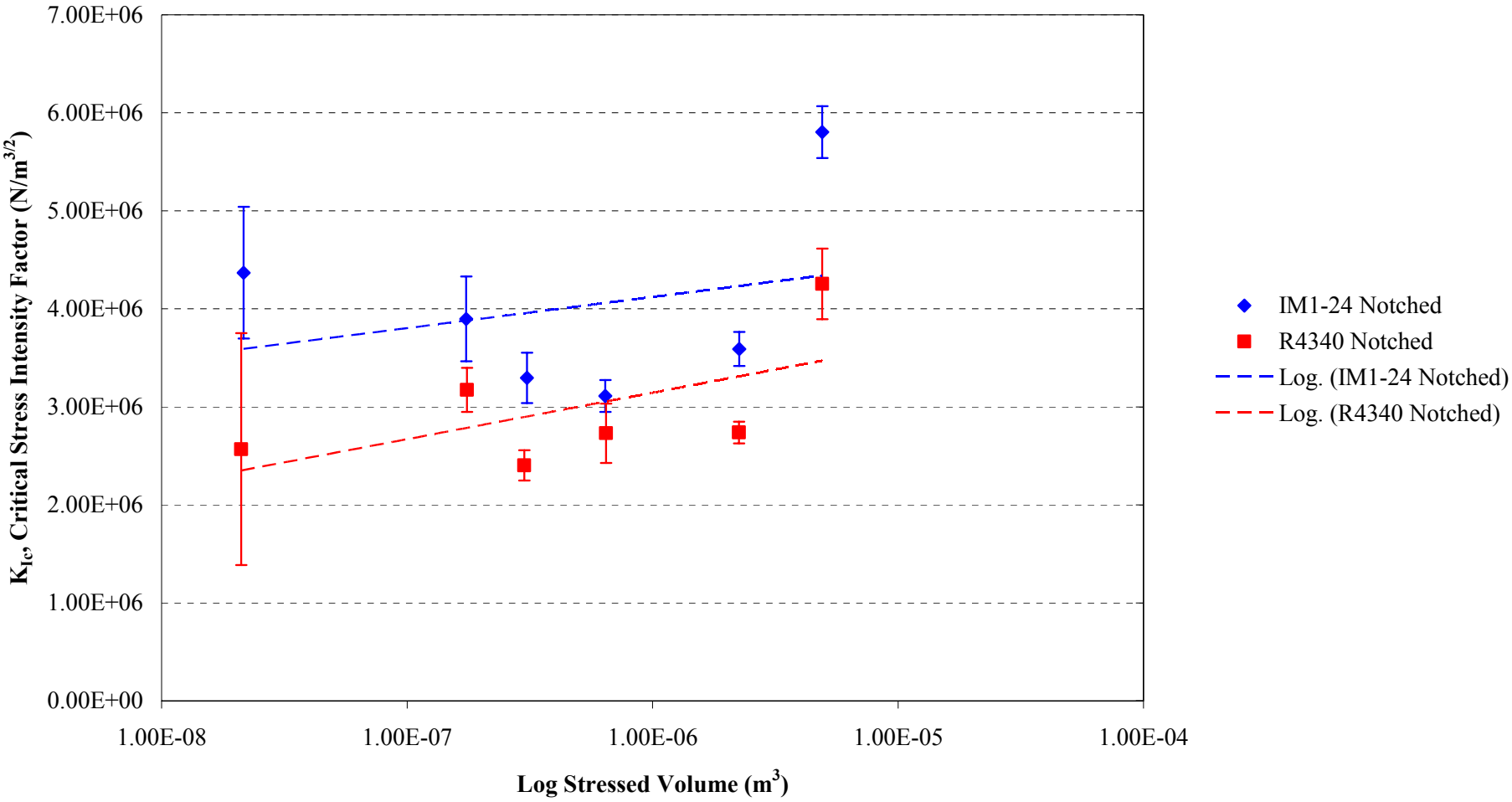

Graph 7.1.17 – Plot of volume versus critical stress intensity factor for notched IM1-24 graphites under 3-pt flexural loading.

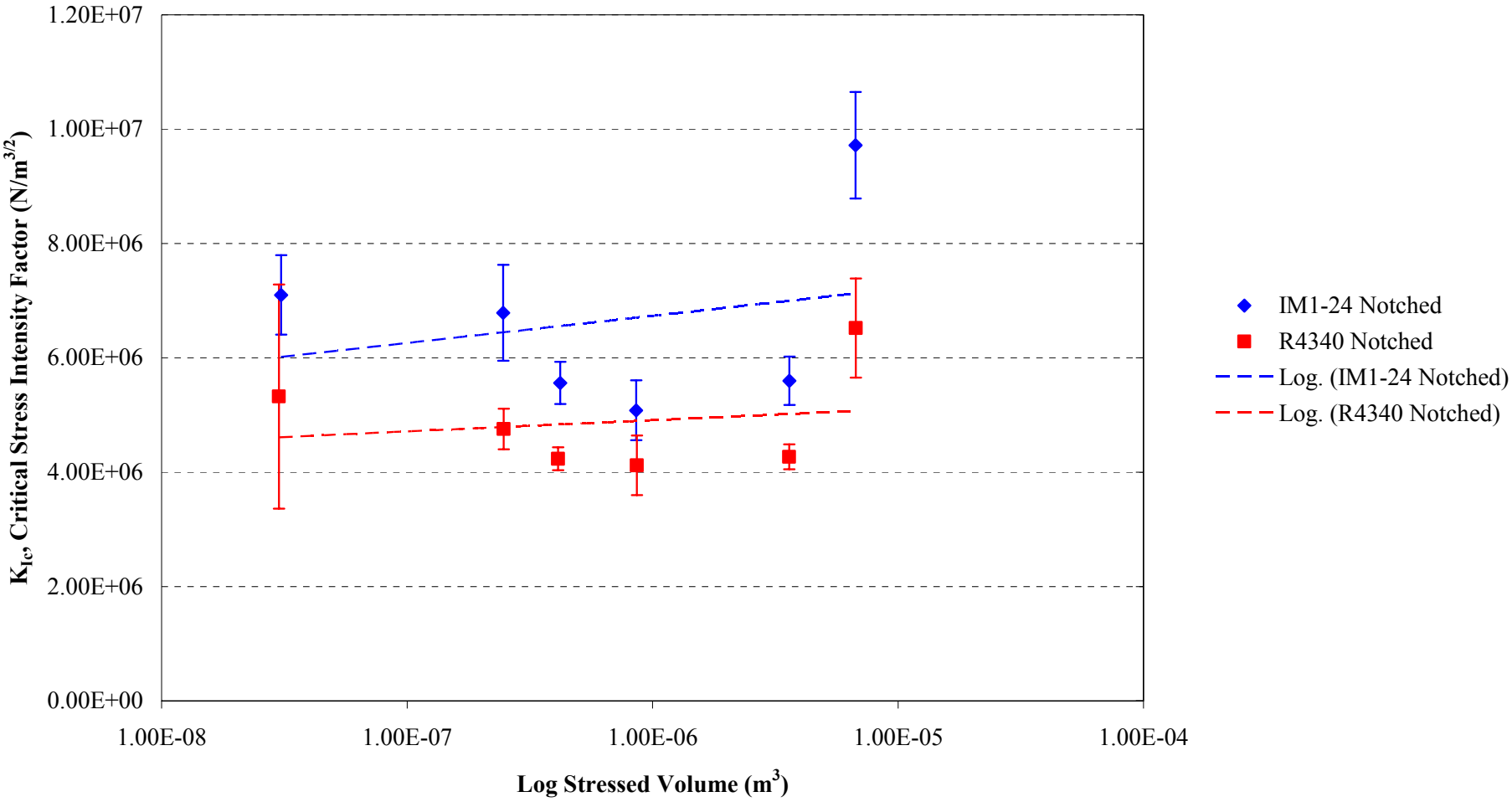

Graph 7.1.18 – Plot of volume versus critical stress intensity factor for notched IM1-24 graphites under 4-pt flexural loading.

On completion of the unnotched testing programme, the specimens containing notches to simulate a pre-cracked component were tested under 3-point and 4-point flexural loading. The tests were carried out under the same conditions as those for the unnotched specimens. Graphs 7.1.13 to 7.1.18 display the trends seen for some of the properties calculated.

During the execution of the notched specimen testing programme, a number of observations were made in how the two materials and the individual specimen sizes behaved under the two different loading conditions, with particular reference to the variation of values recorded for each specimen size. Under 3-point flexural loading, the *A* sized specimens had the greatest variation in maximum load at failure, this being approximately 16% of the average failure load, whilst as the specimen sizes increased the variation in failure load decreased with the *F* sized specimens having a variation of approximately 5% of the average failure load. Under 4-point flexural loading the observations of the initiation of fracture were very similar and the variation in maximum load did not decrease with increasing specimen size.

For the R4340 graphite under 3-point flexural loading, unlike the IM1-24 graphite, the R4340 graphite had a large variation in failure load for each of the specimen sizes, the greatest being seen in the smallest size, with a variation of approximately 48% of the average failure load. Under 4-point loading the variation was less, but still in excess of the values seen for IM1-24.

It can be seen in the previous notched specimen graphs that the change in material properties as the specimen volume increases for the notched specimens is markedly different from that of the unnotched specimens, most notably in that the IM1-24 graphite now becomes the stronger of the two materials. Previously the R4340 graphite, in the majority of cases, registered the higher values of the parameters being measured (*e.g.* stress, strain, flexural strength), but when introducing a crack into the specimens the IM1-24 graphite proves to be the stronger (if only slightly) material.

For the two measurements taken during the experiments (maximum load attained and maximum deflection), very little difference could be seen between the 3-point and 4-point flexural tests. The first significant difference noted between the two types of test

occurred when the nominal stresses at maximum load were calculated. Graphs 7.1.13 and 7.1.14 depict the change in nominal stress with increasing volume, and show that under 4-point flexural loading the nominal stress increases significantly when the *F* sized specimens are tested, unlike the 3-point flexural case where there is a decrease in nominal stress. This is due to the increased stressed volume occurring in the 4-point flexural tests *i.e.*, the stress is distributed over a greater amount of material and therefore an increased stress is required to initiate fracture.

The increased stress to failure does not impact upon the subsequent results that are calculated and displayed in the graphs, as can be seen. Graphs 7.1.15 and 7.1.16 show the plots of effective surface energy (γ_F) against volume for the 3-point and 4-point flexural test notched specimens, respectively. The trend of decreasing energy with increasing volume can be seen again (as with the unnotched specimens), though as the specimens now contain notches the *F* specimens do not skew the results in the same way as they had previously. In the instance of the notched specimens, the largest specimen size appears to require the least energy to cause the surfaces of the material to separate, suggesting that the failure of the pre-cracked sample is independent of the geometry. However, there appears to be no identifiable pattern overall for this parameter, and the results for both the 3-point and 4-point flexural tests differ quite dramatically in the values produced (the values for the 4-point flexural tests are almost double those for the 3-point flexural tests).

With regards the final two graphs, the plane strain fracture toughness calculation returns to showing that the individual specimen sizes do provide repeatable results, with the data obtained displaying very similar patterns for both types of material and load situation. For the 3-point flexural case (graph 7.1.17), the K_{Ic} value is seen to initially decrease through the specimen sizes *A* to *D*, then increase for the last two sizes (dramatically so for the *F* specimens), indicating a point at which the materials require more energy to initiate fracture. This can be expected with increasing cross-sectional area, and hence a greater proportion of bulk material. In graph 7.1.18 the same trend is seen more clearly under the 4-point flexural loading, with a clearer definition of this being shown between the *D* and *E* specimen sizes.

The notched specimen results indicate that the microstructure of IM1-24 graphite is better able to withstand loading whilst containing a crack than the R4340 graphite. R4340 has a very fine grain and almost homogenous microstructure, with no inherent particles that would arrest or divert a crack once it has been initiated. Indeed, as it is a more brittle material, any flaws or defects present will reduce its ability to withstand stresses and strains significantly. The random microstructure of IM1-24 graphite lends itself to being more resistant to crack propagation than R4340 graphite, but the unnotched flexural loading has shown that it requires less stress to initiate catastrophic failure.

The results obtained through the experimental programme will be discussed further in Chapter 8 - Discussion in relation to those obtained through the microstructural modelling and how these results can be utilised for describing the behaviour of graphite at a range of scales. The experimental values taken from the tests and the values calculated can be viewed in Appendix D on the CD-ROM in the following files:

- IM1-24 Test Sample Dimensions.xls
- R4340 Test Sample Dimensions.xls
- Unnotched IM1-24 Results.xls
- Unnotched R4340 Results.xls
- Notched IM1-24 Results.xls
- Notched R4340 Results.xls

Additionally, all the graphs generated in the course of the analysis can also be viewed within these files under the relevant worksheet tab.

7.2 Fracture Observations

Throughout the testing programme, observations were made on the fracture of each test specimen under the different loading conditions, particularly for the flexural experiments, with the locations of the fracture initiation sites and the crack path within

the failed specimen noted. These observations provided further comparison for the materials mechanical behaviour.

Under compressive loading the failure of the specimens was explosive and generally with a small amount of buckling occurring prior to failure. Inspection of the IM1-24 specimen fragments showed that for the smallest size *A* specimens the mechanism of failure was shear as the fracture plane occurred at 45º to the applied force, with all the specimens breaking into two distinct fragments approximately equal in size. As the specimen size increased, a different failure mechanism occurred. 70% of the *B* size specimens exhibited shear failure through the approximate centre of the sample, but the remaining 30% fractured with a combination of shear and lateral strain failure at the upper or lower end of the specimen (nearest the platen and applied force), with small fragments initially breaking away from the bulk. For the *C* and *D* specimens, shear failure through the centre was again the dominant failure mode, but there was an increase in the number of specimens failing under lateral strain (40%), and the number of fragments produced. All ten *E* sized specimens failed catastrophically due to lateral strain failure, resulting in high degree of fragmentation. The majority of *F* specimens failed via shear, with fracture path being diagonally across the whole specimen (45º to the applied force).

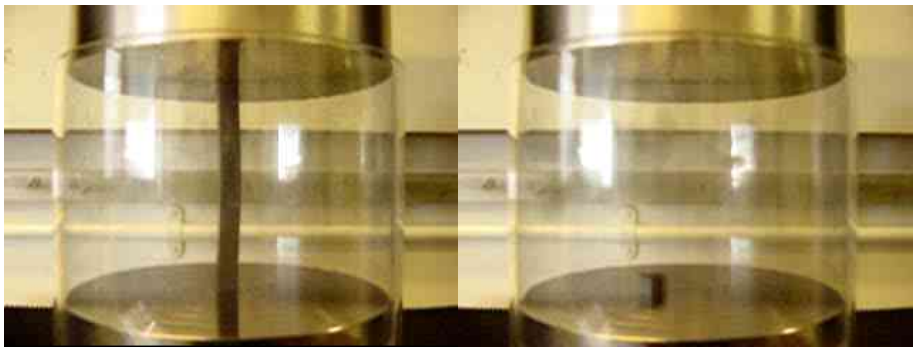

Figure 7.2.1 – Two frames in sequence during the compression test of an 'E' size specimen of IM1-24 graphite, demonstrating that the high energy fracture of the specimen prevents standard video capture of the fracture process.

It is interesting to note that some of the tests were video captured by a digital camera and that when viewed frame-by-frame at the point of failure the fragments appear to disappear, demonstrating the high velocity of the fragments during fracture. Figure 7.2.1 shows two frames from the compression test of an IM1-24 *E* specimen as fracture

occurs, the second frame appears to only contain the base of the specimen, though the other fragments are present.

For the R4340 graphite compression tests, all the specimens at all sizes exhibited critical strain failure with a high degree of fragmentation occurring. For the majority of specimens, the areas nearest the compression platens showed the highest degree of damage, with very few specimens fracturing around the centre. The only additional observation made relates to the *F* size specimens, whose failure was preceded by small fragments of material breaking away from the corners of the sample at approximately 90% of the failure load.

The observations for the IM1-24 compression tests indicate that there is a dimension at which shear failure stops occurring and strain failure begins. A specific value cannot be concluded from this testing programme, however, the results indicate that the length of the specimens may be a significant factor as the longest specimens exhibited strain failure whilst the shortest exhibited shear failure with both specimens having the same ratio of length to cross-sectional area.

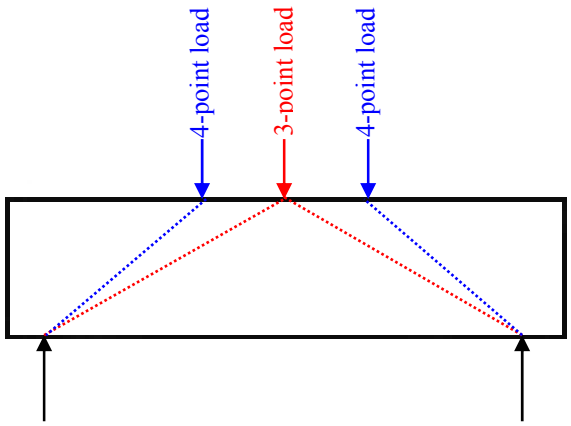

Figure 7.2.2 – Expected fracture area for 3-point (red) and 4-point (blue) loading (for illustrative purposes only).

Under flexural test conditions it is expected that fracture will occur in the stressed area of the specimen (within the confines of the red and blue lines depicted in Figure 7.2.2). Observing the fracture path in this region indicates that the test setup and loading conditions are correct. For both material types and all unnotched specimen sizes, failure occurred in this region.

For the IM1-24 graphite specimens under 3-point loading, the fracture path occurred through the stressed zone in all cases. All the specimen sizes exhibited the same failure mechanism (lateral strain failure), but the *F* sized specimens displayed indentation on the upper and lower surfaces where contact with the loading points were made. At approximately 50% of the failure load, small fragments of material broke away from the bulk around the support and loading points. For these particular specimens the failure load was approximately 6 kN, whereas the other specimens failed at loads typically under 1 kN, indicating that the increased cross-sectional area was able to withstand a much greater load with small sections of material fracturing before failure of the whole. Additionally, the first *F* specimen to be tested exhibited a degree of shear failure, with the crack path originating at one of the support points and propagating to the centre of the specimen before failure occurred. This phenomenon was observed in half the *F* specimens tested under 3-point loading. In isolated cases relating to no specific specimen size, the condition to meet the end of the test (10% of the maximum load) was reached before the specimen had fractured all the way through. This occurred with one of each of the *A*, *C* and *E* specimens and could be attributed to the fracture path encountering a large area of porosity at which very little load is required to propagate the crack further, or possibly a movement in the test equipment that would cause the load on the specimen to decrease.

The IM1-24 graphite under 4-point loading exhibited strain failure through the stressed zone for all specimen sizes, though several specimens contained an element of shear failure as the crack propagated around a Gilsocarbon particle (6 specimens in total). As with the 3-point flexural tests, several of the *F* sized specimens experienced minor indentation on the upper and lower surfaces due to the relatively high load required to cause failure.

The fracture surface of the R4340 graphite is considerably different to that of the IM1-24 graphite due to the much finer grain structure of the material (see Figure 7.2.3). For the R4340 graphite under 3-point loading, all specimens fractured though the centre of the specimens sized *A* to *E*, creating two approximately equal halves. As with the IM1-24 graphite, the *F* sized specimens underwent indentation of the surfaces in contact with the support and loading points, and for several specimens, fragments of material broke away from the bulk at between 80% and 90% of the final failure load. The fracture path

of the *F* specimens varied to those of the other sizes, with the crack being vertically orientated (3 samples) or propagating diagonally through the stressed zone (7 samples), though lateral strain failure was still the fracture mechanism. This effect was not observed in any of the other specimen sizes and could be due to the increased load required to initiate failure causing instability in the test rig.

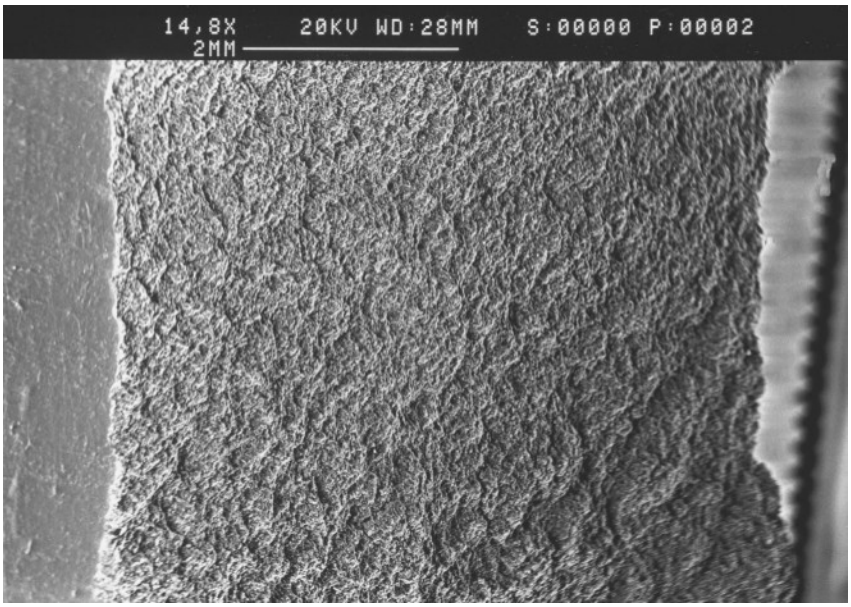

Figure 7.2.3 – SEM image of the fracture surface of R4340 graphite demonstrating the finer grained material.

Observations made of the 4-point loading specimens under failure appeared to be the same as those of 3-point loading, with some minor differences. Specimen sizes *B* to *E* demonstrated classic brittle failure with lateral strain failure occurring in the centre of the load span and changing to shear failure as the crack propagates. An example of this can be seen in more detail in Figures 7.2.4 and 7.2.5.

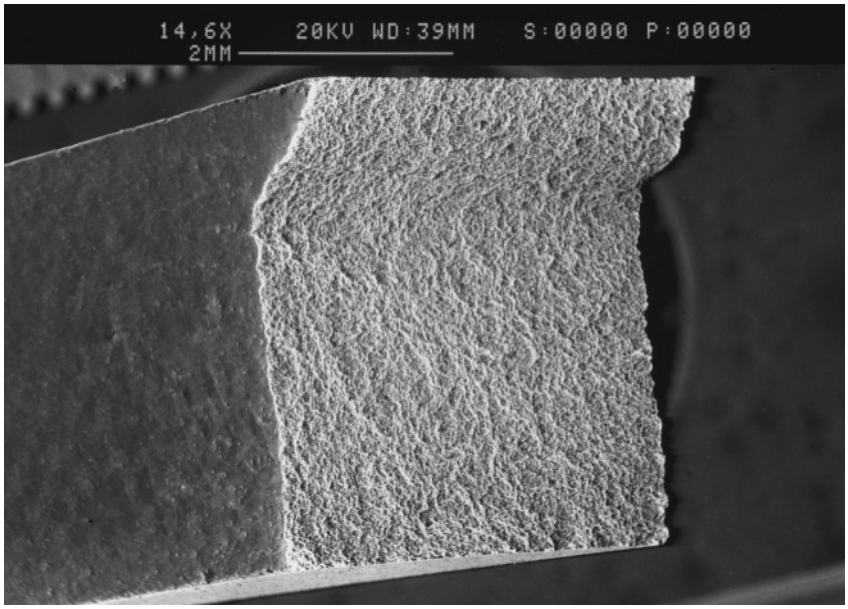

Figure 7.2.4 – SEM image of an R4340 E specimen after failure under 4-point loading (left hand side of specimen).

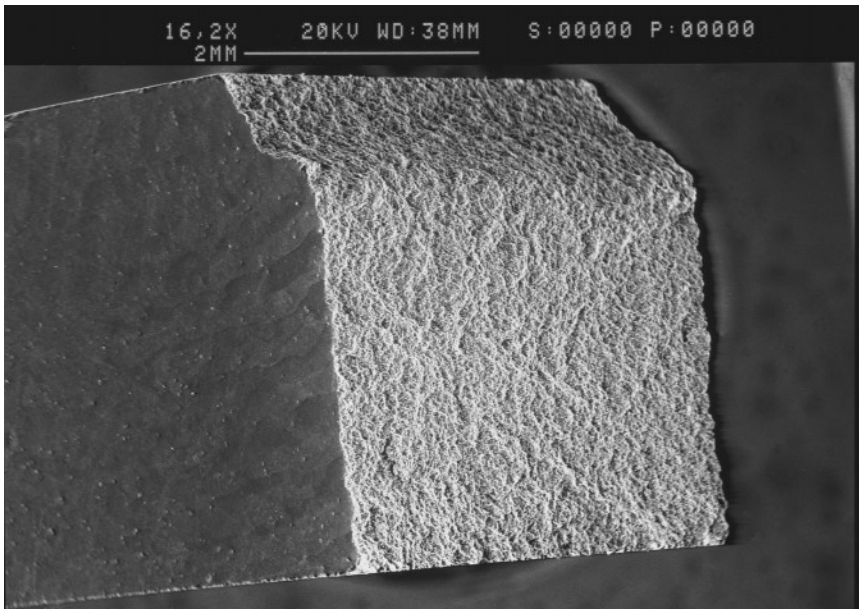

Figure 7.2.5 – SEM image of an R4340 E specimen after failure under 4-point loading (right hand side of specimen).

Typically, fracture surface examination is performed using optical and scanning electron microscopy due, but with the advancement in technology more techniques are becoming available that enable more accurate viewing of fracture surfaces. For example, being able to map the topography of a fracture surface gives a 3-dimensional representation and can enable a more accurate picture of the mechanisms of failure. It can also benefit in the calculation of fracture parameters in that if the precise fracture

surface area can be measured rather than the standard 2-dimensional approximation, a more accurate result can be obtained. Figure 7.2.6 shows an example of the topography of the fracture surface of IM1-24 graphite after failure under compression, with Figure 7.2.7 depicting the actual specimen used for the scan. The image was produced by Eleys' Tracecut software that generates a 3-dimensional image based on a specimen 'scanned' by tracing the surface with a fine stylus connected to a system of microswitches that recognise vertical movement. Currently this process is not fully suitable for fracture surfaces that contain fine detail (features less than 0.3 mm in size due to the limiting diameter of the stylii) and hence could not be utilised in full for this thesis, but do aid in gaining a better picture of the results of failure. With an improved resolution it is possible to see the advantages of this particular technique, giving the ability to manipulate the fracture surface in 3 dimensions, analyse the fracture mode through reassembling the failed component, and accurately measuring the fracture surface area to name just a few.

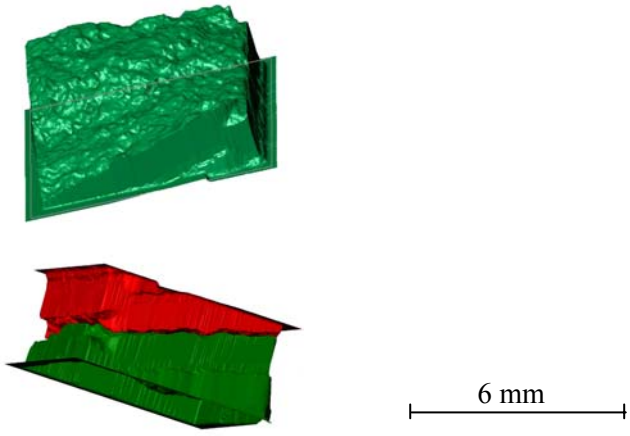

Figure 7.2.6 – Eley Tracecut scan of the fracture surface of graphite. Top - a representation of one of the fracture surfaces; Bottom – realignment of the two fracture surfaces.

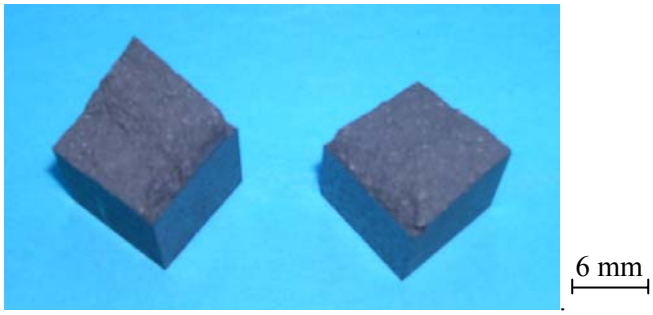

Figure 7.2.7 – Fracture surfaces of the graphite specimen used for the Tracecut scan (failure occurred under compressive loading).

7.3 Summary

Chapter 7 has detailed the results obtained from the mechanical testing programme designed to gain additional data on graphite material properties and provide validation for the modelling programme. On examining the results obtained from the testing programme it becomes apparent that the measured properties of graphite are dependent on both the test employed to determine the property, and the size and geometry of the test specimen used. Several of the calculated properties of IM1-24 graphite are lower in value than those given in literature (*e.g.* compressive strength and secant Young's modulus), whilst the fracture toughness value is higher than that classically used for IM1-24 graphite, though still appropriate for a ceramic material. A wide variation in results was seen in all tests performed, causing large deviations around the mean at the smaller specimen volumes which are seen to reduce at the larger specimen volumes. However, in line with the expectations of the material, the strength of IM1-24 graphite under both compression and flexural testing was observed to decrease with increasing volume.

The results observed for the reference graphite (R4340) follow those obtained for IM1-24 graphite relatively closely. Very similar trends can be seen on graphs 7.1.1 to 7.1.18 under all loading conditions. This similarity implies that all tests for both materials were performed under the same conditions and in the same manner, and that there is a high confidence in the accuracy of the data obtained.

Further analysis of the results obtained from the testing programme and how these results relate to the modelling programme can be seen in Chapter 8 – Discussion.

Part D: Discussion, conclusions and further work

Chapter 8 – Discussion

On the completion of both the conceptual modelling and the mechanical testing programme, a large amount of data was collated and analysed to provide both validation for the finite element model predictions and to increase the understanding of the failure of graphite components. The following chapter discusses the predictions of the finite element models and how they compare both to the mechanical testing data and to the literature available on graphite. The chapter also highlights observations made during both the conceptual modelling and mechanical testing programme and determines the validity of both.

From the analysis of the pore distributions through the models, it became clear that although the models were designed with a view to predicting stress and strain effects within the microstructure of IM1-24 graphite, the random generation of the microstructures themselves did not produce models that fully represented IM1-24 graphite. Indeed, at the larger scales the models appear more like the mechanical testing reference material R4340 graphite (discussed in Chapter 6 – Experimental Details) than IM1-24 graphite. This has led to the summation that IM1-24 graphite may not be a wholly random microstructure, and that the manufacturing methods and extrusion process may influence some uniform structure in the material. Figure 8.1 below illustrates the similarities between the randomly generated microstructure and that of R4340, the model has been colour corrected to display the porosity as black areas in the image.

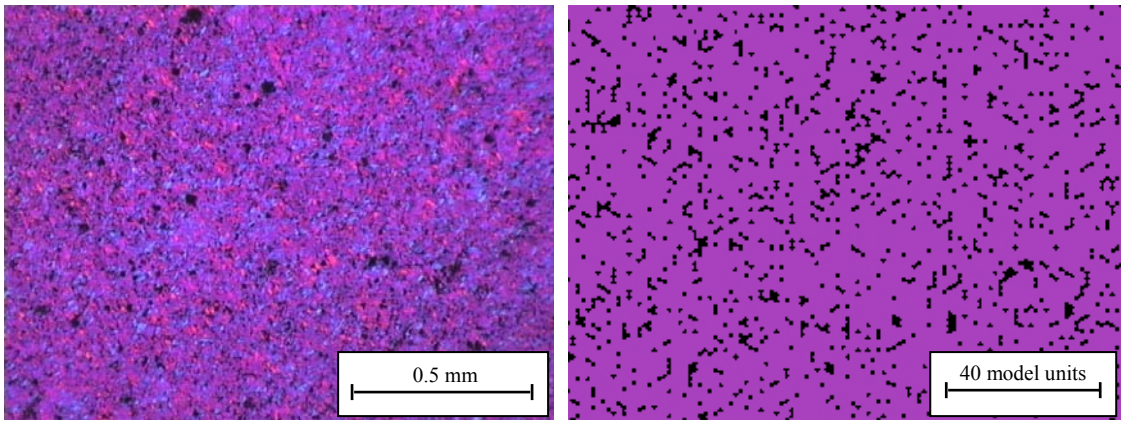

Figure 8.1 – Comparison of R4340 graphite (left) to a randomly generated model microstructure (right).

It is possible to see that there is more similarity between the generated model and R4340 graphite than there is to IM1-24 graphite shown in Figure 8.2. This creates some concern over the predictions that have been made by the conceptual models as the material property inputs are based on those for IM1-24 graphite.

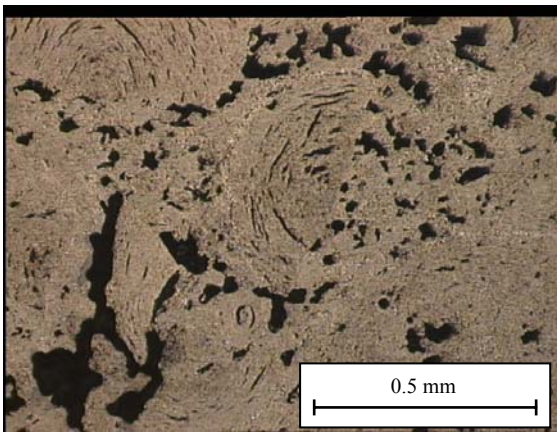

Figure 8.2 – Microstructure of IM1-24 graphite.

It can be said that the models microstructure is more reminiscent of finer grained graphites with smaller conglomerations of pores and filler particles than IM1-24 graphite. However, the predictions made by the models can still provide insight into the behaviour of IM1-24 graphite under tensile and compressive loading.

On the analysis of the stress and strain distributions through the model it was observed that the stiffer of the two materials present in the model (the binder phase) carried more of the stress than the filler particles, and that the highest concentrations of stresses and strains were not necessarily located around the largest pores. This is not in line with the

weakest link theory put forward by Weibull (1939), and suggests that it is possible for the material to fail in regions of solid material. As cracks follow the path of least resistance it is more than likely the site that would initiate failure contains a higher proportion of binder material with a conglomeration of pores nearby. Figure 8.3 illustrates this with the area labelled *A* marking the largest pore chain in the model and *B* marking the region of maximum stress.

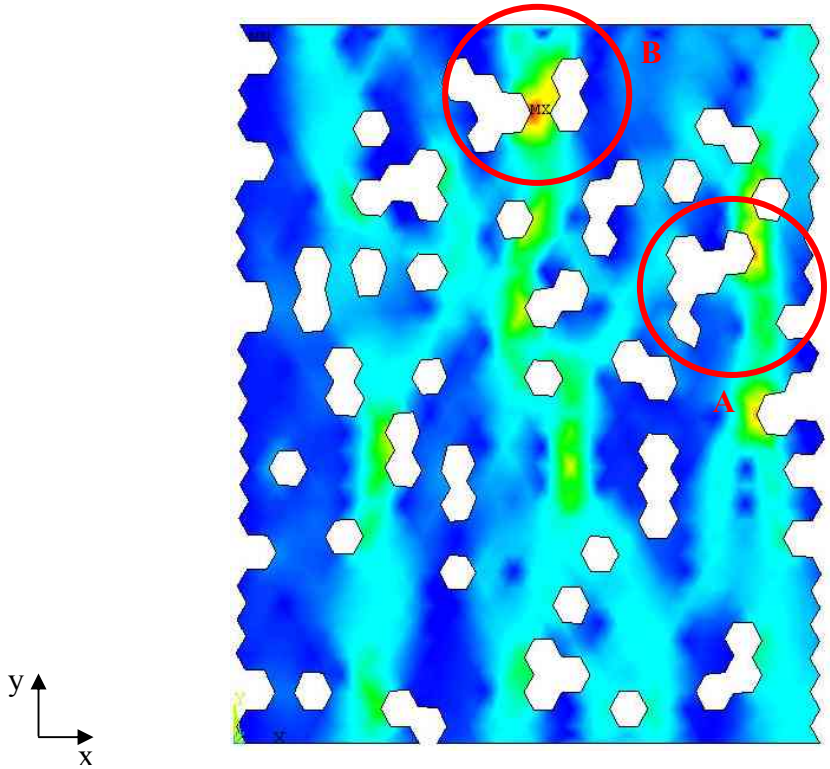

Figure 8.3 – 1st principal stress of a 20 x 20 model under tension.

This observation of the highest stresses being located in the regions densely populated by binder material is also noted by Steer (2003). The Ligament Model uses the structural engineering principle that stiffness attracts load, and employs the theory that when microstructural elements are linked and displaced, the elements carry the load in proportion to their stiffness. If the Young's modulus of the ligaments are not equal then as the load is increased some ligaments will break but will not necessarily cause failure as the load can be transmitted along the remaining ligaments. The model predictions made by ANSYS fall in line with this theory. Figure 8.4 shows the same image as Figure 8.3 but with the locations of the filler particles highlighted. The majority of the stress can be seen to be carried through the binder material, away from the filler particles that have a higher elastic modulus. The areas of highest stress can be seen to

occur in the regions of binder that are in close proximity to pores, suggesting that these areas would be likely to fail first with the remainder of the material being able to distribute the load in that event.

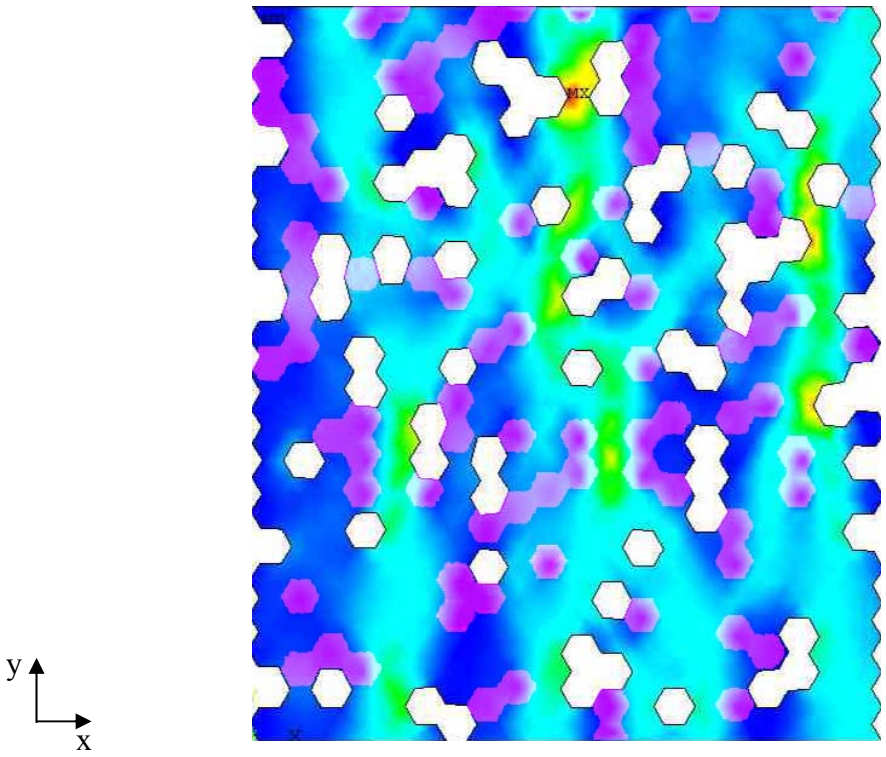

Figure 8.4 – 1st principal stress of a 20 x 20 model with filler particle position overlay.

As detailed in Chapter 4 –Conceptual Modelling, the material properties chosen for the inputs to the model were selected with care to ensure that the properties for the filler and binder phases of IM1-24 graphite were correct. As it has transpired, the random generation of the model structure has not strictly represented the graphite microstructure, and not all the values obtained are not an exact match to those expected of IM1-24 graphite. The overall porosity of the models (including the inherent porosity within the Gilsocarbon particles) does equate to 20% at all but the smallest model sizes, which can be attributed to the small scale not being a fully representative cross-section of the material. The measured strain values after displacement for the Von Mises strain equal 0.22% under tensile loading and 2.2% under compressive loading which would be expected due the displacement of the models. However, the 1st principal strain values are somewhat lower than this (0.16% and 0.8%, respectively). This could be because the determination of the 1st principal strain is done solely from the reactions in the *y*-direction and does not fully consider the small strains present in the *x*-direction.

The calculation of the secant Young's modulus also does not fit the expected literature value for IM1-24 graphite. The average value determined under tension was approximately 25 x 10^{10}, and under compression was 8.6 x 10^{10}. These are in excess of both the literature values and the results of the mechanical testing programme. This can also be attributed to the fact that the generated microstructure is not representative of the actual IM1-24 microstructure, and the model is only considering the stress and strain in 2-dimensions.

On comparing the predicted trends from the conceptual modelling to data available within literature, some encouraging information was seen. Greenstreet *et al.* (1969) was one of the few sources available that have studied the same types of graphite under tension and compression. Taking data from their paper and plotting the stress versus strain under both tension and compression produced Graph 8.1.

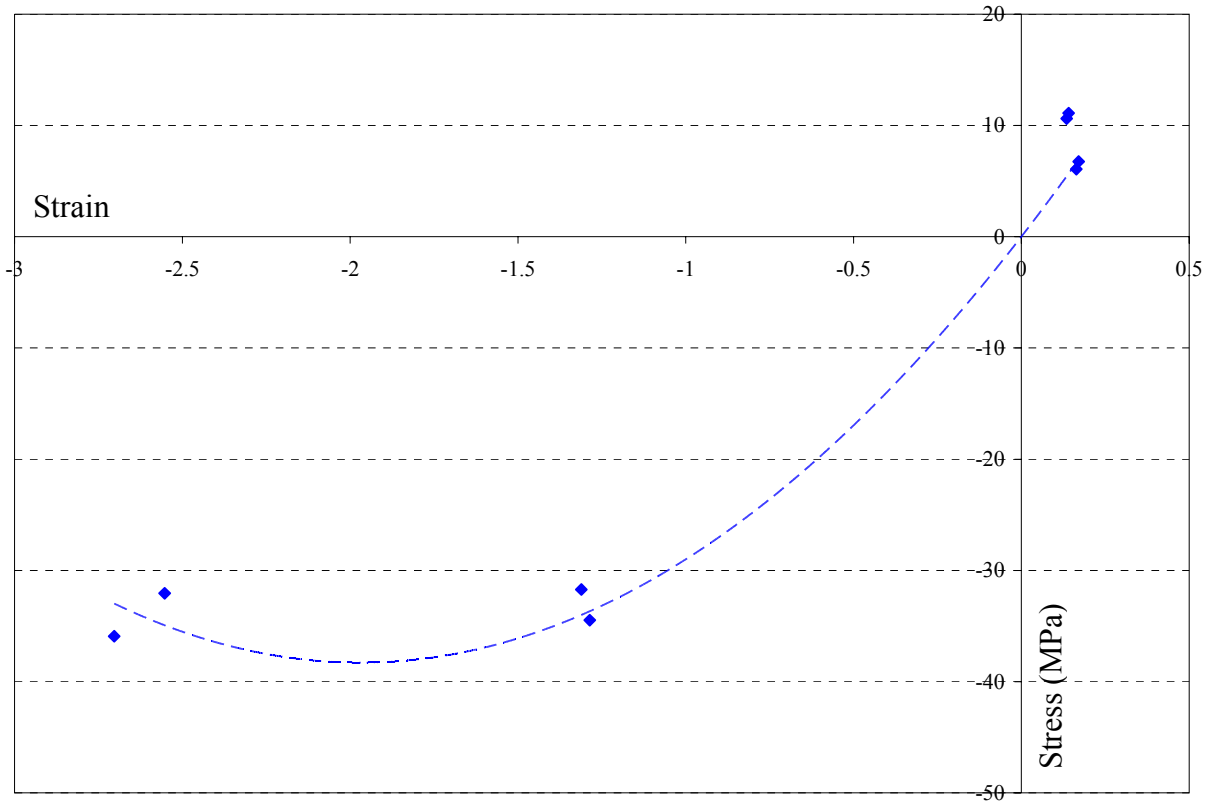

Graph 8.1 – Stress-strain curve for tension and compression from data obtained from Greenstreet *et al.* (1969).

Comparing the distribution of the data with that of Graph 8.2 which shows the stress plotted against strain for the predicted model results it can be seen that although the

figures do not match (and would not be expected to), the distribution of the data is very similar.

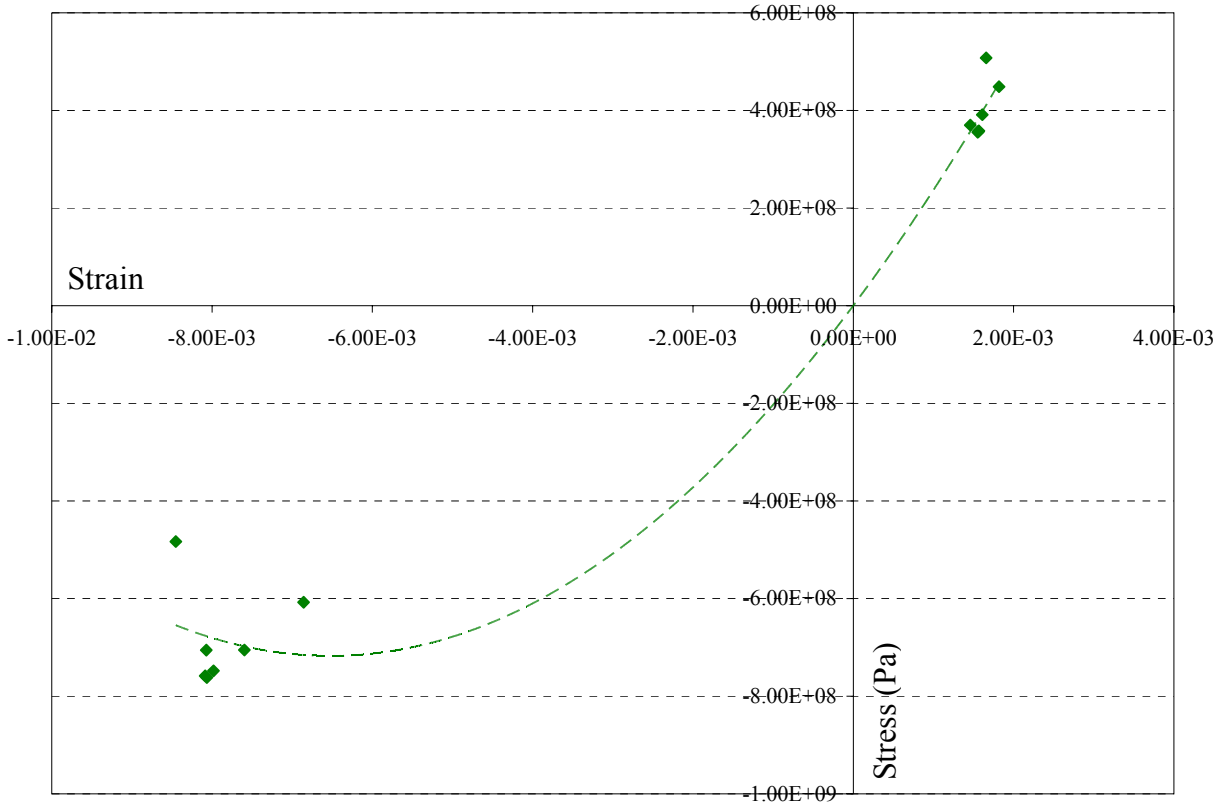

Graph 8.2 – Plot of stress against strain for the predicted 1st principal results from the conceptual modelling.

For using the experimentally derived data as a validation tool for the conceptual modelling programme, it initially has to be verified against data available in the literature. The typical values for UK nuclear graphites are given in Table 8.1, and the average values obtained from the experimental programme are shown in Table 8.2.

Density	**Young's Modulus**	**Compressive Strength**	**Flexural Strength**
1.804 - 1.819 g/cm^3	9.5 - 12 GPa (Dynamic)	~ 80 MPa	24.4 - 28.9 MPa

Table 8.1 – Typical UK nuclear graphite mechanical properties (Nuclear Electric, 1996).

Density	Young's Modulus	Compressive Strength	Flexural Strength
1.748 g/cm^3	2.13 - 2.72 GPa	60 - 70 MPa	13.7 - 30 MPa

Table 8.2 – Experimentally derived values for IM1-24 graphite.

As can be seen from the above tables, the experimentally derived values are lower than those given in the literature. This could be due to a number of reasons, primarily that the graphite being tested was not reactor grade IM1-24 graphite. It had a lower measured density and therefore is more likely to have been reflector grade graphite. This would account somewhat for the lower compressive strength value. Also, the specimen sizes have a distinct effect on the strength of the material.

As demonstrated by Brocklehurst (1977) under tension as the specimen size increases, the strength of the specimen increases. Under compression a similar effect would be seen with higher strength values being recorded as a greater load is required to fracture the specimens under compression. Under flexural loading, Brocklehurst observed an initially increasing strength followed by a steady decrease as the specimen sizes became greater than 1 cm^3. In the experimental programme under both 3-point and 4-point loading the same effect was observed as all the specimen sizes were greater than 1 cm^3. The change in strength with increasing specimen size seen throughout the testing programme is in line with previous studies, even if the values obtained are not the same as those anticipated for IM1-24 graphite.

The variation of strength results obtained under 3-pt and 4-pt flexural loading may be due to the stress states induced by each of the flexural loading conditions. Under 3-pt flexural testing the maximum bending moment occurs at the point of loading which causes the highest stress concentrations to occur in the centre of the specimen. Under 4-point testing the maximum bending moment occurs across the region between the two points of contact on the loaded surface. The bending moment for each loading condition dictates the areas of the specimens that are stressed and consequently the region in which failure is likely to occur. Referring to figure 7.2.2, under 3-point loading a test specimen has a smaller stressed area than that under 4-point loading, suggesting that there is a reduced probability that a critical flaw will be present to

initiate failure. This reduced probability implies that there will be a greater variation in results at smaller specimen volumes than seen at larger specimen volumes.

On initial viewing of the results this explanation appears valid for the IM1-24 graphite specimens under 3-point flexural loading, as the specimen sizes increase, the deviation from the mean flexural strength decreases. However, when examining the 4-point flexural results it can be seen that the deviation from the mean flexural strength value does not always decrease with increasing specimen size, the 'C' sized specimens have a larger standard deviation than all the other specimen sizes. The same effects are also observed in the R4340 graphite specimens. This suggests that although differing volumes of material are stressed under both 3-point and 4-point loading, the probability of a large or critical flaw being present may not directly affect the strength of the graphite. As seen in the stress distributions produced by the modelling programme, the highest concentration of stress is not necessarily located near the largest pore in the model.

However, whether failure is initiated by a critical flaw or not, it is clear that the volumes under stress in 3-point and 4-point loading are smaller than the physical volume of the specimen and, in the case of the smaller specimen sizes in particular, these volumes may not be representative of the actual microstructure of the bulk material (*i.e.* smaller pores or flaws will have a greater affect on the ability of the material to withstand loading). This raises the question of whether the test specimens currently machined from the trepanned material from an AGR core are the correct size for predicting scaled up properties of nuclear graphite.

The reference material (R4340 graphite) results obtained from the testing programme are interesting in that they are for a much finer grained graphite than IM1-24 with the tests showing the material to be more brittle. R4340 graphite displayed very similar trends to those of the IM1-24 graphite but with slight value differences (see Table 8.3). Interestingly, through displaying more brittle behaviour than IM1-24 graphite, R4340 graphite is more analogous to irradiated IM1-24 graphite, with the results obtained through testing the material under compressive and flexural loading being closer to the reported values in the literature for UK nuclear graphite.

Density	Young's Modulus	Compressive Strength	Flexural Strength
1.777 g/cm^3	2.31 - 2.54 GPa	86 - 106 MPa	23 - 59 MPa

Table 8.3 – Experimentally derived values for R4340 graphite.

As with the values obtained from the literature, the experimentally derived values do not fit the values from the FEA models. However, the trends observed from the experiments on the varying specimen sizes do indicate that the models are at least showing the expected behaviour, *i.e.* increasing stress and strain with increasing model size under compression and tension.

The following analysis uses the average 1st principal stress through the whole of the model as the data obtained from the modelling programme, as it is assumed that this is more analogous to the testing results where the stress is calculated based on the specimen area.

Producing Ashby plots of the test results in order to compare them to the modelling results has shown that the two sets of data are not in line, the modelling results are not fully comparable with the testing results. Below are several Ashby plots to demonstrate this. For all the plots referring to volume, the modelling volumes have been adjusted so that they can be compared on the same graph. The units used in the modelling programme were arbitrary and have not been set to any scale (*i.e.* 1 unit could be 1 mm, 1 cm, 1 m, *etc.*).

In Graph 8.3 the Young's modulus can be seen to be fairly constant with increasing volume in the larger size models but the testing results do not display this. It was expected that the modelling values would not be the same as the testing results as different geometries were being analysed. The modelling results show a large variation at the smaller volumes, becoming more consistent at higher volumes. This indicates a convergence to the virtual materials volume, meaning that in a strictly static sense the Young's modulus is constant. Additionally, the smallest size models might be too small to give reliable results (as with Brocklehurst's (1977) observation on small scale graphite specimens); the smallest sized model effectively contains only one pore which would make it much smaller than the test specimens.

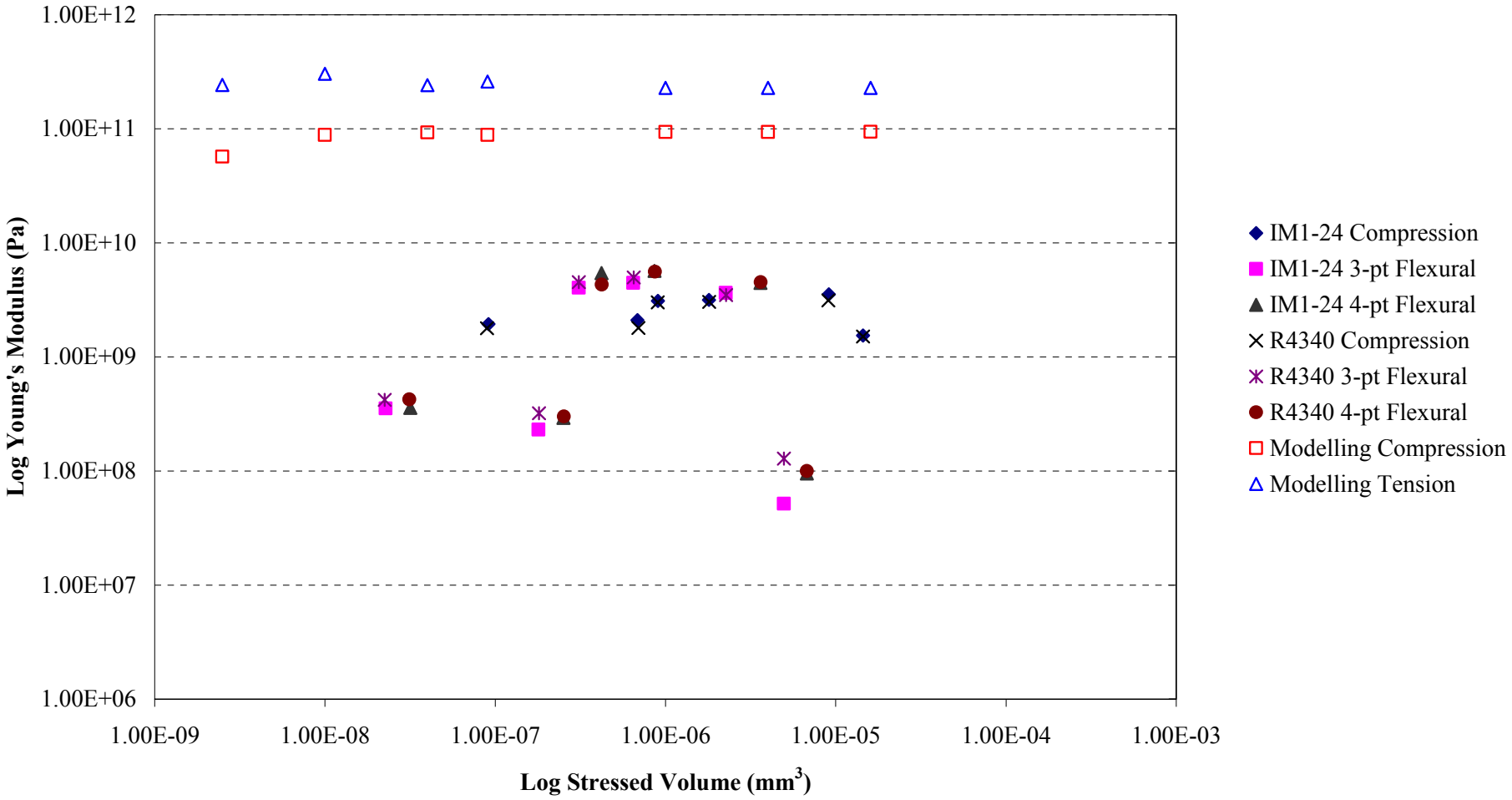

Graph 8.3 – Ashby plot of Young's modulus vs. stressed volume (the modelling volume has been normalised by dividing by a factor of 10).

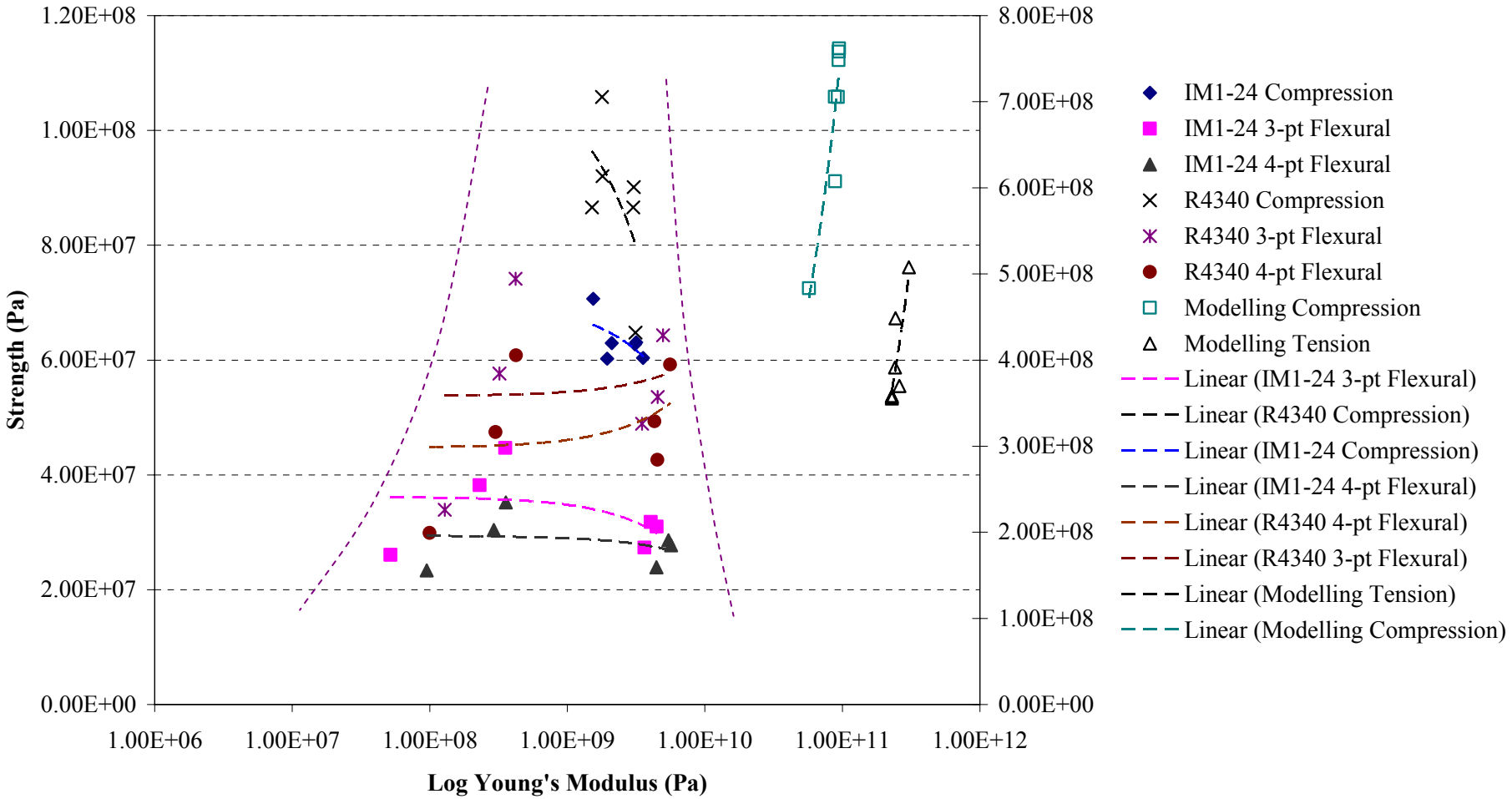

Graph 8.4– Ashby plot of strength vs. Young's modulus (modelling results are plotted against the right axis, testing results against the left axis).

Although there is a lot of information on Graph 8.4 what is clear is that the compression and flexural tests for the IM1-24 and R4340 graphites follow similar patterns, whereas the modelling results do not compare favourably. It seems to be that through choosing to displace the models by a fixed distance (2% in compression and 0.2% in tension), and taking readings of the results at this point has caused constant strain through the models which is preventing straight forward comparison with the testing data. The difficulty of comparison is highlighted by the band of experimental data within the lighter dotted lines, showing that the real world materials have a relatively constant strength over increasing Young's modulus which is at odds with the models' constant Young's modulus.

Graph 8.5 also contains a large amount of information, but the modelling results can be seen to have constant strain values, whilst the testing results have decreasing strain (if the largest specimen is not taken into account due to its differing geometry, highlighted on the graph). Graph 8.6 shows the comparison of stress and strain which highlights the same point.

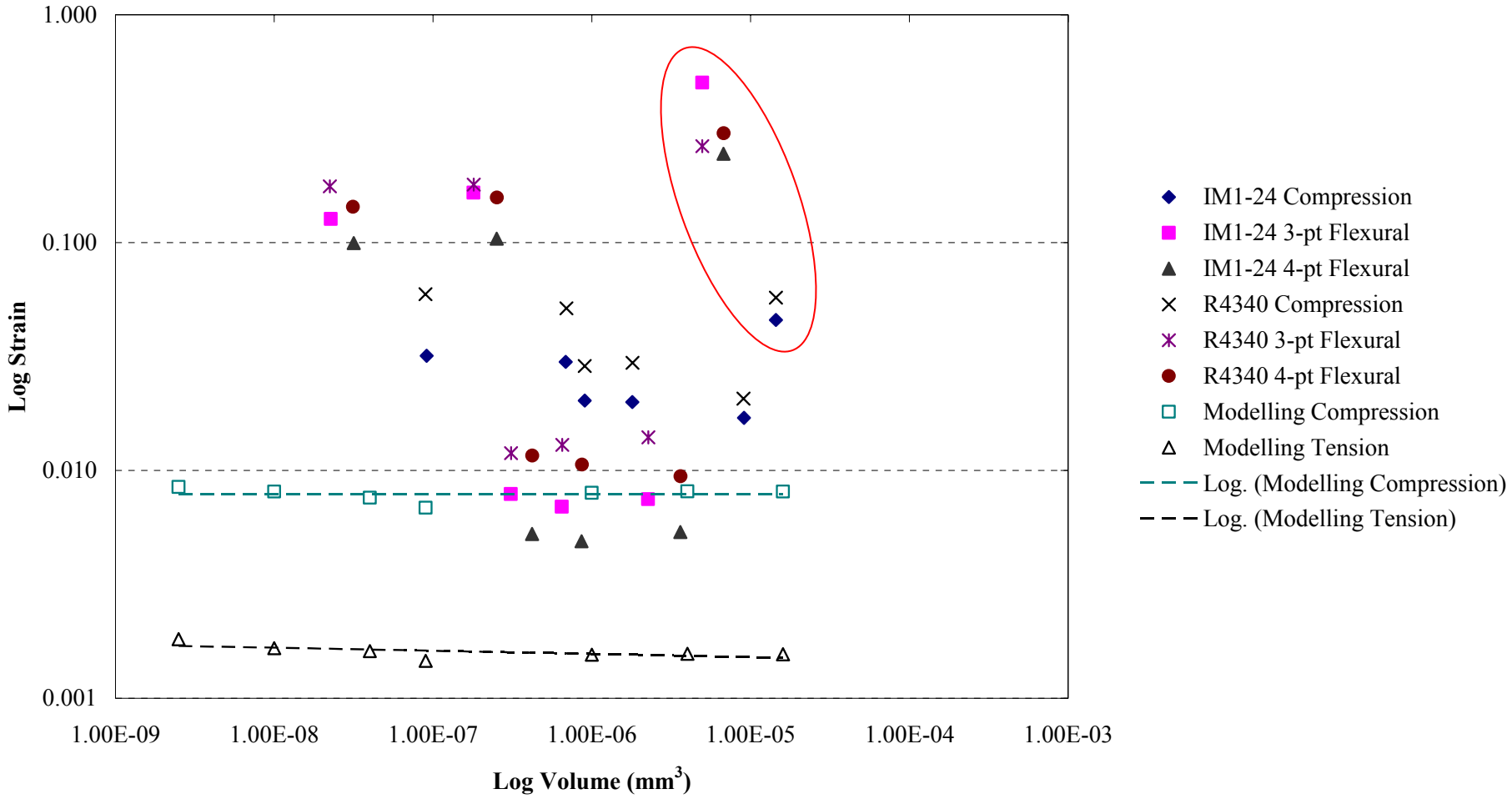

Graph 8.5 – Ashby plot of strain vs. volume for the modelling and testing programmes.

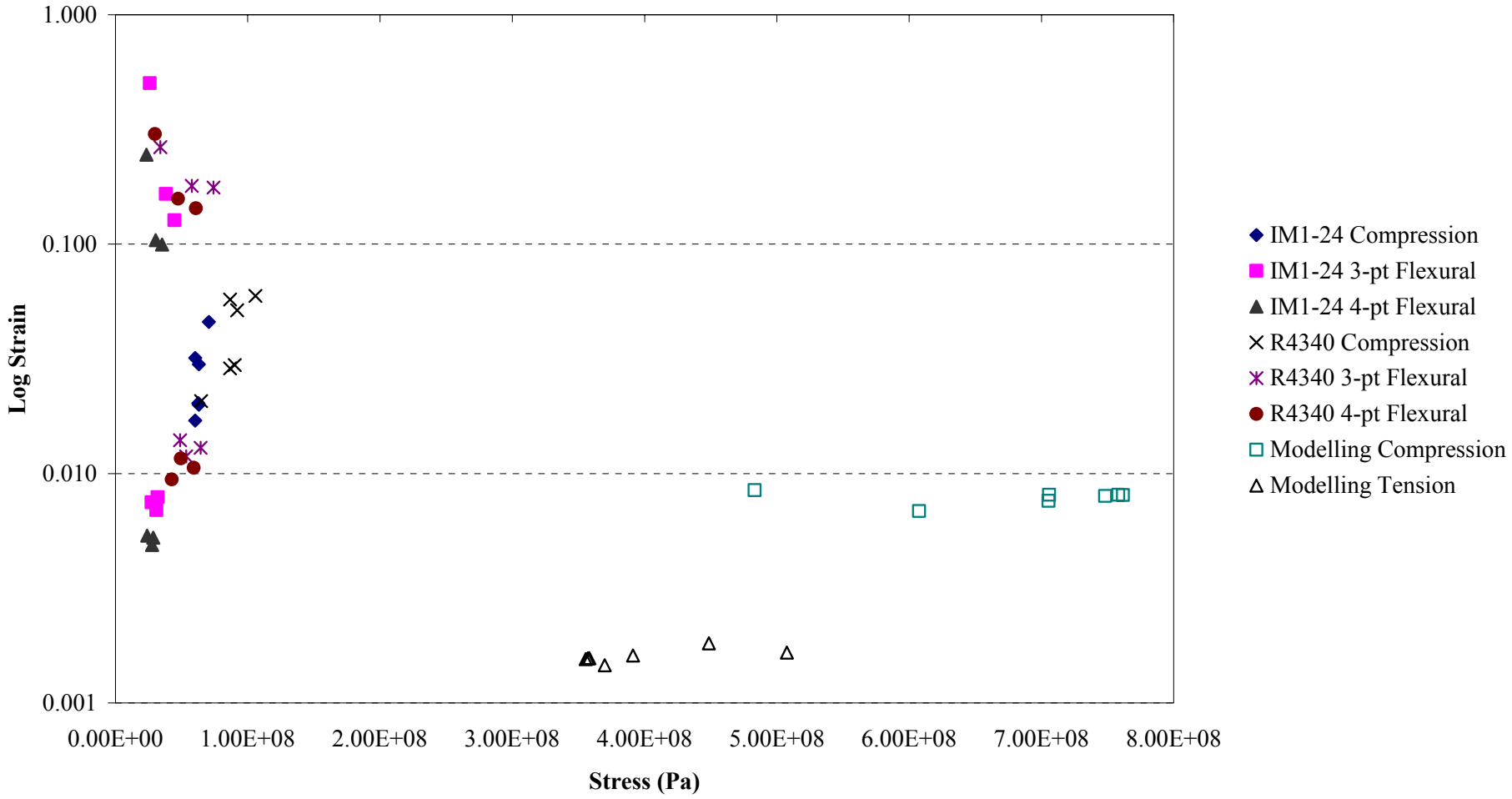

Graph 8.6 – Ashby plot of strain vs. stress for the modelling and testing programmes.

Graphs 8.5 indicates that as the specimen sizes increase the fracture strain decreases, as is seen in many real world materials (*e.g.* a short ruler is harder to snap than a large ruler). This would assist in explaining the 'fall off' in strength in the work by Brocklehurst (1977). As Young's modulus is assumed to be constant, as the specimen sizes increase the fracture strain decreases and so must the strength.

Graph 8.6 examines the stress-strain relationship for the modelling and testing programmes. It is clear from the spread of data that there is no correlation between the two sets of results. The testing results display an increasing stress with increasing strain relationship (though not easily visible on the graph), whilst the modelling stress increases with constant strain.

Graph 8.7 is purely strength versus strain for the testing results, showing that each test method (compression, 3-pt and 4-pt flexural) has its own stress-strain pattern which is followed by the two types of material. The R4340 graphite exhibits higher strength with increasing strain in all instances due its less porous and more homogenous structure than IM1-24 graphite. These properties make the material less elastic than IM1-24 which enables it to withstand higher strains and in turn have a higher resistance to fracture.

Taking just the data for compression from the testing and modelling results, Graph 8.8 attempts to show the stress-strain graph to look for any similarities within this area. The modelling values are plotted on the right hand axis, whilst the testing values are plotted on the left hand axis. There is too much variation in the modelling compression results to enable a comparison, and whilst the tension results look promising, the gradient of the trend line is too steep to correlate with the testing results. The compression models would fit with the tension models, but for one result of the 30 x 30 models which is significantly lower than the rest.

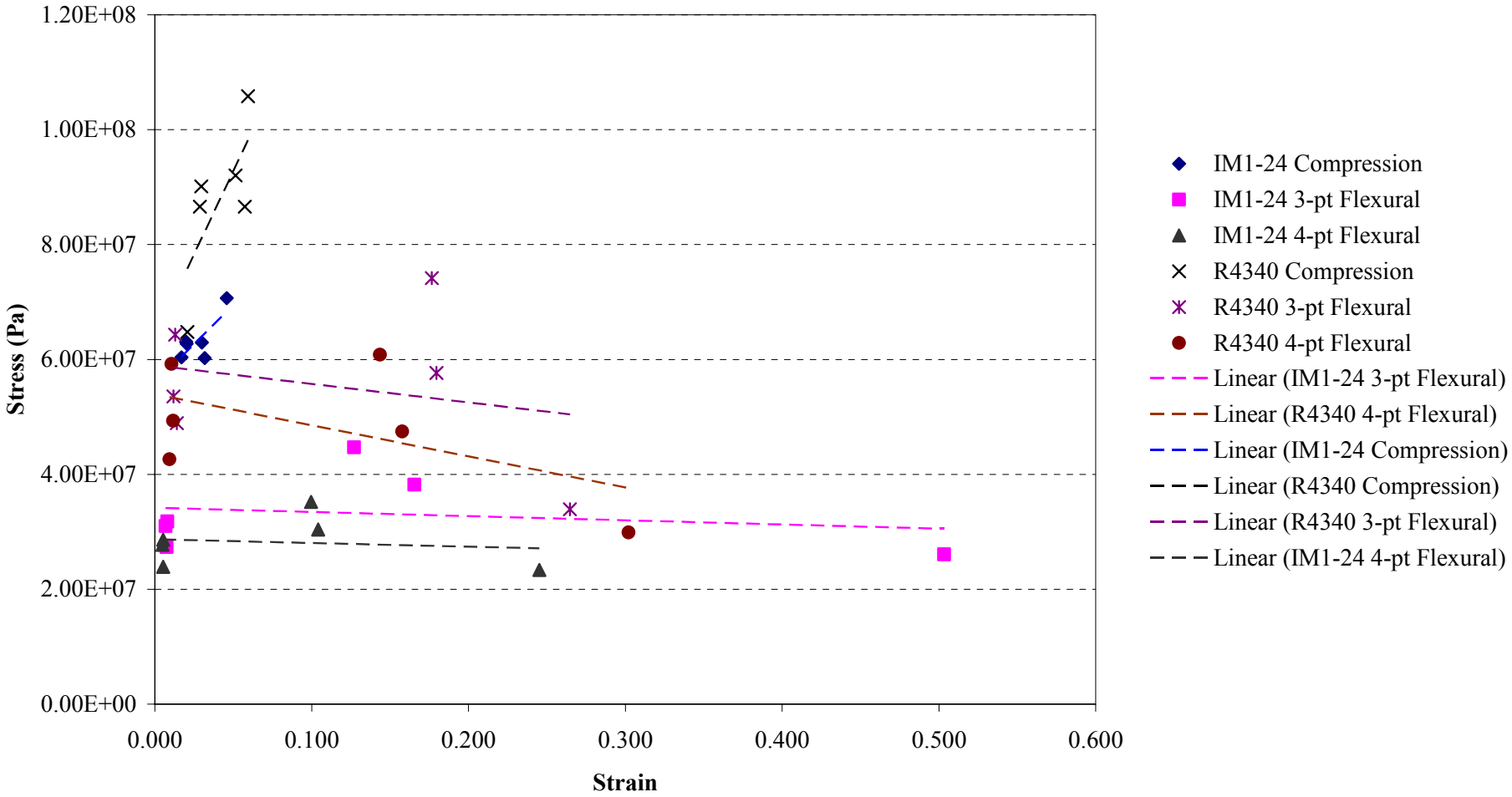

Graph 8.7 – Stress vs. strain for both materials under all modes of testing.

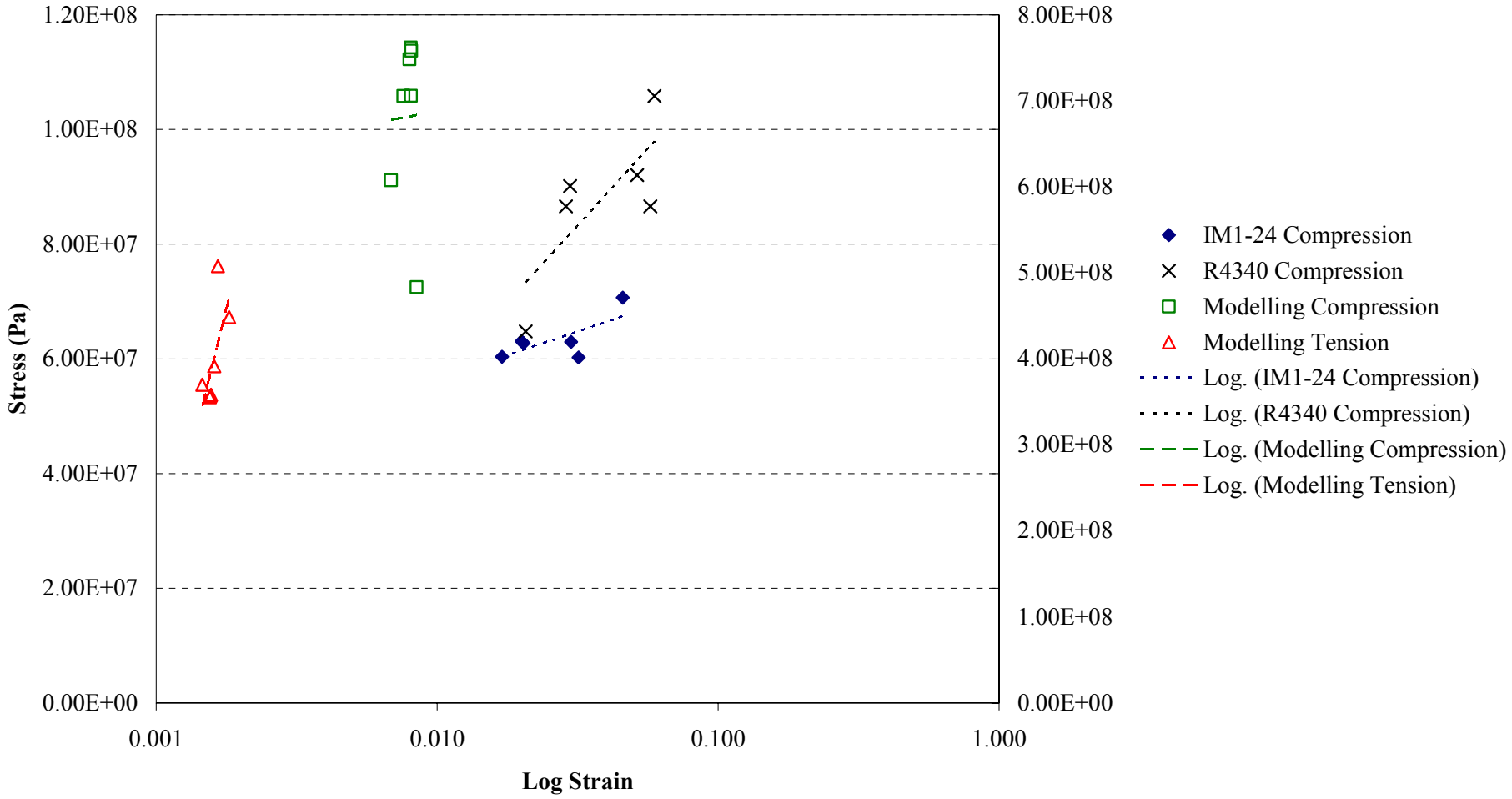

Graph 8.8 – Stress vs. strain for the compression test results and the modelling programme.

Looking at the stress versus the deflection (Graph 8.9 with the compression modelling plotted on the right hand axis to better display the results), the testing results show a trend of fairly constant stress with increasing deflection, which is to be expected as the strength should be a material constant. The modelling results show this to some degree, but as before, mainly with the larger sized models. The smaller size models have a large variation in stress value, particularly those in tension. Again, if the 30 x 30 model that displayed the significantly lower 1st principal stress value could be discounted, the compression modelling results would be similar in trend to the testing data.

Graph 8.10 shows deflection versus volume, and is the only graph in which modelling and testing truly represent each other. Whilst there are no meaningful results from this, it shows that the displacements applied to the models are logical with the increase in size and that potentially the models (given the correct geometries) might at least be able to predict a trend for the maximum deflection of a graphite, though this is based on knowing the failure strain of the material. A common pattern of increasing maximum deflection with increasing volume is seen across both graphite materials and the modelling data in compression and tension.

Graph 8.11 shows the stress versus the volume for all the testing and modelling results. The approximate trend of the tension results indicate that at least the models are predicting in line with the testing data. The issue of the 30 x 30 results in compression is again skewing the results. What is hard to reconcile with this data is that both compression and tension should be expected to follow the same trend (i.e. either increasing or decreasing), which they do if the displacement direction is taken into account (positive or negative), but comparing to the compression test data makes things a bit more difficult. The testing data for IM1-24 under compression shows an increasing stress with increasing volume, whilst the R4340 shows a decreasing stress with increasing volume. It can only be assumed that the difference in microstructure makes the IM1-24 better able to distribute load internally under compression than the R4340. However, both materials show a small variation in strength over the volumes tested, whilst the models show a rather steeper increase/decrease over volume.

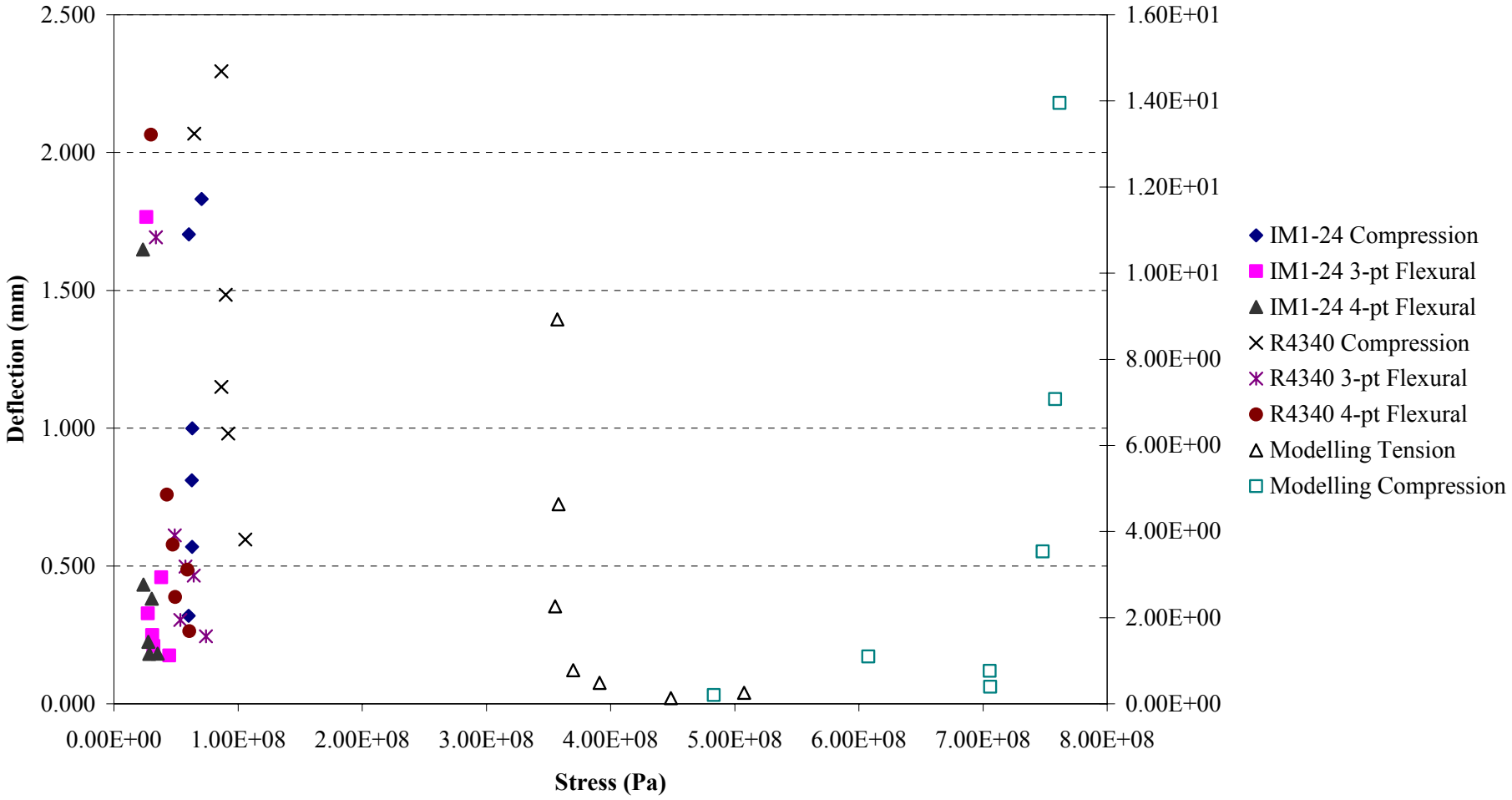

Graph 8.9 – Deflection vs. stress for both the modelling and testing programmes.

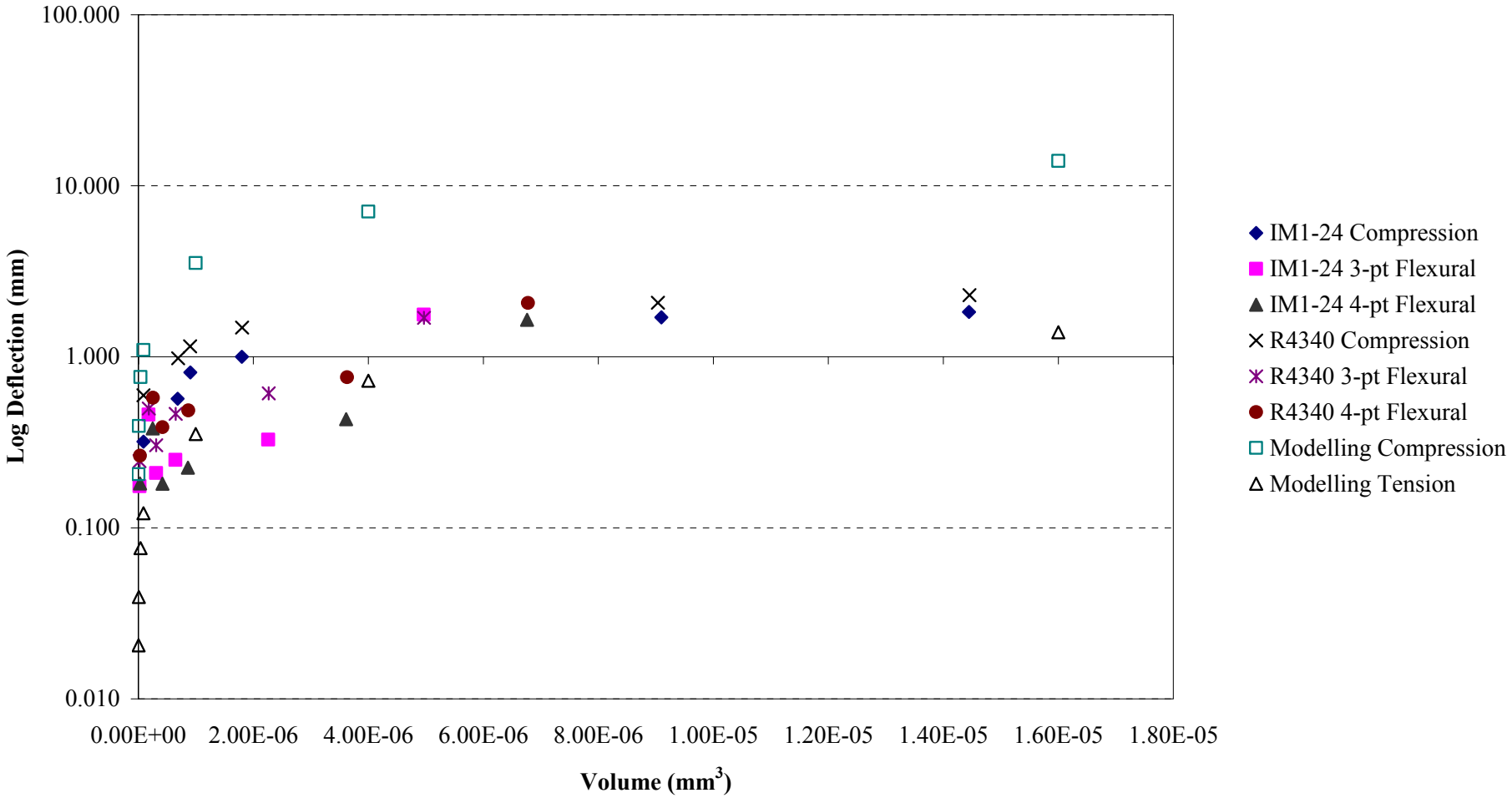

Graph 8.10 – Deflection vs. volume for both the modelling and testing programmes.

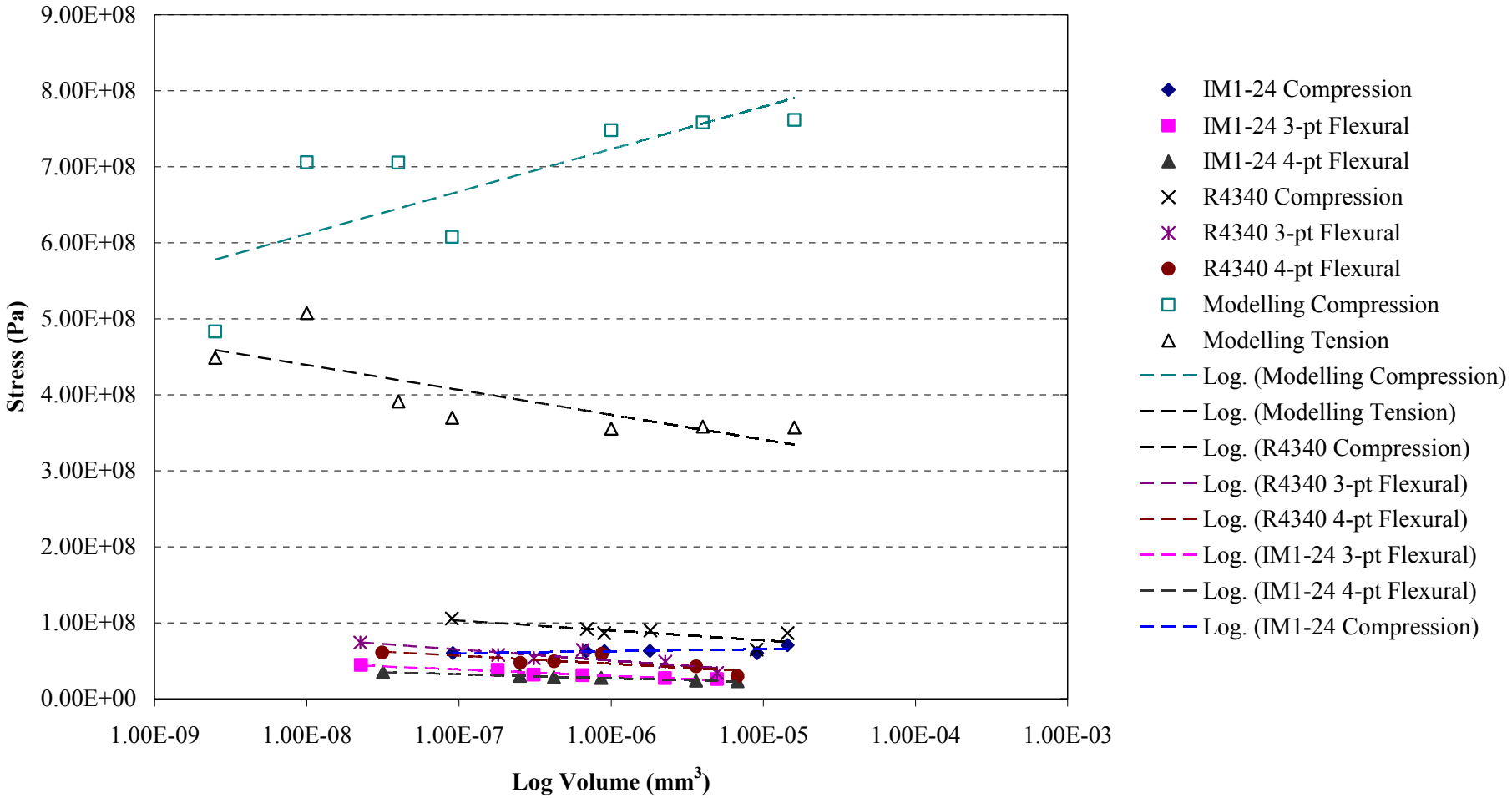

Graph 8.11 – Stress vs. volume for both the modelling and testing programmes.

Earlier in this chapter a number of points were made regarding the insight the models have provided:

- stress distribution,
- load being distributed through the stiffer sections of material,
- high stress points not necessarily being at the largest flaw,
- potential for predicting where a crack would initiate,
- tension/compression results plotted a similar distribution to Greenstreet (1969).

Additional to these points, when the models are analysed at various points from initial loading to the maximum strain being applied, they show similar behaviour to that of the test results. Graphs 8.12 and 8.13 depict the stress-displacement relationship under compression and 3-point flexural loading, respectively. It can be seen under both loading conditions that as the specimen size increases, the maximum stress at failure decreases. Graph 8.14 shows the stress-displacement relationship for varying model sizes (05 x 05 to 30 x 30), which follows the same trend as those seen in the testing results. As the size of the model is increased, the gradient of the stress-displacement becomes shallower. It can be construed that the modelling data shows that there is an almost constant failure stress, though this is due to the each model having a fixed displacement applied. As mentioned previously, as the models are considered to be elastic by ANSYS, there is no failure of the model. However, if a failure criteria could be introduced then it is expected that the stress-displacement pattern would follow that of the testing programme results.

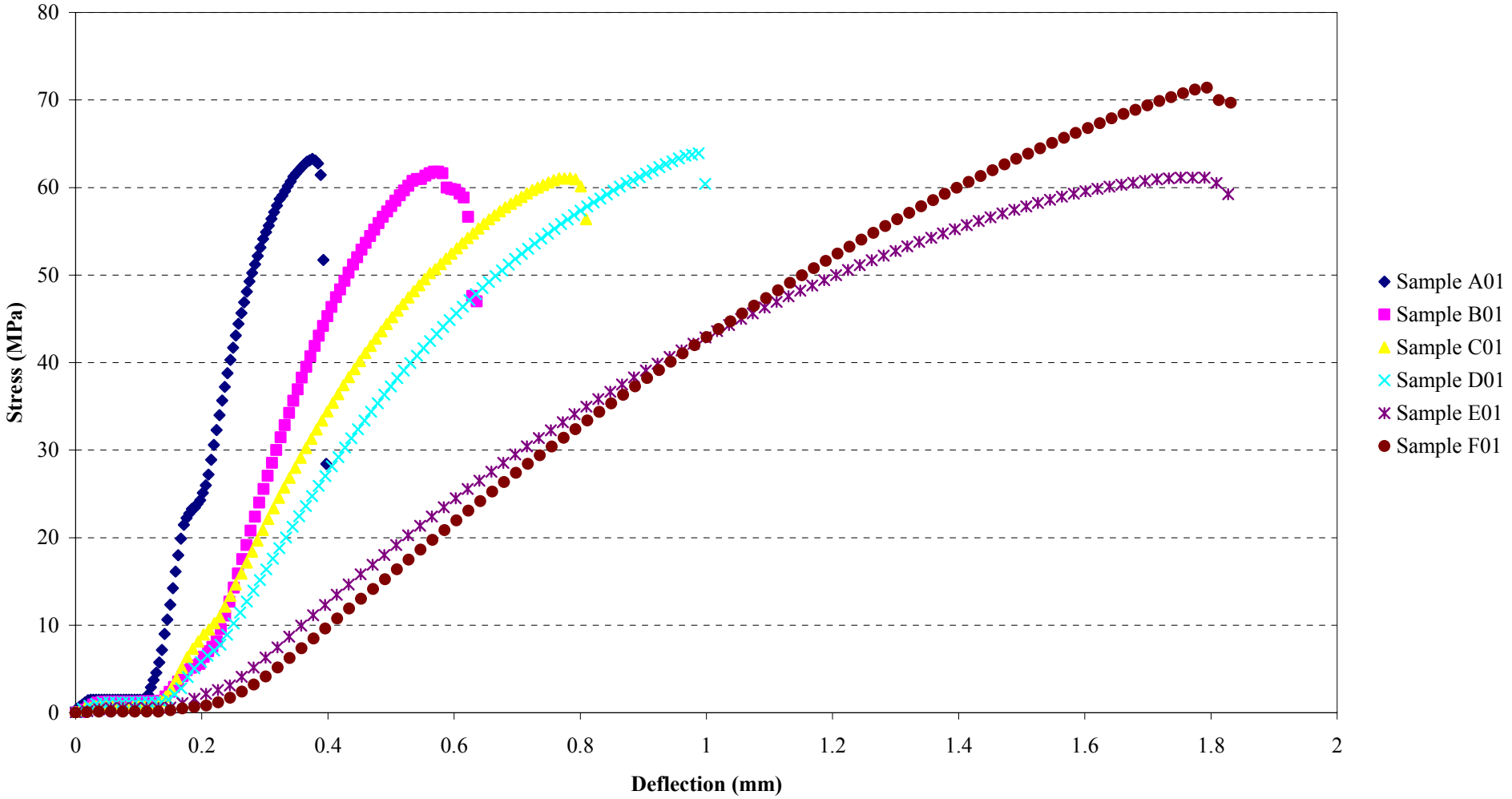

Graph 8.12 – Load deflection curves for several different sized specimens during compression testing.

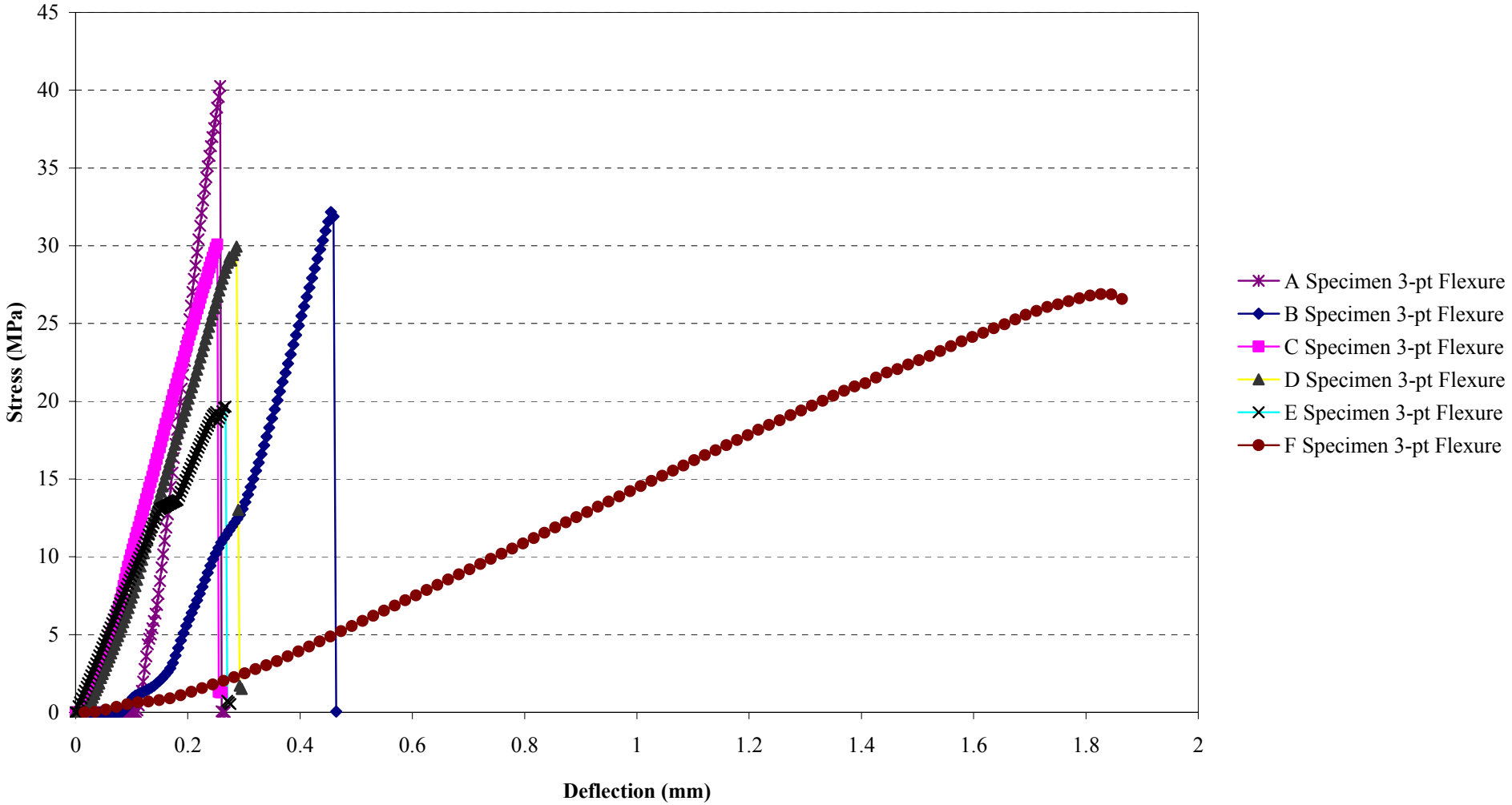

Graph 8.13 – Stress vs. deflection for several test specimens under 3-pt flexural loading.

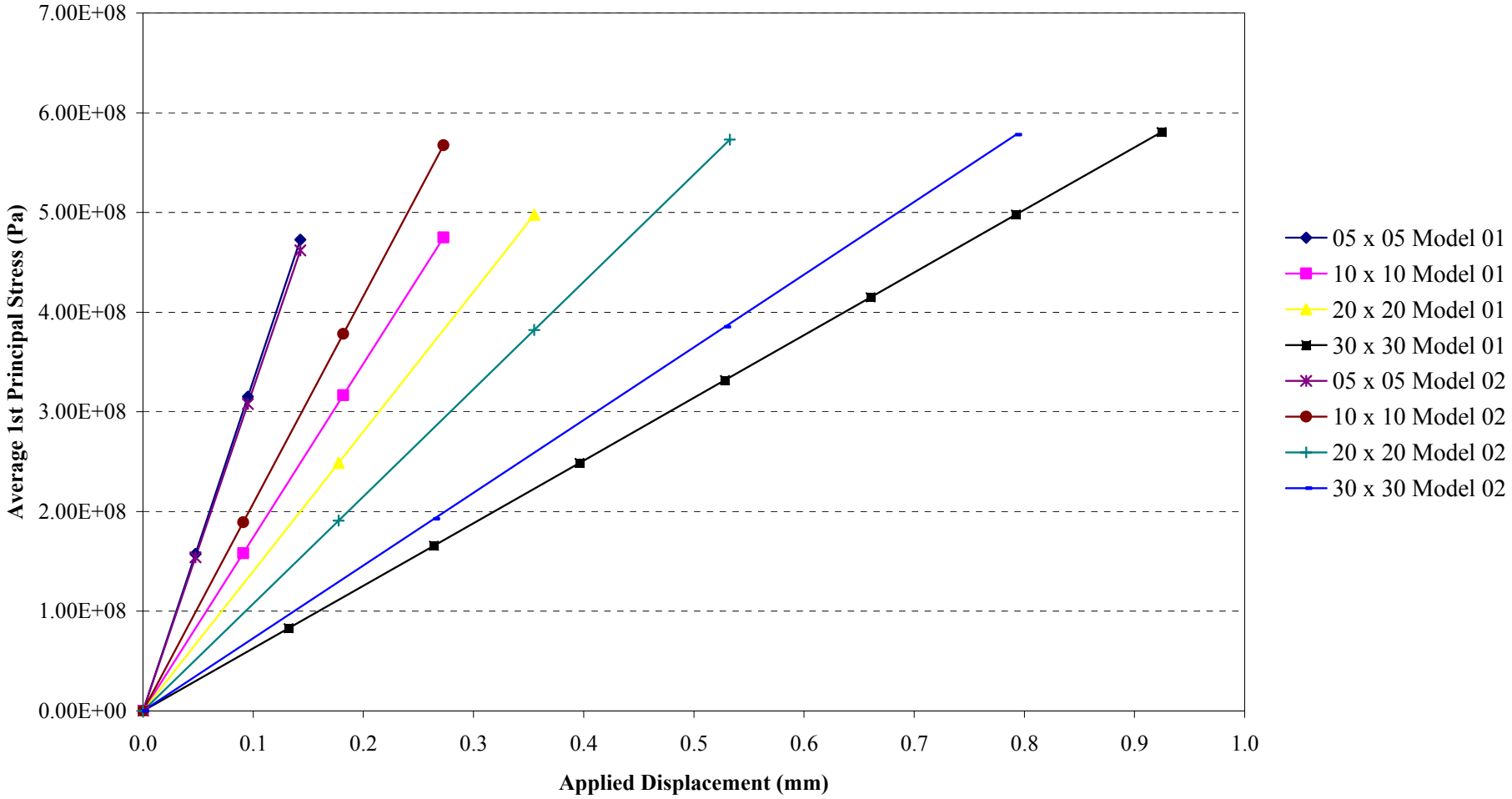

Graph 8.14 – Stress vs. displacement at varying points of displacement for several model sizes during analysis.

What can be seen from this comparison is that whilst the results from the modelling programme do not provide a definitive solution that can be compared directly to the testing programme, the construction of the models is appropriate and follow the same displacement behavioural pattern when their size is increased. The overall findings of the research are detailed in the next section, Chapter 9 – Conclusions.

Chapter 9 – Conclusions

The previous eight chapters have detailed the problems surrounding the issues involved in predicting and determining the strength of nuclear graphites based on the known material properties at the small scale. They have included a review of the existing literature relevant to the research as well as background information on the techniques employed by other researchers; the design and development of a conceptual FEA model that utilises random microstructures created using a C++ program that can have predefined material properties applied to them for analysis; the predictions for stress, strain, Young's modulus, strain energy and stress intensity made by the conceptual models; the design of a series of experiments and the production of the required testing apparatus; the execution of a mechanical testing programme to investigate the effect of specimen size on strength; and the use of data obtained from all sources to validate the conceptual models.

As stated at the beginning of this thesis the main objectives were to develop an abstract computer model to investigate the relationship between scale and material properties, to produce validation data for the computer models, and to determine a relationship between scale and strength. The first two of these objectives have been met fully, the third proved to be more difficult than originally thought.

The development of the conceptual FEA models has been successful, if not entirely true to the main material it was to simulate. IM1-24 graphite is a complex material that was assumed to have a random microstructure. Only by randomly creating a microstructure with the inherent properties of IM1-24 graphite has doubt been cast on this. The lack of similarity between the models developed and the microstructure of IM1-24 graphite suggests that during the manufacturing process some uniformity or orientation of particles is produced. The abstract way that the modelling approach was conceived

served to ensure that only the important features were concentrated upon, namely the pores, binder material and filler particles. The underpinning concept was logically thought through and the use of hexagons to simplify the models construction and solving should have yielded a representative result, but the results could not be validated by the data obtained from the testing programme. Surprisingly, the models produced had more in common visually with the reference material (R4340 graphite) that was utilised through the testing programme.

However, although the numerical values obtained from the FEA models were not accurate, the models themselves appear to correlate well with the expected behaviour of brittle materials. The stress and strain distributions follow the same pattern that has been observed in other literature, as do the compression-tension results. The trends for changes in a material property with increasing model size also follow those observed in the testing programme and it can be assumed that had the inputs for the model dimensions been more representative of the IM1-24 graphite microstructure, the trends and predictions would have been much closer. A large amount of data was collected through the completion of the testing programme which enabled a wide selection of information to compare the conceptual modelling to. It is hoped that this data can be used to further the model and produce a more accurate method of predicting material properties at any given size.

Some aspects of the modelling programme have been successful, but producing a numerically valid prediction of the behaviour of IM1-24 graphite has not been achieved yet. There are several key reasons for this:

1. The models are all assumed to be elastic in nature; as part of the abstraction process the complication of producing parameters upon which failure would occur have not been included. Due to this, increasing the model sizes will only produce higher values for increasing volume when studying maximum stresses and strains. As seen in the modelling results, the strain through the models has proved to be one of the most problematic areas when comparing the data to the experimental results. Analysing the average stress through the models has yielded more promising results.

2. The possibility that the smallest sized models are too small; it would be very difficult to test the microstructure represented in the smallest sized model in the real world, and the results obtained for these smallest sized models are not necessarily indicative of the behaviour of the material. However, the variation observed in the results from the smallest models does show that the microstructural makeup has a significant impact on the properties of the material, and that small scale specimens are not representative of the true material properties.

3. The limitation of the software; this relates directly to the building of the models, not the solutions, as it is believed that the models would solve regardless of size. The software has a limit for the number of entities that can be operated on at any one time and this has hampered the ability to model larger scale models. More specifically, when attempting to analyse the 400 x 400 models the time taken to construct the models was too great to enable the more than two to be solved.

4. The constraints and loads applied to the models; the selection of displacing the models by the failure strain of IM1-24 graphite is logical and has worked with regards modelling volume and displacement, but has had the side effect of producing constant strain through the models that prevents easy comparison with the experimental data.

Each of the reasons listed can be rectified and suggestions on how to achieve them are discussed in Chapter 10 – Further Work.

Despite being unable to easily validate the numerical results of the modelling programme with those gained from the testing programme, the abstract approach taken to model the microstructure of graphite has been successful. A method of generating random microstructures with inherent porosity has been developed which, with minor adjustments to the C++ code, can be used to study other types of graphite or ceramic materials. The models produced are displaying logical stress and strain patterns through the microstructure that are representative of results only recently published in literature, and could prove useful in better identifying the mechanisms of failure in unirradiated nuclear graphite. A comprehensive testing programme has been developed and

executed that has added to the existing knowledge of graphite material properties. The results from the testing programme suggest that determining the accurate material properties of graphite is highly dependent on the size and geometry of the specimen under testing. The testing programme has also indicated that whilst there is a relationship that exists between scale and properties, the current testing and property scaling methods employed by the nuclear industry may not be providing the most accurate results.

It was never expected that a definitive answer to the issues of scale would be produced through the completion of the programmes detailed in this thesis; indeed this is possibly just the first stage that can be expanded and improved upon. With such complex material, as any type of graphite is, it is very difficult to arrive at a robust solution that fits all situations. The methods and techniques described can be employed to assist in analysing the problems associated with scale and, in conjunction with the increasing amount of knowledge and data, it is hoped an answer will eventually be found.

Chapter 10 – Further Work

As stated in the previous chapter, the results presented herein are not fully conducive to providing a definitive answer to the issues of scale and how material properties are affected with increasing specimen size. There are a number of avenues that can be followed based on the concepts presented here, particularly in the area of the conceptual modelling.

The random generation of the graphite microstructure works well, but is not representative of IM1-24 graphite. Further work in this area would involve factoring in the size of Gilsocarbon particles in relation to the surrounding features and being able to join filler particles together to create a larger conglomeration that more closely resembles this. Conversely, the current randomly generated structure more closely resembles fine grained ceramics and as such revising the material property setting program to allow user input property values would enable the analysis of other ceramic materials. Additionally, the mode of loading for the models can be adjusted to encompass 3-point and 4-point flexural loading. Much data was obtained in this particular area and was not able to be fully utilised in validating the models.

Solutions to the issues stated in Chapter 9 – Conclusions that can be considered for further work are:

1. Revision of the abstraction process to determine if the assumption of plastic behaviour can be incorporated without overcomplicating the models. The addition of a failure criteria within the model or the determination of the applied displacement based on realistic failure would assist greatly in generating meaningful comparison data. To avoid the issues of constant strain a time-step approach could be taken whereby a model is displaced by a percentage of the

overall failure strain, an assumption of failure of the area of highest stress or strain could be made and this removed from the analysis. This could be repeated until the full displacement is reached.

2. Assigning specific sizes to the model units, rather than the arbitrary ones used in the development of the models, would lead to the more realistic modelling of components with the opportunity for more accurate comparison to test data.

3. Automating the model generation in ANSYS. The software can be programmed with its own coding language that could be used to automate certain aspects of the model building procedure. This would cut down user interaction and allow larger models to be created.

4. Change the method of loading the model. Instead of having an applied displacement, a specific load could be applied to the model that could potentially eliminate the constant strain issue observed in the current models. This could produce results that will also be better suited for comparison to test data.

From the remarks it becomes apparent that true validation of the modelling programme will come from producing models that can be compared easily to test data, which suggests that the best option for a successful programme would be to model the same components as those tested. This would allow validation of the models and highlight areas that need improvement/refinement before the models can be used to further investigate the issues of scale in nuclear graphite (or other ceramic) components.

References

Absi, J., Glandus, J. C., Numerical Seperation of Bi-Modal Strength Distributions, **2002**, *Journal of the European Ceramic Society*, 22, 593 - 601, Elsevier Science Ltd.

Ahmed, K. M., The Dynamic Response of Multi-Layers AGR Core Brick Arrays, **1987**, *Nuclear Engineering and Design*, 104, 1 - 66, North-Holland, Amsterdam.

Alain, E., Tomlinson, A., Mays, T. J., Analysis of Sub-Micron Porosity in AGR Moderator Graphites, **2001**, British Energy Generation Ltd. Report: BWD/4002870, University of Bath.

Allard, B., Rouby, D., Fantozzi, G., Dumas, D., Lacroix, P., Fracture Behaviour of Carbon Materials, **1991**, *Carbon*, 29, 3, 457 - 468, Pergamon Press plc.

Amelicnkx, S., Delavignette, P., Heerschap, M., Dislocations and Stacking Faults in Graphite, **1965**, *Chemistry and Physics of Carbon (Ed. P. L. Walker)*, 1, 3 - 71.

ANSYS Corporation, ANSYS 7.0 Help Documentation, **2002**, ANSYS Corporation.

Arai, T., Cords, H., Nickel, H., Improved Graphite Damage Model for Predicting Property Changes of HTGR Graphites Under Isothermal and Non-Isothermal Irradiations, **1992**, *Journal of Nuclear Science and Technology*, 9, 29, 831 - 838, Atomic Energy Society of Japan.

Arai, T., Ioka, I., Ishihara, M., Statistical Assessment of Uniaxial Strengths of a Fine-Grained Isotropic Graphite for Nuclear Applications, **1991**, *JSME International Journal*, Series I, 34, 4, 470 - 476.

Ashby, M. F., Jones, D. R. H., Engineering Materials 2, **1998**, Butterworth-Heinemann.

ASTM C651-70 (Reapproved 1977), Standard Test Method for Flexural Strength of Manufactured Carbon and Graphite Articles Using Four-Point Loading at Room Temperature, **1977**, American Society for Testing and Materials.

ASTM C695-91, Standard Test Method for the Compressive Strength of Carbon and Graphite, **2005**, American Society for Testing and Materials.

ASTM D790-80, Standard Test Methods for Flexural Properties of Plastics and Electrical Insulating Materials, **1980**, American Society for Testing and Materials.

ASTM E399, Standard Test Method for Plane Strain Fracture Toughness of Metallic Materials, **1981**, American Society for Testing and Materials.

Aukett, M., Issues of Scale in Nuclear Graphites, **2003**, Third Year Thesis, 1 - 62, University of Hull.

Bazant, Z. P., Size Effect Aspects of Measurement of Fracture Characteristics of Quasibrittle Material, **1996a**, *Advanced Cement Based Materials*, 4, 128 - 137, Elsevier Science Inc.

Bazant, Z. P., Size Effect, **2000**, *International Journal of Solids and Structures*, 37, 69 - 80, Pergamon Press plc.

Bazant, Z. P., Daniel, I. M., Li, Z., Size Effect and Fracture Characteristics of Composite Laminates, **1996b**, *Journal of Engineering Materials and Technology*, 118, 317 - 323, Transactions of the ASME.

Bazant, Z. P., Novak, D., Probabilistic Nonlocal Theory for Quasibrittle Fracture Initiation and Size Effect. I: Theory, **2000**, *J. Engineering Mechanics*, 126, 2, 166 - 174, ASCE.

Berre, C., Fok. S. L., Marsden, B. J., Babout, L., Hodgkins, A., Marrow, T. J., Mummery, P. M., Numerical Modelling of the Effects of Porosity Changes on the Mechanical Properties of Nuclear Graphite, **2006**, *Journal of Nuclear Materials*, 352, 1 - 5, Elsevier B.V.

Blackburn, N. P., Ford, P. J., Impact Models for Nuclear Reactor Graphite Components Under Seismic Loading, **1996**, Nuclear Energy - *Journal of the British Nuclear Engineering Society*, 35, 6, 375 - 384.

Boucher, M. A., Graphite, **1994**, *Canadian Minerals Yearbook*, 24.1 - 24.9.

British Standards Institute, Methods of Test for Plane Strain Fracture Toughness (KIc) of Metallic Materials, **1987**, BS 5447:1977 (Updated 1987), British Standards Institute.

British Standards Institute, Bend Testing of Metals, **1964**, BS 1639:1964 (Updated 1989), British Standards Institute.

British Standards Institute, Advanced Technical Ceramics - Monolithic Ceramics - Mechanical Properties at Room Temperature, **1996**, DD ENV 843-2:1996, British Standards Institute.

Brocklehurst, J. E., Fracture in Polycrystalline Graphite, **1977**, *Chem. Phys. Carbon*, 13, 145 - 279.

Brocklehurst, J. E., Adam, R. W., Mechanical Tests on Graphite with Simulated Radiolytic Oxidation Gradients, **1983**, UKAEA Report ND-R-853(S).

Brown, W. F., Strawley, J. E., Plane Strain Crack Toughness Testing of High Strength Metallic Materials, **1969**, ASTM STP No. 410.

Buch, J. D., Mechanical Behaviour Model for Graphites, **1976**, Properties Related to Fracture Toughness, ASTM STP 605, 124 - 144, American Society for Testing and Materials.

Burchell, T. D., A Microstructurally Based Fracture Model for Polygranular Graphites, **1996**, *Carbon*, 34, 3, 297 - 316, Pergamon Press plc.

Burchell, T. D., Tucker, M. O., McEnaney, B., **1987**, *In Materials for Nuclear Reactor Core Applications*, 95 - 103, NES, London.

Carpenter, E. W., Norfolk, D. J., Lattice of Power: Graphite Core Life, **1984**, *Nuclear Energy - Journal of the British Nuclear Engineering Society*, 23, 2, 83 - 96.

Case, E. D., The Effect of Microcracking Upon the Poisson's Ratio for Brittle Materials, **1984**, *Journal of Materials Science*, 19, 3702 - 3712, Chapman and Hall Ltd.

Castillo, E., López-Aenlle, M., Ramos, A., Fernández-Canteli, A., Kieselbach, R., Esslinger, V., Specimen Length Effect on Parameter Estimation in Modelling Fatigue Strength by Weibull Distribution, **2006**, *International Journal of Fatigue*, 28, 1047 - 1058, Elsevier Ltd.

Clegg, R. A., Hayhurst, C. J., Numerical Modelling of the Compressive and Tensile Response of Brittle Materials Under High Pressure Dynamic Loading, **2000**, *Shock Compression of Condensed Matter - 1999*, 321 - 324, American Institute of Physics.

Clift, S. E., Hartley, M. S., Neighbour, G. B., McEnaney, B., Finite Element Analysis of Blunt Indentation Tests, **1997**, Nuclear Electric Report: BB/G/40930A, University of Bath.

Colengelo, V. J., Heiser, F. A., Analysis of Metallurgical Failures, **1987**, John Wiley & Sons, Inc.

Daehn, G.S., Brehm, H., Lee, H., Lim, B-S., A Model for Creep Based on Microstructural Length Scale Evolution, **2004**, *Materials Science and Engineering*, A, 387 - 389, Elsevier B.V.

Davidge, R. W., Tappin, G., The Effective Surface Energy of Brittle Materials, **1968**, *Journal of Materials Science*, 3, 165 - 173, Chapman and Hall Ltd.

Eto, M., Ishiyama, S., Burchell, T., Yahr, G., Biaxial Strength and Fracture Criterion for HTGR Graphites, **1997**, *J. Nuclear Science and Technology*, 34, 5, 476 - 483.

Felbeck, D. K., Atkins, A. G., Stength and Fracture of Engineering Solids - Second Edition, **1996**, 380 - 389, Prentice-Hall Inc.

Fett, T., Ernst, E., Munz, D., Badenheim, D., Oberacker, R., Weibull Analysis of Ceramics Under High Stress Gradients, **2003**, *Journal of the European Ceramic Society*, 23, 2031 - 2037.

Fok, S. L., Finite Element Analyses of Static Displacements and Forces in AGR Graphite Cores with Failed Components, **1997**, Nuclear Electric Report: EPD/AGR/REP/0275/97, Nuclear Electric Ltd.

Fok, S. L., Mitchell, B. C., Smart, J. Marsden, B. J., A Numerical Study on the Application of the Weibull Theory to Brittle Materials, **2001**, *Engineering Fracture Mechanics*, 68, 1171 - 1179, Pergamon Press plc.

Glasstone, S., Sesonske, A., Nuclear Reactor Engineering, **1963**, D. Van Norstrand Company, Inc.

Gopalaratnam, V. S., Shah, S. P., Softening Response of Plain Concrete in Direct Tension, **1985**, *ACI Journa*l, 310 - 323.

Greenstreet, W. L., Smith, J. E., Yahr, G. T., Mechanical Properties of EGCR-Type AGOT Graphite, **1969**, *Carbon*, 7, 15 - 45, Pergamon Press.

Griffith, A. A., The Phemonema of Rupture and Flow in Solids, **1921**, *Trans. Roy. Soc. (London)*, 221, 163 - 198.

Grover, S. B., Metcalfe, M. P., Graphite Materials Testing in the ATR for Lifetime Management of Magnox Reactors, **2002**, *INEEL Conference Paper: INEEL/CON-02-00370*, 1 - 8.

Hacker, P., Modelling the Co-Efficient of Thermal Expansion in Nuclear Graphites, **2001**, PhD Thesis, The University of Bath.

Hacker, P. J., Neighbour, G. B., McEnaney, B., The International Database on Irradiated Nuclear Graphite Properties, **1998**, Health and Safety Executive Report: NUC 56/10/1, University of Bath.

Hacker, P. J., Neighbour, G. B., McEnaney, B., The Coefficient of Thermal Expansion of Nuclear Graphite with Increasing Thermal Oxidation, **2000**, *J. Phys. D: Appl. Phys.*, 33, 991 - 998, IOP Publishing Ltd.

Haecker, C-J., Garboczi, E. J., Bullard, J. W., Bohn, R. B., Sun, Z., Shah, S. P., Voigt, T., Modeling the Linear Elastic Properties of Portland Cement Paste, **2005**, *Cement and Concrete Research*, 35, 1948 - 1960, Elsevier Ltd.

Hall, G., Marsden, B. J., Fok, A., The Microstructural Modelling of Nuclear Grade Graphite, **2006**, *Journal of Nuclear Materials*, 353, 12 - 18, Elsevier B.V.

Hall, G., Marsden, B. J., Smart, J., Fok, A., Finite Element Modelling of Nuclear-Grade Graphite, **2002**, *Nuclear Energy - Journal of the British Nuclear Engineering Society*, 41, 6, 53 - 62.

He, S., Gotts, J. A., A Computational Study of the Effect of Distortions of the Moderator Cooling Channel of the Advanced Gas-Cooled Reactor, **2005**, *Nuclear Engineering and Design*, 235, 965 - 982, Elsevier Science B.V.

Holt, R. M., Kjølaas, J., Larsen, I., Li, L., Gotusso Pillitteri, A., Sønstebø, E. F., Comparison Between Controlled Laboratory Experiments and Discrete Particle Simulations of the Mechanical Behaviour of Rock, **2005**, *International Journal of Rock Mechanics & Mining Sciences*, 42, 985 - 995, Elsevier Ltd.

Irwin, G. R., Fracture, **1958**, *Handbuch der Physik*, 6, 551, Springer-Verlag, Berlin.

Ishiyama, S., Oku, T., Eto, M., Fatigue Failure and Fracture Mechanics of Graphites for High Temperature Engineering Testing Reactor, **1991**, *Journal of Nuclear Science and Technology*, 28, 5, 472 - 483, Atomic Energy Society of Japan.

James, G., Modern Engineering Mathematics (Second Edition), **1996**, 464 - 465, Addison-Wesley Publishing Company.

Jenq, Y., Shah, S., A Two Parameter Fracture Model for Concrete, **1985**, *Journal of Engineering Mechanics*, 111, 1227 - 1241.

Kalpakjian, S., Manufacturing Engineering and Technology: Third Edition, **1995**, 86 - 93, Addison-Wesley Publishing Company.

Kelly, B. T., The Physics of Graphite, **1981**, Applied Science, Essex, England.

Kelly, B. T. Brocklehurst, J. E., High Dose Fast Neutron Irradiation of Highly Oriented Pyrolytic Graphite, **1971**, *Carbon*, 9, 783 - 789.

Kennedy, C. R., The Brittle Ring Test for Graphite, **1993**, *Carbon*, 31, 3, 519 - 528, Pergamon Press Ltd.

Kennedy, C. R., Montegomery, S. C., Statistics of Fracture in Two Grades of Isotropic Graphite, **1990**, *Journal of Nuclear Materials*, 171, 49 - 53, Elsevier Science Publishers B.V.

Kim, C-S., Massa, T. R., Rohrer, G. S., Modeling the Relationship Between Microstructural Features and the Strength of WC-Co Composites, **2006**, *International Journal of Refractory Metals & Hard Materials*, 24, 89 - 100, Elsevier Ltd.

Kotsovos, M. D., Pavlović, M. N., Non-Linear Finite Element Modelling of Concrete Structures: Basic Analysis, Phenomenological Insight and Design Implications, **1986**, *Eng. Comput.*, 3, 243 - 250, Pineridge Press Ltd.

Lewis III, D., Oyler, S. M., An Experimental Test of Weibull Scaling Theory, **1976**, *J. Am. Ceram. Soc.*, 59, 11 - 12, 504 - 510.

Li, Y., Li, X., Chang, L., Wu, D., Fang, Z., Shi, Y., Understandings on the Scattering Property of the Mechanical Strength Data of Solid Catalysts, **1999**, *Catalysts Today*, 51, 73 - 84, Elsevier Science B.V.

Mar, A., Dennis, J. L., Morris, T. R., Symington, I., Theoretical Modelling of Tensile Cracks in AGR Graphite Components: A Review of Current Capabilities and the Potential for Future Developments, **2002**, British Energy Generation Ltd. Report: GCDMC/A/P(02)326, Wilde and Partners Ltd.

Marayama, T., Kaito, T., Onose, S., Shibahara, I., Change in Physical Properties of High Density Isotropic Graphites Irradiated in the "JOYO" Fast Reactor, **1995**, *Journal of Nuclear Materials*, 225, 267 - 272, Elsevier Science B.V.

Matsumori, N., Penn, J., Nakamura, N., Teramoto, Y., Evaluating the Accuracy of Thermomechanical Analysis Expansion Coefficient Measurement in a Wide Temperature Range, **1991**, ASTM STP No. 1136, 32 - 48, American Society for Testing and Materials.

Matsuo, H., Effect of Oxidation on Physical Properties of Neutron Irradiated Nuclear Grade Graphite, **1986**, *Journal of Nuclear Materials*, 138, 222 - 226, Elsevier Science Publishers B.V.

Matsuo, H., Fujii, K., Imai, H., Irradiation-Induced Property Changes of Thermally Oxidized Nuclear Graphites, **1988**, *Journal of Nuclear Materials*, 152, 283 - 288, Elsevier Science Publishers B.V.

Matsuo, H., Tamotsu, S., Irradiation Behaviours of Nuclear Grade Graphite in Commercial Reactor (III), **1985**, *Journal of Nuclear Science and Technology*, 4, 22, 313 - 319.

McEnaney, B., Mays, T., Relationships Between Microstructure and Mechanical Properties in Carbon-Carbon Composites, **1993**, *Essentials of Carbon-Carbon Composites*, The Royal Society of Chemistry.

McGregor, R., Practical C++, **1999**, 9 - 191, Que.

McLachlan, N., Modelling of AGR Graphite Core Displacements and Forces under Static Loading Using ABAQUS: User Guide, **1996**, Nuclear Electric Report: EPD/GEN/REP/0170/96, Nuclear Electric Ltd.

Meriam, J. L., Kraige, L. G., Engineering Mechanics Volume One: Statics (Third Edition), **1993**, 289 - 292, John Wiley & Sons, Inc.

Mistree, F., Allen, J. K., Living Systems Applications: Designing at a High Level of Abstraction, **1993**, *Behavioural Science*, 38, 2, 124 - 138.

Mitchell, B. C., Smart, J., Fok, S. L., Marsden, B. J., The Mechanical Testing of Nuclear Graphite, **2003**, *Journal of Nuclear Materials*, 322, 126 - 137, Elsevier B.V.

Mrozowski, S., Mechanical Strength, Thermal Expansion and Structure of Cokes and Carbons, **1954**, *Proc. 1st and 2nd conf. on carbon*, Waverley Press, USA.

NAFEMS, How To - Understand Finite Element Jargon, **1994**, NAFEMS Finite Element Methods and Standards.

Nakayama, J., Direct Measurement of Fracture Energies of Brittle Heterogeneous Materials, **1965**, *J. Am. Ceram. Soc*., 48, 11, 583 - 587.

Neighbour, G. B, Hacker, P. J., Wilson, M., The Rogue Brick Experiment, **2000a**, British Energy Generation Ltd. Report: GCDMC/A/P(00)184, University of Bath.

Neighbour, G. B, McEnaney, B., An Investigation of Acoustic Emission from an Irradiated Nuclear Graphite, **1995**, *Journal of Nuclear Materials*, 223, 305 - 311, Elsevier Science B.V.

Neighbour, G. B., Personal Communication, **2003**.

Neighbour, G. B., Personal Communication, **2004**.

Neighbour, G. B., Modelling of Dimensional Changes in Irradiated Nuclear Graphites, **2000**, *J. Phys. D: Appl. Phys.*, 33, 2966 - 2972.

Neighbour, G. B., Microstructural Processes Leading to Fracture in Nuclear Graphites, **1993**, PhD Thesis, University of Bath.

Neighbour, G. B., Hacker, P. J., The Variation of Compressive Strength of AGR Moderator Graphite with Increasing Thermal Weight Loss, **2001**, *Materials Letters*, 51, 307 - 314, Elsevier Science B.V.

Neighbour, G. B., Hacker, P. J., McEnaney, B., Appraisal of Mechanical and Thermal Properties of AGR Moderator Graphite at High Weight Loss, **2000b,** British Energy Generation Ltd. Report, University of Bath.

Neville, D. J., Kennedy, J. B., An Alternative to the Weibull Function for Some Cases, **1991**, *Journal of Mechanical Design*, 113, 195 - 199.

Nuclear Electric, Compendium of CAGR Core and Sleeve Data Methods, **1996**, Nuclear Electric Report: CSDMC/P28.

O'Kelly, K. U., Carr, A. J., McCormack, B. A. O., Minimum Solid Area Models Applied to the Prediction of Young's Modulus for Cancellous Bone, **2003**, *Journal of Materials Science: Materials in Medicine*, 14, 379 - 384, Kluwer Academic Publishers.

Osetsky, Yu. N., Bacon, D. J., Void and Precipitate Strengthening in α-iron: What We Can Learn From Atomic-Level Modelling?, **2003**, *Journal of Nuclear Materials*, 323, 268 - 280, Elsevier B.V.

Östburg, G., Some Reflections on Relationships Between Structure, Properties, and Performance of Engineering Materials, **2003**, *Materials and Design*, 24, 255 - 262, Elsevier Science Ltd.

Ouange, P., Neighbour, G. B., McEnaney, B., Crack Growth Resistance in Nuclear Graphites, **2002**, *J. Phys. D: Appl. Phys.*, 35, 927 - 934, Institute of Physics Publishing.

Pandolfi, A., Conti, S., Ortiz, M., A Recursive-Faulting Model of Distributed Damage in Confined Brittle Materials, **2006**, *Journal of Mechanics and Physics of Solids*, 54, 1972 - 2003, Elsevier Ltd.

Parrington, R. J., Fractography of Metals and Plastics, **2002**, *Practical Failure Analysis*, 2, 5, 16 - 46.

Phillips, R., Multiscale Modelling in the Mechanics of Materials, **1998**, *Solid State and Materials Science*, 3, 526 - 532, Current Chemistry Ltd.

Piat, R., Schnack, E., Modeling the Effect of Microstructure on the Coefficients of Thermal Expansion of Pyrolytic Carbon, **2003**, *Letters to the Editor - Carbon*, 41, 2159 - 2179, Elsevier Ltd.

Precision Ceramics, Tech Data, **2002**, http://www.precision-ceramics.co.uk/machinables.htm.

Prince, N., Experience in the Design of Graphite Moderator Structures, **1977**, *Paper presented to the Nuclear Engineering Society*.

Prince, N., Technology of Graphite Moderator Structures, **1979**, *Nuclear Energy - Journal of the British Nuclear Engineering Society*, 18, 4, 267 -275.

Quinn, G. D., Weibull Strength Scaling for Standardized Rectangular Flexure Strength Specimens, **2003**, *J. Am. Ceram. Soc.*, 86, 3, 508 - 510.

Reinhardt, H. W., Cornelissen, H. A. W., Hordijk, D. A., Tensile Tests and Failure Analysis of Concrete, **1986**, *Journal of Structural Engineering*, 112, 11, 2462 - 2477, ASCE.

Reynolds, W. N., Physical Properties of Graphite, **1968**, Elsevier Co. Ltd.

Rice, R. W., Monolithic and Composite Ceramic Machining Flaw-Microstructure-Strength Effects: Model Evaluation, **2002**, *Journal of the European Ceramic Society*, 22, 1411 - 1424, Elsevier Science Ltd.

Rice, R. W., Comparison of Stress Concentration Versus Minimum Solid Area Based Mechanical Property-Porosity Relations, **1993**, *Journal of Materials Science*, 28, 2187 - 2190, Chapman and Hall.

Rice, R. W., Comparison of Physical Property-Porosity Behaviour with Minimum Solid Area Models, **1996**, *Journal of Materials Science*, 1509 - 1528, Chapman and Hall.

Rice, R. W., Microstructural Dependence of Mechanical Behaviour of Ceramics, **1977**, *Treatise on Materials Science Technology, Volume II: Properties and Microstructure*, 199 - 379, Academic Press, New York.

Rice, R. W., Evaluation and Extension of Physical Property-Porosity Models Based on Minimum Solid Area, **1996**, *Journal of Materials Science*, 31, 102 - 118, Chapman and Hall.

Rodriguez, J., Allibert, C. H., Chaix, J. M., A Computer Method for Random Packing of Spheres of Unequal Size, **1986**, *Powder Technology*, 47, 25 - 33, Elsevier - Sequoia.

Sakai, M., Bradt, R. C., Fracture Toughness Testing of Brittle Materials, **1993**, *International Materials Reviews*, 38, 2, 53 - 78, The Institute of Materials (London).

Sakai, M., Urashima, K., Inagaki, M., Energy Principle of Elastic-Plastic Fracture and its Application to the Fracture Mechanics of a Polycrystalline Graphite, **1983**, *J. Am. Ceram. Soc.*, 66, 12, 868 - 873.

Salazar, A., Pastor, J. Y., Llorca, J., In Situ Observation of Damage Nucleation in Graphite and Carbon/Carbon Composites, **2002**, *Carbon*, 40, 609 - 616, Elsevier Science Ltd.

Scarrott, C., Tunnicliffe Wilson, G., Building a Statistical Model to Predict Reactor Temperatures, **2001**, *Journal of Applied Statistics*, 38, 3 & 4, 497 - 51, Taylor & Francis Ltd.

Schneider, T., Greil, P., Schober, G., Strength Modelling of Brittle Materials with Two- and Three- Dimensional Pore Structures, **1999**, *Computational Materials Science*, 16, 1 - 4, 98 - 103, Elsevier Science B.V.

She, S., Landes, J.D., Statistical Analysis of Fracture in Graphite, **1993**, *International Journal of Fracture*, 63, 189 - 200, Kluwer Academic Press.

Slagle, O. D., Deformation Mechanisms in Polycrystalline Graphite, **1967**, *Journal of the American Ceramic Society*, 50, 10, 495 - 500.

Spychalski, W., Kurzydłowski, K. J., Ralph, B., Computer Study of Inter- and Intragranular Surface Cracks in Brittle Polycrystals, **2002**, *Materials Characterization*, 49, 45 - 53, Elsevier Science Inc.

Steer, A. G., A Structural Approach to the Description and Determination of its Physical Properties, **2003**, Private Publication.

Tarum, C. D., Classification and Analysis of Weibull Mixtures, **1999**, SAE Technical Paper Series (1999-01-0055).

Tattersall, H. G., Tappin, G., The Work of Fracture and its Measurement on Metals, Ceramics and Other Materials, **1966**, *Journal of Materials Science*, 1, 296 - 301, Chapman and Hall Ltd.

Taylor, W. R., Clift, S. E., Warner, M. D., Neighbour, G. B., Kinematic Study of Radially Keyed Graphite Moderator Cores, **1997**, Health and Safety Executive Report: NUC 56/382, 1 - 35, University of Bath.

The Quality Portal, Design of Experiments - In Brief, **2002**, http://www.thequalityportal.com/q_know02.htm.

Theocaris, P. S., The Limits of Poisson's Ratio in Polycrystalline Bodies, **1994**, *Journal of Materials Science*, 29, 3527 - 3534, Chapman and Hall Ltd.

Todinov, M. T., Estimating the Probabilities of Triggering Brittle Fracture Associated With the Defects in the Materials, **2001**, *Materials Science and Engineering*, A302, 235 - 245, Elsevier Science B.V.

Torquato, S., Truskett, T. M., Debenedetti, P. G., Is Random Close Packing of Spheres Well Defined?, **2000**, *Physical Review Letters*, 84, 10, 2064 - 2067, The American Physical Society.

Tucker, M. O., Rose, A. P. G., Burchell, T. D., The Fracture of Polygranular Graphites, **1986**, *Carbon*, 24, 5, 581 - 602, Pergamon Journals Ltd.

Tucker, M. O., Wickham, A. J., Graphite Performance and Integrity Assessment, **1990**, *The Commissioning and Operation of AGRs Seminar*, IMechE, 1 - 15.

Union Carbide, An Inside Story: The Role of Nuclear Graphite, Union Carbide promotional material.

Warner, M. D., Taylor, W. R., Clift, S. E., Neighbour, G. B., Kinematic Study of Radially Keyed Graphite Moderator Cores, **1998**, Health and Safety Executive Report: NUC 56/382-Ext 1, 1 - 38, University of Bath.

Warren, P. D., Fracture of Brittle Materials: Effects of Test Method and Threshold Stress on the Weibull Modulus, **2001**, *Journal of the European Ceramic Society*, 21, 335 - 342.

Weibull, W., Statistical Theory of the Strength of Materials, **1939**, *Ingenioersvetenskapsakad*, 152, 45, Handl.

Weibull, W., Statistical Distribution Function of Wide Applicability, **1951**, *J. Appl. Mech.*, 18, 3, 293 - 297.

Wikipedia, Abstraction, **2006**, http://en.wikipedia.org/wiki/Abstraction.

Wilkinson, D. S., Pompe, W., Oeschner, M., Modeling the Mechanical Behaviour of Heterogeneous Multi-Phase Materials, **2001**, *Progress in Materials Science*, 46, 379 - 405, Elsevier Science Ltd.

Wong, T-F., Wong, R. H. C, Chau, K. T., Tang, C. A., Microcrack Statistics, Weibull Distribution and Micromechanical Modeling of Compressive Failure in Rock, **2006**, *Mechanics of Materials*, 38, 664 - 681, Elsevier Ltd.

Zhao, S. B., Thoughts About the Exponential Item in Formulas Calculating Tensile Strength for High-Porosity Materials, **2002**, *Materials and Design*, 23, 497 - 499, Elsevier Science Ltd.

Zhou, M. Zhai, J., Modelling of Micro-mechanical fracture using a cohesive finite element method, **2000**, *Shock Compression of Condensed Matter - 1999*, 623 - 628, American Institute of Physics.

Appendix A - Literature Review

When commencing any research project it is vital that previous literature is searched, examined and digested to both ensure that work is not unnecessarily being repeated and to collate information and data that could prove useful at a later point in the study. Such a review also expands the researchers' knowledge of the subject area and aids in the understanding of additional concepts that may have to be incorporated. The modern researcher has access to many varied means of searching for the desired information, from the traditional library to the searchable 'online' databases of journals and theses.

One of the most convenient ways to search through the masses of information that can be available on any given subject is to utilize the internet and its many websites devoted to listing the entries from journals and periodicals, as well as individual articles. These sites are often maintained by the publishers of journals and periodicals and therefore are usually up to date with their information and of great use when looking for recent work within a specific field. In addition to these, there are also websites available through the ATHENS system that enable the users to search through submitted theses and academic publications, allowing the user to determine whether the study has been, or is being, undertaken at another college, university or institution.

The following is a brief account of how a search for previous or existing work on the "Issues of Scale in Nuclear Graphite Components" was performed, and a review of the results that were returned by the various websites and academic sources.

The first step to be taken in the search for relevant literature is to decide how the search is to be performed. This usually takes the form of the user typing a number of keywords or phrases into a search engine on a website and seeing whether the returned information (or 'hits') is suitable for inclusion in the literature review. This approach

requires the selection of keywords and appropriate internet search engines or websites to ensure that the widest possible search is performed. For the purposes of this study, the keywords listed in Table A.1 were selected to be used.

The majority of search engines match words exactly and therefore all variations of the words to be searched upon need to be included. However, some sites offer the option of using a 'wildcard' character which enables letters to be replaced with a symbol (such as *) that allows more than one word to be searched for at the same time, e.g. the word oxid* will search for oxide, oxidation and oxidise (as well as other variations) within the texts. An additional special character that can be used within a search is the '+' symbol. This allows different words to be joined into a phrase (or search string) so that more than one word can be searched for at once, e.g. reactor+core would search for the phrase 'reactor core' within the documents (or alternatively, some webpages use the phrase enclosed by quotation marks to return the results for that specific phrase within a document).

Using combinations of the short-listed keywords it was possible to search through various journal, article and theses websites in order to find relevant research undertaken on the subjects required. In addition to this, subscription to specialist newsgroups enabled newly published article details to be delivered direct to the researcher and keeping any relevant information up to date.

As well as the electronic databases, the same set of keywords was also utilised in searching the library catalogues for background information on the subject matter. However, speaking to peers and colleagues still remains a strong resource for researchers in tracking down elusive articles and papers.

Analysis		
Bend	Bending	
Biaxial		
Brick	Bricks	
Brittle		
Carbon		
Ceramic	Ceramics	
Cleavage		
Coefficient		
Component	Components	
Compression	Compressive	Compress
Core		
Crack	Cracks	Cracked
Critical		
Deformation		
Elastic	Elasticity	
Element	Elements	
Elongation		
Energy	Energies	
Expansion		
Experiment	Experiments	Experimental
Failure		
Fatigue		
Finite		
Flaw		
Flexural		
Fracture		
Function	Functionality	Functional
Geometry	Geometrical	
Graphite		
Load		
Macro	Macrostructure	
Material		
Micro	Microstructure	

Model	Modelling	Models
Moderator	Moderators	
Modulus		
Nuclear		
Oxidation	Oxidise	Oxidised
Physical		
Plastic		
Polycrystalline		
Polygranular		
Propagation		
Property	Properties	
Radiation	Radiolytic	
Reactor	Reactors	
Relationship	Relate	Related
Sample		
Scale		
Shear		
Size		
Small		
Specimen		
Stiffness		
Strain	Strains	
Strength		
Stress	Stresses	
Structure	Structural	
Tension	Tensile	
Testing	Test	Tests
Theory	Theoretical	
Thermal	Thermally	
Toughness		
Volume		
Weibull		
Yield		
Young's		

Table A.1 – List of literature search keywords

Appendix B - Model Generation Instructions

The following is a list of step-by-step instructions to be used for the creation and analysis of a graphite microstructure model in ANSYS. The following files and programs are required:

ModGen – Version 2.exe,
MatSet – Version 2.exe,
ANSYS 7.0 (or higher).

This guide assumes the user is familiar with ANSYS in terms of the location of commands and a fundamental knowledge of the ANSYS command language.

B.1 Generating the model .log files

1. Run the ModGen – Version 2.exe file.

2. Enter the required parameters:

    - Input Number Of Units Across;
    - Input Number Of Units High;
    - Enter Maximum Percentage Of Porosity;
    - Input Extrusion Depth.

3. The first two parameters determine the model dimensions in the x and y directions. The porosity parameter limits the amount of porosity in the model meaning that voids in the model will never go above the stated level, but can be

any percentage below this. The extrusion depth determines the thickness of the model and its default value is 1, giving thickness but enabling the study to be essentially 2-dimensional. To generate a true 2-dimensional model, set this value to 0.

4. Select "Generate" and an output of the ANSYS log file will be displayed. This can be reviewed and edited to create the required abstract microstructure. Note: for the creation of any model above 70x70 unit size the "AGlue, All" must be removed (this is to prevent ANSYS from locking up. A work around for this operation is detailed later).

5. Name and save the .log file in the required location.

B.2 Generating the material .log files

1. Run MatSet – Version 2.exe file.

2. Enter the filename including the .log extension.

3. Enter the total number of areas (entities) in the model (this is calculated using mn+n where m is the number of units vertically and n is the number of units horizontally).

4. Enter the number of porous entities in the model, determined by reading the total number of areas from the ANSYS window (see instructions later) and subtracting this from the total number of entities.

5. Enter whether it's an area or volume.

6. The output .log file will be generated in the folder in which the program is stored.

B.3 Building the model in ANSYS

Import the model .log file using File -> Read input from… (select the location the pre-generated files are stored at). This step will build the microstructural model to be analysed.

Note: if the model is 70 x 70 units or under, then all the areas in the model will be automatically glued together (as defined in the .log file). If the model is larger than this then the gluing operation will have to be performed manually. Due to the large number of calculations involved in this process, it has been discovered that ANSYS will stop responding if it has to glue more than 5000 areas at one given time.

To manually glue a model, open the pre-processor menu -> Operate -> Booleans -> Glue -> Areas. This will open a dialog box that can be used to select the areas that need to be glued together. Use the "box select" option and define the first set of areas to be glued (ensuring no more than 5000 are selected) and allow the process to complete. The next set can then be selected for the same operation. Care must be taken to include a small section of the original process so that the whole model is glued together. This process can be repeated as many times as is necessary until all the areas are joined together.

The next step is to assign the material properties to the model, this is simply done by using the File -> Read input from… command to read in the material .log file. This will produce the "filler" and "binder" particles for the model. These can be displayed graphically through the following process:

- Select -> Entities…
  Choose "Areas" and "By Attributes"
  Select "Material Num" and "From Full"
  Input the material number (e.g. 2 for the filler particles, 1 for the binder) in the "Min, Max, inc" section
  Click "Sele All" then either "Apply", "OK" or "Replot"

This will display the selected material on the screen and store the array in ANSYS memory.

- Select -> Comp/Assembly -> Create Component…
  Give the component a name (e.g. material 2)
  Specify what it is comprised of (in most cases areas)
  Select OK
  This will create a predefined component for ease of selection of materials in the model.

- Select -> Everything
  PlotCtrls -> Style -> Colours -> Component Colours…
  The material 2 colour can then be specified and made distinct from the rest.

The model is now ready for meshing, i.e. setting up all the nodes and elements within the areas to allow the analysis to run. Select Meshing -> Meshtool, set the number of elements per line to 1 using the set lines option, and mesh all areas using the default settings. The element type has already been set in the model log file (4-noded 2-dimensional element, PLANE42) and the process will take a short while, with the progress being displayed at the top of the screen. A warning screen may be displayed during this process (regarding the suitability of SHELL elements in structural analyses) but it is not applicable to these analyses and can be ignored.

Once meshed, the constraints and loads need to be applied to the model. These are to be applied in several places, the bottom centre node, the lower surface and the upper surface.

- Solution -> Loads -> Apply -> Displacement -> On Keypoints
  Select the centre keypoint at the bottom of the model in order to fix it in all degrees of freedom (All DOF). This provides stability to the model and will eliminate any pivot points that can cause anomalous results.

- Solution -> Loads -> Apply -> Displacement -> On Lines

Select all the lines at the base of the model (zero displacement) in the y-direction. This can be done by selecting the very bottom set of lines with the "box select" function. Use "Apply" for this process rather than "OK".

Select all the lines at the top of the model (using the same technique as above) and displace these by 0.2% of the overall model height. The model height can be determined by using Pre-processor -> Model Checking -> KP Dist, and selecting a keypoint at the base and at the top and reading the distance from the screen.

All the constraints and loads should now be displayed on the screen and the model is ready for solving. If it is a large model and the producing it has taken several hours (this can occur for the models above 100 x 100 unit size) then it is advisable to save the database at this point using File -> Save as… and specifying a filename.

To solve the model: Solution -> Solve -> Current LS.

B.4 Viewing the results

Once the solution has been completed all the results can be viewed using the Post-processor.

- Post-processor -> Plot Results -> Nodal Solution

  This will open a dialogue box for viewing the individual results, most commonly used are the top three options: Displacement, Stress and Strain. Von Mises stress/strain and USUM (sum of the displacements in all directions) are the ones recorded (maximum values for the analysis are displayed as SMX and highlighted on the model).

- Post-processor -> Element Table -> Define Element Table

  This option is used to define two specific results, Stress Intensity (SINT) and Strain Energy (SENE). These must be defined before the results can be displayed. To do this, follow the above command path, select "add" and scroll

to the desired property. These results can be plotted using the Plot Element Table command, selecting average at common nodes before plotting.

Any of the results can be saved using Plot -> Hard Copy -> To File… command. This enables the user to select a picture file format and specify a file name for the image. Each of the saved files are stored in the working directory (usually C:\ANSYS), this is the same for the saved database files.

- Post-processor -> List Results -> Nodal Solution
  This command will produce a full list of the results for the reactions at each node as well as a summary of the reactions giving the maximum and minimum values in each direction. These list files can be saved in the same way as any simple text file.

Appendix C – ANSYS Graphical Predictions

The following contains a selection of the output plots from ANSYS to illustrate the predictions that have been obtained. The complete set of output plots can be viewed in Appendix D on the included CD-ROM in the folder ANSYS Predictions, and selecting the model size required and the loading condition (*i.e.* tension or compression).

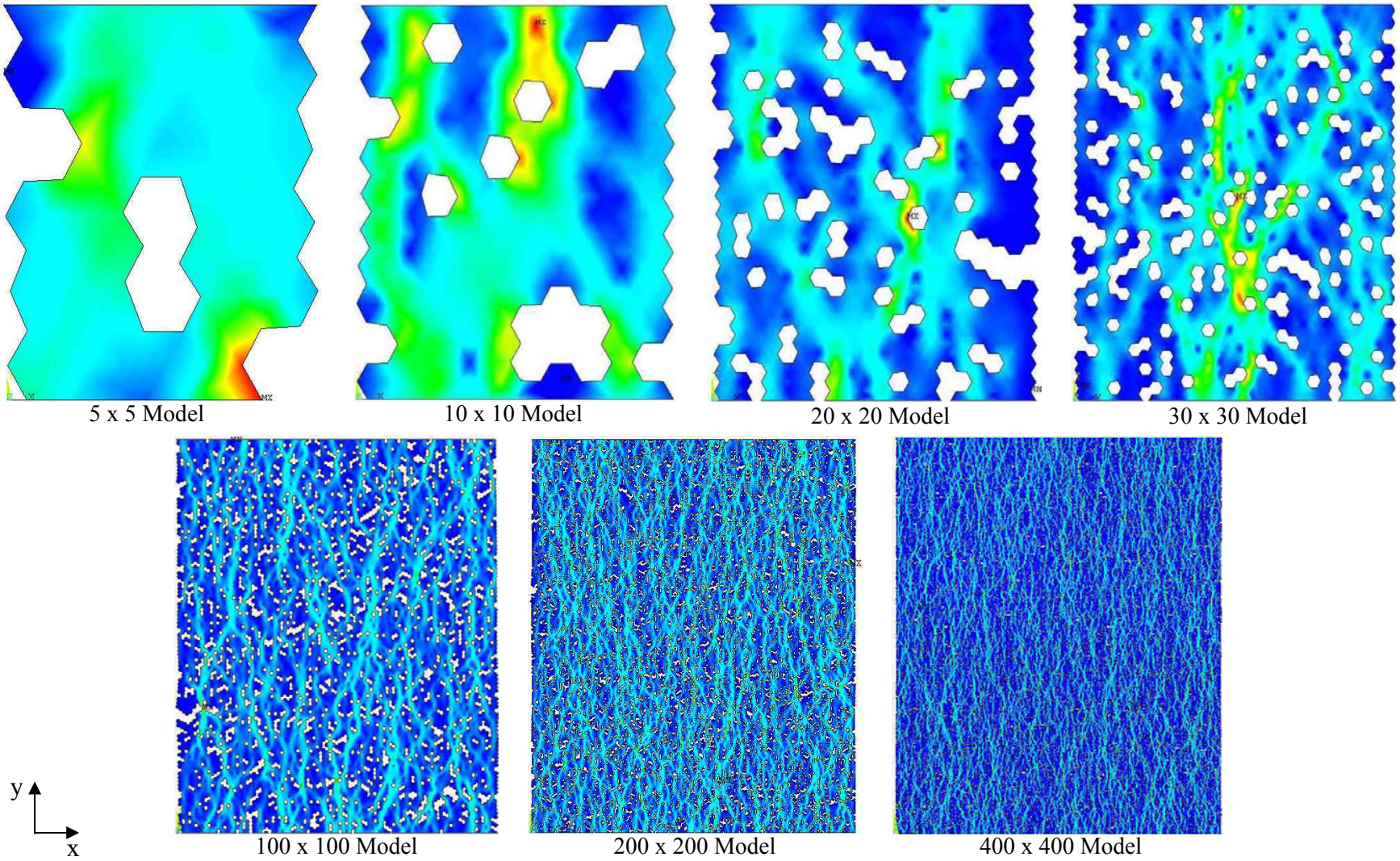

Figure C.1 – 1st principal stress predictions under tensile loading.

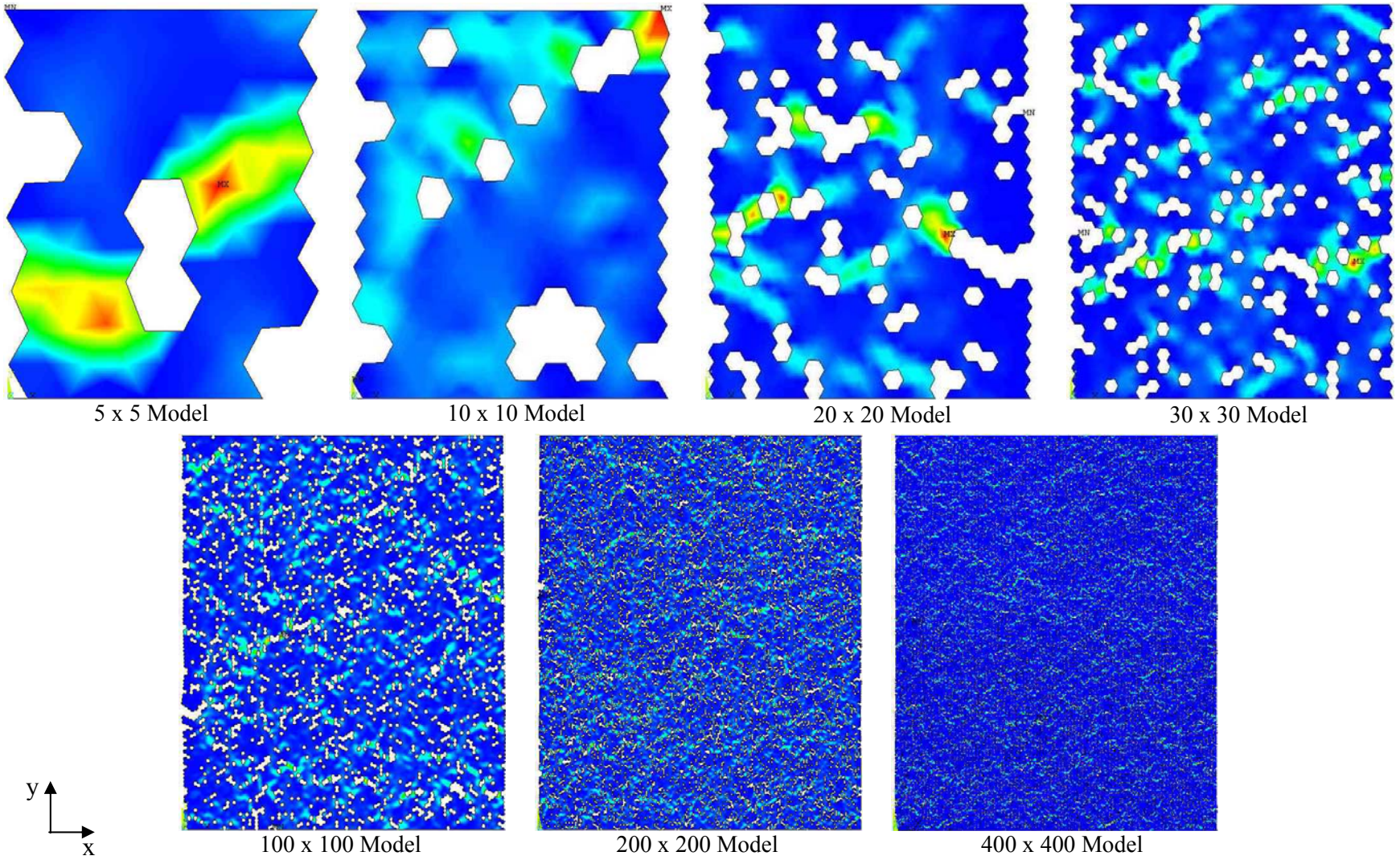

Figure C.2 – 1st principal strain predictions under tensile loading.

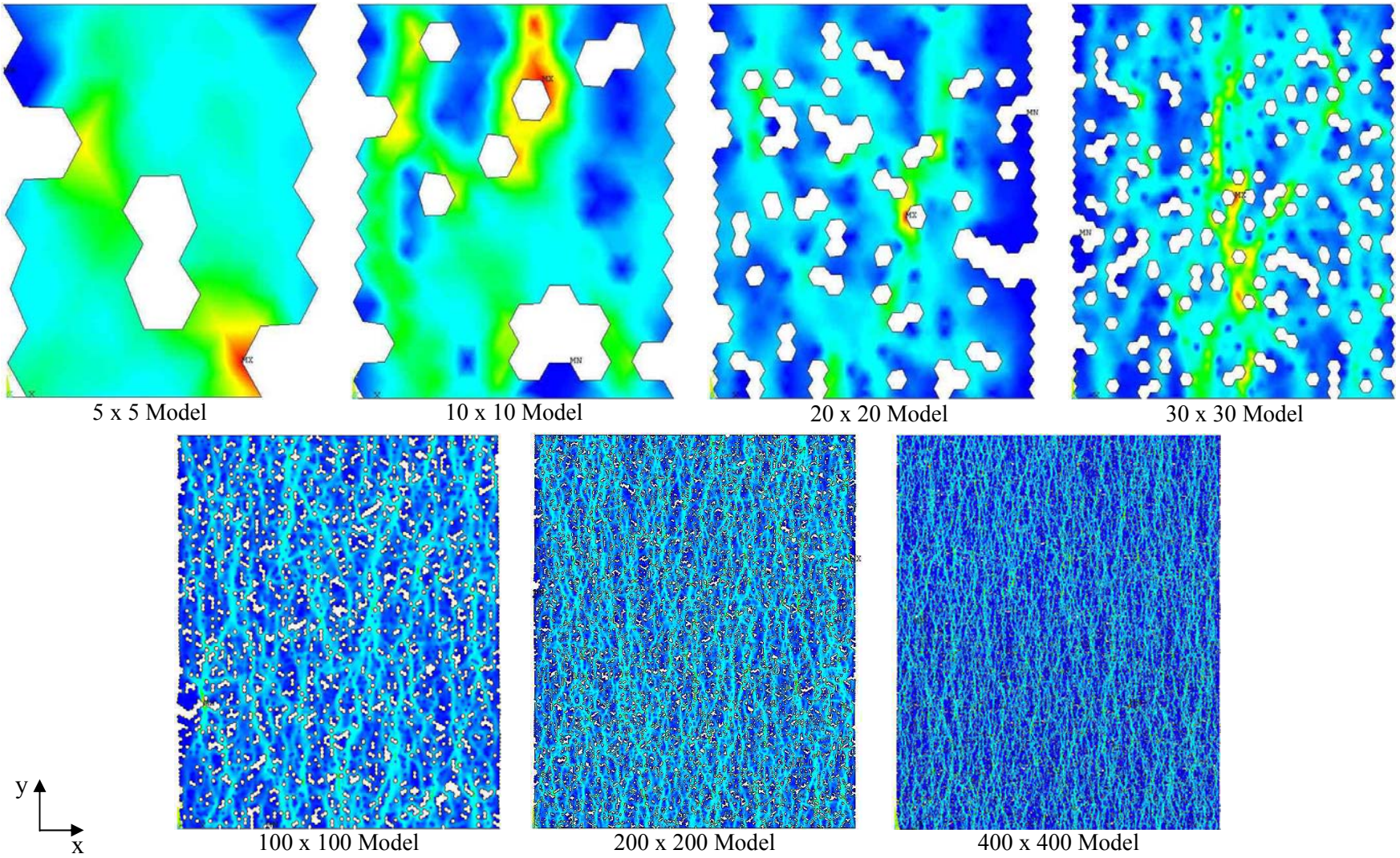

Figure C.3– Stress intensity predictions under tensile loading.

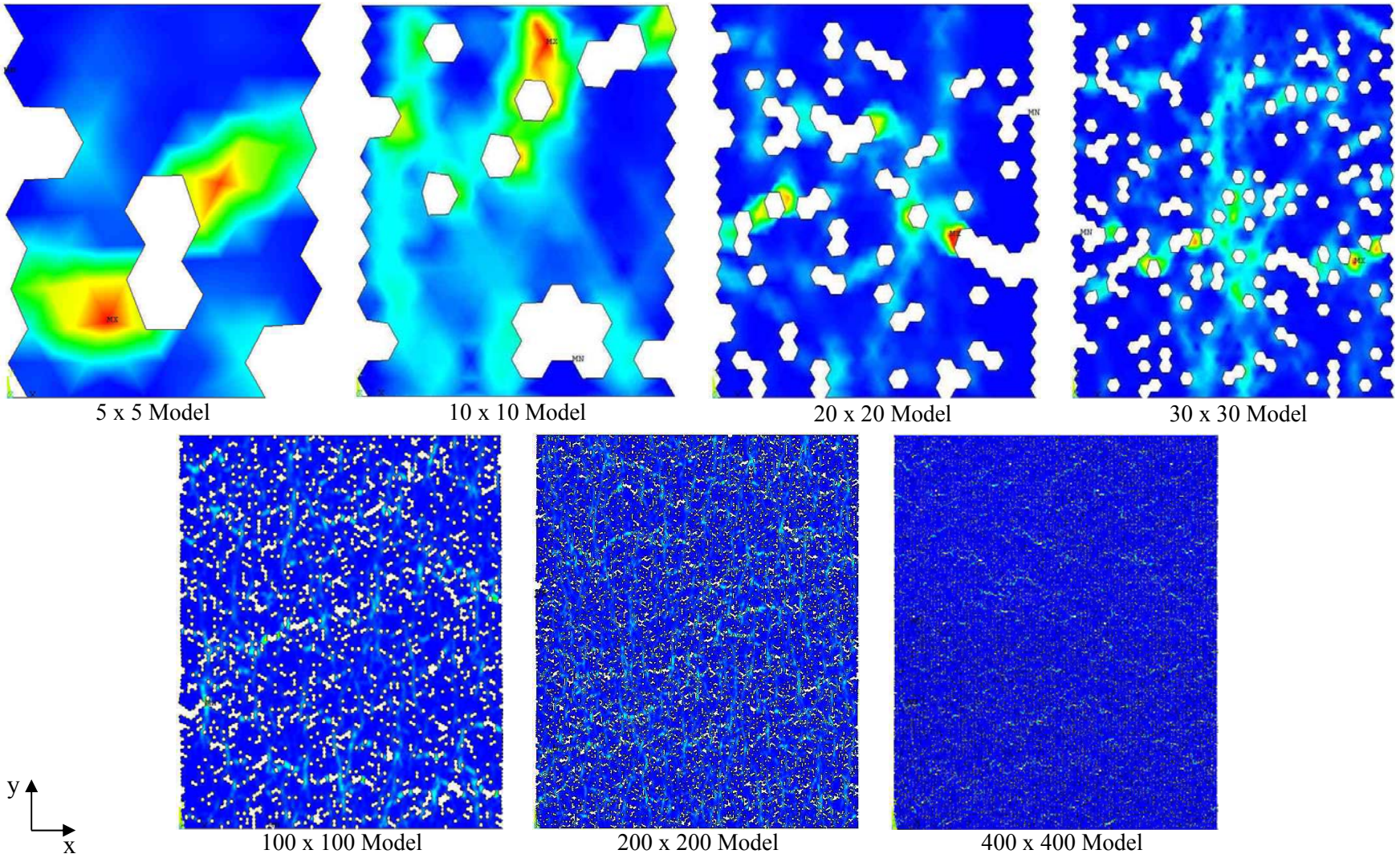

Figure C.4 – Strain energy predictions under tensile loading.

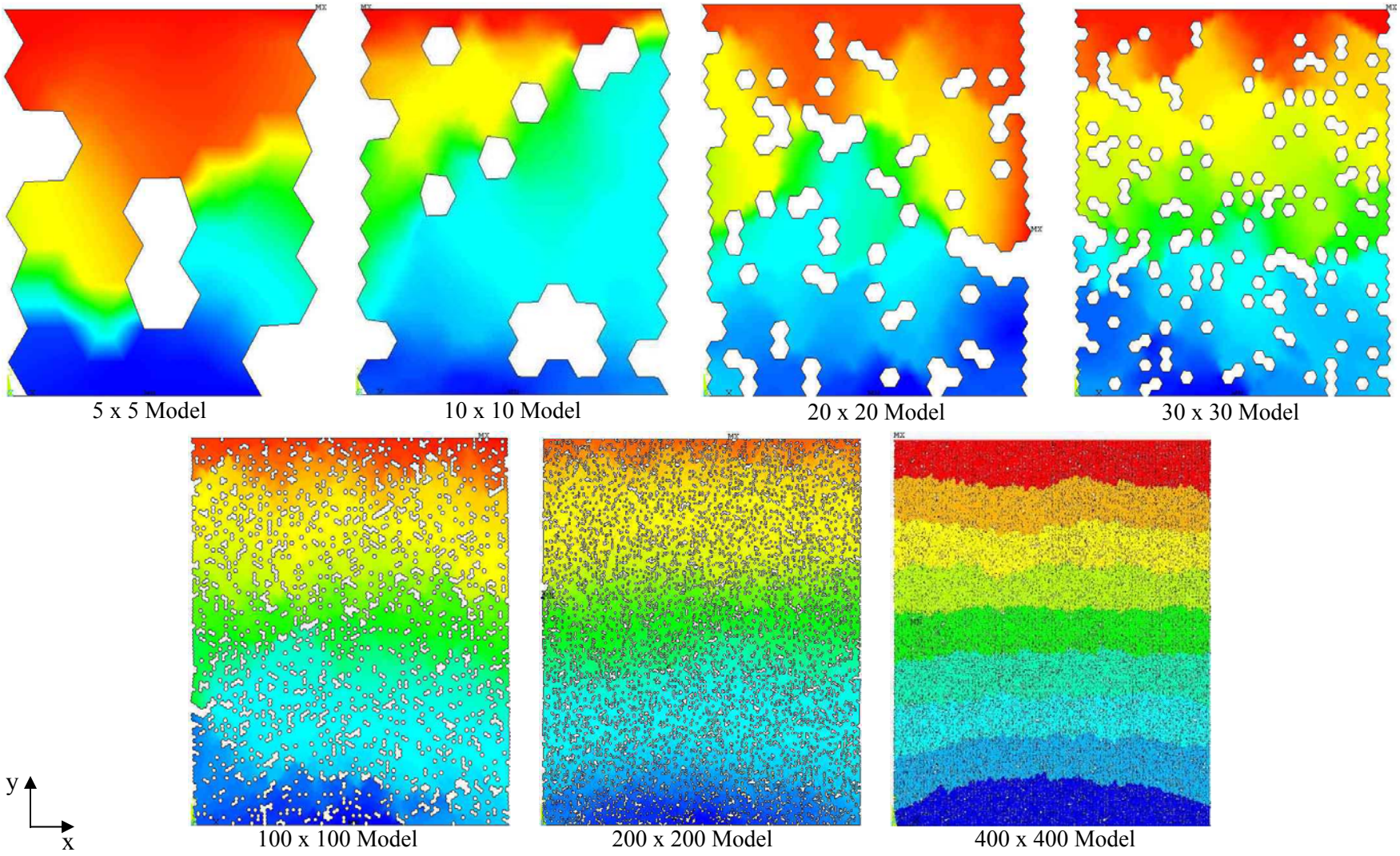

Figure C.5 – Displacement predictions under tensile loading.

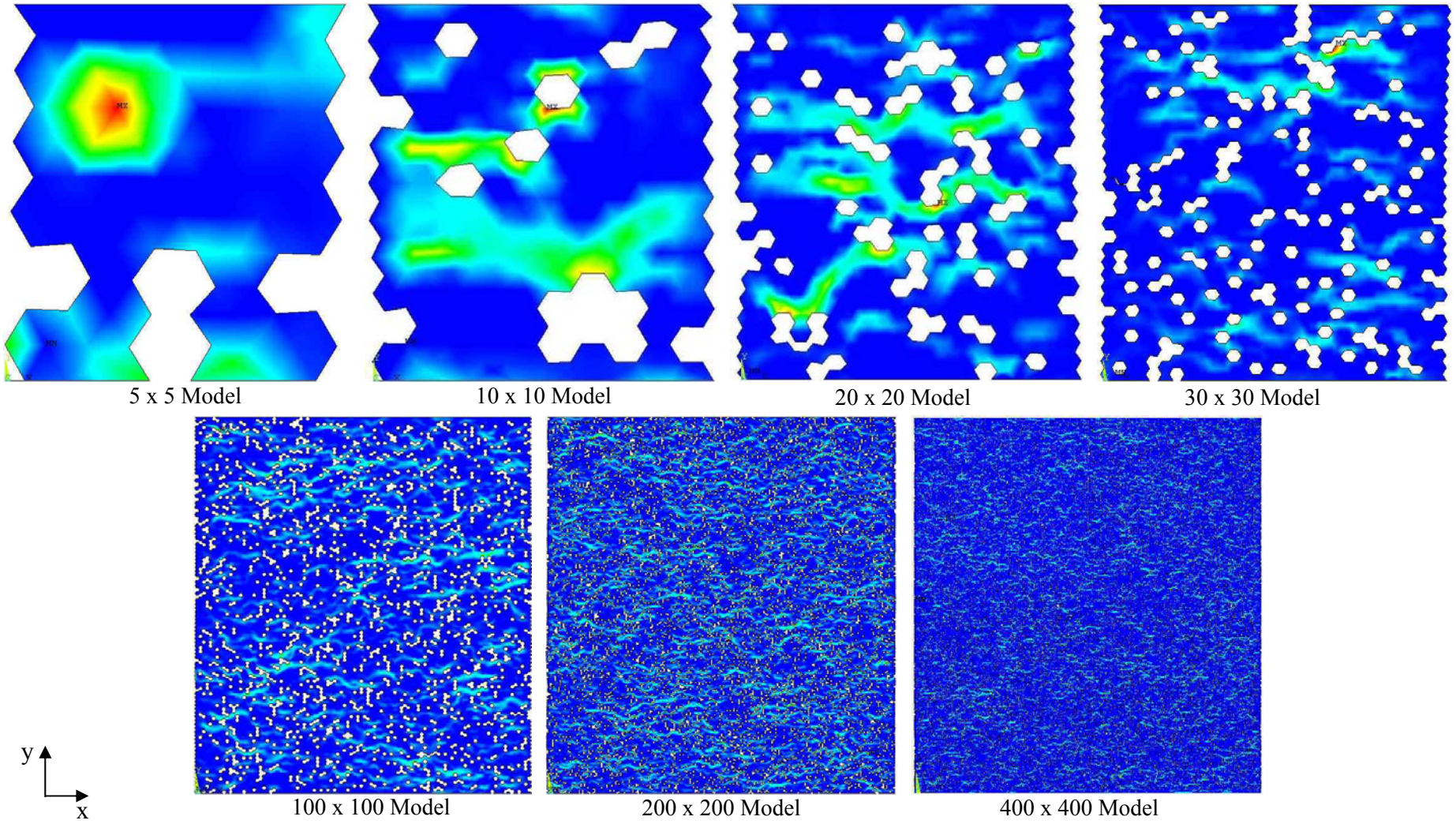

Figure C.6 – 1st principal stress predictions under compressive loading.

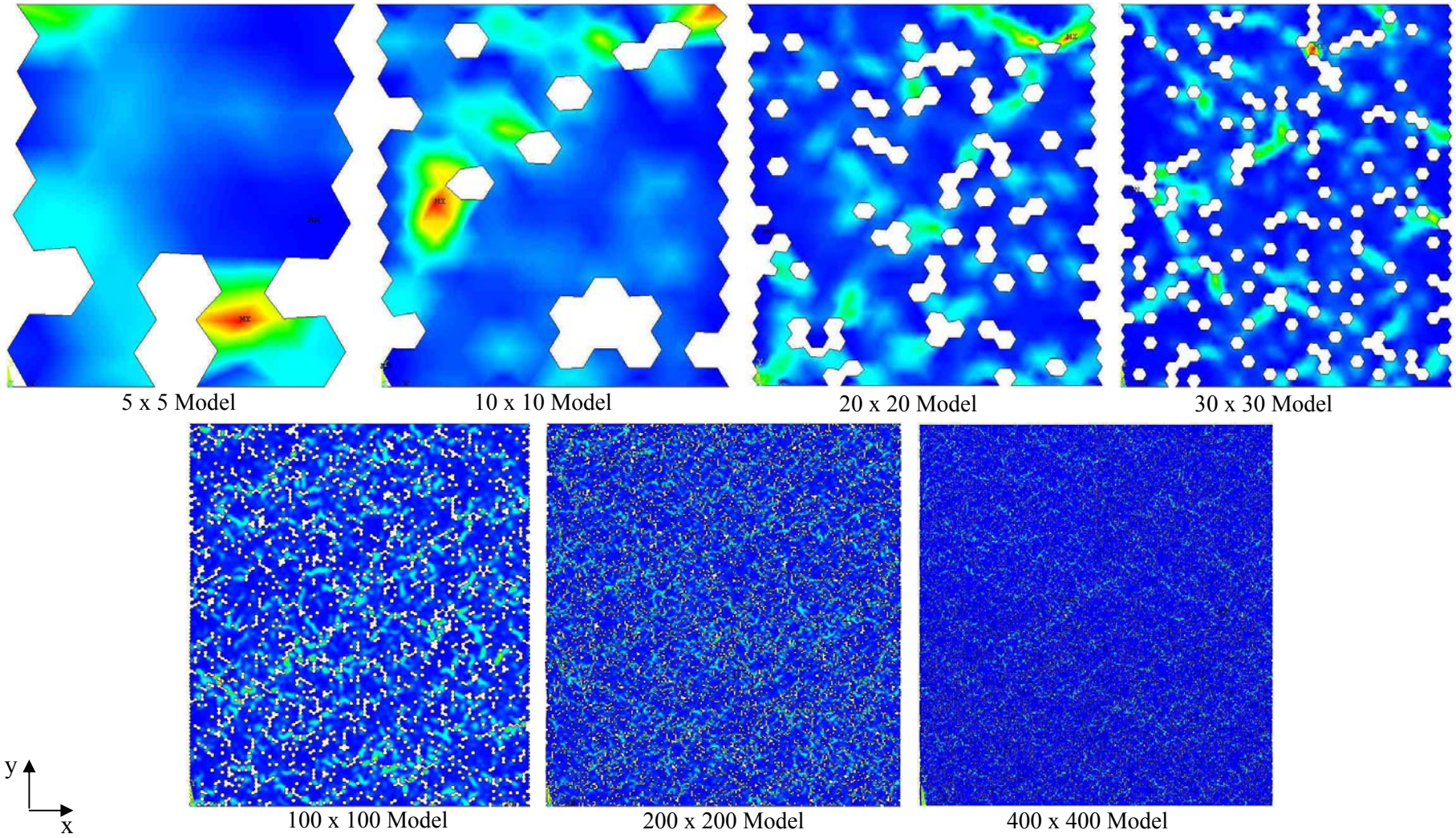

Figure C.7 – 1st principal strain predictions under compressive loading.

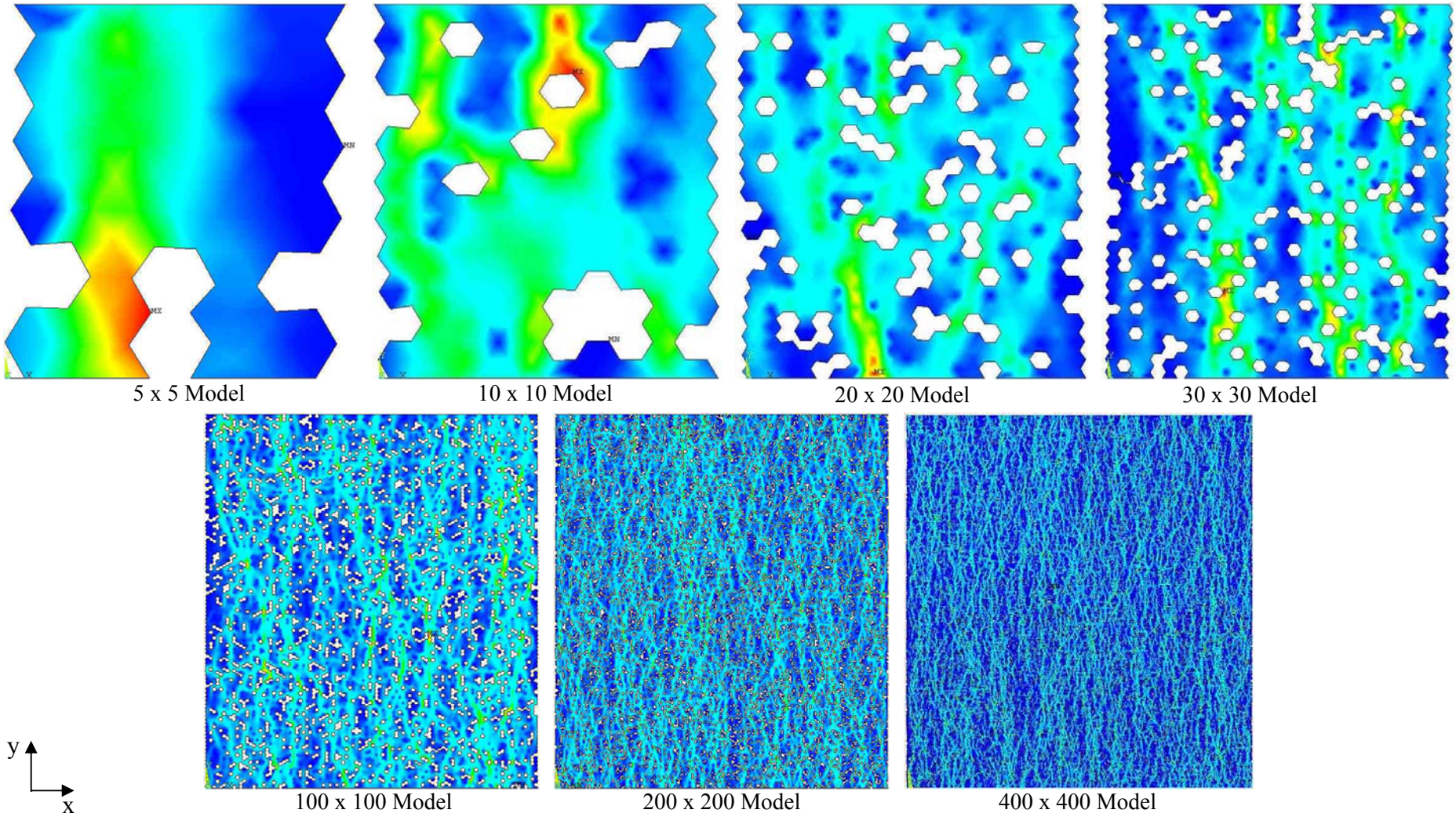

Figure C.8 – Stress intensity predictions under compressive loading.

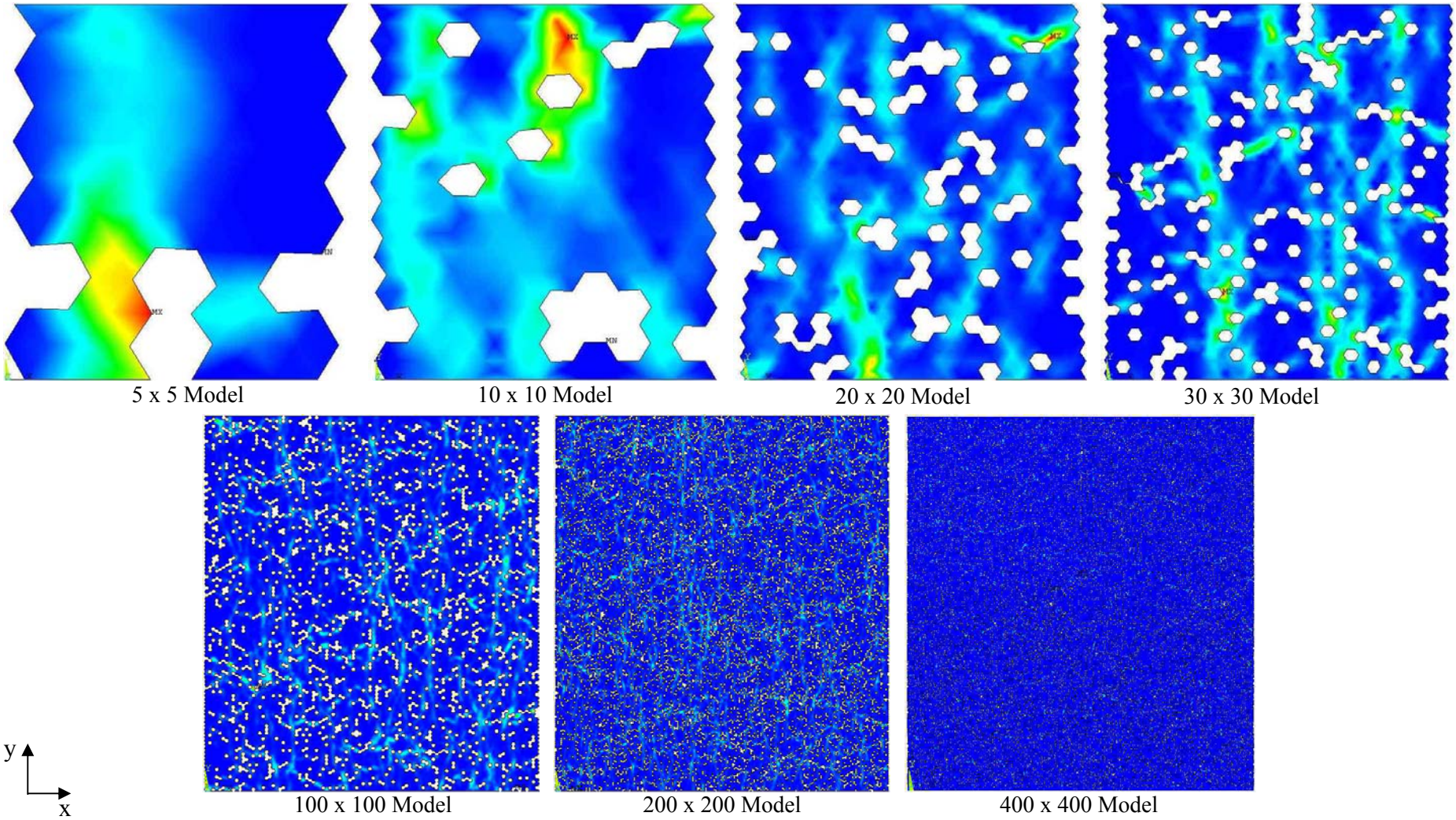

Figure C.9 – Strain energy predictions under compressive loading.

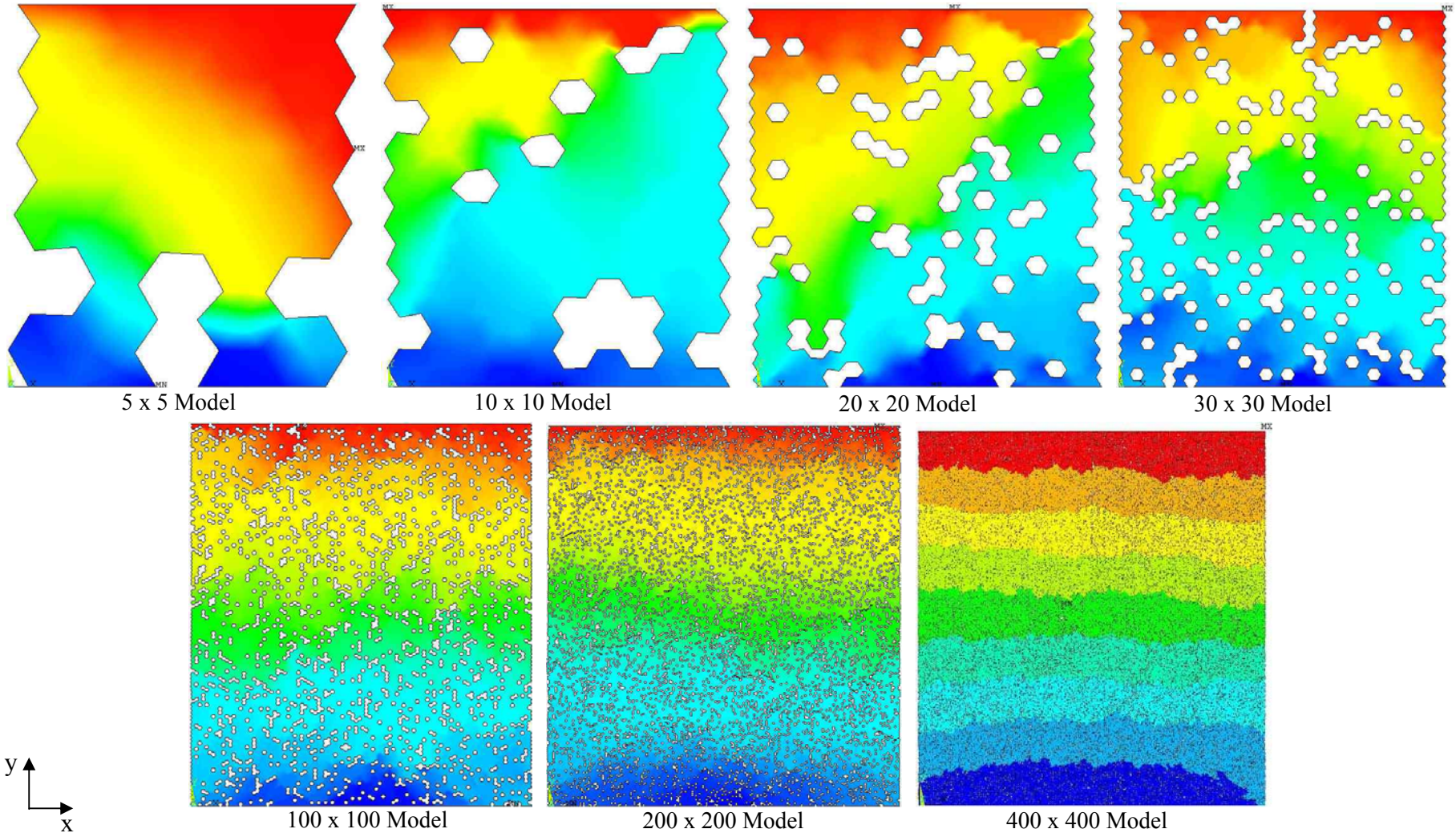

Figure C.10 – Displacement predictions under compressive loading.

Appendix D – CD ROM

The attached CD ROM contains relevant files to the research and discussion presented herein. The file structure of the CD ROM is as follows:

C++ Programs
- Material Setter (C code for the material setter program)
- Model Generator (C code for the model generator program)
- Required Files (Files for installation of programs)

Experimental Apparatus Drawings (Working drawings of the test equipment)

Modelling Programme
- ANSYS Results Files (Images from the modelling programme)
  - 05 x 05
  - 10 x 10
  - 20 x 20
  - 30 x 30
  - 100 x 100
  - 200 x 200
  - 400 x 400
- Modelling Programme Summary (Summary of the modelling results)

Testing Programme
- Notched Specimen Results (Results for notched specimen testing)
- Sample Dimension (All catalogued specimen dimensions)
- Testing Programme Summary (Results of the whole testing programme)
- Unnotched Specimen Results (Results for unnotched specimen testing)

Thesis Electronic Copy (.pdf file of this thesis)